Charm Jets in Photoproduction at HERA

Sanjay Padhi

Department of Physics
McGill University, Montreal, Canada
December 2003

A thesis submitted to the Faculty of Graduate Studies and Research in partial fulfillment of the requirements for the degree of Doctor of Philosophy

Abstract

Charm Jets in photoproduction have been studied in electron-proton collisions with the ZEUS detector at HERA, using an integrated luminosity of 120 pb^{-1}. Jets were reconstructed using the longitudinally invariant k_T-clustering algorithm. The dijet cross section for events containing at least one $D^{*\pm}$ charmed meson was measured as a function of various observables sensitive to hard scattering and the structure of the photon. The results are compared with predictions from leading-order parton-shower Monte Carlo simulations and with next-to-leading-order QCD calculations.

Differential cross sections of dijets as a function of the angle between the charm jet and the proton-beam directions in the dijet rest frame have been measured for samples enriched in direct or resolved photon events. The angular distribution shows a steep rise for resolved photon events in the photon direction, providing a clear first evidence for the existence of charm originating from the photon. The shallower rise for direct photon events as well as for the resolved photon events in the proton direction are consistent with the quark exchange diagrams.

The charm fragmentation function has also been measured for the first time at HERA. The fragmentation variable z is given by the ratio of $E + p_{\|}$ for the D^* meson and that for the associated jet, where E is the energy and $p_{\|}$ the longitudinal momentum relative to the jet axis. The measured cross section was compared to different fragmentation models incorporated in both leading- and next-to-leading-order frameworks and to the results from e^+e^- experiments.

Résumé

La production de jets charmés en photoproduction a été étudiée dans les collisions électron-proton à HERA avec le détecteur ZEUS. La luminosité intégrée était de 120 pb^{-1}. Les jets ont été reconstruits grâce à l'algorithme longitudinalement invariant de regroupement k_T. La section efficace des événements à jets doubles et contenant au moins un méson charmé $D^{*\pm}$ a été mesurée en fonction d'observables sensibles à la diffusion "dure" et à la structure du photon. Les résultats sont comparés avec les prédictions de simulations Monte-Carlo de premier ordre et de calculs QCD de second ordre.

Les sections efficaces différentielles des doubles jets on été mesurées en fonction de l'angle entre le jet charmé et la direction du proton dans le système du centre de masse des jets pour des échantillons enrichis en photons directs ou résolus. Les distributions angulaires démontrent une croissance prononcée dans la direction du photon dans les cas résolus, révélant ainsi, pour la première fois, l'existence de charme provenant du photon. La croissance plus lente dans la direction du proton dans les deux cas est consistente avec les diagrammes d'échange de quarks.

La fonction de fragmentation du charme a également été mesurée pour la première fois à HERA. La variable de fragmentation z est définie par le rapport des $E+p_{\|}$ du méson D^* et du jet qui lui est associé, où E est l'énergie et $p_{\|}$ est la quantité de mouvement longitudinale dans la direction de l'axe du jet. La section efficace mesurée est comparée à différents modèles de fragmentation incorporés dans le cadre de prédictions de premier et second ordres, ainsi qu'aux résultats des expériences e^+e^-.

Contents

Acknowledgments

The remarkable achievements of the HERA machine group were essential for the successful completion of this work. I am deeply grateful to my supervisor François Corriveau for his support throughout the period of my studies at McGill and research at DESY. I am grateful to Uri Karshon, Matthew Wing and Leonid Gladilin for their endless help and support during the study of these perturbative and non-perturbative aspects of QCD outlined in this thesis. I would like to thank Jon Butterworth and Malcolm Derrick for interesting discussions and suggestions during the editorial board process. Many people have contributed to the production of this thesis in many ways; to those not mentioned individually by name I apologise.

In various stages during my work I have benefited from discussions with several theoretical physicists, in particular, I would like to thank Stefano Frixione, Manuel Drees, Carlo Oleari and Hannes Jung for their suggestions. My special thanks goes to Nikolai Zotov and once again Hannes Jung for the useful discussions about k_T-factorisation approach.

Working as a Run Coordinator for the ZEUS Collaboration was indeed a great experience and opportunity to be part of this great scientific community. A very special thanks goes to Wolfram Zeuner, also to the component experts and colleagues Dorian Kcira and Stefan Goers with whom we made the ZEUS detector running at the beginning of HERA II.

Many thanks to all members of the Canadian High energy Physics group at ZEUS in particular to Sebastian Gliga with whom I shared many activities outside physics. The time spent in Hamburg was unforgettable, thanks to the colleagues and friends in and outside DESY and in particular to Friederike and her parents as well as Durgada and Utpalda.

Finally, I would like to dedicate the thesis to my parents who despite very limited resources gave me enormous support which can't even be expressed in words.

Chapter 1

Introduction

When around thirty years ago the charm quark was discovered [1] and consequently interpreted [2] as the first heavy quark, it came as a big surprise. The discovery of the bottom quark [3] along with the top quark [4] thereafter completed the heavy quark sector. Heavy quark physics subsequently provided a means for understanding the dynamics of the strong interactions. Quantum Chromodynamics (QCD) is the theory of strong interactions among the constituents of hadrons (quarks) via the exchange of massless gauge bosons (gluons), which themselves carry colour and interact with each other. Because of colour confinement, quarks and gluons cannot be directly observed, but give rise to sprays of particles called 'jets'. Heavy quark or charm initiated jets can therefore be used to study the dynamics of the hard scattering by providing a hard scale based on their heavy mass.

High-energy collisions at the HERA *ep* collider between a quasi-real photon (radiated from the electron beam) and a proton provide an ideal ground to probe the structure of the photon. However, given the Heisenberg uncertainty principle, the structure of the photon arises from quantum mechanical fluctuations in which it can split into quark anti-quark pairs, which can then further develop a hadronic structure. The photon structure can thus be probed by studying the fraction of the photon's momentum contributing to the production of the two jets. Measuring the angular distribution of the outgoing jets associated with at least one charmed meson allows the dominant subprocess to be determined. If one of the jets is ex-

plicitly tagged as a charm jet, the sign of the dijet scattering angle can be defined. Although the charm quark has not been observed to be a constituent of the photon and, if indeed it originates from the photon, the charm jet should lie in the photon hemisphere.

The nature of these charm-initiated jets thus constitutes an intuitive test of perturbative QCD (pQCD) and also allows to gain insight into the dynamical processes responsible for the transition from partons to hadrons. The hard process produces the charm quark which is then bound by soft interactions to the light ones into a hadronic final state, resulting in the observed $D^{*\pm}$ mesons having a fraction of the momentum of the original c-quark. This transition from a c-quark to a charmed meson (or fragmentation function) can be studied by using the fraction of the jet energy carried by the $D^{*\pm}$ meson along the jet axis. The definition of such energy fraction was developed in this thesis for *ep* collisions, and the resulting function has the same features as the those studied at e^+e^- collisions.

The analyses of the dijet angular distributions and charm fragmentation at HERA described above are presented in this thesis. First, the theory of hard photoproduction is presented. Then, in chapter 3, heavy quark production as well as recent results from different colliders are given. In chapter 4, the HERA collider and the ZEUS detector are presented, emphasizing the components used for the analyses. The relevant physics simulations are discussed in chapter 5. Jet production and the jet reconstruction algorithms are discussed in chapter 6, followed by the detailed event and kinematic reconstruction leading to the analyses presented in chapters 8 and 9. In the first analysis (chapter 8), the dijet angular distributions in charm photoproduction are presented, probing the hard scattering dynamics as well as the structure of the photon. The second analysis (chapter 9) provides the first measurement of the charm fragmentation function at HERA. Chapter 10 summarises the results presented in this thesis.

Chapter 2

Theory of Hard Photoproduction

The photon is a fascinating particle. Its concept originated in the first years of quantum mechanics. The study of electromagnetic interactions with matter then played a prominent role throughout the history of quantum theory. At first, the photon was regarded as structureless, and the theory was very successful in predicting various spectral lines and their intensities and in understanding other processes such as the atomic photoelectric effect. As the scale of available energies increased, it was found that through an interaction with a Coulomb field the photons could materialize as pairs of electrons. Although not usually thought of in these terms, this phenomenon was the earliest manifestation of photon structure.

The first generation of photon-nucleon fixed-target scattering experiments (for a review refer to [5]) revealed that in these reactions, the photon behaves like a vector meson (e.g., $\rho, \omega, \phi, ...$) with the quantum numbers of the photon, spin = 1, parity = -1 (Fig. 2.1). The anomalous photon component shown as a blob indicates that many diagrams can contribute to this process.

The lifetime[1] for a given state of the photon (say ρ meson), for $E_\gamma \sim 10$ GeV corresponds to $\triangle t = 2E_\gamma / m_\rho^2 \sim 3 \times 10^{-23}$ s = 9 fm, which is of the order of

[1] The convention $c = \hbar = 1$ and $\dfrac{e^2}{4\pi} = \alpha = \dfrac{1}{137.04}$ is used.

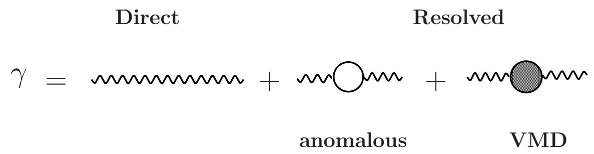

Figure 2.1: *Schematic representation of the different states of the photon: apart from the bare photon state (direct), the photon can fluctuate into quark-anti-quark pairs without forming a hadronic bound state (anomalous), or form a vector meson (VMD). The photon can therefore interact directly or through its resolved states.*

magnitude of a resonance lifetime. Therefore one can expect that the interacting photons behave like vector mesons (or more generally like a sum of vector meson states). This idea has led to a successful description of photon nucleon interactions (Vector Meson Dominance VMD [6]) which are well satisfied in interactions with small transverse energy in the final state.

With the increase in center-of-mass (CM) energies, several fixed target experiment at CERN and FNAL found significant deviations from the VMD model by observing an excess [7] of final-state hadrons with large transverse momenta. This could only be explained with the advent of QCD as the theory of strong interactions. In QCD the photon can either directly interact with quarks and gluons in the hadronic target (direct photon process) or could also resolve into a hadronic structure (resolved photon process) and the partonic constituents of the photon could participate in the hard scattering leading to jets in the final states. After the evidence for jet structure in the final state was reported [8], it led to a successful test of QCD. In the following section a short review of photon spectra is given, followed by an intuitive development of QCD as a theory and its application to photonic processes.

2.1 Virtual Photons

In current experiments at HERA, the photons are produced by highly energetic leptons, such that the photons carry only a fraction of the energy y of the incoming lepton ($y = E_\gamma/E_e$, where E_γ is the photon energy and E_e the initial energy of the electron). The photon spectra can then be understood in terms of y and the negative squared four momentum transfer Q^2, from the lepton. Various processes can then be distinguished in terms of the fluctuation time, based on the 'available energy scales' like Q^2.

- For a highly virtual photon ($Q^2 \gg 1$ GeV^2) to be emitted from an electron with energy $E_{e\gamma}$, the fluctuation time is given by:

$$\triangle t \approx 1/(E_{e\gamma} - E_e) = \frac{2E_\gamma}{Q^2}. \tag{2.1}$$

  The time of fluctuation for $E_\gamma = 1000$ GeV, $Q^2 = 400$ GeV^2 is $\triangle t(e \to e\gamma) = 1$ fm.

- For the emission of a quasi-real photon ($Q^2 \approx 0$ GeV^2) with no transverse momentum in the collinear limit (see 5.2.1), the corresponding time is

$$\triangle t = \frac{2E_\gamma}{Q^2_{min}}, \tag{2.2}$$

  where

$$Q^2_{min} \equiv \frac{m_e^2 y^2}{1-y}. \tag{2.3}$$

  and m_e is the mass of the electron. The ratio in Eq. 2.3 gives the smallest virtuality ($Q^2_{min} \approx 10^{-7}$ GeV^2), of photons that are generated by the electrons. At photon energies $E_\gamma = 1000$ GeV, the fluctuation time is $\triangle t(e \to e\gamma) \approx 4$ μm.

- Fluctuations of the photon into a quark anti-quark pair $q\bar{q}$ depend on the fraction of energy x_γ, carried by the quark relative to photon energy E_γ. For quasi-real photons,

$$\triangle t = \frac{2E_\gamma x_\gamma (1 - x_\gamma)}{m_q^2 + p_{t,q}^2} \tag{2.4}$$

  where m_q and $p_{t,q}$ are the mass and transverse momentum of the (anti-) quark. Assuming symmetric energy sharing (symmetric configuration) between the light quark ($m_q^2 + p_{t,q}^2 \approx \Lambda^2_{QCD}$, see chapter 3.) and its anti-quark with small $p_{t,q}$ at $E_\gamma = 1000$ GeV, the fluctuation time is $\triangle t(\gamma \to q\bar{q}) = 1000$ fm.

Therefore, the formation of a $q\bar{q}$ pair from a virtual photon is only allowed if the time of the $q\bar{q}$ fluctuation lies within the lifetime of the $e\gamma$ state. A subsequent formation of a gluon from the (anti-) quark $q \to qg$ has a lifetime which is then suppressed by the energy fraction x_γ and the quark energy fraction z, which is taken by the gluon: $x_\gamma \cdot z(1 - z)$. Using $x_\gamma = 0.5$ and an asymmetric energy sharing between the quark and massless gluon of $z = 0.1$ results in a lifetime which is 20 times shorter than the $\gamma \to q\bar{q}$ fluctuation.

In summary, since the lifetime of the exchanged photon is long with respect to the characteristic time of the hard-subprocess, the electron beam can be considered as a source of approximately massless, collinear photons, so that HERA can effectively be considered as a γp collider. This scenario is referred to as *photoproduction*. While at large $Q^2 \gg 1$, defined as the Deep Inelastic Scattering (DIS) regime, the time $\triangle t(\gamma \to q\bar{q})$ is therefore limited by the time $\triangle t(e \to e\gamma)$.

The collisions between protons and quasi-real photons as studied in this thesis at HERA correspond to energies around 8 - 39 TeV in the proton rest frame[2]. Therefore the $q\bar{q}$ fluctuations from the photon typically last $\sim 10^4$ fm, whereas the fluctuation involving gluons is 1-2 orders of magnitude shorter. Since the time of the photon fluctuations is large enough, both the direct and resolved photon interactions are possible.

2.1.1 The Equivalent Photon Approximation

As a source of quasi-real photons can be obtained from electrons, it is important to know the energy spectrum and the amount of photons which can be obtained from such a source. This can be obtained by calculating the electron-proton scattering in the equivalent photon approximation (EPA) [9]. In this approximation one considers a field of fast charged particles (electrons) radiating a flux of photons with energy distribution $n(y)$, where y denotes the fraction of the photon energy relative to

[2] within the fractional energy range $0.167 < y < 0.77$.

the electron energy. Electromagnetic electron-proton scattering can therefore be reduced to photon-proton interactions:

$$d\sigma_{ep}(y, Q^2) = \sigma_{\gamma p}(y) dn(y, Q^2) \tag{2.5}$$

where $\sigma_{\gamma p}$ is the total photo-absorption cross section and Q^2 is the virtuality of the photons. The first photon spectra were calculated by Weizsäcker and Williams [10] neglecting the virtuality of the photon and terms involving the longitudinal photon polarization. This approximation is usually referred to as the Weizsäcker-Williams approximation (WWA). By integrating the emission of quasi-real photons in a logarithmically large interval $Q^2_{min} \leq Q^2 \leq Q^2_{max} \ll 1$ GeV^2 and in a small fractional energy bin dy, the equivalent number of photons can be obtained as:

$$dn(y, Q^2_{max}) = f_{\gamma/e}(y, Q^2_{max}) dy \tag{2.6}$$

with

$$f_{\gamma/e} = \frac{\alpha}{2\pi}\left[\frac{1+(1-y)^2}{y}\ln\frac{Q^2_{max}}{Q^2_{min}} - 2m_e^2 y\left(\frac{1}{Q^2_{min}} - \frac{1}{Q^2_{max}}\right)\right] \tag{2.7}$$

Here α is the fine structure constant and Q^2_{min} is the kinematic lower limit given by Eq. 2.3. Fig. 2.2 a) shows the energy spectrum of quasi-real photons emitted by electrons for $Q^2_{max} = 0.01$ GeV^2. The number of photons decreases at large photon energies $y > 0.2$ by an order of magnitude, but rises steeply towards small photon energies $y < 0.2$.

The accuracy of the WWA has been studied for many processes [9]; in the case of photoproduction at HERA, the WWA is found to be better than 1%. For jet production with transverse jet energies $E_t^{jet} \gg \sqrt{Q^2}$ and un-tagged electrons with $Q^2 < 4$ GeV^2, corrections to the WWA modify [16] the cross section typically by 5%. The total photon-proton cross section, $\sigma_{tot}^{\gamma p}$, as a function of γp center-of-mass energy ($W_{\gamma p}$) is shown in Fig. 2.2 b). At lower energies, the process where the photon fluctuates into a vector boson dominates the cross section, while at higher $W_{\gamma p}$ energies the VMD cannot explain the observed excess in the final state. It can however be explained in terms of parton-parton scattering within QCD, which will be discussed in the following section in more detail. It should be noted that the

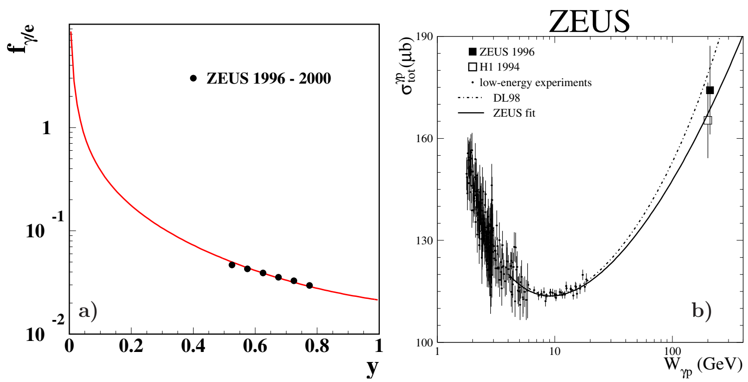

Figure 2.2: **a)** *The energy spectrum of quasi-real photons emitted by electrons is shown as a function of the scaled photon energy $y = E_\gamma/E_e$, for a maximum virtuality of $Q^2 = 0.01$ GeV^2, the data compared is for dijet events associated with charm quarks presented in chapter 8, assuming the symmetric configuration between c and $\bar{c}$, i.e. $x_\gamma > 0.5$.* **b)** *Measurement of the total photon-proton cross section at different center-of-mass (CM) energies (open square: H1 [11], full square: ZEUS [12], filled circles: the low-energy data [13]). The dotted dashed curve shows the DL98 parameterization [14] and the solid curve is from ZEUS fit [15].*

"VMD" label is synonymous with that part of resolved photon interactions where the quark anti-quark pair of the photon forms a bound state before the scattering process.

2.2 QCD as a Theory

Quantum Chromodynamics (QCD) is the theory of strong interactions, one of the four fundamental forces in nature. It describes the interactions between quarks and gluons, and in particular how they bind together to form the class of particles called hadrons. In the 1970's QCD was developed as a field theory where the strong interaction is mediated by a massless spin-1 boson, the gluon. The crucial difference between QED (Quantum Electrodynamics) and QCD is that gluons carry colour and hence couple to each other, whereas photons do not carry charge. This means that the strong coupling 'runs' in an opposite direction to the electromagnetic coupling and becomes very large at low momenta, ensuring that the coloured quarks and gluons are confined within colour singlet hadrons. The basic interactions that occur in almost all colliders are not between the quark themselves, rather between the composite hadrons, which is the basis of so called Parton Model as described below.

2.2.1 The Quark Parton Model

Feynman's parton model [17] assumed that the proton is composed of free point-like constituents, called partons. The basic idea was based upon an intuitive picture of inclusive high energy scattering of composite systems, where one requires a very large momentum transfer. Suppose, for example, that hydrogen atoms are collided against each other and it is required to have pairs of electrons with large momentum transfer in the final state. The most likely mechanism for producing such an event is the collision of two electrons from the two incoming hydrogen atoms as shown in Fig. 2.3. If the transverse momenta of the electrons are much larger than the hydrogen atom binding energy, to a good approximation the cross section can be calculated from the elementary electron-electron scattering, applied to a beam of incoming free electron. The fact that a high transverse momentum is required, implies that the binding of the electrons to the nuclei cannot have an important effect, in other words electrons behave as free particles in the collision. Although after the two electrons collide, the remaining constituents of the original atoms (i.e the protons in the case of hydrogen) can also be found in the final state, thus the high momentum transfer is instead needed for the reaction to take place in a very short transverse distance. This requirement of high momentum transfer is generally referred as 'hard scattering'. On the other hand, if the momentum transfer were of the same size as the momentum of the electron in the atom, the binding properties of the system could no longer be neglected, hence the interaction would be referred

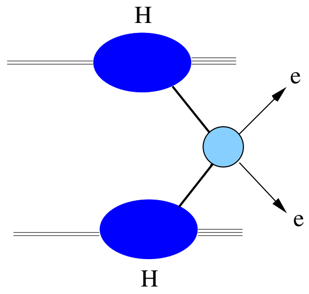

Figure 2.3: *Scattering of two hydrogen atoms.*

to as 'soft scattering', and would depend on phenomenological "binding energy" models to describe the cross section.

Assuming now that the same hydrogen atom is moving in a relativistic system, in which all the constituents have velocities of the order of c, the speed of light, and comparable energies, the distribution of these constituents within the system due to time dilation may then be considered as 'frozen' (non-interacting). The hard scattering cross section would then depend only on the probability of finding a constituent within the system.

Deep Inelastic Scattering (DIS) : A Practical example

Consider an incoming high energy lepton that scatters from a hadronic system (proton) via the exchange of a virtual gauge boson. Depending on the exchange boson, two major processes can occur. If the exchange particle does not carry any electrical charge (γ, Z^0), the process is called *neutral current* DIS, leading to the same lepton in the final state as in the initial state. On the other hand, if the exchange boson carries an electric charge ($W^{\pm}$) with a different final state (such as a neutrino) from the initial lepton, it is then called *charged current* DIS. In the following, only neutral current processes will be considered, although most of the arguments can also be applied to charged current events.

Based on the assumptions made for the hydrogen atoms, we apply simple rules:

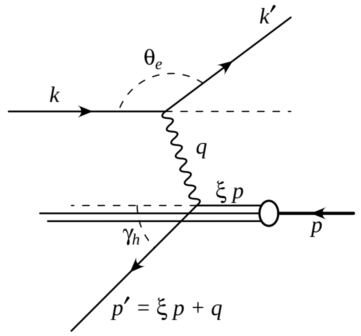

Figure 2.4: *Deep inelastic scattering at HERA.*

the cross section to be considered is of the colliding partons. We then assume that the hadron beam is a beam of partons, with momentum distributed according to the Parton Distribution Functions (PDF), while neglecting the transverse momenta of the partons and their masses.

As illustrated in Fig. 2.4, k and k' are the incoming and scattered lepton 4-momenta respectively and p is the 4-momentum of the incoming proton. At a given center-of-mass energy ($\sqrt{s}$), the kinematical variables of the process are described by two variables among the following Lorentz-invariant quantities:

$$Q^2 = -q^2 = -(k-k')^2, \qquad x = \frac{Q^2}{2p\cdot q} \tag{2.8}$$

$$y = \frac{p\cdot q}{p\cdot k} = 1 - \frac{p\cdot k'}{p\cdot k} = \frac{1-\cos\theta_e}{2} \quad \text{(Partonic CM frame)} \tag{2.9}$$

where, Q^2, is the negative square of the momentum transfer and specifies the virtuality of the exchange boson. For $Q^2 \gg 0$ the process is in the DIS regime, whereas for $Q^2 \sim 0$, the process takes place in the photoproduction regime, where a real photon collides with the proton. The variable y in the partonic CM frame relates to the electron scattering angle θ_e and in the laboratory frame is the fractional energy loss of the electron.

In the "infinite momentum frame" of the proton, where the proton momentum is large such that all the constituents move along the proton direction and all masses can be neglected, the conservation of 4-momentum implies:

$$0 \approx m^2 = (\xi p + q)^2 = (\xi p)^2 - Q^2 + 2\xi(p\cdot q)\ ; \tag{2.10}$$

$$\Rightarrow \xi \approx \frac{Q^2}{2\,p\cdot q} = x\ , \tag{2.11}$$

Therefore, the Bjorken scaling[3] variable x [18], is simply the fraction ξ of the longitudinal proton momentum carried by the parton in the hard scatter. The corresponding partonic process is the scattering of a charged parton[4] with the lepton. The cross section for this process, assuming a single boson is exchanged, can be written as [19]:

$$\frac{d^2\sigma^{ep}}{dQ^2dx} = \frac{4\pi\alpha^2}{Q^4}\left(1 - y + \frac{y^2}{2}\right)\cdot\sum_q e_q^2 f_q^p\left(x, Q^2\right) \tag{2.12}$$

where $f_q^p(x, Q^2)$ is defined as the probability to find a parton of type q inside the proton with fractional momentum x, at the probed scale Q^2, of the total proton momentum, the sum running over all charged partons. The functions f_q^p are the parton distribution functions (PDF). Experimentally one measures s, y and x, without imposing any conditions on the hadronic final state. The parton model from Eq. 2.12 makes rather remarkable predictions:

1. It shows that DIS cross section scales with energy (s or Q^2) at fixed x and y. It means that if one measures a hadronic cross section at an experiment with a given energy, one can exactly predict the total hadron cross section at some other collider with higher energies (Scaling).
2. The functional form of the cross section depends on y, which is the characteristic of vector interaction with fermions and thus is the direct evidence of the fact that charged partons are fermions (*spin* - $\frac{1}{2}$).

[3] Scaling means that if a cross section is expressed in terms of dimensionless parameters (like x and y), in the limit of high energy the cross section scales like the energy in the process, according to its canonical dimension ($\frac{d\sigma}{dxdy} \propto \frac{1}{Q^2}$).
[4] a quark or an anti-quark.

Usually Eq. 2.12 is rewritten using new functions F_1 and F_2, called structure functions,

$$\frac{d^2\sigma^{ep}}{dQ^2dx} = \frac{4\pi\alpha^2}{xQ^4}\left[(1-y)F_2(x) + \frac{1}{2}y^2 2xF_1(x)\right] \tag{2.13}$$

which are related to the parton distribution function of the proton by

$$F_2\left(x,Q^2\right) = \sum_q e_q^2 x f_q^p\left(x,Q^2\right) \tag{2.14}$$

$$F_1 = \frac{1}{2x}F_2. \tag{2.15}$$

This latter relation between F_1 and F_2 is known as the Callan-Gross relation [20]. A third structure function F_3 for the proton must be introduced for the description of scattering through the exchange of heavier Z^0 and $W^\pm$ bosons.

The scaling phenomena of the parton model were first observed in a DIS experiment at SLAC [21] around 1968 as shown in Fig. 2.5. Even more spectacular was the observation in e^+e^- annihilations that the total hadron production cross section was found to be proportional to the muon pair cross section at high energies. On the other hand the experimental confirmation of the Callan-Gross relation along with the y dependence (existence of spin-$\frac{1}{2}$ charged partons) of the cross section allowed the identification of Feynman's partons with Gell-Mann's quarks and the model was called the Quark-Parton Model (QPM). It should be mentioned that the fractional charge of the partons was confirmed using neutrino-nucleon scattering and the postulated number of three valence quarks in the proton and neutron obtained from the Gross-Llewellyn Smith (1969) sum rule[5]

$$\int_0^1 \frac{dx}{2}\left({F_3}^{\nu p}(x) + {F_3}^{\nu n}(x)\right) = \int_0^1 dx\Big[u_v(x) + d_v(x)\Big] = 3\ , \tag{2.16}$$

was experimentally confirmed to be 3.2 ± 0.6 [22].

[5] The sum rule counts the number of valence quarks in the nucleon.

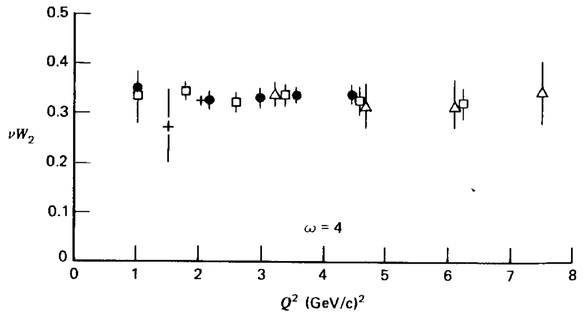

Figure 2.5: *The scaling behaviour in terms of structure function F_2 (denoted by νW_2; where $\nu = \frac{Q^2}{2M\,x}$ is the energy of the exchanged boson) is shown as a function of Q^2 for $\omega = \frac{1}{x} = 4$ as measured at SLAC.*

2.2.2 Improved Parton Model

Although the Quark-Parton Model gives a reasonable description of the experimental results for lepton-nucleon interactions, it cannot explain how the charged partons are bound together to form the proton. Also the assumption that the proton consists solely of charged quarks implies that the sum of the momenta of the charged partons would be equal to that of the proton;

$$\int_0^1 dx \sum_q x f_q^{(p)}(x) = 1 \tag{2.17}$$

Experimentally, this value was found to be ≈ 0.5 [23]. This, along with the confirmation of the number of valence quarks (Eq. 2.16) implied that the protons not only consist of charged spin-$\frac{1}{2}$ partons (quarks) but also of neutral particles. Evidence for the existence of these neutral particles (gluons) was found in 1979 via the observation of 3-jet events in e^+e^- annihilation at DESY [24].

The QPM approach, where the proton consists only of quarks was then modified to include gluons. This then became the foundation of QCD, where quarks interact via the exchange of gluons. Gluons themselves can split into quark pairs or gluons.

But the inclusion of gluons also creates the possibility for them to split into quark pairs which can have a transverse momentum component. In the case of DIS the gluon can even couple to longitudinally polarized photons. Thus the leading order prediction of Callan-Gross is violated by incorporating these radiative corrections. One then defines $F_L = F_2 - 2xF_1$ as the longitudinal structure function. The cross section from Eq. 2.13 can then be rewritten as

$$\frac{d^2\sigma^{ep}}{dQ^2dx} = \frac{4\pi\alpha^2}{xQ^4}\left[[1+(1-y)^2]F_2(x) - y^2 x F_L(x)\right] \tag{2.18}$$

Thus in case of scaling F_L must vanish and as such a non-zero F_L as in Fig. 2.6 a) is a further indication of the QCD corrections to the QPM. Fig. 2.6 b) shows the scaling behaviour at medium x and its violation for high and small x with increasing Q^2.

In DIS, when the virtual photon meets the fast moving proton at low Q^2, it can only resolve partons that are about the size or larger than its associated wavelength[6] λ. Thus the resolution of low Q^2 photons is limited to the valence quark of the protons. With increase in Q^2, the wavelength λ shrinks hence additional structure originating from the inner radiations (gluon radiation from a quark and/or gluon splitting) of the protons can be resolved (made 'visible'). These partons with the given momentum fraction x, see their momenta reduced due to these inner radiations and with increase in Q^2 the large number of "visible" sea quarks and gluons leads to a steep rise in the parton density F_2^{em}. At large x, where the valence quarks dominate, the quark density F_2^{em} falls with an increase in Q^2.

2.3 Perturbative QCD Framework

As can be seen from the previous section (also Fig. 2.7), just by introducing gluons in the QPM picture, not only was the scaling violated, but also major divergencies/singularities come into play. Based on the assumption that no strongly interacting particles appear in the initial state, these divergences can be classified as Ultraviolet and Infrared, as described below.

[6] The wavelength $\lambda \propto \frac{\hbar c}{\sqrt{Q^2}} = \frac{0.197}{|q|}$ GeV fm.

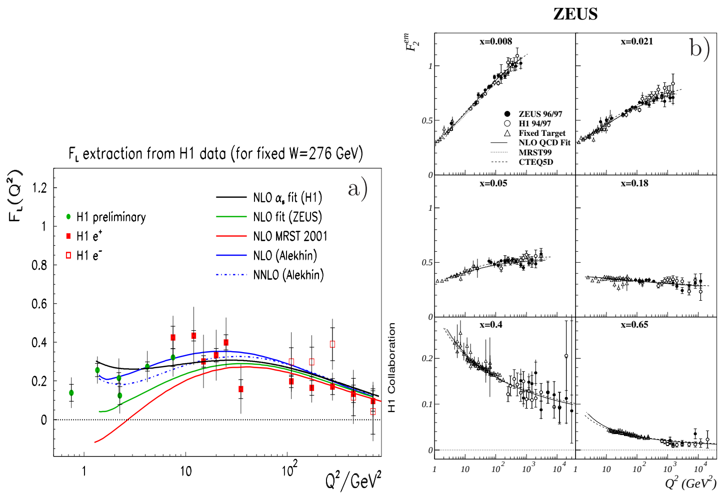

Figure 2.6: *a) Q^2 dependence of $F_L(x, Q^2)$ at fixed γP center-of-mass energy, $W = 276$ GeV measured by H1 [25]. The curves represent various parameterisations within a given theoretical calculation at next-to-leading and next-to-next-leading orders (NLO and NNLO). b) The results [26] from ZEUS (solid points) and H1 (open points) for F_2^{em} versus Q^2, for six bins at fixed x, are compared with results from fixed target experiments NMC, BCDMS and E665 (triangles).*

2.3.1 Ultraviolet Divergencies

Consider a virtual photon, with virtuality $Q^2 = -q^2$, much larger than the typical hadronic scales. The cross section at 0^{th} order (Born level) of the strong coupling simply comes from diagram a of Fig. 2.7. The ratio of the hadronic cross section to the cross section for the production of say a $\tau^+\tau^-$ lepton pair is given by [27]:

$$R_0 = \frac{\sigma(\gamma^* \to hadrons)}{\sigma(\gamma^* \to \tau^+\tau^-)} = 3\sum_q e_q^2, \tag{2.19}$$

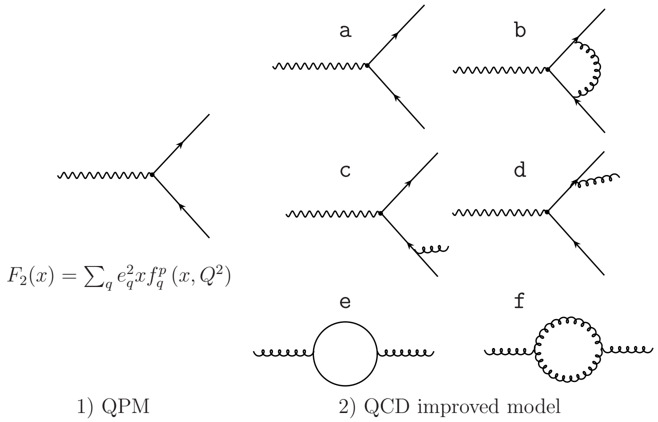

Figure 2.7: *Diagrams for QCD calculation up to the order of α_s.*

where q runs over the light quark species[7], and e_q is the electric charge of the quark of flavour q. The factor of 3 accounts for the colours[8] of each quark. The correction of order α_s (strong coupling constant) to R_0 comes from the interference of the virtual diagram `b` with diagram `a`, plus the square of the real emission graphs (`c` + `d`). After adding the diagrams with self-energy (`e` + `f`) on the fermion lines, the corrected value of R_0 becomes

$$R = \begin{cases} R_0\left(1 + \frac{\alpha_s}{\pi}\right) & \text{order } \alpha_s, \\ R_0\left(1 + \frac{\alpha_s}{\pi} + \left[c + \pi b_0 \log\frac{M^2}{Q^2}\left(\frac{\alpha_s^2}{\pi}\right)^2\right]\right) & \text{order } \alpha_s^2, \text{ with } b_0 = \frac{33-2n_f}{12\pi}. \end{cases} \quad (2.20)$$

where n_f is the number of light flavours. The ultraviolet (UV) cutoff parameter $M = \mu{\cdot}\exp(1/\epsilon)$ comes from dimensional regularisation [29] in $d = 4-2\epsilon$ dimensions. Hence, as $\epsilon \to 0 \Rightarrow M \to \infty$. Thus the expression for R becomes divergent. This is called Ultra-Violet divergence. The divergence can be dealt using the principle of

[7] The formula is valid in all cases as long as one neglects the quark masses.

[8] The quantum number colour was needed in order not to violate the Pauli principle and thus could explain the formation of Ω^- (after its discovery [28]), made out of three strange (s), quarks with same flavour and spin.

renormalisation. By redefining α_s in terms of an arbitrary scale μ_R

$$\alpha_s(\mu) = \alpha_s + b_0 \log\frac{M^2}{\mu_R^2}\alpha_s^2 \quad (2.21)$$

the result in terms of $\alpha_s(\mu_R)$ instead of α_s is then given by:

$$R = R_0\left(1 + \frac{\alpha_s(\mu_R)}{\pi} + \left[c + \pi b_0 \log\frac{\mu_R^2}{Q^2}\right]\left(\frac{\alpha_s(\mu_R)}{\pi}\right)^2\right) + \mathcal{O}(\alpha_s(\mu_R)^3) \quad (2.22)$$

The formula for R is finite, so that any deviation from R_0 can be used to evaluate $\alpha_s(\mu_R)$. For τ leptons, Eq. 2.22 at the Z mass, $\alpha_s(m_Z) = 0.122 \pm 0.006$ [27] was found to be in remarkable agreement with the LEP1 results 0.124 ± 0.021 [30].

The consequence of the above procedure results in expressing the coupling constant in terms of μ_R, called the renormalisation scale. The redefinition of α_s or the content of renormalisation is much deeper. It states that up to any order in perturbation theory, one can remove all UV divergences from a physical quantity just by redefining the coupling constant. From Eq. 2.21 the lowest order in an expansion of α_s is given by:

$$\alpha_s(\mu_R) = \frac{1}{b_0 \log \mu_R^2/\Lambda_{QCD}^2} = \frac{12\pi}{(33-2n_f)\log Q^2/\Lambda_{QCD}^2}; \quad \mu_R = Q. \quad (2.23)$$

Λ_{QCD} is the hadronic scale parameter that defines the value of α_s at large scales. The parameter Λ_{QCD} is only defined through the formula for $\alpha_s(\mu_R)$ and the formula has meaning only for large $\mu_R > \Lambda_{QCD}$. One then defines $\mu_R^2 = Q^2$, such that no large logarithms appear in the perturbative expansion (Eq. 2.22) to be performed. This is applicable down to Λ_{QCD}, which has been experimentally determined to be $\Lambda_{QCD} = 0.2 \pm 0.1$ GeV [31]. For $Q^2 \gg \Lambda_{QCD}^2$, the events are referred to as DIS events. For the low Q^2 photoproduction region, Q^2 cannot be a hard scale, thus the transverse momentum of the jets may define a scale for the event. This hard scale allows the possibility of comparing experimental results with perturbative QCD calculations. There are two further important consequences of Eq. 2.23.

1. As $Q^2 \to \infty \rightsquigarrow \alpha_s(Q^2) \to 0$: means that quarks and gluons behave like quasi-free particles when probed at high energies. This property is called '**asymptotic freedom**'.

2. As $Q^2 \to \Lambda^2_{QCD} \rightsquigarrow \alpha_s(Q^2) \to \infty$: implies that the coupling becomes stronger as the separation between q and $\bar{q}$ increases and the perturbation series breaks down at low Q^2. Because of the gluon self-coupling, the exchanged gluons will attract each other (unlike photons) and so the colour lines of force get constrained to a tube-like region (called a flux tube) between the quarks. If this tube has a constant energy density per unit length (κ), then the potential energy ($V(r) \sim \kappa r$) of the interaction will increase with the separation, so the quarks and gluons can never escape the hadron. This is called "**Infrared slavery**", which is believed to be the origin of the confinement mechanism and explains why free quarks are not observed [32].

2.3.2 Infrared Divergencies - Evolution Equations

In the previous section it was found that the total corrections to α_s at a given order are finite and using renormalisation the UV effects can be reabsorbed into a redefinition of the strong coupling constant. Now if the individual real contributions with a gluon in the final state and the virtual contributions where only the quark-anti-quark pair in the final state are considered (as shown in Fig. 2.8), they are individually infinite. The cross section for producing the extra gluon can be divergent in three regions:

- when the emitted gluon is in the direction of the outgoing quark,
- when the emitted gluon is in the direction of the outgoing anti-quark,
- when the emitted gluon is soft.

The first two kinds of divergences are called collinear divergences, while the last one is called a soft divergence. All are of infrared (IR) type, which means they involve long distances. The cross section is sensitive to long distance effects, like the fermion masses, the hadronisation mechanism, etc. and there is nothing like renormalisation for the IR divergences. We define these as "final-state" IR effects.

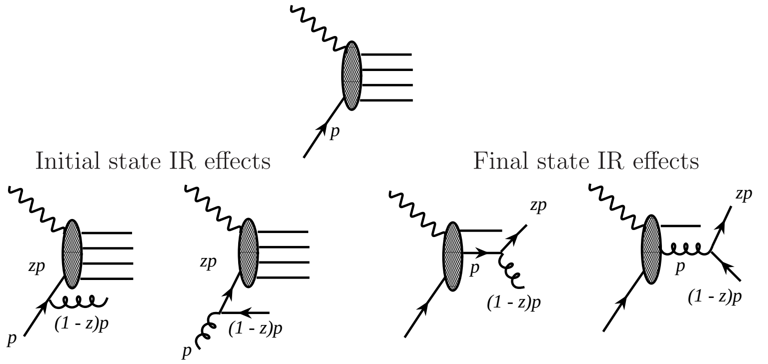

Figure 2.8: *Initial and final state Infrared divergences.*

In the case of hadron initiated interactions, there can exist initial state soft and collinear singularities which contribute to the hard scattering, defined as "initial-state IR effects" in this thesis.

Factorisation

In order to separate the infrared divergences within the hadrons from the hard interaction which is calculable in perturbative QCD (pQCD), the soft (non-perturbative) processes need to be isolated. The regularisation mechanism by which one can separate (factorise) the theoretical description into calculable hard and soft parts is called factorisation.

As can be seen from the hydrogen atom example, the requirement of the hardness of a process leads to a separation between the part which can be calculable ("perturbative" or "short distance") and the soft process ("long distance") which depends on the binding energy models. QCD also justifies the existence of such soft processes where the pQCD breaks down due to infrared slavery. Thus, the non-calculable final-state IR divergences can either be incorporated inside a certain model (like parton showers, see chapter 5) or can be absorbed inside the fragmentation (transition from partons to hadrons). The fragmentation functions can then, not only depend on a certain factorisation scale μ_F (similar to μ_R), but are also universal (hard process independent) as is the case with PDFs (see below).

To deal with initial-state IR effects, consider the parton density as predicted by the QPM. Using a similar procedure as in section 2.3.1 for the ratio R, the parton density from Eq. 2.14 can be modified to:

$$\frac{F_2(x,Q^2)}{x} =$$

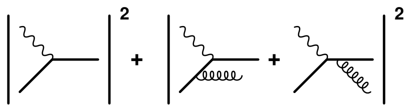

$$\begin{aligned}
&= \sum_q e_q^2 \int_x^1 \frac{dy}{y} q(y) \left[\delta(1-\frac{x}{y}) + \frac{\alpha_s}{2\pi}\mathcal{P}_{qq}(\frac{x}{y})\log\frac{Q^2}{\lambda^2}\right] \\
&= \sum_q e_q^2 \int_x^1 \frac{dy}{y} q(y) \left(\mathbb{I} + \frac{\alpha_s}{2\pi}\log\frac{Q^2}{\lambda^2}\mathcal{P}_{qq}(\frac{x}{y})\right); \quad \mathbb{I} = \delta(1-\frac{x}{y}) \\
&= \sum_q e_q^2 \left(q(x) + \Delta q(x,Q^2)\right)
\end{aligned} \tag{2.24}$$

where $q(y) = f_q^p(y)$ is the quark structure function, λ is a lower limit on the transverse momentum to regularise IR divergences which occur as the square of the transverse momentum tends to zero. This is known as IR cutoff. The splitting function $\mathcal{P}_{ij}(z)$ represents the probability of a parton j emitting a parton i, and then having a momentum fraction $z = x/y$. From Eq. 2.24, the IR correction term $\Delta q(x,Q^2)$ can be written as:

$$\Delta q(x,Q^2) \equiv \frac{\alpha_s}{2\pi}\log\frac{Q^2}{\lambda^2}\int_x^1 \frac{dy}{y} q(y)\mathcal{P}_{qq}(\frac{x}{y}) \tag{2.25}$$

The quark structure function can be calculated for any Q^2, given some reference value $q(x, Q^2 \sim Q_0^2)$ by considering the change in $\Delta q(x,Q^2)$ for a small change in $\log Q^2$:

$$\frac{dq(x,Q^2)}{d\log Q^2} = \frac{\alpha_s}{2\pi}\int_x^1 \frac{dy}{y} q(y)\mathcal{P}_{qq}(\frac{x}{y}) \tag{2.26}$$

In general, for a given parton density function $[f_i(x,\mu^2)] = [q_i(x,\mu^2), g(x,\mu^2)]$ of a flavour i with the splitting function $\mathcal{P}_{ij}$, Eq. 2.26 be rewritten as:

$$\begin{aligned}
\frac{\partial f_i(x,\mu)}{\partial\mu^2} &= \int_x^1 \frac{dy}{y}\sum_j \mathcal{P}_{ij}(x/y) f_i(x/y,\mu), \\
or \quad \frac{\partial f_i(\mu)}{\partial\mu^2} &= \sum_j \mathcal{P}_{ij} f_i(\mu)
\end{aligned} \tag{2.27}$$

This is called Altarelli-Parisi equation [33]. The splitting function $\mathcal{P}_{ij}(x/y)$ at any order can have the expansion:

$$\mathcal{P}_{ij}(x/y) = \frac{\alpha_s(\mu_R)}{2\pi}\mathcal{P}_{ij}^0(x/y) + \left(\frac{\alpha_s(\mu_R)}{2\pi}\right)^2 \mathcal{P}_{ij}^1(x/y) + ... \tag{2.28}$$

where $\mathcal{P}_{ij}^0(z = x/y)$ from [34] is the leading order splitting function, as shown Fig. 2.9. It represents the probability of a parton j of momentum fraction y emitting a parton i of momentum fraction x. Its non-vanishing terms are:

$$\begin{aligned}
\mathcal{P}_{qq}^0(z) &= \mathcal{P}_{\bar{q}\bar{q}}^0(z) = \frac{4}{3}\frac{1+z^2}{1-z}, \\
\mathcal{P}_{qg}^0(z) &= \mathcal{P}_{\bar{q}g}^0(z) = \frac{1}{2}\left[z^2 + (1-z)^2\right], \\
\mathcal{P}_{gq}^0(z) &= \mathcal{P}_{g\bar{q}}^0(z) = \mathcal{P}_{qq}(1-z) = \frac{4}{3}\frac{1+(1-z)^2}{z}, \\
\mathcal{P}_{gg}^0(z) &= 6\left[\frac{z}{1-z} + \frac{1-z}{z} + z(1-z)\right].
\end{aligned} \tag{2.29}$$

The next-to-leading order $\mathcal{P}_{ij}^1$ functions can have new terms with $\mathcal{P}_{q_iq_j}^1$ for $i \neq j$ and $\mathcal{P}_{q_i\bar{q}_j}^1$ for any i and j can be found in [35].

In summary, while attempting to get the radiative corrections to a partonic process, large corrections appear which depend on the unknown low scale dynamics λ. However, these large corrections are then reabsorbed into a redefinition of parton densities. The parton density redefinition does not depend upon the hard process in question and hence is universal and can allow to make predictions for one process after measuring the PDFs in another. The physical cross section $\sigma(p)$ for a process p, can then be defined in terms of these new parton densities $f(\mu)$:

$$\sigma(p) = f(\mu)\otimes\hat{\sigma}(p,\mu_R), \tag{2.30}$$

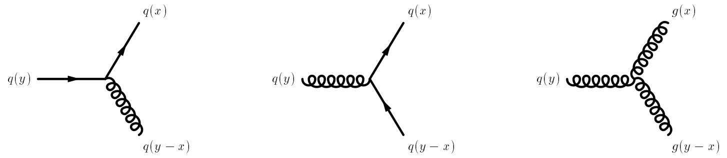

$\mathcal{P}_{qq}(\frac{x}{y}) = \mathcal{P}_{gq}(\frac{y-x}{y})$ $\quad \mathcal{P}_{qg}(\frac{x}{y}) = \mathcal{P}_{qg}(\frac{y-x}{y})$ $\quad \mathcal{P}_{gg}(\frac{x}{y}) = \mathcal{P}_{gg}(\frac{y-x}{y})$

Figure 2.9: *The splitting functions at lowest order in α_s. The diagram on the left shows the gluon radiation by a (anti)quark and the two diagrams on the right show the gluon splitting into two partons.*

where $\otimes$ is the convolution operator. Eq. 2.30 is the QCD-improved parton model formula. It forms the basis for the application of perturbative QCD to phenomena initiated by hadrons. Now, instead of the partonic cross section in the QCD-improved parton model, the *short distance* cross section $\hat{\sigma}$ was obtained by subtracting the infrared sensitive (*or long distance*) part from the partonic cross section. Thus, the short-distance cross section gets controlled by the high momenta scale $\mu_R \sim Q$ of the hard process which can then be calculated in perturbation theory. On the other hand, the scale $\mu = \mu_F$ introduced in the new PDF $f(\mu)$ is called the factorisation scale. The considerable difference from the "naive" Parton Model formula is the appearance of the scale μ_F in the parton densities. The scale at which α_s is evaluated is the renormalisation scale and both are assumed in this thesis to be equal to the hard scale.

The consequence of the above procedure is that the new PDF $f(\mu_F)$ contains uncalculable long distance effects to be measured by using Eq. 2.30 with some reference hard process, which is typically chosen to be DIS. One can then extract $f(\mu_F)$ at a given scale, given the fact that the left hand side of Eq. 2.30 is μ independent and that the short-distance cross section $\hat{\sigma}$ is calculable in pQCD and thus also its scale dependence. This allows to compute the parton densities at any scale, once measured at a given initial value Q_0.

2.3.3 DGLAP Evolution

The integro-differential equations resulting from the parton evolution as a function of Q^2 are called Dokshitzer-Gribov-Lipatov-Altarelli-Parisi (DGLAP) equations [33, 36]. They consist of terms where either a gluon is radiated from a type of parton or by considering a parton evolved from a gluon in a pair production process. The evolution of the quark density distribution in Eq. 2.26 can be modified to include gluon radiations as shown in Fig. 2.9. The same procedure can also be applied to the evolution of gluon density distribution by considering gluons resulting from quarks or gluons. The resulting evolution equation[9] as a function of Q^2 can be written as:

$$\frac{dq_i(x,Q^2)}{d\log Q^2} = \frac{\alpha_s(Q^2)}{2\pi}\int_x^1 \frac{dy}{y}\left[q_i(y,Q^2)\mathcal{P}_{qq}(x/y) + g(y,Q^2)\mathcal{P}_{qg}(x/y)\right],$$

$$\frac{dg(x,Q^2)}{d\log Q^2} = \frac{\alpha_s(Q^2)}{2\pi}\int_x^1 \frac{dy}{y}\left[\sum_i \left(q_i(y,Q^2)\mathcal{P}_{gq}(x/y)\right) + g(y,Q^2)\mathcal{P}_{gg}(x/y)\right] \qquad (2.31)$$

where $q_i(x,Q^2)$ is the quark density function for a given quark flavour i and $g(x,Q^2)$ is the gluon density function. In terms of convolution notation $\otimes$, the DGLAP equations take the form:

$$\frac{dq_i(x,Q^2)}{d\log Q^2} = \frac{\alpha_s(Q^2)}{2\pi}\left[\mathcal{P}_{qq}\otimes q_i(x,Q^2) + \mathcal{P}_{qg}\otimes g(x,Q^2)\right],$$

$$\frac{dg(x,Q^2)}{d\log Q^2} = \frac{\alpha_s(Q^2)}{2\pi}\left[\sum_i \mathcal{P}_{gq}\otimes q_i(x,Q^2) + \mathcal{P}_{gg}\otimes g(x,Q^2)\right] \qquad (2.32)$$

The solution of the DGLAP equation in the leading logarithm approximation (LLA) represents the parton distributions as a function of x at any Q^2, provided that their x dependence at an input scale Q_0^2 is known. The minimum value of Q_0^2 cannot be presently calculated so it relies on an experimental determination. The solutions are based on the assumption that the i^{th} emitted gluon "ladders" corresponding to the terms $(\alpha_s \log Q^2)^i$, are ordered in their transverse momenta k_{T_i} as shown in

[9] At leading order $\mathcal{P}_{ij} = \mathcal{P}^0_{ij}$ unless otherwise stated.

Fig. 2.10 (left)

$$k_{T_1}^2 \ll k_{T_1}^2 \ll \ldots \ll k_{T_{n-1}}^2 \ll k_{T_n}^2 \ll Q^2 \tag{2.33}$$

It should be noted that the terms in Eq. 2.28 are truncated to the first order (leading order, LO) to arrive at these evolution equations. The next to leading order (NLO corresponding $\mathcal{P}_{ij}^1$) terms will modify these equations, which again means truncating the splitting function at a given order. According to Catani [37], this truncation of the splitting function at a fixed perturbative order is equivalent to assuming that the dominant dynamical mechanism leading to scaling violations is the evolution of the parton cascade with strongly ordered transverse momenta. For small $x \rightarrow 0 \Rightarrow \mathcal{P}_{gg} \approx \frac{6}{z}$ (from Eq. 2.29) and at large $Q^2 \rightarrow \infty$, the solution [38] of the gluon density function for a rung with running α_s at a given momentum fraction x_0 is given by:

$$xg(x,Q^2) \sim G_0 \exp\left[2\sqrt{\frac{3}{\pi b_0}}\sqrt{\log\frac{x_0}{x}\log\frac{\alpha_s(Q^2)}{\alpha_s(Q_0^2)}}\right] \tag{2.34}$$

with $G_0 = xg(x,Q_0^2) \sim$ constant and the gluon distribution grows faster than any power of $\log\frac{x_0}{x}$ as $x \rightarrow 0$. $x < x_0$ defines the small-x region, whereas $Q^2 > Q_0^2$ is the large-Q^2 region. Eq. 2.32 thus predicts flatness at a medium-Q_0^2 and a steep rise of gluon density $g(x,Q^2)$ at low-x.

In simple words at some $Q^2 \sim Q_0^2$, the photon starts to resolve the point-like valence quarks within the proton in DIS. As Q^2 increases, such that $Q^2 \gg Q_0^2$, the resolution power increases and the quark itself (surrounded by a sea of partons) is "seen". Thus DGLAP basically describes this change of parton densities with varying spatial resolution of the probe.

2.3.4 BFKL Evolution

The steep behaviour of the gluon density at low x has then led to further development in pQCD. As can be seen from the Double Leading Logarithmic (DLL) solution Eq. 2.34, there exist terms like $\log(x_0/x)\log(Q^2/Q_0^2)$. Thus at small-$x$, but moderate Q^2, one can have $\alpha_s\log(Q^2) \ll \alpha_s\log(\frac{1}{x})$, which needs resummation of 'large' terms

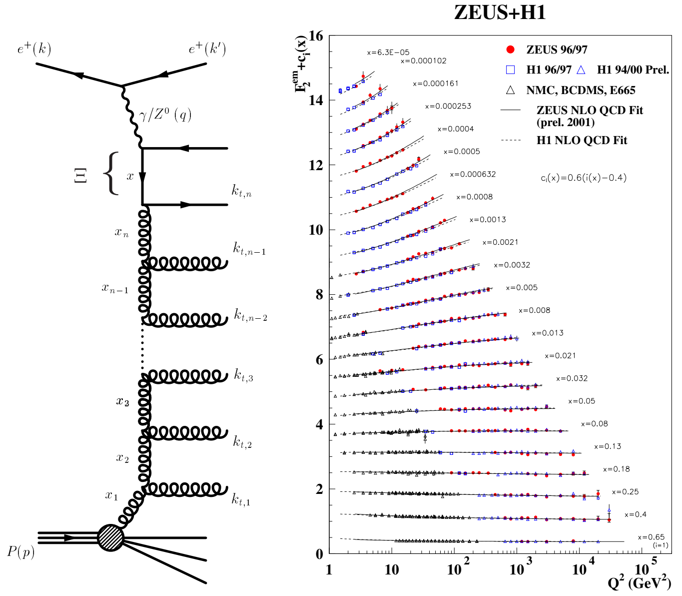

Figure 2.10: *Parton evolution diagram (left). The ZEUS [26] and H1 [39] results for F_2 versus Q^2 are shown (right) for fixed x. The fixed target results from NMC, BCDMS and E665 (triangles). The ZEUS and H1 NLO QCD fits (curve) are also shown (right).*

like $\alpha_s\log(\frac{1}{x})$ to all orders by keeping full Q^2 dependence. This was done by Balitskii, Fadin, Kuraev and Lipatov [40] and is called BFKL evolution equations. The low-x terms have been taken into account by summing $(\alpha_s\log(1/x))^n$ gluon emission terms which are no longer ordered in transverse momentum rather:

$$x_1 > x_2 > x_3 > \ldots > x_n \tag{2.35}$$

where x_i is the fraction of the longitudinal momentum carried by the rungs in Fig. 2.10 (left). The solution of BFKL equation at leading order in $\log(\frac{1}{x})$ and fixed α_s gives a very steep power law behaviour. Such a steep rise has been observed experimentally [41] and is illustrated in Fig. 2.10 (right), although it is not clear whether this is in fact due to standard DGLAP evolution since it cannot exclude the effects of BFKL dynamics.

2.3.5 CCFM Evolution

Although BFKL describes how high momentum partons in the proton are dressed by a cloud of gluons localised in a fixed transverse spatial region of the proton, it however can only be calculated at leading order. Progress has been made since then to achieve 'unified' treatment for both x and Q^2 dependencies of the parton distribution and structure functions throughout the kinematical plane. The most important of which is the CCFM evolution scheme [42] (Catani, Ciafaloni, Fiorani and Marchesini). According to the CCFM evolution equations, the emission of gluons ("ladders") during the initial cascade is only allowed in an angular-ordered region of phase space. The maximum allowed angle Ξ is defined by the hard scattering quark box, producing the quark pairs (Fig. 2.10 (left)). The CCFM evolution with respect to the evolution variable or scale $\bar{q}^2$ can be written as [43]:

$$\bar{q}^2 \frac{d}{d\bar{q}^2} \frac{x\mathcal{A}(x, k_T^2, \bar{q}^2)}{\Delta_s(\bar{q}^2, Q_0^2)} = \int dz \frac{d\phi}{2\pi} \frac{\tilde{P}(z, (\bar{q}/z)^2, k_T^2)}{\Delta_s(\bar{q}^2, Q_0^2)} x' \mathcal{A}\left(x', k_T^{2\prime}, (\bar{q}/z)^2\right), \qquad (2.36)$$

where the splitting function $\tilde{P}(z, (\bar{q}/z)^2, k_T^2)$ is related to the two scales $\bar{q}$ and k_T. The introduced Sudakov form factor $\Delta_s(\bar{q}^2, Q_0^2)$ is simply the probability of evolving from Q_0^2 to $\bar{q}^2$ without branching. The unintegrated parton density $\mathcal{A}(x, k_T^2, \bar{q}^2)$ (identical to $g(x, Q^2)$ in the collinear DGLAP picture) describes the probability of finding a parton carrying a longitudinal momentum fraction x and transverse momentum fraction k_T at the factorisation scale $\mu = \bar{q}$. The scale $\bar{q}$ with the given ratio of energy fraction z_i, in the $(i-1) \to i$ branching, is related to the angle of the emitted gluon ξ_i, which satisfies the following relation:

$$\begin{aligned} z_{i-1}\bar{q}_{i-1} < \bar{q}_i = x_{i-1}\sqrt{s\xi_i} < x_{n-1}\sqrt{s\Xi} \\ \text{where,} \quad \xi_0 < \xi_1 < \xi_2 < ... < \xi_n < \Xi \end{aligned} \qquad (2.37)$$

This is called the angular ordering. In CCFM the scale $\bar{q}$ (coming from the maximum angle) can be related to the evolution scale in the collinear parton distributions [43]

$$\bar{q}^2 \sim x_g^2 \Xi s \approx Q^2 \qquad (2.38)$$

At small-x, where $\mathcal{A}$ becomes independent of Q^2 and k_T is limited by the kinematics, the integral equation for $\mathcal{A}(x, k_T^2, \bar{q}^2)$ can be approximated by the BFKL equation. However, at moderate x, k_T ordering is implied and the DGLAP equation for the integrated gluon distribution $g(x, Q^2)$ is recovered. The k_T dependence as a separated scale apart from the factorisation scale $\bar{q}$ (related to the gluon angle emission) in the evolution scheme is called the k_T-factorisation approach [44]. The details of which can be found later in section 5.2.2.

2.4 Photon Structure Function F_2^γ

The hadronic part of the hydrogen atom example (as discussed in section 2.2.1), the proton in DIS, is a relativistic system. One can then expect that a good fraction of its energy should be carried by its binding force, that is to say, by the gluons. Thus, the gluon PDF was found to be sizeable. But is this applicable to all hadrons, especially photons, when they are considered to have a hadronic structure ?

2.4.1 QPM's View about Photon Structure

The splitting of a photon into a quark anti-quark pair can be calculated in the same way as was done earlier for gluons. When a photon splits into a $q\bar{q}$ pair, the quark carries an energy fraction x_γ of the photon energy. As the quark and anti-quark densities in the photon are symmetric, their fractional momenta are coupled in every process. According to the inverse relation [45]:

$$f_{q/\gamma}(x_\gamma) = x_\gamma f_{\gamma/q}(1/x_\gamma) \qquad (2.39)$$

which simply means that the probability of finding a quark in the photon $f_{q/\gamma}$ is proportional to the probability of finding a photon in a quark $f_{\gamma/q}$. The functional form of $f_{\gamma/q}$ is the same as that of $f_{\gamma/e}$ from Eq 2.7 (ignoring the correction term $2m_e^2 y(1/Q^2_{min} - 1/Q^2_{max})$) scaled by the square of the quark charge e_q:

$$f_{q/\gamma} = e_q^2 \frac{\alpha}{\pi} \left(x_\gamma^2 + (1-x_\gamma)^2\right) \log \frac{Q^2}{m_q^2}. \tag{2.40}$$

Here m_q is a measure of the mass of 'free' quarks. By summing over all colours and flavours one obtains the prediction for the photon structure function F_2^γ in order to compare to the experimental results[10]. Replacing x by x_γ and f_q^p by $f_{q/\gamma}$ in Eq. 2.14 leads to:

$$\begin{aligned} F_2^\gamma[QPM] &= x_\gamma \sum_{n_c,n_f=i} e_q^2 f_{q/\gamma}(x_\gamma, Q^2), \\ &= 3\sum_i e_q^4 \frac{\alpha}{\pi} x_\gamma \left[x_\gamma^2 + (1-x_\gamma)^2\right] \log \frac{Q^2}{m_q^2}. \end{aligned} \tag{2.41}$$

The photon structure function F_2^γ as predicted by the QPM has the following features compared to Eq. 2.14, which are completely different from hadronic structure function:

- the photon structure function directly depends on the scale Q^2 at which it is probed by the virtual photon, whereas in the hadronic world Q^2 only enters via the QCD evolution equations,
- the quark charge e_q contributes to the fourth power, while it contributes quadratically in the hadronic structure functions,
- the photon structure function increases with increasing energy fraction x_γ of the quark from the photon.

[10] The measurement of the analogous QED process $f_{\mu/\gamma}$ resulted in a precise determination of the muon μ, mass [46].

2.4.2 QCD Corrections to the QPM's view

The QCD corrections to the QPM photon structure function can be calculated for instance from the DGLAP evolution equations. Adding the point like coupling of the photons to quarks, one can rewrite Eq. 2.32 to:

$$\begin{aligned} \frac{df_{q_i/\gamma}}{d\log Q^2} &= \frac{\alpha}{2\pi}\mathcal{P}_{q_i\gamma} + \frac{\alpha_s}{2\pi}\left\{\sum_{k=1}^{n_f}\left[\mathcal{P}_{q_iq_k} + \mathcal{P}_{q_i\bar{q}_k}\right]\otimes f_{q_k/\gamma} + \mathcal{P}_{q_ig}\otimes f_{g/\gamma}\right\} \\ \frac{df_{g/\gamma}}{d\log Q^2} &= \frac{\alpha}{2\pi}\mathcal{P}_{g\gamma} + \frac{\alpha_s}{2\pi}\left\{\sum_{k=1}^{n_f}\left[\mathcal{P}_{gq_k} + \mathcal{P}_{g\bar{q}_k}\right]\otimes f_{q_k/\gamma} + \mathcal{P}_{gg}\otimes f_{g/\gamma}\right\} \end{aligned} \tag{2.42}$$

where the splitting function $\mathcal{P}_{q\gamma}$ gives the probability of the photon radiating a quark. The sums run over all quark flavours n_f. The leading order ($\mathcal{P}_{ij}^0$ from Eq. 2.29) QCD prediction for the quark density in the photon leads to:

$$f_{q/\gamma} = e_q^2 \frac{\alpha}{\pi} \left(x_\gamma^2 + (1-x_\gamma)^2\right) \log \frac{Q^2}{\Lambda^2_{QCD}} \tag{2.43}$$

The corresponding photon structure function without including any bound states between the quark and anti-quark is

$$F_2^\gamma(x_\gamma, Q^2) = 3\sum_i e_q^4 \frac{\alpha}{\pi} x_\gamma \left[x_\gamma^2 + (1-x_\gamma)^2\right] \log \frac{Q^2}{\Lambda^2_{QCD}}. \tag{2.44}$$

The main difference between the photon structure function F_2^γ and the proton structure function is due to the point-like coupling of the photons to quarks. This leads to a rise in F_2^γ towards large values of x, whereas the structure function of the proton decreases. The logarithmic evolution of F_2^γ with Q^2 shows a positive scaling for all values of x, in contrast to the scaling violations observed for proton structure function, which exhibits positive scaling violations for low-x and negative scaling violation at large-x (Fig. 2.10 (right)). Also, due to the dependence of the quark charge, the F_2^γ for light quarks is dominated by the contributions from u quarks.

Since the strong coupling constant is at first order $\alpha_s \propto \left(\log(Q^2/\Lambda^2_{QCD})\right)^{-1}$, the photon structure function from Eq 2.44, accounting for both point-like and anomalous contributions is expected to be proportional to the ratio of the electromagnetic and strong coupling constants:

$$F_2^\gamma(x_\gamma, Q^2) \propto \frac{\alpha}{\alpha_s}. \tag{2.45}$$

The photon structure function F_2^γ can be directly measured in deep inelastic electron-photon scattering experiments, where the photon can probe the structure of the virtual photon coming from an electron. The experimental results and the parameterisations used in this thesis, are discussed below.

2.4.3 Parameterisations to Photon Structure Functions

There are several parton distribution functions for photons constructed in a similar way to the parton distribution functions of protons. They are based on the full evolution equations Eq. 2.42 both for real and virtual photons in the leading and next-to-leading order framework. The various PDFs for the photon differ in the assumptions made about the starting scale Q_0^2, as well as in the amount of data used in fitting their parameters. The distributions basically fall into three classes depending on the theoretical concepts used. The first class consists of the DG, LAC and WHIT parton distribution functions [47], which are purely phenomenological fits to the data, starting from an x-dependent ansatz. The second class of parameterisations base their input distribution functions $\{f_{q/\gamma}(x_\gamma, Q_0^2), f_{g/\gamma}(x_\gamma, Q_0^2)\}$ on the theoretical concepts which are derived from the measured pion structure functions, assuming VMD and the additive quark parton model. This is done in the case of GRV [48, 49], GRSc [50] and AFG [51]. The third class consists of SaS [52] distributions which use the ideas of the two classes above, and in addition relates the input distribution functions to the measured photon-proton cross section. The SaS distributions were only computed at leading order with independent point-like and hadron-like components. The point-like component was further sub-divided into a *state* distribution which describes the PDFs within the $q\bar{q}$ distribution. Thus, these distributions are only useful in Monte Carlo programs when using parton showering (see chapter 5) and will not be further discussed.

PDFs like GRV and AFG computed at higher orders (HO) and used in this thesis are described below.

1. GRV [48, 49] : Glück, Reya and Vogt (GRV) provided leading and next-to-

leading order parameterisations, which are evolved at very low starting scales $Q_0^2(\text{LO}) = 0.25$ GeV^2 and $Q_0^2(\text{NLO}) = 0.30$ GeV^2, respectively. Here the valence quark distributions in the photon have the same shape as in the pion structure functions based on VMD arguments. The gluon content is set proportional to the valence quark content. A proportionality factor κ is introduced to account for the sum of ρ, ω and ϕ mesons. The functional form of the starting distribution is $f_{q/\gamma} = f_{\bar{q}/\gamma} = \kappa(4\pi\alpha/f_\rho^2)^2 f_\pi(x, Q_0^2)$, where $xf_\pi(x, Q_0^2) \sim x^b(1-x)^c$. The parameter $1/f_\rho^2 = 2.2$ is taken from [53], leaving κ as the only free parameter, which is obtained from a fit to the data [54, 55] in the region $0.71 < Q^2 < 100$ GeV^2. The point-like contribution was chosen to vanish at $Q^2 = Q_0^2$ and is dynamically generated using the full evolution equations as was done in the case of the hadron-like component with $\Lambda_{QCD} = 0.2$ GeV for massless quarks. Here the charm density is zero if the invariant mass of $c\bar{c}$ system is below the mass threshold[11] $W^2 < 4m_c^2$. The charm and bottom quarks are treated as massless and are included for large W values during the evolution. The LO and NLO predictions are shown in Fig. 2.11 (left) for $Q^2 = 0.8, 1.9, 15$ and 100 GeV^2. The behaviour of the LO and NLO predictions are rather different at low and at high values of x, due to the correction terms in the evolution equations.

2. AFG [51] : Aurenche, Fontannaz and Guillet (AFG) provided NLO parameterisation with a more elaborate ansatz for the vector meson input at $Q_0^2 = 0.5$ GeV^2. The main difference between GRV-HO and AFG-HO parameterisations is the choice of the factorisation scheme and the additional scale factor K in order to adjust the VMD contribution. In standard AFG-HO set the parameter $K = 1$, otherwise K is obtained from a fit to published data [54]. The factorisation scheme is chosen such that the PDF becomes process independent, i.e. universal. The evolution is then performed in the massless scheme for three flavours with $Q^2 < m_c^2 = 2$ GeV^2 and the fourth flavour with $Q^2 > m_c^2$ with $\Lambda_{QCD} = 0.2$ MeV. No PDF containing the bottom quarks were used. In Fig. 2.11 (right) the higher order prediction of F_2^γ from AFG-HO is compared to the GRV-HO prediction for

[11] At HERA $W_{\gamma p}$ is defined to be the γp center-of-mass energy.

three values of $Q^2 = 2, 15$ and 100 GeV^2. At low Q^2 there are large differences between the two predictions, which tend to get smaller as Q^2 increases.

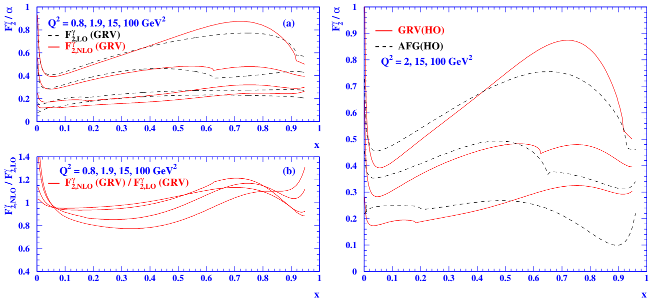

Figure 2.11: *Comparison of the higher order structure function F_2^γ from GRV and AFG.*

2.4.4 Experimental Review

Various measurements of the photon structure function, F_2^γ, have been performed since the first results by PLUTO [56] in 1981. Such measurements can be classified into two categories. Firstly, the shape of F_2^γ is measured as a function of x at fixed Q^2, specially at low-x. Secondly, the evolution of F_2^γ with Q^2, which from Eq. 2.42 is expected to be logarithmic. Fig. 2.12 (left) shows the Q^2 dependence of the data [57] at large parton fractional energies between $0.0055 < x < 0.90$. The structure function F_2^γ rises with increasing Q^2 at a rate almost compatible with a linear dependence on $\log Q^2$. At low Q^2 the anomalous photon component, which is the main interest of this thesis, can be tested by the parton energy distribution and the scale dependence as predicted by Eq. 2.44. In Fig. 2.12 (right) the measurement of F_2^γ is shown for fixed average values of Q^2: 1.9, 2.4, 3.8, 4.3 and 5.0 GeV^2 as a function of x. The data is expected to show a rise in the distributions with decreasing x values as

expected for a dominant hadron-like component from Eq. 2.44, whereas the rise towards high-x justifies the dominant point-like behaviour. Both the x and the scaling behaviour confirm the QCD prediction on the anomalous component of the photon.

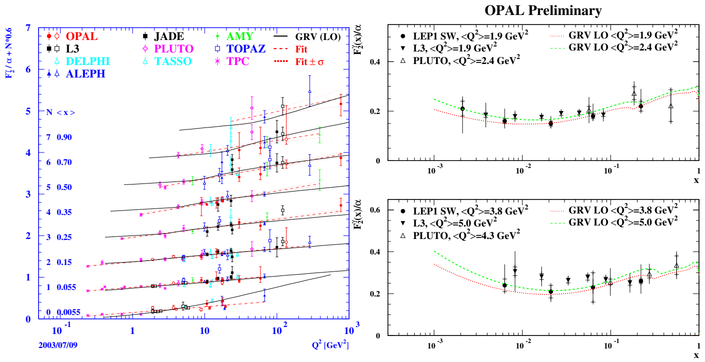

Figure 2.12: *Summary of the measurements of the Q^2 evolution of F_2^γ (left). F_2^γ measured at the lowest x attainable at LEP with fixed Q^2 (right).*

Photon structure at HERA

Although HERA is well known for precise determination of proton structure function over a wide range of Q^2 giving rise to scaling dependence at low, medium and high-x (Fig. 2.10) [58], it also provides a unique ground for measurement of the real (or quasi-real) and virtual photon structures. As the main thrust of this thesis is towards photoproduction, the virtual structure of the photon measured in DIS, where the parton from the proton probes the structure of the highly virtual photon ($Q^2 \gg 1$ GeV^2) will not be discussed. Also as can be seen from Fig. 2.12 (right), there is not much data from e^+e^- to constrain the x dependence for $Q^2 < 1$ GeV^2. This is the region where not only the hadron-like component is dominant, but also a sizeable gluon density of the photon can be expected. In hard photoproduction, the proton momentum fraction x (also defined as $x_p^{\rm obs}$ for the observed experimental analysis) carried by the parton participating in the interaction, can be expressed as:

$$x \simeq M_{jj}^2/W_{\gamma p}^2$$

where M_{jj} represents the invariant mass of the two outgoing partons and $W_{\gamma p}$ is the γp centre-of-mass energy. In the kinematic range of this thesis, i.e. for $W_{\gamma p} \sim \mathcal{O}(10^2)$ GeV, with hadronic jets of $M_{jj} \sim \mathcal{O}(10^1)$ GeV, the variable x is of the order of $\sim 10^{-2}$. For these values, Fig. 2.13 shows that the gluon distribution function inside the proton is much higher than the valence and sea quarks ones [59].

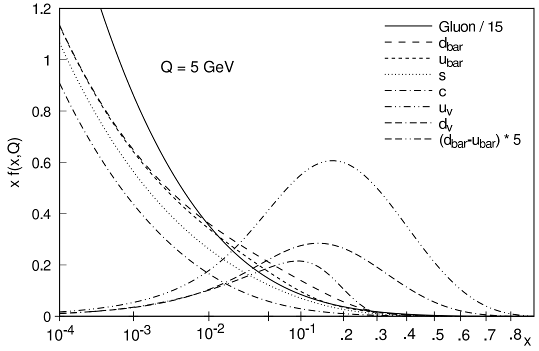

Figure 2.13: *Quark and gluon distribution function at $\mu = Q = 5$ GeV, given by the CTEQ Collaboration (CTEQ5M) [59]. The gluon distribution is scaled down by a factor of 15, and the $(\bar{d} - \bar{u})$ is scaled up by a factor of 5.*

The first evidence of the hard scattering process in γp collisions, was the observation [60] of jets with large transverse energy. Thereafter, the processes with a hadron-like component called resolved photon processes were observed [61], via the observation of large energy deposits in the rear direction consistent with a photon remnant. The distinction between the point-like coupling (direct photon process) and resolved photon events was made based on the photon energy fraction x_γ that takes part in the hard interaction. These two components in the observed cross

section were estimated by using Monte Carlo simulations. Fig. 2.14 [62] shows the observed spectrum. The agreement in shape between data and MC is good except below $x_\gamma^{\rm obs} = 0.3$ even when a Multiparton Interaction (MPI) model [63] is included.

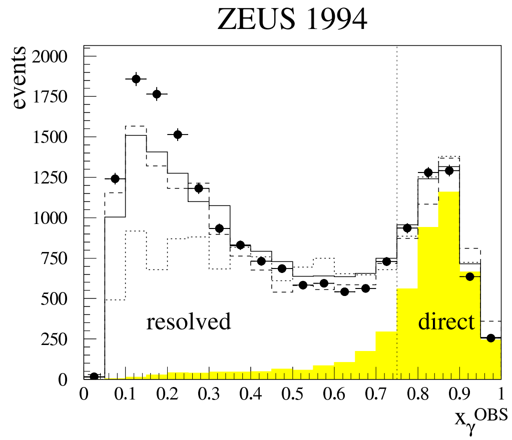

Figure 2.14: *The $x_\gamma^{\rm obs}$ distribution [62] in dijet events for data (black dots) compared with HERWIG with and without MPI (solid and dotted line), and PYTHIA (dashed line) simulations. The shaded area represents the direct photon component only predicted by HERWIG and the vertical line is the experimental cut to separate direct and resolved subprocesses.*

After the observation of the existence of resolved photon events in the inclusive sample, the dijet angular distribution, which is sensitive to nature of the propagator, was measured [64]. A basic prediction of QCD is that the angular distribution of the outgoing partons in resolved processes will be enhanced at a high scattering angle $|\cos\theta^*|$ with respect to the direct photon processes. This property is expected to be preserved in the next-to-leading order (NLO) calculations. In addition to the dependence upon the incoming flux of partons, this prediction is also sensitive to the relative colour factors for each subprocess and to the spins of the quark and the

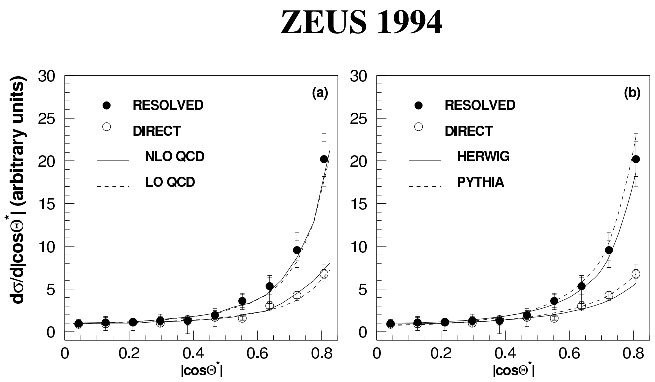

Figure 2.15: *Dijet angular distribution for resolved (black dots) and direct (open dots) processes, compared to LO and NLO QCD predictions [64], and also to HERWIG and PYTHIA simulations.*

gluon propagators. Already measurements of dijet angular distribution in $p\bar{p}$ events have shown good agreement with the perturbative QCD predictions [65] in fermionic and bosonic exchange processes [66]. The dijet scattering angle $|\cos\theta^*|$ calculated from the rapidity difference between the two jets, was measured in the photoproduction regime by ZEUS [64]. Direct and resolved processes were distinguished by the experimental observable determining photons fractional energy $x_\gamma^{\rm obs}$. Fig. 2.15 shows the distribution for samples with direct and resolved photon processes. Both of these distributions were normalised to one at $|\cos\theta^*| = 0$. The measurement shows a much steeper rise in the resolved γp angular distribution than in the direct γp processes. In the same Fig. 2.15 a), the data are compared with analytical LO and partial NLO calculations [67]. Both calculations are compatible with the data. In summary, the basic QCD prediction, that different sub-processes have different angular distributions of the parton scattering angle, was confirmed by the dijet data. Similar results have been recently reported in photon-photon collisions [68].

The above results are for inclusive dijet production, i.e there is no requirement of any heavy quark involvement. As the analysis in this thesis is towards the charm

jets, measuring the angular distribution of the outgoing jets will allow the dominant subprocesses to be determined and to verify the QCD predictions. If indeed most of the resolved-photon charm dijet events are produced from the photon, a gluon-exchange contribution, as will be seen in Fig. 8.15 a)-b), should dominate. This results in a steep rise of the cross section towards high $|\cos\theta^*|$ values. The other diagrams of Fig. 8.15 c)-e) involve quark exchange and thus should not show such a sharp rise. If one of the jets is explicitly tagged as a charm jet, the sign of $\cos\theta^*$ can be defined. If the charm originates from the photon, the charm jet generally lies in the photon hemisphere.

The phenomenology of heavy quarks, especially of charm, will be discussed and is the subject of the next chapter. The results shown here, however, provide an interesting baseline for comparison with future results as the effects of charm should be observed.

Chapter 3

Heavy Quark Production

Heavy quarks such as charm provide the opportunity to study perturbative QCD with an additional hard scale besides the transverse energy of the associated jets: the charm mass. For the quark to be "heavy", its mass has to be larger than the QCD scale $\Lambda_{QCD} \sim 200-300$ MeV. The quarks of the standard model fall naturally into two classes: u, d and s are light quarks, whereas c, b and t are heavy quarks. For heavy quarks, the effective coupling constant $\alpha_s(m_Q)$ is small implying that on length scales comparable to the Compton wavelength $\lambda_Q \sim 1/m_Q$ the strong interactions are perturbative and much like the electromagnetic interactions. In the next section, the perturbative formalism of the heavy quarks in high energy photon-proton collisions is presented, followed by a review of experimental results. The importance of the charm jets in understanding both the perturbative and non-perturbative parts of QCD is discussed.

3.1 A Perturbative Formalism

In the perturbative formalism of heavy quark photoproduction at leading order (LO), there are two types of processes responsible for the photoproduction of charm: direct and resolved processes.

In direct processes, the photon acts as a point-like object interacting with a parton from the proton. In these processes the photon participates in the hard scatter via either boson-gluon fusion (BGF) shown in Fig. 3.1 a), or QCD Compton scattering. In the QCD Compton process, the photon couples to a charm quark within the proton, which then radiates a gluon before hadronisation. In BGF the photon couples to the charm quark coming from a gluon of the proton, which split into a $c\bar{c}$ pair. Due to the large gluon density in the studied kinematic range (discussed in section 2.4.4), BGF is the dominant direct photon process.

In resolved photon processes, the photon acts as a source of incoming partons (quarks or gluons) and only a fraction of its momentum participates in the hard scatter. Examples of resolved photon diagrams at LO are shown in Fig. 3.1 b)-c). In gluon-gluon fusion (Fig. 3.1 b), a gluon from the photon interacts with a gluon from the proton. However, in Fig.3.1 c) a charm quark from the photon can also interact with a gluon from the proton. In the final state two charm jets or a gluon and a charm jet can be produced.

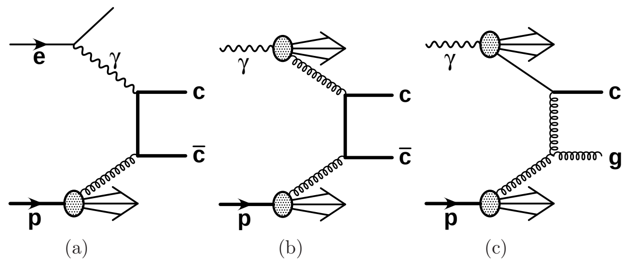

Figure 3.1: *Leading order direct a) and b)-c) resolved photon processes.*

In a generalised form, these LO direct and resolved photon processes can be represented as shown in Fig. 3.2. The dotted line shows the cut-offs between the hard and soft non-perturbative parton distribution functions. The factorisation scales μ_P and μ_γ for the proton and the photon are generally both taken equal to $\sqrt{p_T^2 + m_c^2}$, where m_c is the charm mass and p_T is the mean transverse momentum of the two outgoing charm quarks. As the hard process is independent of the factorisation scale, a variation of scale should only affect the parton distribution functions.

The cross section for the production of the LO direct and resolved subprocess can be written as:

$$\sigma_{\gamma P} = \sigma_{\gamma P}^{dir} + \sigma_{\gamma P}^{res} = F_j^P(\mu_P) \otimes \hat{\sigma}_{\gamma j}(\mu_R) + F_i^\gamma(\mu_\gamma) \otimes F_j^P(\mu'_P) \otimes \hat{\sigma}_{ij}(\mu_R) \tag{3.1}$$

The second part is derived from Eq. 2.30. The $\hat{\sigma}$ represents the perturbatively calculable $2 \to 2$ scattering matrix elements and F_j^P and F_i^γ are the parton density functions of the proton and photon respectively. At next-to-leading order (NLO) there exists contributions from $2 \to 3$ parton scattering, which are dependent on the factorisation scale. The two components are usually written as [69]:

$$\sigma_{\gamma P} = F_j^P(\mu_P) \otimes \hat{\sigma}_{\gamma j}(\mu_R, \mu_P, \mu_\gamma) + F_i^\gamma(\mu_\gamma) \otimes F_j^P(\mu'_P) \otimes \hat{\sigma}_{ij}(\mu'_R, \mu'_P, \mu_\gamma) \tag{3.2}$$

which is the sum of the point-like and hadronic components. Here μ_R and μ'_R are the renormalisation scales, μ_P and μ'_P are the factorisation scales for collinear singularities from the strong interactions, and μ_γ is the factorisation scale for collinear singularities arising from the electron vertex.

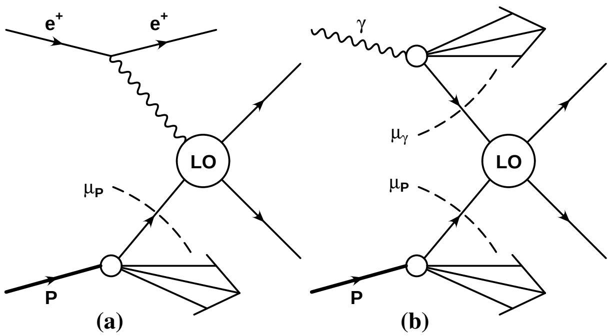

Figure 3.2: *Generic representation for leading order direct and resolved photon processes.*

In order to extend Eq. 3.2 to even higher orders, one also needs to include an explicit dependence of the structure functions upon the renormalisation scale. The renormalization scale in the structure function is usually kept equal to the factorization scale. The hadronic and photonic parton densities obey the usual Altarelli-Parisi evolution equations in the scale $\mu_F (= \mu_P)$ as described in the previous chapter.

For a given partonic centre-of-mass energy, $\sqrt{s}$, the short distance cross section which depends on both the scales for the order $\mathcal{O}(\alpha_s^3)$ [70] is given by,

$$\hat{\sigma}_{ij} = \frac{\alpha_s(\mu_R^2)}{m_c^2} f_{ij}(\rho, \mu^2/m_c^2), \tag{3.3}$$

where the parameter $\rho = 4m_c^2/s$, and for simplicity $\mu = \mu_F = \mu_R$. The dimensionless function f_{ij} has the following perturbative expansion [70]:

$$f_{ij}(\rho, \mu^2/m_c^2) = f_{ij}^{(0)}(\rho) + g^2(\mu^2)\left[f_{ij}^{(1)}(\rho) + \bar{f}_{ij}^{(1)}(\rho)\log(\mu^2/m_c^2)\right] + \mathcal{O}(g^4) \tag{3.4}$$

Details of the lowest and higher order functions $f_{ij}^{(0)}$ and $\bar{f}_{ij}^{(1)}$ are given therein. These higher order correction terms are the coefficients of $\log(\mu^2/m_c^2)$, and are determined by renormalisation group arguments. They use the explicit form of the Altarelli-Parisi splitting functions.

In addition, the photonic parton densities also have an inhomogeneous evolution in μ_γ, which at leading order, is given by the first part of Eq. 2.42. There the scale Q^2 can be replaced by μ_γ^2. Thus, by varying the scale μ_γ the amount of $2 \to 3$ processes at NLO and the amount which are in fact simply LO processes varies. As can be seen from the μ_γ dependence in Eq. 3.2, the separation of the point-like and hadronic components is not unambiguously defined beyond the LO in perturbation theory. On the other hand, the point-like and hadronic components are each constant with respect to the variation of all the other mass scales that enter Eq. 3.2.

From Eq. 3.4, the perturbative expansion contains a dependence on the charm mass ($m_c > \Lambda_{QCD}$), hence the faster convergence of the perturbative expansion which leads to more reliable cross section predictions. Two different schemes and their combinations exist that predict the charm production at next-to-leading order. In the following, the massive-quark or fixed order scheme and the massless-quark schemes are discussed.

3.1.1 Fixed Order Scheme

In the massive-quark or fixed order next-to-leading order scheme[1] [71] (FO NLO), the heavy quark is on mass-shell and it only appears in the final state, but not as an active parton inside the incoming photon or proton. Thus, only the gluons and light quarks (u, d, s) are assumed to be the active partons contributing to the structure functions of the photon and proton. The predicted cross section factorises (separates) into a partonic hard scattering cross section convoluted with light quark and gluon densities. The charm quark is dynamically produced and follows, at LO, the two hadronic channels:

$$gg \rightarrow c\bar{c}, \quad q\bar{q} \rightarrow c\bar{c}. \tag{3.5}$$

The former process is expected to dominate over the latter by significant factors depending on the parameterisations used [72]. The NLO calculations [69] for photo-production are heavily based on the hadroproduction calculations. The calculations are implemented in the form of a "parton" event generator, which was used in this thesis to compute the distributions accurate to next-to-leading order in the strong coupling constant. This approach has the advantage that not only distributions like rapidity or transverse momentum can be predicted, but also the total cross section.

Depending on whether there is an exchange of hard or soft gluons, the short distance cross section depends on an arbitrary renormalisation scale, μ, which separates the regions of short- and long-distance physics. If μ is chosen such that $\Lambda_{QCD} \ll \mu \ll m_c$, the effective coupling constant in the region between μ and m_c is small, and perturbative theory can be used to compute the short-distance corrections. These corrections have to be added to the matrix elements, which only contain the long-distance physics below the scale μ. The non-vanishing charm mass allows the definition of the open-charm cross section, whereas for light quarks, the short-distance cross section must be convoluted with the fragmentation functions, in order to cancel final-state collinear divergences.

On the other hand, the presence of mass makes the calculation of the matrix

[1] The FO NLO is referred as NLO throughout this thesis.

elements more involved, thus only when the coefficient of the coupling constant is small can the results be reliable. The major limitation comes when the p_T in the $\log(p_T^2/m_c^2)$ terms becomes large, which causes the perturbative series (see Eq. 3.4) to diverge as $p_T \gg m_c$. The same is true for higher partonic centre-of-mass energy, where the $\log(s/m^2)$ term becomes divergent. However, for those kinematic regions which are not affected by these large logs, the charm mass sets the hard scale.

3.1.2 Massless Scheme

In the massless-quark or zero-mass Variable-Flavour-Number Scheme (VFNS) [73], the heavy quark is treated as massless at large p_T and appears as an active parton in the incoming proton or photon parton density functions. The mass singularities of the form $\log(p_T^2/m_c^2)$ can then be absorbed into the structure and fragmentation functions in the same way as for the light u, d, s quarks. As a result of this method the hadronic component also includes processes like:

$$gc \rightarrow gc, \quad qc \rightarrow qc. \tag{3.6}$$

which are often termed as "charm excitation" from the photon or proton. Such processes are also included in the FO NLO calculations, but only as higher order corrections to the point-like component.

At large values of $p_T \gg m_c$, the results of such a calculation, in the structure function language, are expected to be more reliable as it sums the large logs, $\log(p_T^2/m_c^2)$ as opposed to calculating the contribution of $2 \rightarrow 3$ subprocesses in the fixed order of perturbation theory. However, limitations arise when $p_T \sim m_c$ and the total cross section for this region cannot be calculated.

An attempt made to combine the results from FO NLO to suitably subtracted VFNS with Perturbative Fragmentation Functions (PFFs), resulted in the fixed order next-to-leading logarithm (FONLL) scheme [74]. As the FONLL scheme interpolates between the FO NLO and VFNS with PFFs, it is expected to give more reliable predictions for heavy quark production.

3.2 Charm Production at HERA

The *ep* collider HERA offers new opportunities to study the production mechanism of heavy quarks and to test the perturbative QCD predictions. The dominant contributions are from photoproduction events, where the electron is scattered at a small angle, producing photons of almost zero virtuality $Q^2 \simeq 0$ GeV^2. In this case, as outlined in the previous chapter, the electron can be considered to be equivalent to a beam of on-shell photons, whose distribution in energy is given by the Weizsäcker-Williams approximation. The low virtuality regime has been extensively studied in fixed-target experiments, which will be discussed in the next sections. At HERA, the available centre-of-mass energy is about one order of magnitude larger than at fixed-target experiments (300 GeV versus $\sim$ 30 GeV). This energy regime is totally unexplored in photoproduction and several new features are expected to arise. In the following section, the charm quark identification methods at HERA are discussed, followed by new experimental results, which are then compared with the theoretical calculations discussed previously.

3.2.1 Identification of Charm at HERA

The reconstruction of charmed mesons in the HERA experiments H1 and ZEUS is based on either mass or lifetime tags. The former is generally done using the invariant mass of the tracks identified with a specific decay channel, predominantly producing D mesons. Only a small fraction of charm quarks fragment into baryons e.g Λ_c, Ξ_c, Ω_c, etc. In the fragmentation process (see Fig. 3.3) for D meson production, the coloured charm quark gets associated with either a u or a d quark to form a $D^0(\bar{D}^0)$ or $D^{\pm}$ meson either in the ground state or a short lived excited state such as $D^{*\pm}$. The charged decay products of the charmed mesons, such as $D^{*\pm}$ can be observed in the central tracking detector (CTD). As the branching ratio of these mesons are relatively small, a high statistics sample is needed to have a clean signal.

The D^* mesons[2] studied in this thesis were reconstructed using the following decay channel:

$$D^{*+} \to D^0 \pi_S^+ \to (K^- \pi^+)\pi_S^+, \tag{3.7}$$

where the charge conjugate process is also implied. The branching ratio, $\mathcal{B}$, of the

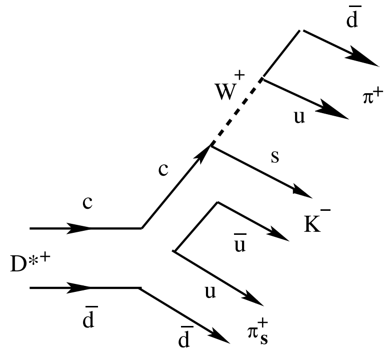

Figure 3.3: *Schematic diagram of the D^{*+} meson decay. The flavour content of the meson and its decay products are also shown.*

decay chain [75]:

$$\mathcal{B}(D^{*+} \to D^0 \pi_S^+) = 67.7 \pm 0.5\% \quad \text{and} \quad \mathcal{B}(D^0 \to K^- \pi^+) = 3.80 \pm 0.09\%. \tag{3.8}$$

The probability for a charm quark to fragment into D^{*+} mesons [76] was obtained by combining together four different measurements from Z^0 decays performed in e^+e^- annihilation at LEP:

$$f(c \to D^{*+} X) = 23.5 \pm 0.7 \pm 0.7\%. \tag{3.9}$$

The mass difference ΔM between the D^* and D^0 mesons is slightly above the threshold of the pion mass m_π and was hence, used as a tag:

$$M(D^*) = 2010.0 \pm 0.5 \text{ MeV} \quad \text{and} \quad M(D^0) = 1864.5 \pm 0.5 \text{ MeV}.$$

[2] $D^{*\pm}$ is referred to as D^* for the rest of this thesis.

This mass difference $\Delta M \equiv M(D^*) - M(D^0) = 145.42 \pm 0.05$ MeV [77] yields a low momentum pion ("soft pion", π_S) from the D^* decay and prominent signals (see Fig. 7.17) just above the threshold of $M(K\pi\pi_S) - M(K\pi)$ distributions, where the phase space contribution is highly suppressed [78]. Alternatively, in the presence of a vertex detector (H1 experiment), background for producing the charmed hadrons can be reduced by identifying [79] the secondary vertices from the primary interaction point.

Recent results on the production of the D^* meson [80, 81] have allowed an extensive comparison with the massive, the massless and the new improved FONLL schemes in the photoproduction regime. These preliminary results from both HERA experiments have superseded the previous measurements [82], in which comparisons were also made with massive and massless calculations. The cross section for inclusive $D^{*\pm}$ mesons in photoproduction was recently measured by H1 Collaboration [81] in the kinematic region $Q^2 < 0.01$ GeV^2, γp centre-of-mass $171 < W_{\gamma p} < 256$ GeV, $p_T(D^*) > 2.5$ GeV and $|\eta(D^*)| < 1.5$ as a function of the transverse momentum $p_t(D^*)$, pseudorapidity $\eta(D^*)$ and $W_{\gamma p}$.

In the "3-flavour massive" scheme [71], the Peterson parameterisation was used to model the charm fragmentation with $\epsilon = 0.035$ [83]. The renormalisation and the factorisation scales have been set to $2\mu_R = \mu_F = 2\sqrt{m_c^2 + p_T^2}$, with the parton densities CTEQ5D [59] and GRV-G HO [84] for the proton and photon, respectively. The charm mass was taken to be $m_c = 1.5$ GeV and the fraction of c-quark hadronising to the D^{*+} meson was set to $f(c \to D^{*+}) = 0.235$ [76]. To estimate the uncertainty of the calculation, the renormalisation scale has been varied by a factor 0.5(2.0) as an upper (lower) limit. The "4-flavour massless" scheme uses the BKK scheme [85] for fragmentation and the scales $\mu_R = \mu_F = 2\sqrt{m_c^2 + p_T^2}$ for the central prediction. CTEQ6M [86] and AFG [51] were used for the parton densities for the proton and photon. On the other hand FONLL predictions, using the Kartvelishvili ansatz [87] following a fit (unpublished), were also compared to the data.

Fig. 3.4 a)-b) compares the measured differential cross section $d\sigma/dp_T$, of all three NLO schemes to the data [81]. The massive prediction lies below the data in the

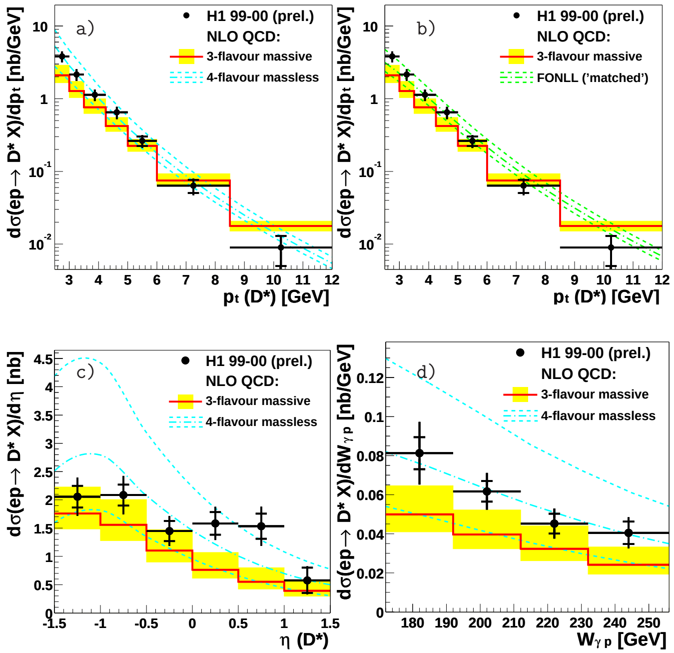

Figure 3.4: *Differential D^* photoproduction cross sections measured by the H1 collaboration [81] as a function of a)-b) $p_T(D^*)$, c) $|\eta(D^*)|$ and d) W. The data are compared with various theoretical calculations.*

low p_T regime, whereas the FONLL prediction is closer to the data and the massless prediction is in good agreement with the data. The η distributions for massive and massless schemes are shown in Fig. 3.4 c). Neither calculation can describe the shape of the measured cross section, which shows an enhancement compared with the theory in the forward direction (see [81]). Both NLO predictions for $d\sigma/dW$ in Fig. 3.4 d) can describe the shape of the data.

Inclusive photoproduction of D^* mesons has been measured [80] with the ZEUS detector in almost the same kinematic region: $Q^2 < 1$ GeV^2, γp centre-of-mass

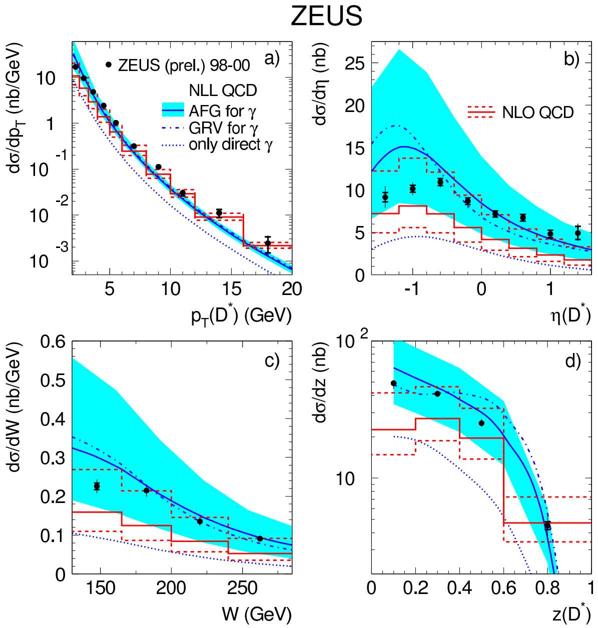

Figure 3.5: *Differential cross sections for D^* photoproduction events [80], as a function of a) $p_T(D^*)$, b) $\eta(D^*)$, c) $W(D^*)$ and d) $z(D^*)$. FO NLO predictions with nominal parameters are given by the solid histogram. The VFNS predictions (labeled as NLL) are shown by the solid curves. The GRV photon parameterisation and direct photon predictions are given by dash-dotted and dotted lines.*

energies $130 < W_{\gamma p} < 280$ GeV, $1.9 < p_T(D^*) < 20$ GeV and $|\eta(D^*)| < 1.6$ using an integrated luminosity of 79 pb^{-1}. The measured differential cross sections were compared with FO NLO, VFNS and FONLL QCD predictions. In Fig. 3.5 the differential cross sections as a function of a) $p_T(D*)$, b) $\eta(D^*)$, c) $W(D^*)$ and d) $z(D^*)$ are compared with the FO NLO and VFNS QCD calculations, where $z(D^*)$ is the fraction of the photon energy carried by the charmed meson in the proton rest frame. The precision of the data is enormously better than the theoretical uncertainties.

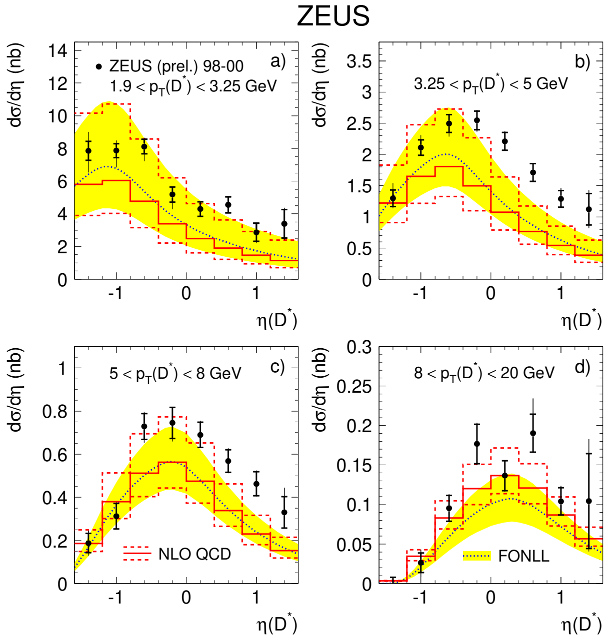

Figure 3.6: *Differential cross section $d\sigma/d\eta$ for inclusive D^* photoproduction [80] in four p_T regions, compared to FO NLO (histograms) and FONLL (curves) predictions.*

The uncertainties for VFNS are larger than for the FO NLO calculation: these were obtained by varying the charm mass and the renormalisation scales simultaneously. The central FO NLO predictions are below the data, especially in the proton direction ($\eta > 0$) and the low z region. The VFNS prediction is closer to the data, in particular it is better than FO NLO for $d\sigma/dz$ and for positive pseudorapidity. The direct photon processes alone in VFNS cannot describe the data distribution and hence a significant resolved contribution is required. As expected, the VFNS scheme shows sensitivity to the variation in the photon structure function parameterisation.

Given the precision of the ZEUS data, the differential cross sections for different $p_T(D^*)$ regions as a function of $\eta(D^*)$ are compared to the FO NLO and FONLL predictions in Fig. 3.6. These along with the above mentioned comparisons allow to identify the region of phase space where the discrepancy between the data and the calculations can be localized. The data is close to the upper limit of the uncertainties of the predictions and is significantly above both the FO NLO and FONLL predictions at medium p_T and positive η. As expected, due to the inherited properties from FO NLO, the FONLL is close to the former at low p_T, but is surprisingly below FO NLO at large p_T.

3.3 Charm Production at Other Experiments

Charm production has been extensively studied at a number of fixed target experiments with both hadron and photon beams, with a centre-of-mass energy around $10 - 40$ GeV. A review of hadroproduction can be found in [88]. In the case of photoproduction, the theoretical uncertainties are expected to be smaller and the pQCD predictions should be more reliable. Single inclusive distributions have been measured at CERN by the WA92 collaboration [89], using a π^- beam, and also at FNAL by E769 collaborations [90] with pion, proton and kaon beams of 250 GeV. Fig. 3.7 show the comparison between the single-inclusive p_T^2 distributions measured by the WA92 and E769 collaborations in πN collisions and the FO NLO QCD predictions. The solid curves represent the partonic cross sections predicted by the NLO calculation for charm, without any non-perturbative input (such as fragmentation function). The effect of non-perturbative phenomena coupled to pQCD was then studied by introducing an intrinsic transverse momentum for the incoming partons ("k_T kick") and by convoluting the partonic cross section with a Peterson fragmentation function (see section 5.4.3.2) with $\epsilon = 0.06$. The fragmentation process degrades the parent charm-quark momentum, and softens the p_T^2 distribution. The arbitrary non-perturbative k_T kick on the bare quarks results in a hardening of the p_T^2 spectrum, overshooting the data. On the other hand, the combination of

the k_T kick with the fragmentation function yields a better description of the data by the theoretical calculation although it is better suited with a large charm mass $m_c = 1.8$ GeV.

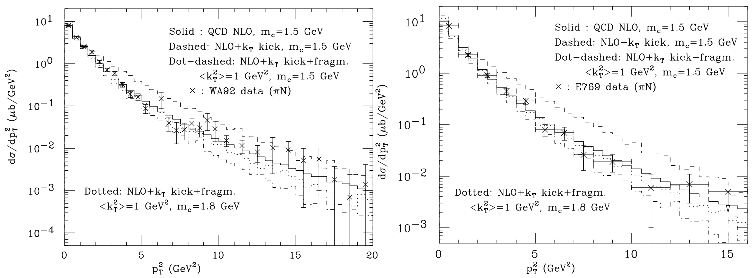

Figure 3.7: *The p_T^2 distribution for charmed hadrons measured by WA92 [89] (left) and E769 [90] (right), compared to the NLO QCD predictions, with and without the inclusion of non-perturbative effects.*

The results from the two-photon analysis at LEP2 on the other hand appear to be reproduced within errors by the NLO calculation. An inspection of the p_T spectrum [91] reveals that data lie rather at the upper side of the uncertainty of the theoretical prediction, in particular for small transverse momenta.

Recent measurements on charm production at TEVATRON II were made by CDF with an upgraded trigger system. The charm production cross-section was measured with a subset of the Run II dataset. The results [92] are shown in Fig. 3.8 in comparison with resummed QCD calculations in the FONLL scheme. The data tends to be above the central prediction, but roughly follows the behaviour of the upper theoretical scale uncertainty.

In summary, the results from fixed target experiments yield more questions than they answer, mainly due to the limited kinematic ranges and the differences between experiments. The adhoc use of k_T kick along with fragmentation does not necessarily contribute to the justification of the universality of the charm fragmentation

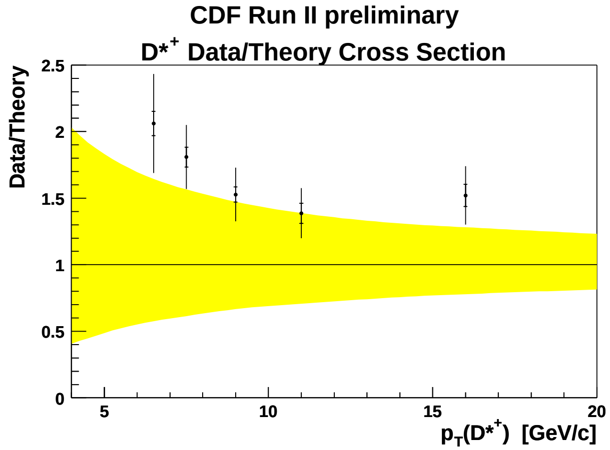

Figure 3.8: *Charm meson production rate at the Tevatron [92], normalised to resummed QCD predictions in the FONLL scheme. The shaded region shows the theoretical uncertainties.*

function. Although the LEP results give reasonable agreement with the theoretical predictions, both the HERA and CDF results show inconsistencies at lower p_T of the produced charmed mesons but are in general close to the upper theoretical limits.

The elements of charm production have been measured but do not reveal a consistent picture. The issue of the massive or massless treatment of the charm quark has also not been clarified, as the NLO QCD prediction in different schemes fail in various regions of the phase space. These points will be discussed and some of them answered in the forthcoming chapters.

3.4 Charm Jets

The study of charm jets should not only provide a thorough test of pQCD but could also answer several of the questions discussed above. The advantage of charm

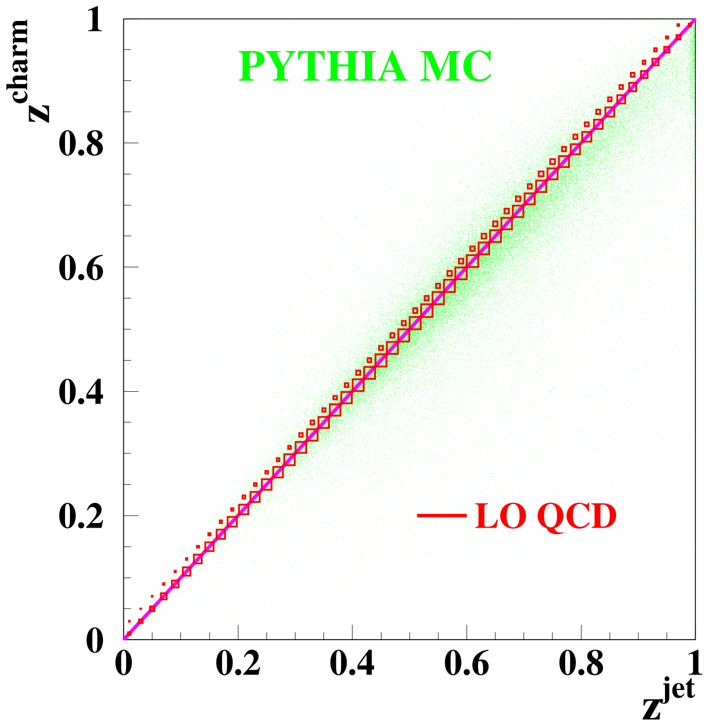

Figure 3.9: *Correlation between $z^{jet} = (E + P_\parallel)_{(D^*)}/(E + P_\parallel)_{jet}$ versus $z^{charm} = (E + P_\parallel)_{(D^*)}/(E + P_\parallel)_{charm}$, using LO QCD calculations and PYTHIA simulations.*

jets over other inclusive measurements is that the transverse momentum of jets initiated by a charm quark can provide the scale, whereby the large terms of the form $\log(p_T^2/m_c^2)$, due to the collinear gluon emission, can be included in the jet. Also, non-perturbative issues like the fragmentation function can be studied from the jet energy fraction taken by the charmed meson. In Fig. 3.9, the distribution of D^* mesons relative to the charm from the hard scatter (z^{charm}) is compared to that from D^* associated hadronic jet (z^{jet}). The definition of z is defined in section 7.1.2. Clearly a very good correlation between the two can be observed. The LO QCD comparison suggests that indeed all charm quarks produced from the hard scattering do represent the D^* associated hadronic jet. Due to additional parton showering in PYTHIA, a slight deviation in the correlation is expected, but the strong correlation between z^{charm} and z^{jet} suggests that the charm quark is well contained in the jet associated with the D^* meson.

Detailed measurements sensitive to perturbative and non-perturbative (fragmentation) aspects of QCD, using charm jets are presented in the analyses in chapters 8 and 9.

Chapter 4

Experimental aspects

In this chapter a brief overview of the HERA accelerator complex and the ZEUS detector is given. Emphasis is placed on those detector components important for the analyses in this thesis. A thorough description of the ZEUS detector can be found elsewhere [93].

4.1 The HERA Collider

HERA (**H**adron **E**lektron **R**ing **A**nlage) [94] is the world's first lepton-proton collider and is located at DESY in Hamburg, Germany. It consists of two separate accelerators, one each for the lepton and proton beams. It is designed to collide electrons or positrons, accelerated up to 27.5 GeV with protons of 820 or 920 GeV energy, yielding a centre-of-mass energy of $\sqrt{s} \simeq \sqrt{4E_eE_p} \sim 300$ GeV. Compared to previous fixed target experiments which have probed nucleon structure, the centre-of-mass energy at HERA is an order of magnitude higher and therefore a new kinematic region is accessible: for example, an incident electron beam up to ~ 48 TeV would be required, in order to reach the same centre-of-mass energy in a fixed target experiment, where $\sqrt{s} \simeq \sqrt{2E_em_p}$.

The HERA tunnel is 6.3 km in circumference and is situated 15-25 m under

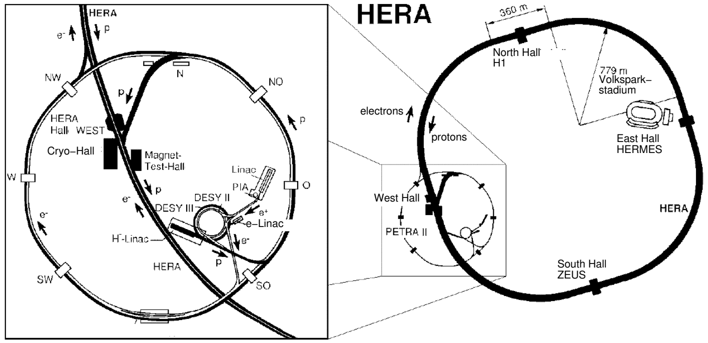

Figure 4.1: *The layout of HERA is shown on the right, along with the location of the four experimental halls. The pre-accelerators are shown in the blow-up on the left.*

ground level. It consists of four segments, each 360 m long, joined by four arcs with a radius of 779 m (see Fig. 4.1). Electrons ("electron" is used generically to refer to both electrons and positrons for the rest of this thesis) and protons are accelerated in two different rings, using conventional and superconducting magnets, respectively.

There are four experiments along the HERA ring. The multipurpose detectors H1 and ZEUS (located in the North and South Hall, respectively) measure $e^{\pm}p$ interactions with beams colliding every 96 ns at zero crossing angle. A review of the physics studied using the H1 and ZEUS experiments can be found elsewhere [95]. The HERMES experiment (located in the East Hall) uses polarized electrons in collision with an internal polarized gas target (hydrogen, deuterium or He^3) in order to investigate the nucleon spin structure. The HERA-B experiment (located in the West Hall) was designed to use collisions of the proton beam halo with wire targets, to study CP Violation in the B-meson system.

4.1.1 Operational Details

Fig. 4.1 shows a schematic layout of the HERA facility and its pre-accelerator system. The proton acceleration chain starts with negative hydrogen ions (H^-) which

are accelerated to 50 MeV in a LINAC. The electrons are then stripped off the H^- ions to yield protons which are injected into the proton synchrotron DESY III where they are accelerated up to 7.5 GeV in 11 bunches with the same 96 ns bunch spacing as in the HERA ring. They are further accelerated in PETRA up to 40 GeV and then injected into the HERA proton storage ring. This process continues until HERA is filled with 210 bunches, which are then accelerated using conventional radio frequency cavities to reach the final energy of 820 GeV or 920 GeV.

The electron pre-acceleration chain starts in the LINAC II, where the lepton beam is accelerated up to 450 MeV. The electrons are then injected into DESY II and, once accelerated up to 7.5 GeV, into PETRA II, where they reach an energy of 14 GeV. They are then transferred into the HERA lepton ring and further accelerated to their final energy of 27.5 GeV.

Electrons and protons are grouped in bunches of $\mathcal{O}(10^{10})$ particles. During normal operation, some of the 210 positions are left empty ('pilot bunches'), in order to study the background conditions. Non-colliding bunches, where either the electron or the proton bunch is empty, enable the measurement of beam related backgrounds. Empty pilot bunches, where neither of the two is filled, allow the study of backgrounds from cosmic ray muons. The bunch crossing interval of 96 ns results in a nominal interaction rate of around 10 MHz.

The analyses in this thesis were performed using data collected with the ZEUS detector at HERA during 1996 – 2000. In this period, HERA collided electrons with energy $E_e = 27.5$ GeV and protons with $E_p = 820$ GeV (1996 – 1997) or $E_p = 920$ GeV (1998 – 2000), corresponding to integrated luminosities of 38.6 ± 0.6 pb^{-1} and 81.9 ± 1.8 pb^{-1} and to centre-of-mass energies $\sqrt{s} = 300$ GeV and $\sqrt{s} = 318$ GeV, respectively.

4.2 The ZEUS Detector

The ZEUS detector is a multipurpose magnetic detector designed to study ep scattering at HERA. It covers most of the 4π solid angle, except for small regions around the beam pipe. ZEUS was commissioned in the Spring of 1992 and since then it has undergone several detector upgrades (essentially adding new components) driven by the physics and technical understanding gained during the first years of data taking.

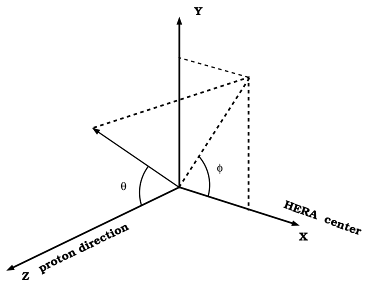

Figure 4.2: *The ZEUS coordinate system.*

The ZEUS coordinate system (see Fig. 4.2) is a right-handed Cartesian system, with the origin at the nominal interaction point (IP), the Z-axis pointing in the proton beam direction (referred to as the "forward direction"), and the X-axis pointing towards the centre of HERA. The polar angle, θ, is measured with respect to the proton beam direction, where the forward direction corresponds to $\theta = 0$ and the electron beam direction at $\theta = \pi$. The azimuthal angle, ϕ, is measured with respect to the X-axis. The Y-axis points up.

The centre of mass at HERA is boosted in the forward direction with respect to that of the two incoming beams due to the asymmetric energies. Thus the final state variables can be defined in terms of quantities such that they transform simply under longitudinal boosts. One such quantity is the rapidity y,

$$y = \frac{1}{2} \ln \left(\frac{E + p_z}{E - p_z} \right), \tag{4.1}$$

which is additive under the restricted class of Lorentz transformations corresponding to a boost along the Z-axis. Rapidity differences are boost invariant. Experimentally, since the angle θ from the beam direction is measured directly in the detector, the rapidity can be replaced by the pseudorapidity variable η,

$$\eta = -\ln \tan(\theta/2), \tag{4.2}$$

which coincides with the rapidity in the mass $m \to 0$ limit.

The longitudinal and transverse cross-sectional views of the ZEUS detector in the $Z - Y$ and $X - Y$ planes are shown in Fig. 4.3 and Fig 4.4, respectively. As can be seen, the detector layout is longitudinally asymmetric with respect to the IP: this is due to the large momentum imbalance between the electron and proton beams. A brief outline of the major detector components is given below. The main components used in the analyses will be described in some detail in the following sections. Starting from the interaction point and moving radially outwards in Fig. 4.3, one

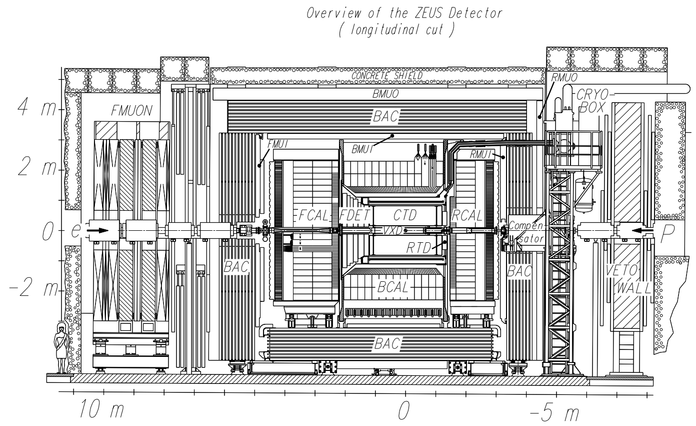

Figure 4.3: *Longitudinal cross-sectional view of the ZEUS detector along the beam direction.*

can find the vertex detector (VXD), the innermost component in the ZEUS experiment. However, the VXD was removed during the 1995/1996 shutdown. Recently a new silicon microvertex detector (MVD) [96] was installed in the Spring of 2001. Therefore, in the 1996 − 2000 configuration, the central tracking detector (CTD) is the nearest component to the IP. It is complemented by forward and rear tracking detectors (FTD, RTD). For charge and momentum determination, the tracking system is surrounded by a super-conducting solenoid providing a central magnetic field of 1.43 T.

The ZEUS calorimeter is located outside the superconducting magnet. It is a compensating (see section 4.2.2) high resolution uranium-scintillator calorimeter and it is divided into forward, barrel and rear sections (FCAL, BCAL and RCAL). To improve the discrimination between electromagnetic and hadronic showers for the low energy particles (< 5 GeV), silicon diodes have been added in the FCAL and

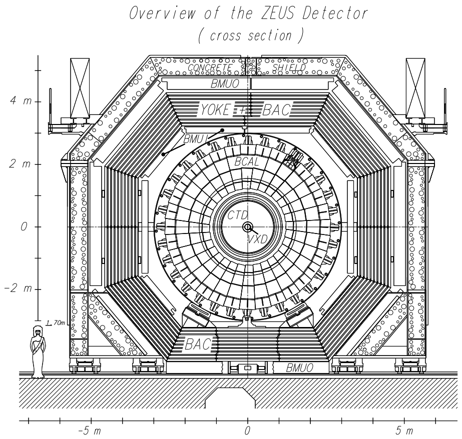

Figure 4.4: *Transverse cross-sectional view of the ZEUS detector along the beam direction.*

RCAL at the electromagnetic shower maximum (and form what is called the hadron-electron separator, HES). The whole uranium calorimeter is enclosed by an iron yoke, which provides the return path for the solenoid magnetic field flux and serves as an absorber for the backing calorimeter (BAC). The BAC measures energy leakage from the main calorimeter. Limited streamer tube chambers for muon identification are located inside (FMUI, BMUI, RMUI) and outside (FMUON, BMUON, RMUON) the yoke.

A small angle rear tracking detector (SRTD) is situated between the RTD and the RCAL, covering a radius of ~ 34 cm around the beam pipe. To measure electrons with an even smaller scattering angle, a small electromagnetic beam pipe calorimeter

(BPC) was installed in 1995 in the “beam pipe hole” of the RCAL. In 1997 the position resolution of the BPC was improved by the installation of a silicon tracker in front of the BPC, the beam pipe tracker (BPT). In 1998 a small forward plug calorimeter (FPC) was installed in the FCAL pipe “hole” to extend the calorimetric coverage by one unit in pseudorapidity.

Additional detectors are located outside the main detector along the beam pipe: at distances of about $24 - 90$ m from the interaction point, the leading proton spectrometer (LPS) is installed inside the proton beam pipe. It consists of 6 silicon strip detector stations which measure protons scattered at small angles. At $Z = 105.6$ m, a lead-scintillator calorimeter (FNC) is installed to measure the forward neutrons coming from protons. In the rear direction, at $Z = -7.3$ m a scintillator hodoscope with iron wall (VETO) are used to reject proton beam related background. The luminosity (LUMI) detectors consist of two small lead-scintillator calorimeters (LUMI-e, LUMI-γ), installed at $Z = -34$ m, and $Z = -104$ m, in order to detect bremsstrahlung events for the luminosity measurements. The LUMI detectors are also used to identify the scattered electrons and the radiative photons for the photoproduction and DIS events, respectively.

4.2.1 The Central Tracking Detector (CTD)

The CTD [97] is a cylindrical drift chamber designed to measure the momentum and direction of charged particles with a high precision and as such is essential for the complete reconstruction of the hadronic decay products of charmed mesons. The chamber is 205 cm long and has inner and outer radii of 18.2 cm and 79.4 cm, respectively. The resulting angular coverage is $15^o < \theta < 164^o$. The CTD consists of 72 radial layers of sense wires which are arranged into nine superlayers (SL). A group of eight wires in the $r - \phi$ plane of each superlayer defines a cell. One octant of the CTD is shown in Fig. 4.5. The five odd superlayers have wires parallel to the chamber axis and are called axial superlayers. The remaining four even layers

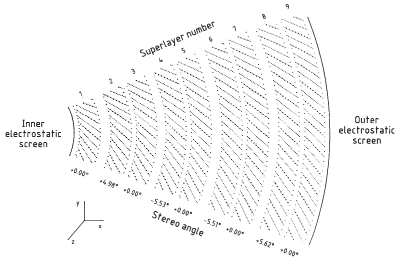

Figure 4.5: *X-Y cross section through one octant of the CTD. The wires of the even numbered superlayers are slightly tilted with respect to the beam axis (stereo superlayers). The values of this angle are displayed below the corresponding superlayer.*

are stereo superlayers, which have wires at a small angle ($\pm 5^o$)[1] with respect to the beam, thereby providing good Z position measurement (~ 1.4 mm resolution). The first three axial layers (SL1, SL3, SL5) are also equipped with a z-by-timing system in which the arrival times (t_1, t_2) of a pulse at the two opposite ends of a wire are measured and the Z position is determined from the time difference $|t_1 - t_2|$. This provides fast information about the Z position of a track which is then used for the trigger purposes. The drift chamber is filled with a gas mixture of argon (Ar), carbon dioxide (CO_2) and ethane (C_2H_6) in the ratio 83:05:12. The gas is bubbled through ethanol. This mixture has been chosen on the grounds of safety and protection against whisker growth, although an argon-ethane mixture (50:50) would provide a better resolution and less noise.

When a charged particle traverses the CTD, it ionises the gas, creating electron-ion pairs along its trajectory. Under the action of an electric field (1.82 kV/cm) and radial magnetic field (1.43 T), the freed electrons drifts towards the positive sense wires (with an approximately constant velocity of 50 μm/ns), whereas the positive ions are accelerated towards the negative field wires. In the field of these

[1] The stereo angle chosen (5^o) is such that the angular resolution in polar and azimuthal angles are roughly equal.

sense wires, avalanche-like multiplication of the electrons occurs, with a factor of about 10^4. The produced sizable pulse is then read out and digitised by 8-bit flash analogue to digital convertors (ADCs). The path of the charged particles can then be reconstructed using the hit pattern and the known drift times. The measurement of the curvature of the tracks in the magnetic field of the solenoid can be used to determine the transverse momenta, p_T, of the particles, which along with the polar angle measurement allows the full determination of the particle momenta. The relative transverse momentum resolution of the CTD, obtained from parameterising the detector simulation (tuned with data) on the generated tracks coming from the $D^{*\pm} \to D^0 \pi_S^\pm \to K^\mp \pi^\pm \pi_S^\pm$ channel, is given by[2] [97]:

$$\frac{\sigma(p_T)}{p_T} = 0.0058 p_T \oplus 0.0065 \oplus \frac{0.0014}{p_T}, (p_T \text{ in GeV}) \tag{4.3}$$

where the first term corresponds to the resolution of the hit positions, the second term to smearing from multiple scattering within the CTD and the last term to multiple scattering before the particle enters into the CTD.

4.2.1.1 Track Reconstruction

A detailed description of track reconstruction can be found in [98], but is here briefly described. In the track finding algorithm, each track candidate begins as a "seed" of 3 hits in an outer axial superlayer, which is extrapolated towards the vertex. The pattern recognition procedure first reconstructs the longest tracks, which are successfully continued from SL9 all the way down to SL1. Shorter tracks, whose track seed was found in SL7, are then reconstructed and the process continues until the inner SLs are reached. Tracks with too many shared hits are removed from the algorithm. Each track candidate is then fitted to a 5 parameter helix model, by evolving the trajectory through the magnetic field. From the helix model fit, the tracks are then classified as either not coming from the primary vertex (VCTRHL) or tracks from the primary vertex (VCTPAR). The resolution of the ZEUS tracking

[2] Here $\oplus$ stands for addition in quadrature.

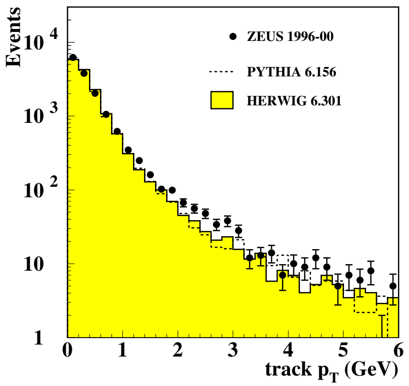

Figure 4.6: *The p_T distribution of tracks in the CTD for jet events associated with D^* mesons. The Monte Carlos are normalised to the data.*

during the 1996−2000 data taking period, in the absence of MVD, was not sufficient to enable the identification of secondary vertices arising from charmed (D^*) mesons. Thus, in order to select the D^* candidates coming from the primary interaction vertex, only VCTPAR tracks were used for the analyses.

Fig. 4.6 shows the p_T distribution of VCTPAR tracks for data and Monte Carlo events with an identified jet-associated D^* meson. There is a reasonable agreement between data and Monte Carlo, which quantifies the correctness of both the detector simulation and the underlying distribution.

4.2.2 Uranium-Scintillator Calorimeter (UCAL)

In order to reconstruct jets, essential for the analyses in this thesis, the measurement of the energy of all particles is needed, including both charged and neutral particles. The full reconstruction of jets is performed using either the calorimeter cells alone, or a combination of tracks and calorimeter cells, where a cell is the smallest subdivision of the calorimeter.

The ZEUS calorimeter [99] (UCAL) is a high resolution uranium-scintillator

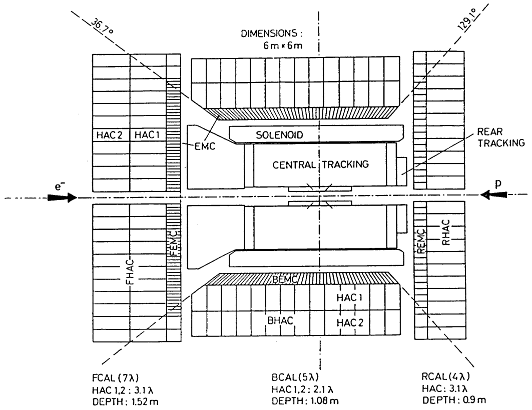

Figure 4.7: *View of the UCAL geometry.*

calorimeter. It completely surrounds the solenoid and the tracking detectors, as shown in Fig. 4.7. It consists of alternating layers of 3.3 mm thick depleted uranium (98.1% U^{238}, 1.7 % Nb, 0.2 % U^{235}) plates, which act as absorbers, and 2.6 mm thick organic scintillators (SCSN-38 polystyrene) as active material for readout purposes. The thickness of the plates has been specifically chosen such that the calorimeter has equal response to electrons and hadrons of the same energy ($e/h = 1.00 \pm 0.02$). This property of the calorimeter makes it a "compensating" calorimeter. In this way optimum accuracy for the absolute value and the resolution of hadronic energies is achieved. The main features of the ZEUS calorimeter are:

- hermeticity over a large solid angle (coverage of 99.7% of the solid angle);
- energy resolution for hadrons of $\sigma(E)/E = 35\%/\sqrt{E} \oplus 2\%$;
- energy resolution for electrons of $\sigma(E)/E = 18\%/\sqrt{E} \oplus 2\%$;
- calibration of the absolute energy scale to 1% [100];

Part of the UCAL	Polar angle	Pseudorapidity
FCAL (forward)	$2.2° < \theta < 36.7°$	$4.0 > \eta > 1.1$
BCAL (barrel)	$36.7° < \theta < 129.1°$	$1.1 > \eta > -0.74$
RCAL (rear)	$129.1° < \theta < 176.2°$	$-0.74 > \eta > -3.4$

Table 4.1: *CAL sections and the angular ranges covered by them. The polar angle and the pseudorapidity ranges are calculated with respect to the nominal interaction point.*

- precise angular resolution for particles ($\leq$0.1 mrad);
- short signal-processing time at the nano-second level.

The UCAL consists of three parts: the forward (FCAL), the barrel (BCAL) and the rear (RCAL) calorimeters. Table 4.1 shows the angular coverage by them. Each of the calorimeter parts is subdivided into modules, which in turn are segmented into towers. Each tower is longitudinally divided into an inner electromagnetic (EMC) and two (one in RCAL) outer hadronic (HAC) sections. The EMC sections consist of four (two in RCAL) cells with transverse dimensions of 5×20 cm^2 (10×20 cm^2 in RCAL), whereas each HAC section consists of one 20×20 cm^2 cell. As an example, a module of the FCAL is shown in Fig. 4.8, where the readout mechanism is also illustrated: when an incident particle deposits energy, the generated scintillator light of each cell is read out on opposite sides, via a coupling to wavelength shifters guiding the light to the photomultiplier tubes (PMT's). Comparison of the two PMT signals allows the determination of the horizontal impact position. The calorimeter also provides accurate timing information at the nano second level. The timing resolution for each calorimeter cell is $\sigma_t = 1.5/\sqrt{E} \oplus 0.5$ ns, where E (in GeV) is the energy deposited in the cell [99]. The time $t = 0$ is defined to be the time at which the particles originating from ep collisions at the interaction point arrive at the calorimeter. The timing information from the calorimeter is useful to remove both beam-gas and cosmic-ray backgrounds. When particles from proton beam-gas

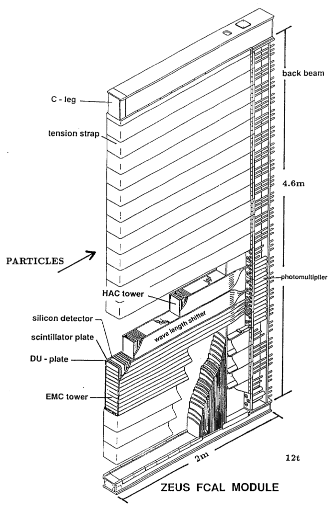

Figure 4.8: *Layout of a FCAL module.*

interactions, which may occur behind the RCAL and deposit energy in the RCAL, this time is negative. Therefore, a cut on the RCAL time can remove a very large number of beam-gas events. The "up-down" time difference, defined as the difference between the time at which energy is deposited in cells at the top and at the bottom of the BCAL, should be zero for deposits related to an ep collision. However, for cosmic rays, this time difference is greater than 10 ns. Therefore, cosmic-ray events can also be removed with the calorimeter timing information.

The calibration of the calorimeter is performed using several tools [101]. The main calibration source is the use of the natural uranium radioactivity, the so-called uranium noise (UNO), which produces a low background current in the photomultiplier. This current is statistically very stable and the deviations from the expected value allow problems encountered during the operation of the photomultipliers to be detected. To calibrate the electronic readout system, charge injectors are used to simulate the signal coming from the photomultiplier. Since the quantity of charge is known, the returned value given by the complete readout system is used to calibrate the effects of the electronics, after subtraction of the noise contribution. These tools, together with beam tests, cosmic ray tests and laser calibration, provide a stable diagnostic mechanism for monitoring and calibration of the calorimeter.

4.2.3 Luminosity Measurement

The luminosity measurement is essential for any cross section calculation and is measured at ZEUS from the rate of bremsstrahlung processes;

$$e \, + \, p \, \rightarrow \, e' \, + \gamma \, + \, p \tag{4.4}$$

Integrating over scattering angles, the cross section can be obtained semi-classically by the Bethe-Heitler formula [102],

$$\frac{d\sigma}{dE_\gamma} = 4\alpha r_c^2 \, \frac{E_e'}{E_\gamma \, E_e} \left(\frac{E_e}{E_e'} + \frac{E_e'}{E_e} - \frac{2}{3} \right) \left(\ln \frac{4E_p \, E_e \, E_e'}{M \, m \, E_\gamma} - \frac{1}{2} \right), \tag{4.5}$$

where E_γ is the photon energy, E_e and E_e' are the energies of the initial and final electrons, E_p is the proton energy, M (m) is the proton (electron) mass, α is the fine structure constant and r_c is the classical electron radius.

The radiative corrections to this process have been calculated and found to be quite small (-0.3%) within the measurable area of phase space. The ZEUS luminosity monitor [103] consists of electron (LUMI-e) and photon (LUMI-γ) sampling lead-scintillator calorimeters as shown in Fig. 4.9. The LUMI-e detector is situated at $Z = -34$ m and the LUMI-γ is situated at $Z = -104$ m. Electrons with scattering angle $\theta_{e'} \leq 6$ mrad and energy $0.2E_e \leq E_{e'} \leq 0.9E_e$ are deflected out of the beam orbit by the HERA magnetic field from the bending dipoles (BH in the figure) and are allowed to leave the beam pipe by a window at $Z = -27$ m. This is then measured at LUMI-e with a resolution of $18\%/\sqrt{E}$ (E in GeV).

The LUMI-γ calorimeter detects photons radiated within a cone of 0.5 mrad around the beam axis. These photons leave the beam pipe via a window at $Z =$

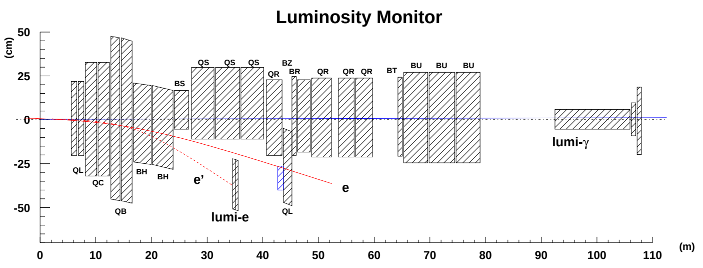

Figure 4.9: *The luminosity monitor (see text).*

-92 m. For photons with energy greater than 5 GeV the acceptance is 98 %. The resolution of the LUMI-γ is similar to the LUMI-e, although for protection from synchrotron radiation it is shielded by a lead filter, effectively reducing the resolution to $25\%/\sqrt{E}$ (E in GeV). In addition, the LUMI-e can be used to tag electrons at low scattered angles with $10^{-7} < Q^2 < 2 \cdot 10^{-2}$ GeV^2 to provide additional information about the event kinematics.

Once the observed ep-bremsstrahlung rate, R_{ep}, is measured, the luminosity is given by $\mathcal{L} = R_{ep}/\sigma_{obs}$; where σ_{obs} is the ep-bremsstrahlung cross section corrected for the detector inefficiencies and acceptances. The luminosity measurement can suffer from a number of background processes, the most problematic being the beam gas bremsstrahlung where the electron interacts with a nucleus (N);

$$e + N \;\rightarrow\; e' \, + \gamma \, + \, N, \tag{4.6}$$

which has a similar signature to the process, as Eq. 4.4. The contribution of these background processes to the total measured rate by the luminosity monitor can be estimated by making use of the pilot electron bunch. For a total counting rate of the luminosity detector, R_{tot}, and pilot-bunch rate, R_{pilot}, if the total current in the electron ring is I_{tot}, and I_{pilot} is the current in the pilot bunches, the actual ep-bremsstrahlung rate for the luminosity can be estimated as:

$$R_{ep} = R_{tot} - R_{pilot} \cdot \frac{I_{tot}}{I_{pilot}} \, .$$

This relationship can then be used inside the Bethe-Heitler expression with corrected acceptances to determine the final luminosity.

4.2.4 Trigger and Data Acquisition System

As mentioned previously a bunch crossing occurs every 96 ns at HERA, which is equivalent to a nominal crossing rate of $\sim$ 10 MHz. However, the total interaction rate is dominated by the interaction of the proton beam with residual gas in the beam pipe at large negative Z. This provides a rate of the order of 10-100 kHz, while the rate of ep physics events in the detector is of the order of 5-8 Hz. The VETO Wall (outlined previously, see also Fig. 4.3, right side), shields the detector partially from particles originating in these beam gas interactions and reduces the rate by one order of magnitude. In addition, other background sources such as electron-gas collisions, halo muons and cosmic rays are also present. Suppression of such backgrounds is achieved by a sophisticated ZEUS three level trigger system [104], where each successive level has more time available to take more complicated trigger decisions. A schematic diagram of the ZEUS trigger and data acquisition systems is given in Fig. 4.10.

4.2.4.1 The First Level Trigger

The First level trigger (FLT) is a hardware trigger, designed to reduce the event rate to $\sim$ 1 kHz. Each component of the ZEUS detector has its own FLT, which stores the data in an electronic pipeline and makes a trigger decision within 2 μs after the bunch crossing. The FLT operates only on a small subset of detector data, calculating crude event observables like regional energy sums, number of tracks and timing information. Each component completes its internal trigger calculations and passes the information for a particular bunch crossing on to the Global First Level Trigger (GFLT). Once the decisions from all the FLT parts are collected by the GFLT, it decides whether to accept or reject the event, and returns this decision to

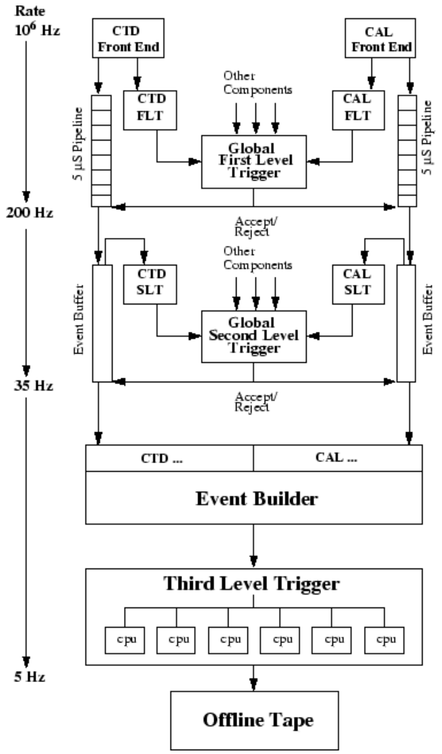

Figure 4.10: *Schematic diagram of the ZEUS trigger and data acquisition system. The effects of the trigger selection on lowering the rate are shown in the lines parallel to the decision diagram.*

the readouts of the different components within 4.6 μs, corresponding to 46 bunch crossings out of a maximum of 52 for the pipeline. At the FLT, most of the beam-gas and beam-halo events are rejected.

4.2.4.2 Second and Third Level Triggers

Following acceptance by the GFLT, the data is then transferred to the Second Level Trigger (SLT). This is software-based and runs on a network of transputers. It is designed to reduce the rate below 100 Hz, where a decision typically takes 30 μs, within a given dead time of about $\sim 3\%$. As in the case of FLT each subcomponent has its own local SLT process (objects like track momenta, the event vertex and calorimeter clusters are reconstructed), passing information to the Global Second Level Trigger (GSLT). If the event is accepted by the GSLT, all the detector components send their data to the Event Builder, which collects the information to reconstruct a complete event. The event is then passed to the Third Level Trigger (TLT), which runs a part of the offline reconstruction on a computer farm of PCs with Intel CPUs. On the TLT level, detailed tracking as well as jet and electron finding are performed. After the final TLT decision, the rate is reduced to 5-10 Hz. Events accepted by the TLT have a typical data size of $\sim$ 100 kB and are written to disk at the DESY computing centre via a fiber-link (FLINK) connection. From then onwards the events are available for the full offline reconstruction and data analysis.

4.2.5 Offline and Detector Simulations

The data previously stored on tape is reconstructed with the ZEPHYR package. During the reconstruction, a preselection logic based on very soft, process oriented requirements is performed. The results of this preselection are coded as Data Summary Tape (DST) bits, which are stored in the header of the event file. Only the header is read for events which do not fulfill the required DST bit logic. This speeds up the selection of events needed to reconstruct jets and charmed mesons for the analyses, over a large volume of data (see section 7.2).

During the reconstruction procedure, the information of the different components is re-analysed by applying corrections given by the data quality monitoring and by the calibration of the different channels on each component. Since the whole

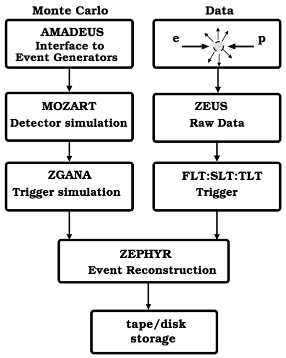

Figure 4.11: *Diagram of the ZEUS reconstruction scheme.*

detector information (like the calibration constants, bad channels, etc.) is available during this stage, the reconstruction procedure makes use of this information. Once reconstructed, the data is then written to disk and is available for the final physics analysis [105].

As can be seen from the complexity of the ZEUS detector, it is quite important to understand the detail detector effects, which can influence the observation of the final state processes. This is done using the Monte Carlo (MC) techniques, in which a detailed detector simulation is performed with the **M**onte **C**arlo for **Z**eus **A**nalysis, **R**econstruction and **T**rigger (MOZART) program (based on GEANT 3.13 [106]). Its kernel is based on the current understanding of each specific component and the detector as a whole, including the material they are made of, their exact geometry and position. The program tracks particles through the whole detector, taking into account physics processes such as energy loss, multiple scattering, particle decays in flight, etc. MOZART contains subprograms for the simulation of the trigger (ZGANA, acting on simulated signals from the different detector components), and for the offline reconstruction (ZEPHYR). Fig. 4.11 shows a schematic diagram of the ZEUS reconstruction scheme for data and MC.

Chapter 5

Physics Simulation

The simulation of physics events in ZEUS is done in two main steps. In the first step, the underlying dynamics of *ep* scattering is simulated by means of so-called 'event generators'. In an event generator, the leading order hard subprocess and the effects of the leading logarithmic parton showers are simulated by using the principles of pQCD. In addition, aspects of soft, non-perturbative physics such as hadronisation and initial state parton density functions are included by using phenomenological models and parameterisations. In the second step, a simulation of the detector and trigger response to the collection of outgoing particles is performed. The output of this simulation, as discussed in section 4.2.5, has the same format as the real data recorded by the detector and can therefore be passed through the same event reconstruction and physics analysis chain. The combination of these two steps involving event generation and event simulation (detector simulation) is called a *Monte Carlo* (MC) simulation.

In this chapter, a description of the important aspects of the event generation is presented. The event generators used for the analyses are CASCADE 1.00/09 [107], HERWIG 6.301 [108] and PYTHIA 6.156 [109]. To calculate the acceptances and to estimate hadronisation effects, HERWIG and PYTHIA are used, whereas CASCADE along with HERWIG and PYTHIA were compared to the measured cross

sections to try and validate the underlying physics in each of the models.

5.1 Overview

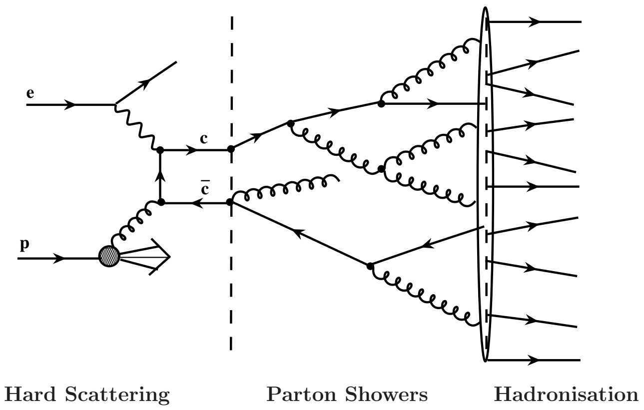

Figure 5.1: *Schematic representation of the different steps in the generation of ep events. The hard scattering is followed by the parton shower (PS) and the hadronisation.*

For any given *ep* scattering process, the generation of simulated events relies on phenomenological approaches which occur at all levels apart from calculation of the matrix elements. This is not done in one step, but rather by "factorising" the problem into a number of stages (see Fig. 5.1), such as hard scattering, parton showers, and hadronisation, as described below. The theoretical justification for dividing the overall structure into various steps is based on the factorisation theorem [110]:

1. **hard sub-process**: a pair of incoming beam particles or their constituents interact to produce one or more primary outgoing particles. This can be calculated

to the lowest order in perturbation theory. The hard momentum transfer scale, together with the colour flow of the subprocess, set the boundary conditions for the initial- and final- state parton showers.

2. **parton shower**: the partons resulting from the hard scattering undergo successive branchings, until their virtuality is smaller than a fixed cut-off scale, typically around 1 GeV.

3. **hadronisation (fragmentation)**: the process by which primarily produced coloured partons transform into colour singlet hadrons. This is a non-perturbative process. It will be addressed in detail in this thesis, both in terms of experimental measurements and phenomenological models.

4. **beam remnant fragmentation**: in the scattering process, the algorithm for initial-state radiation is applied to each particle beam. The shower is then initiated by backward evolution from the hard sub-process. This shower initiator takes only some fraction of the total beam energy, leaving behind a beam remnant to carry the rest. If the shower initiator is coloured, so is the remnant. Being colour-connected to the hard interaction, the beam remnant is part of the same fragmenting system and needs to be reconstructed and connected to the rest of the event. In addition, in collisions where the two incoming beam particles have a composite nature (e.g. hadron-hadron interaction, resolved photoproduction) there is the additional possibility that several parton pairs undergo separate hard or semi-hard scattering known as 'multiple interactions' [111] (See Fig. 5.2).

5.2 Multiparton Production

The description of the hadronic final state at high energy requires the calculation of multiple-parton emissions in QCD. Phenomenologically, this is done by reducing the hard hadron-hadron interactions to parton-parton interactions. The hard process is then expressed as the convolution of the parton distributions in the colliding hadrons with the cross section of the elementary sub-process given by the square

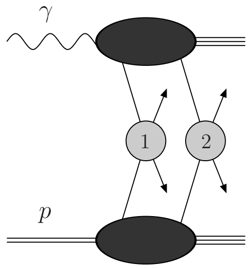

Figure 5.2: *Schematic representation of multiple interactions in γp collision. The 1st blob represents the additional scattering from initial-state radiations, whereas the 2nd shows the hard scattering initiated by the "active" partons from the photon γ, and proton p.*

of the matrix element, calculated in perturbative QCD. Such an approach can be justified in the Leading Logarithmic Approximation (LLA) in LO, or any order in QCD. In the following subsection two different approaches are presented, which were used to study the hard scattering dynamics in this work.

5.2.1 Collinear Approach

The most popular and technically simplest approach is the so-called QCD collinear approximation. In this model all incoming (before the hard scatter) and outgoing (after the hard scatter) particles are assumed to be on the mass shell, $m^2 > 0$; ($m^2 = E^2 - \boldsymbol{p}^2$). They only have the longitudinal components of momenta; the transverse momenta of these incident partons are neglected in the QCD matrix elements in direct analogy with the Weizsäcker-Williams approximation in QED. The virtualities, q^2, of the initial partons are taken into account only through their densities (referred to as the structure functions). These densities are then calculated in the LLA using the DGLAP evolution equation[1] and also fitted to the available experimental data.

[1] Essentially corresponds to the summation of the contributions of the type $(\alpha_s \ln q^2)^n$.

Here the partons are essentially considered to be "frozen" inside the hadrons. The cross section in the collinear approach for heavy quark production in γp interactions can be written in the following factorised form [110]:

$$d\sigma(\gamma p \to c\bar{c}) = \sum_{ij} \int dx_i dx_j F_{\gamma/i}(x_i, \mu_F) F_{p/j}(x_j, \mu_F) d\hat{\sigma}(ij \to c\bar{c}), \qquad (5.1)$$

where $F_{\gamma/i}(x_i, \mu_F)$ and $F_{p/j}(x_j, \mu_F)$ are the structure functions of partons i and j in the colliding hadrons γ and p, μ_F is the factorisation scale and $d\hat{\sigma}(ij \to c\bar{c})$ is the partonic subprocess calculated in perturbative QCD. Here the virtuality of the parton entering the hard scattering matrix element is neglected, or considered as collinear with the incoming hadron. The main uncertainties are the consequences of unknown scales[2], μ_F and μ_R and the charm quark mass, m_c. Both the factorisation and renormalisation scales (usually assumed to be equal) are generally set to be equal to the "hardness" of the treated process. However, which value should be taken: m_c or $m_T = \sqrt{m_c^2 + p_T^2}$, remains to be determined. In this thesis, the maximum uncertainties for the NLO calculations were estimated by simultaneous variation of m_c between 1.3 and 1.7 GeV and μ_R between $m_T/2$ and $2m_T$.

This approach is somewhat successful in describing the experimental data on the total cross sections as well as one-particle distributions for heavy quarks, however it cannot reproduce, for example, the azimuthal correlations [112, 113] of two heavy quarks, as well as the distributions over the total transverse momentum of heavy quark pairs [88], which are determined by the transverse momenta of the incident partons.

5.2.2 Semi-hard or k_T-Factorisation Approach

Another method that accounts for the incident parton transverse momenta is referred to as the k_T-factorisation [44] or the theory of semi-hard interactions [114]. In this approach one considers processes occurring at very small values of $x \sim m_T/\sqrt{s}$,

[2] μ_R, defined as the renormalisation scale, enters into the cross section calculation, $d\hat{\sigma}(ij \to c\bar{c})$.

which pertains directly to heavy quark production at high energies. At these energies ($\sqrt{s} \to$ large $\Rightarrow x \to$ small) the scale of the hard process is set by the heavy quark mass, m_c, and is larger than the QCD scale, Λ_{QCD} (which is of the order of 200-300 MeV). Thus, the logarithmic terms corresponding to $\ln(\frac{1}{x})$ in the evolution equations can no longer be ignored, as was done in the collinear approach. The rapid growth of the parton density for $x \to 0$ causes the parton-parton interactions to become more significant. Thus in order to describe this region, the contributions not only of order $(\alpha_s \ln q^2)^n$, but also $[\alpha_s \ln q^2 \ln \frac{1}{x}]^n$ and $[\alpha_s \ln \frac{1}{x}]^n$ must be summed. This is done using so called unintegrated parton distributions.

Consider the cross section for heavy quark photoproduction via photon-gluon fusion at a centre-of-mass energy $\sqrt{s}$ much greater than m_c. In order to use the k_T -factorisation theorem, which allows the resummation of leading logarithms, one has to consider the elementary subprocess $\gamma g \to c\bar{c}$ in which not only the photon momentum, q, but also the incoming gluon momentum, $k = k_n$, is off-shell. For $m_c^2 \ll s$, k and q get only a small fraction of the proton and electron momenta respectively, thus these momentum fractions can be written as $k \simeq xp_p + k_T$ and $q \simeq yp_e + q_t$; $q^2 = -Q^2 \simeq -q_t^2$, where q_t, k_T and x, y, are the two transverse and the two longitudinal components of the incident partons, respectively. According to the results in [44, 114], the heavy flavour cross section for $m_c^2 \ll s$ is then expressed as:

$$\sigma(ep \to c\bar{c}X) \sim \frac{\alpha}{2\pi} \int \frac{dx}{x} \frac{dy}{y} \frac{dQ^2}{Q^2} d^2k_t [1 + (1-y)^2] \mathcal{F}(x, k_T) \hat{\sigma}(\hat{s}, m_c; k_T, q_t). \qquad (5.2)$$

The cross section, $\hat{\sigma}$, is a generalised subprocess cross section for the off-shell photon and gluon to produce the charm-anticharm pair with the squared centre-of-mass energy $\hat{s}$. The equation is made such that if k goes on-shell ($k_t^2 \to 0$), the usual on-shell expression (Eq. 5.1) can be obtained.

The function $\mathcal{F}(x, k_T)$ is a generalised proton structure function giving the probability (per unit $\ln x$) of finding a gluon at longitudinal momentum fraction x and transverse momentum k_T. When integrated over transverse momentum up to some limit μ (set by the factorisation scale), the generalised structure function becomes the usual structure function, $F(x, \mu^2)$, given the gluon momentum fraction distribu-

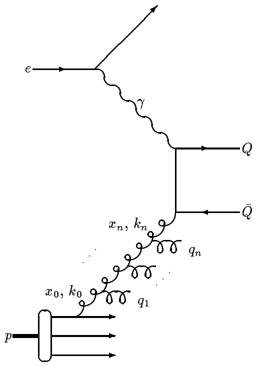

Figure 5.3: *Photoproduction of heavy quark anti-quark pair.*

tion at scale μ^2,

$$\int_0^{\mu^2} d^2k_T x\mathcal{F}(x, k_T^2, \mu^2) = xF(x, \mu^2) \tag{5.3}$$

The transverse momentum k_T arises from the emission of gluons in the course of the evolution of the structure function from the typical hadronic scale up to the scale μ as shown in Fig. 5.3. Based on the approximations used (in Eq..(5.3)), the unintegrated parton distributions can be classified as follows:

i) $x\mathcal{G}(x, k_T^2)$ describes the DGLAP type.

ii) $x\mathcal{F}(x, k_T^2)$ is used for the pure BFKL type.

iii) $x\mathcal{A}(x, k_T^2)$ stands for a CCFM type.

However, based on the above classifications, many parameterisations [115] exist in order to calculate the unintegrated gluon distributions. For example, in the case of charm jets, a direct comparison between three different representations, one coming from a leading-order perturbative solution of the BFKL equations, the second derived from numerical solutions of the CCFM equations and the third from the solutions of a combination of BFKL and DGLAP equations, can be found in [116].

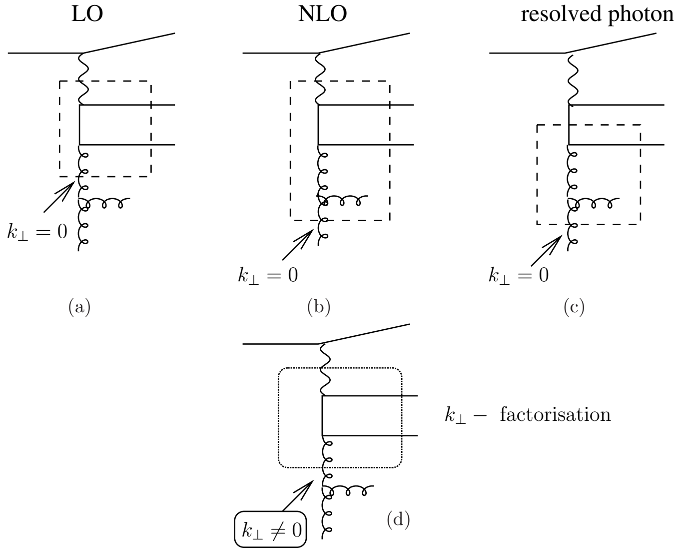

Figure 5.4: *Diagrammatic representation of LO, NLO and resolved photon processes in the collinear approach (top row) and compared to the k_T-factorisation approach.*

In contrast with the collinear approximation, the k_T-factorisation approach takes into account the gluon transverse motion k_T. On average, the gluon transverse momentum decreases from the hard interaction box towards the proton line (from top to bottom of the diagram in Fig. 5.4). The k_T of these gluons which are not included in the hard interaction block (Fig. 5.4 a)) is then determined exclusively by the properties of the evolution equation. Thus, the radiated gluon close to the quark box can have even larger transverse momentum than any of the two quarks involved in the hard subprocess [117], which in the collinear approach (Fig. 5.4 b)) requires a full $\mathcal{O}(\alpha_s^2)$ matrix element for $2 \rightarrow 3$ to be calculated (NLO). The next aspect is that, in any analysis the k_T of the incoming gluons can only be restricted by the kinematics and therefore, the virtuality of either the second or third parton in the ladder (Fig. 5.4 c)) can be higher than the first. This feature in the collinear approach can give rise to resolved photon processes.

Fig. 5.4 summarises the basic ideas of the different factorisation approaches. In the following chapters the comparison of the experimental data to these approaches will be shown. At this stage it can be said, that not only does the k_T-factorisation include at least some of the NLO diagrams [118], but it also includes diagrams of the resolved photon type, with the transition from real to virtual photons [119, 120]. The uncertainties in this approach are estimated not only by the variation of m_c between 1.3 and 1.7 GeV, but also by varying the maximum allowed angle for the quark box, (as shown in Fig. 5.4) to twice or half of its nominal value.

5.3 Initial- and Final-state Radiation

A fast moving hadron may be viewed as a cloud of quasi-real partons. At each instant, an individual parton before or after the hard scattering can initiate a cascade, branching into a number of partons. The partons produced before and after the hard scattering are called initial state and final state radiation, respectively. These partons may not have enough energy to be on mass-shell, and thus they only live for a finite time before recombining. In a hard interaction between two incoming hadrons, when two partons scatter at high p_t, the other partons in the two related cascades are also provided with the necessary energy to be long-lived. Starting from a basic $2 \to 2$ process[3], these other parton related cascades will generate large corrections to the final state topologies ($2 \to 3$, $2 \to 4$, and so on).

Traditionally two approaches exist to model these perturbative corrections. One is the matrix element method, in which Feynman diagrams are calculated, order by order. In principle, this is the correct approach, where the transfer of energy is given by the various $2 \to N$ hard scattering matrix elements, where N is the final parton

[3] The first 2 stands for the two initiators of the cascades, the second stands for the final state partons after the hard scatter.

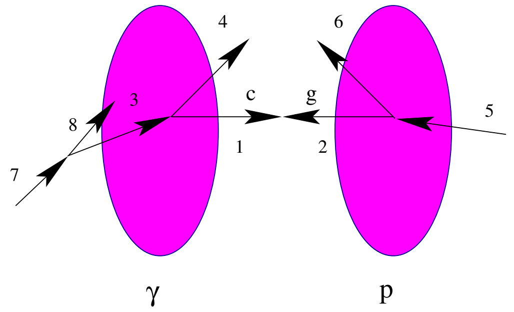

Figure 5.5: *Schematic representation of space-like shower evolution, with hard scattering partons 1 and 2 and emitted time-like partons 4, 6 and 8.*

multiplicity. This approach takes into account the exact kinematics and the full interference between the outgoing partons. In practice, matrix elements can only be calculated for small values of N. The calculation becomes increasingly difficult for higher values of N, in particular for the loop diagrams. Only in exceptional cases have more than one loop corrections been calculated in full, and that too without any loop corrections. On the other hand, there is indirect but strong evidence that multiple soft gluon emission plays a significant role in building up the event structure, e.g at LEP, and this sets a limit to the applicability of matrix elements. Since the phase space available for gluon emission increases with the available energy, the matrix-element approach becomes less relevant for the full structure of events at higher energies. However, it should be noted that the matrix-element approach, due to its predictive power should be used for the specialised studies like α_s determination, angular distribution of jets, triple-gluon vertex, etc., and hence is important for this thesis.

The second possible approach is the parton shower one. Here an arbitrary number of branchings of one parton into two (or more) may be combined, with no upper limit on the number of partons involved. However it is convenient to imagine that the partons on the two branches which led from the two initiators to the hard scattering ($7 \to 3 \to 1$ and $5 \to 2$ in Fig. 5.5) have increasing space-like virtualities, $Q^2 = -m^2 > 0; m^2 = E^2 - \boldsymbol{p}^2$, adjusted such that the partons on all other branches (8, 4 and 6 in Fig. 5.5) may have $m^2 \geq 0$; these latter partons are referred to as the time-like ones. Then the momentum transfer given by the central $2 \to 2$ hard scattering subprocess is enough to ensure that all partons may end up on mass shell. Except for the two hard scatterers, the partons continue essentially along the direction of the respective hadron (γ, p) they belonged to, although occasionally they may have large transverse momenta and give rise to separately visible jets of their own. Other cascades within the two interacting hadrons remain unaffected, i.e do not receive any energy transfers, and then disappear unnoticed into the low-p_t beam remnant.

Thus, the two approaches are complementary and both are used to compare the underlying physics dynamics in this thesis. The matrix element approach has been used within the fixed order NLO scheme, whereas the parton-shower approach was used in all MCs presented below.

5.4 Hadronisation

After the parton shower, the final state consists of quarks and gluons with virtualities (momentum transfer) of the order of the cut-off scale μ_0. At this low momentum transfer (long-distance) QCD becomes strongly interacting and perturbation theory breaks down. In this confinement regime the coloured partons are transformed into colour singlet hadrons, a process which is called either hadronisation or fragmentation. Here one addresses the issue of how the final state partons produce final state hadrons, which however has nothing to do with the initial state. There are several phenomenological models to simulate the fragmentation of hadrons from partons. The three main models are the String or Lund fragmentation, the Cluster fragmentation and the Independent fragmentation models and are described below.

5.4.1 String Fragmentation

In this semi-classical model [121], as the two coloured quarks q and $\bar{q}$ move apart from their common production vertex, the chromo-field between them does not spread through space in the same way as does the electric field between two charges; rather, it is confined to a flux tube about 1 fm across. A simple application of Gauss's theorem shows that as the colour charges separate and the flux tube stretches, the energy stored in the field increases: about 1 GeV for each fm of flux-tube length. As this flux tube stretches, the energy in it grows at the expense of the kinetic energy of the quark, until it far exceeds the mass energy of the lightest hadrons. It therefore readily materialises as hadrons each carrying a fraction of the original momentum of the quark.

This colour field between the quarks is modelled by a uniform string in the Lund model, with an energy proportional to their distance

$$E(r) = \kappa \cdot r, \tag{5.4}$$

where κ is a string constant estimated to be $\kappa \approx 1.0$ GeV/fm. At a typical distance of 2 – 5 fm, the string breaks by forming a new $(q', \bar{q}')$-pair, leaving two colour singlets $(q, \bar{q}')$, $(\bar{q}, q')$. If the invariant mass of either of these string pieces is large enough, further break-ups may occur. A Lund string break-up process is schematically shown in Fig. 5.6. It is important to note the following assumptions:

i) There is no field between a $q\bar{q}$-pair produced at the "initial" vertex.

ii) A string force field is always confining because it has a fixed energy per unit length (κ is constant) and the force field vanishes at the end-point charges.

iii) All hadrons must have positive momenta. There is no defined "first" vertex; they are all equal. In the Lund model, the slowest particles are always produced first in any frame.

iv) Even if the energy of the original pair increases without limit, the multiplicities of production vertices will stay finite.

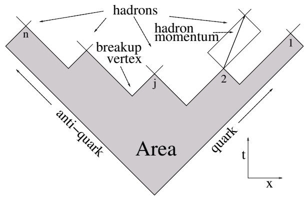

Figure 5.6: *A typical Lund String break-up in space and time coordinates.*

The probability for a string break-up based on the above mentioned assumptions can be given by the following probability distribution function.

$$f(z) \propto z^{-1}(1-z)^{\alpha}\exp(\frac{-\beta \cdot m_{\perp}^2}{z}) \tag{5.5}$$

where $f(z)$ is the probability for producing a hadron with a mass, $m_{\perp}$, taking a fraction z of the remaining light-cone ($E + p_z$ or $E - p_z$) momentum. The free parameters α and β are related to the behaviour for z close to 0 and 1 and are determined from fits to experimental data. The behaviour as $z \rightarrow 0$ is regulated by the factor $(1/z)\exp(-\beta m_{\perp}^2/z)$, which peaks at $z = \beta m_{\perp}^2$ for $\beta m_{\perp}^2 < 1$, while the behaviour for $z \rightarrow 1$ is determined by the factor $(1-z)^{\alpha}$.

For a $(q, g, \bar{q})$ system, the gluons are considered as the internal excitation of the string carrying localized energy and momentum, thus the string is stretched from the quark end via the gluon to the anti-quark. The string then fragments into two $q\bar{q}$ string segments which are boosted with respect to the overall centre-of-mass frame of the initial $(q, g, \bar{q})$ system and then the rest is treated as described before. Now if we generalize this to a system of n partons, which is the case after the parton shower, the produced partons are arranged in a planar configuration, where each parton has an equal and opposite colour to that of its neighbours, from a quark end via a number of intermediate gluons to an anti-quark end (see left side of Fig. 5.7). At each stage, the string iteratively fragments into smaller segments and the transverse momentum, p_t, for each $q\bar{q}$-pair created is generated using a Gaussian distribution in p_x and p_y separately. When the energy of individual strings is too small to enable the partons to separate further, final state hadrons are formed.

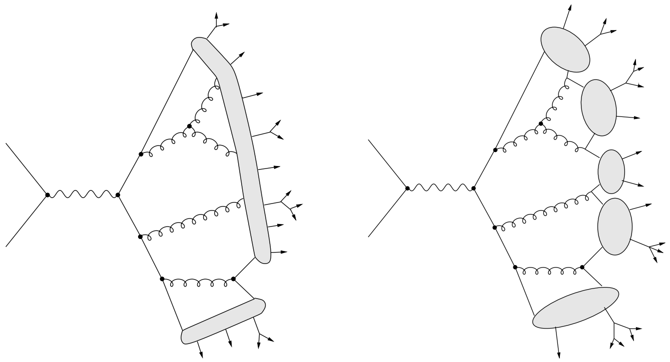

Figure 5.7: *Schematic picture showing a parton shower followed by Lund string fragmentation (left) and Cluster hadronisation (right).*

It should be noted that, as there is no unique prescription that the iterative procedure should start from a quark to the anti-quark end or vice versa, hence the results of the choice for the fragmentation function gives a unique "left-right" symmetry. Hence it is often termed as "Lund symmetric fragmentation function".

5.4.2 Cluster Fragmentation

In the cluster fragmentation model [122], all the outgoing gluons are first split into quark anti-quark or diquark anti-diquark pairs. Then, quarks are combined with their nearest neighbouring (in the colour field) anti-quark or diquark to form colour singlet clusters. These clusters have mass and spatial distributions peaked at relatively low values. For large cluster mass, the q-distributions fall rapidly and are asymptotically independent of the hard sub-process scale. The clusters thus formed are fragmented into hadrons (see Fig. 5.7, right plot). If a cluster is too light to decay into two hadrons, it is allowed to become the lightest hadron of the relevant flavour, adjusting its mass to the appropriate value by momentum exchange with a neighbouring cluster. Massive clusters, below a certain fission threshold, M_f, decay isotropically into pairs of hadrons. Unstable hadrons formed in this way are then allowed to decay. Some clusters are too heavy for isotropic two-body decay and therefore are first allowed to fragment into lighter clusters using an iterative fission model, until the masses of the fission products fall below M_f and subsequently decay into hadrons. The fission threshold M_f is defined according to the formula [123]:

$$M_f^{CLPOW} = (CLMAX)^{CLPOW} + (m_1 + m_2)^{CLPOW} \tag{5.6}$$

where m_1 and m_2 are the quark masses of a given flavour forming a cluster and $CLPOW$, $CLMAX$ are input parameters, tuned in order to reproduce experimental data.

5.4.3 Independent Fragmentation

The simplest scheme, as given by Field and Feynman [124], suggests that generating distributions of hadrons from partons, can be obtained if each parton is allowed to fragment independently. Since then many independent fragmentation schemes have evolved. As the complete list of these independent fragmentation functions is relatively large, only those later used in this thesis are presented below.

5.4.3.1 Bowler's Modifications to Lund

Within the framework of the Artru-Mennessier model [125], Bowler showed that a massive endpoint quark of mass m_Q, leads to modifications of the symmetric fragmentation function. As the production of heavy quarks with a certain mass and transverse momentum in a colour field of quarks is treated as a tunneling phenomenon in the Lund model, the probability to produce a $c\bar{c}$ pair becomes extremely small ($\sim 10^{-11}$). This implies that the string area swept out gets reduced for massive endpoint quarks compared to massless quarks, hence the symmetric scheme for the fragmentation of heavy flavours cannot be applied. The modification to the Lund

symmetric model for heavy quarks is given by [126]:

$$f(z) \propto \frac{1}{z^{1+r_Q b m_Q^2}}(1-z)^a \exp\left(\frac{-b \cdot m_\perp^2}{z}\right). \tag{5.7}$$

In principle the prediction for the modified term $1/(z^{1+r_Q b m_Q^2})$ is $r_Q \equiv 1$, but one can extrapolate smoothly between this and the original Lund symmetric function with r_Q in the range from 0 to 1.

5.4.3.2 Peterson Fragmentation

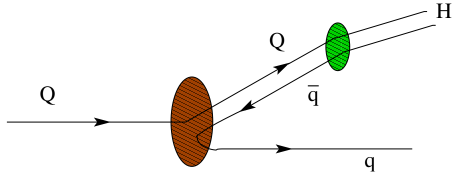

Figure 5.8: *The fragmentation of a heavy quark Q, into a meson $H(Q\bar{q})$.*

The Peterson or SLAC fragmentation function [127] for heavy quarks was developed using the quantum mechanical parton model [128]. The fragmentation function was calculated from transition amplitudes, assuming that when a anti-light quark $\bar{q}$, gets attached to a fast moving heavy quark Q (or a diquark qq for baryon production), it decelerates slightly the heavy quark in the fragmentation process. Then, the amplitude for the fast moving heavy quark Q having energy E_Q and fragmenting into a hadron $H = (Q\bar{q})$ with energy E_H, and a light quark q with energy E_q, is given by:

$$\text{amplitude}(Q \to H + q) \propto \triangle E^{-1} \tag{5.8}$$

For simplicity $m_H \simeq m_Q$ and

$$\begin{aligned}\triangle E &= E_H + E_q - E_Q \\ &= (m_Q^2 + z^2P^2)^{1/2} + (m_q^2 + (1-z)^2P^2)^{1/2} - (m_Q^2 + P^2)^{1/2} \\ &\propto 1 - (1/z) - (\epsilon/1-z)\end{aligned} \tag{5.9}$$

where z is the fraction of the heavy-quark momentum P taken by the hadron H. The parameter $\epsilon \sim m_q^2/m_Q^2$, is the effective ratio of the light to the heavy-quark masses. The fragmentation function $D_Q^H(z)$, is then given by:

$$D_Q^H(z) = \frac{N}{z[1-(1/z)-\epsilon/(1-z)]^2} \tag{5.10}$$

where the normalization N, is fixed by summing over all hadrons containing Q,

$$\sum \int dz D_Q^H(z) = 1 \tag{5.11}$$

The fragmentation function in Eq. 5.10 is then expected to be peaked at $z \simeq 1-2\epsilon$ with a width $\sim \epsilon$. However which value of ϵ for charm production should be used in a given model, is a matter of debate. This not only depends on the heavy quark momentum as $P \to \infty$, but also on the model in which this function should be used. Parameterisations exist for the Peterson ϵ, using fits to e^+e^- data in LO and NLO framework [83], and also within LO+PS (PYTHIA) [129]. However the techniques used to obtain the values are not unique.

In the following subsequent chapters, a detailed analysis is done in both collinear (LO, LO+PS, NLO) and semi-hard frame work (LO+PS) in order to obtain the Peterson ϵ, for the charm production at HERA. These fits and the values obtained in this thesis, are done for the first time in a hadron collider.

5.4.3.3 Kartvelishvili Function

Kartvelishvili, Likhoded and Petrov [87], while trying to find the possible explanation of dimuon production in neutrino induced reactions using charm production, came up with a unique kind of fragmentation function. It was obtained using the following assumptions:

i) The fragmentation of charm quarks into charmed hadrons is assumed to be equal to that of any light quark into usual hadrons.

$$D_c^H(z) = D_q^\pi(z) = Kz^{-1}(1-z), \tag{5.12}$$

where D_c^H is the probability for the $c-$quark fragmentation into the hadron H, which carries the fraction z of the quark momentum and K is the proportionality constant.

ii) The validity of the "reciprocity relation" [130] at $z \sim 1$:

$$D_q^H(z) = f_H^q(z), \tag{5.13}$$

where $f_H^q(z)$ is the $q-$type quark density in the hadron H.

iii) Using the fact that charm quarks are relatively heavy and the assumption on the universality of the quark anti-quark sea, the above mentioned functional form using the Kuti-Weisskopf model [131] can be modified to obtain:

$$D_c^H(z) = Kz^\alpha(1-z), \tag{5.14}$$

where $\alpha = 3$ for the $c-$quark and 9 for the $b-$quark, from calculation predictions.

However, α is a tunable parameter and can be determined using fits to the experimental data for a given model. The Kartvelishvili α in case of charm production was determined in this thesis for the first time within fixed-order LO and NLO frameworks.

5.5 Beam Drag Effects

With a leading charmed meson defined as having a light quark pair in common with the incoming beam, an asymmetry exists between the leading and non-leading charmed mesons. This favours the leading particle in the beam fragmentation region [132]. In a string fragmentation framework due to the colour flow in an event, the produced charm quarks are normally colour-connected to the beam remnants of the incoming particles. This results in the possibility for the charmed meson to gain energy and momentum from the beam remnant in the fragmentation process and thus be produced at a larger rapidity than the initial charm quark (see Fig. 5.9).

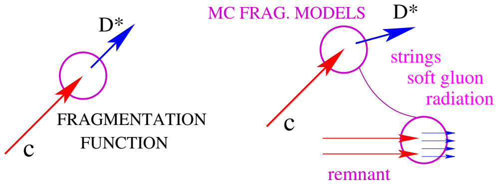

Figure 5.9: *Schematic representation of the beam drag effect. The charm fragmentation to a D^* meson is shown without (left) and with (right) drag effects.*

Fig. 5.10 shows the MC distribution of charmed quarks and charmed hadrons separated in direct and resolved processes. For direct photons the hadrons are found to be shifted (Fig. 5.10 a) in true rapidity, y:

$$y = \frac{1}{2} \ln \frac{E + p_z}{E - p_z} \tag{5.15}$$

in the proton direction, since the charm quarks are colour-connected to the proton beam remnant. In resolved photon processes the photon also has a "beam" remnant, so the charmed hadron is shifted (Fig. 5.10 b) towards the remnant it is connected to.

As a charm initiated jet represents the overall property of the charm quark produced in the hard scattering, there can be a drag effect between the colour connected D^* charmed meson and the beam remnant. For the samples enriched in direct photon events, the photon interacts as a whole, the shift in rapidity is expected to be only in one direction (connected to the proton beam remnant), whereas in the resolved enriched sample, the charmed hadron will be shifted towards the beam remnant to which it is connected (both proton and photon). This assumption of the colour connection to the remnant was verified and it was found to be negligibly small [133] for the analyses presented in this work.

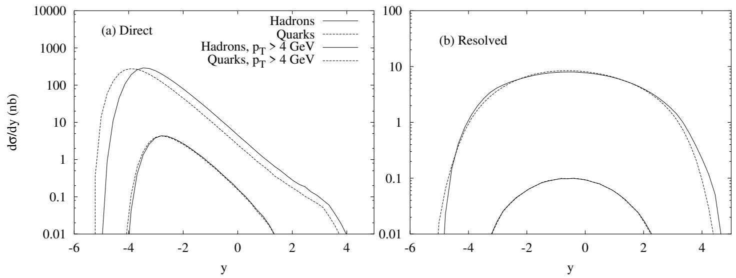

Figure 5.10: *Distribution of charmed hadrons and quarks in rapidity for: (a) direct and (b) resolved photons processes [132].*

5.6 Event Generators for Charm Jets in PHP

In this section the main event generators that are used for the simulation of charmed mesons along with the jets are presented below. These generators incorporate different kinds of hard scattering approaches and fragmentation as discussed above. They were used in this thesis both in their default mode and by changing many parameters such as the initial/final state radiation or the fragmentation in order to compare the underlying physics dynamics with the experimental measurements.

5.6.1 CASCADE Monte Carlo

The MC event generator CASCADE 1.00/09 [107] simulates heavy-quark photoproduction in the framework of the semi-hard or k_T-factorisation approach [114]. The matrix element used in CASCADE is the off-shell LO PGF process. Important partial contributions, which are of NLO and even next-to-next-to-leading-order nature in the collinear (on-shell) approach, are consistently included in k_T-factorisation due to the off-shellness of the gluons entering the PGF process [118].

The CASCADE initial-state radiation is based on CCFM evolution [42], which includes, in the perturbative expansion, the $\ln(\frac{1}{x})$ terms in addition to the $\ln Q^2$

terms used in the DGLAP evolution. To simulate final-state radiation, CASCADE uses PYTHIA 6.1 and the fragmentation into hadrons is simulated with the Lund string model. The cross section is calculated by convoluting the off-shell PGF matrix elements with the unintegrated gluon density of the proton obtained from the CCFM fit to the HERA F_2 data [107]. A charm quark mass of $m_c = 1.5$ GeV was used in this thesis. Although the CASCADE matrix elements correspond to the off-shell PGF direct photon process only, resolved photon processes are reproduced by the CCFM initial-state radiation [119, 120].

5.6.2 HERWIG and PYTHIA Monte Carlos

The MC simulation programs PYTHIA 6.156 [109] and HERWIG 6.301 [108] are general purpose generators, which are used to model the final states. The PYTHIA and HERWIG simulations use on-shell LO matrix elements for charm photoproduction processes. Higher-order QCD effects are simulated in the leading-logarithmic approximation with initial- and final-state radiation obeying the DGLAP evolution [36, 134]. Coherence effects from soft-gluon interference are included. The parton density functions (PDF) CTEQ5L [59] for the proton and GRV-G LO [49] for the photon were used. The LO direct and resolved photon processes were generated proportionally to their predicted MC cross sections, using charm- and beauty-quark masses of $m_c = 1.5$ GeV and $m_b = 4.75$ GeV, respectively. HERWIG uses the equivalent photon approximations (see section 2.1.1) to generate the spectrum of photons radiated from the incoming electrons. The factorisation scale μ^2 used for the hard sub-process is given by:

$$\mu^2 = \frac{2\hat{s}\hat{t}\hat{u}}{\hat{s}^2 + \hat{t}^2 + \hat{u}^2}, \tag{5.16}$$

where $\hat{s}$, $\hat{t}$, and $\hat{u}$ are the Mandelstam variables. PYTHIA on the other hand uses the Weizsäcker-Williams Approximation (see section 2.1.1) to generate the spectrum of radiated photons. The factorisation scale used is the transverse mass of the outgoing

partons m_T^2, given by:

$$\mu^2 = m_T^2 = \frac{1}{2}(m_1^2 + p_{T_1}^2 + m_2^2 + p_{T_2}^2). \tag{5.17}$$

Fragmentation into hadrons is simulated in HERWIG with a cluster algorithm [135] and in PYTHIA with the Lund string model [121].

For all Monte Carlo simulations used in this thesis, the samples corresponding to different data taking conditions were generated in proportion to their luminosities. For PYTHIA and HERWIG, in addition to the D^* decay chain used for the analyses,

Decay chain	Minimum p_t (GeV)
$D^* \longrightarrow D^0(\rightarrow K\pi)\pi_S$	1.25
$D^* \longrightarrow D^0(\rightarrow K_S^0\pi\pi)\pi_S$	1.35
$D^* \longrightarrow D^0(\rightarrow K\pi\pi\pi)\pi_S$	2.3
$D^0 \longrightarrow K\pi$	2.6
$D_s \longrightarrow \phi(\rightarrow KK)\pi$	1.7
$D^+ \longrightarrow \phi(\rightarrow K^+K^-)\pi^+$ + c.c	1.7
$D^+ \longrightarrow (K^+\pi^-)\pi^+$ + c.c	2.8
$\Lambda_c^+ \longrightarrow (K^-p^+)\pi^+$ + c.c	2.8

Table 5.1: *List of generated charm hadrons in PYTHIA and HERWIG Monte Carlo simulations.*

background events that arise from other $D^{*\pm}$ decay modes or similar decay modes of other charm mesons as given in table 5.1, were also simulated. The minimum p_t, used in the generated sample is based on the lowest transverse momentum one can measure with one of these decay channels in the ZEUS detector at the reconstructed level.

The comparison of physical quantities between data and Monte Carlo is left for the respective analyses chapters.

Chapter 6

Jet Production

In QCD, when an incoming parton from one hadron scatters off an incoming parton from the other hadron, they produce two high-transverse-momentum coloured partons which, due to the confinement of colour charge, cannot be directly observed. These coloured partons from the hard scatter evolve via soft quark and gluon radiation and eventually hadronise to form a "spray" of roughly collinear colour singlet hadrons called jets. The nature of these soft radiations, as shown in Fig 6.1 a) is such that the radiated partons and subsequently the formed hadrons will remain collimated around the original parton direction. Thus the reconstructed final state jets can be related to the original partons emerging from the hard interaction. As the quarks and gluons cannot be directly observed, the resulting quark/gluon initiated jet is a kinematical signature of the underlying dynamics. The first observation of such hadronic jets [136] in e^+e^- collisions provided a striking confirmation of this picture.

The jet definition used in the observation mentioned above was very intuitive and qualitative (i.e. a large amount of hadronic energy in a small angular region). In order to make a quantitative comparison between theory and experiment, a precise algorithm which can be unambiguously used both in theoretical calculations and experimental measurements needs to be used to define a jet. It should be mentioned

that in the jet definition discussions, the word 'particle' is used for any set of four-momenta, which can essentially mean partons for theoretical calculations, hadrons in the MC models or energy deposits detected in a calorimeter.

6.1 Jet Physics and Algorithms

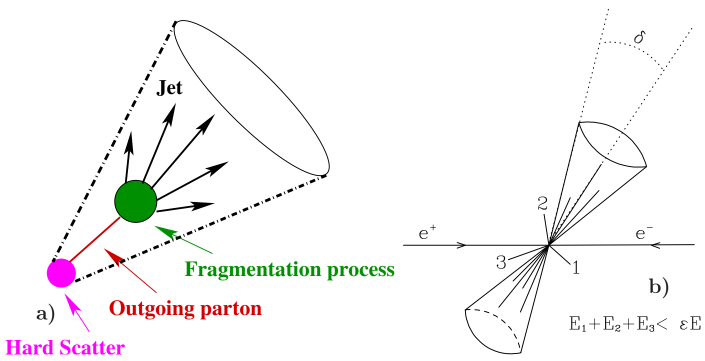

Figure 6.1: **a)** *Schematic representation of a jet production initiated by the outgoing parton* **b)** *Sterman-Weinberg jets.*

The first attempt to define a jet cross section which is calculable and finite in perturbation theory was made by Sterman and Weinberg [137] for e^+e^- annihilations. It was the first time the language of quarks and gluons was used for reinterpreting these partons in terms of hadronic jets, which also means the parton to hadron corrections were intrinsically assumed to be negligible. An event contributes to the Sterman-Weinberg jet cross section if one can define two cones of opening angle δ that contain all the energy of the event, excluding at most a fraction $\epsilon \ll 1$ of the total, as shown in Fig 6.1 b).

The Sterman-Weinberg cross section σ_{SW}, for the process $e^+e^- \to q\bar{q}g$, assuming zero quark masses, can have contributions from three distinct kinds of final state.

At the order of α_s^2, contribution of soft quarks and anti-quarks outside the jets were not considered, nor with both quarks and anti-quarks in the same jet.

1. One jet may consist of a quark or anti-quark plus hard gluon (energy $\gg \epsilon E$).
2. There may be a quark in one jet, an anti-quark in the other and a soft gluon of energy $\ll \epsilon E$ which may or may not be in one of the jets.
3. There may be just a quark and an anti-quark, one in each jet.

The total jet cross section from the above three contributions is given by [137] :

$$\sigma_{SW} = \sigma_0(1 - \alpha_s C_F \log \epsilon \log \delta) \tag{6.1}$$

where σ_0 is the Born cross section for $e^+e^- \to q\bar{q}$. The above Eq. 6.1 is finite, as long as ϵ and δ are finite. Furthermore, as long as ϵ and δ are not too small, one can see from Eq. 6.1, that the fraction of events with two Sterman-Weinberg jets is 100%, up to a correction of order α_s. At high energy, most events have a large fraction of the energy contained in opposite cones, i.e. events are two-jet events. As the energy becomes larger, α_s becomes smaller, therefore smaller values of ϵ and δ can be used to define jets; in other words higher energetic jets become thinner.

In summary, although the pQCD expansion was done for quarks and gluons, one can start representing them as hadronic final state jets. However there are many difficulties in using such a definition for a jet algorithm.

The main problem is the difference in the event structure studied in hadron (lepton)-hadron and e^+e^- annihilations. Although the basic hard scattering process is same, the initial state is purely electromagnetic in the case of e^+e^- and thus, the entire final state arises from short distance interaction of the virtual photons (or Z^0) leading to $q\bar{q}$ pairs. On the other hand in case of hadronic collisions, there are a large number of initial state partons, from which only "active partons" from the incident hadron participate in the hard scattering. Thus only a fraction of the hadrons in the final state gets associated with the hard scattering process. The

remaining partons correspond to the soft interactions leading to remnant jets which, in first approximation, can be treated as uncorrelated with the hard process. These remnant jets are sprays of particles with small transverse momenta, but possibly very large momenta along the beam axis. Moreover, the active partons also produce additional initial state QCD radiation, which is not present in e^+e^- events. These differences in the event structure then led to differences in the jet definition and corresponding algorithm.

However, in order to have a generalised jet algorithm, one needs to have the following conditions satisfied :

i) Infrared (i.e. insensitive to "soft" radiation) and collinear safety.

ii) Low sensitivity to hadronisation. A small hadronisation correction implies closer correspondence between the final state partons and the final state hadrons.

iii) Stability at the boundary regions.

iv) Order independence (same jets at parton, hadron and detector level).

v) Identical implementation in experimental observables and in the corresponding calculations at all orders of perturbation theory with partonic final states.

vi) Detector independence, invariance under boosts, stability with respect to luminosity and minimisation of resolution smearing or angular bias.

vii) Maximal reconstruction efficiency and ease of calibration.

At present there are two kinds of jet algorithms in use: the cone-type algorithm initiated by Sternman-Weinberg [137] and the cluster-type algorithm first introduced by the JADE collaboration [138] as described below.

6.1.1 The Cone Algorithm

The cone algorithm define jets using fixed geometrical structures, which are positioned in the angular space occupied by the particles, such that the energy or the transverse energy (based on the Snowmass Accord [139]) is maximised. To use such an algorithm, the main requirements are the geometrical definition of the 'cone' (which is usually a circle in the angular space with a given radius) and some criteria such that the 'remnant jets' (in hadron collisions) and the overlapping of the cones can be avoided. Here the particles are combined in the pseudo-rapidity η, and azimuthal angle ϕ, phase space. All particles within a cone of radius R,

$$R = \sqrt{(\eta_{Jet} - \eta_i)^2 + (\phi_{Jet} - \phi_i)^2} = \sqrt{\Delta\eta^2 + \Delta\phi^2} \leq R_0, \tag{6.2}$$

are combined into a jet of transverse energy E_T

$$E_T = \sum_i E_i \sin\theta_i = \sum_i E_{T_i} \tag{6.3}$$

where i runs over all particles in the cone. The value of R_0 is typically around $0.7 \leq R_0 \leq 1$. Moreover, both the R_0 and the resulting E_T threshold do not only depend on the criteria needed to avoid overlapping cones and remnant jets but also on detector resolutions. The jet axis is then defined by:

$$\eta_{Jet} = \frac{1}{E_T} \sum_i E_{T_i} \eta_i \tag{6.4}$$

$$\phi_{Jet} = \frac{1}{E_T} \sum_i E_{T_i} \phi_i \tag{6.5}$$

The procedure is first applied on a pair of particles and is then repeated for a certain number of iterations until E_T, η_{Jet}, ϕ_{Jet} are stable with the jet cone remaining fixed. The main advantage of the cone algorithm is that it can easily be applied to calorimetric measurements where energy deposits in calorimeter cells are treated as single particles.

6.1.2 The Cluster Algorithm

The original cluster algorithm as introduced by the JADE collaboration [138] follows a different approach: instead of globally finding a jet axis direction, it starts by finding pairs of particles that are 'nearby' in phase space and merge them together

to form new 'pseudoparticles'. For each pair of particles (or clusters) i and j with an angle, θ_{ij}, between them and energies E_i and E_j respectively, the quantity

$$y_{ij} = \frac{2E_iE_j(1 - \cos\theta_{ij})}{E_{cm}^2} \simeq \frac{m_{ij}}{E_{cm}^2}, \tag{6.6}$$

where m_{ij} is the invariant mass of the objects and E_{cm} is the centre-of-mass energy of the interaction. If y_{ij} is smaller than a predefined resolution parameter y_{cut} the objects are combined. The procedure continues iteratively until the event consists of a few well-separated pseudoparticles, which are the output jets. As can be seen, no requirement on the E_T of the jets is applied and the jet multiplicity only depends on the y_{cut} parameter. The algorithm was later modified by replacing the reference scale W^2 by Q^2 for deep inelastic scattering. However as there was no unique definition of 'closeness' in phase-space, several algorithms using different definitions have been developed, leading to the one used in this thesis.

k_T algorithm :

The k_T algorithm developed by Catani, Dokshitzer and Webber [140] uses the relative transverse momentum of the two particles, rather than their invariant mass that is used for clustering particles. It uses a two-step process. In the first step, it performs the pre-clustering of particles into a class of final state jets which originates from the hard ("macro jets") and soft ("remnant jets") interactions. The second step aims at resolving jets within the macro jets.

During the pre-clustering stage, two particles or at a later stage two clusters i and j are merged if the transverse momentum $k_{T_{ij}}$ of the least energetic of the two objects is smaller than a predefined transverse resolution scale $k_{T,cut}^2$,

$$k_{T_{ij}}^2 = 2\min(E_i^2, E_j^2)(1 - \cos\theta_{ij}) < k_{T,cut}^2. \tag{6.7}$$

where θ_{ij} is the angle between the momenta vectors and E_i and E_j the corresponding energies. In addition, a similar parameter $k_{T_{iR}}$ related to the distance of particle i to the remnant-jet, is calculated according to

$$k_{T_{iR}}^2 = 2(1 - \cos\theta_{iR})E_i^2, \tag{6.8}$$

where θ_{iR} is the angle between i and the incoming beam direction. After this separation a scale E_T is introduced and the procedure is iterated until the smallest of all $\{k_{T_{ij}}, k_{T_{iR}}\}$ is greater than E_T. If this is not the case, the two particles having the smallest values are combined into a new cluster and a new iteration is performed. Any particle combined with the beam remnant (smallest $k_{T_{iR}}$) is considered as the spectator jet and is not included in the next iteration. If the two particles combined are "real", then a recombination scheme has to be introduced to define the four-momentum of the new cluster, which is then considered in the next iterations.

In the second step, all particles which were not assigned to the spectator jets are considered. The process is similar to that used in the first step, with the exception of the selected scale which is chosen such that it can resolve more jets within the macro jets. This parameter sets the scale to resolve the jets, whereas the first one (E_T) is the scale that separates the hard and soft processes. Due to this distinctive separation of processes initiating the jets, the k_T-algorithm is expected to be the least affected by hadronisation effects [141].

The longitudinally invariant k_T-cluster algorithm :

The original k_T-algorithm was then modified by Ellis and Soper [142] by incorporating the longitudinally invariant variables (E_T, η and ϕ) necessary for the boosted hadron collision environment. It also satisfies many conditions outlined in the previous section 6.1, and hence has been used to define jets for both analyses presented in this thesis. As shown in Fig. 6.2, the algorithm starts with a list of particles (e.g. partons, hadrons or calorimeter cells) called protojets which are characterized by their transverse energy $E_{T,i}$, pseudorapidity η_i and azimuthal angle ϕ_i.

The algorithm shown in Fig. 6.2 proceeds according to the following steps:

1. For each protojet, define $d_i = E_{T,i}^2$ and for each pair of protojets define:

$$d_{ij} = \min(d_i, d_j)\frac{(\eta_i - \eta_j)^2 + (\phi_i - \phi_j)^2}{K^2} = \min(d_i, d_j)\frac{\Delta R_{ij}^2}{K^2}. \qquad (6.9)$$

   The parameter $K \sim 1$ is an adjustable parameter of the algorithm which plays the role of a jet radius in the (η, ϕ) plane. Theoretically, the value $K = 1$

   is strongly preferred, as it treats initial and final-state radiation on an equal footing [142].

2. In the limit of small opening angles $\Delta\theta_{iR}$ with respect to the beam remnant,

$$d_{i,R} = \min(d_i, d_R).\Delta R_{i,R}^2/K^2 \sim \min(d_i, d_R).\Delta\theta_{iR}^2/K^2 \sim k_{T,iR}^2 \qquad (6.10)$$

   the expression reduces to the square of the transverse momentum $k_{T,iR}$ of the particle i with respect to the beam remnant direction.

3. find the smallest element $d_{min} = \min\ \{d_{ij}, d_{i,R}\}$

4. if $d_{min} = d_{ij}$, particles i and j are merged together into a new pseudoparticle k in accord with the Snowmass convention [139]:

$$\begin{aligned} E_{T,k} &= E_{T,i} + E_{T,j} && (6.11)\\ \eta_k &= [E_{T,i}\eta_i + E_{T,j}\eta_j]/E_{T,k} && (6.12)\\ \phi_k &= [E_{T,i}\phi_i + E_{T,j}\phi_j]/E_{T,k} && (6.13) \end{aligned}$$

5. if $d_{min} = d_{iR}$ the protojet i is complete and is added to the output list.

The procedure is repeated till no remaining cluster is left and all the particles have been assigned to protojets. During each iteration, one particle is removed, so that the number of iterations is always equal to the number of original final state particles. Now from the sample of the protojets, the final jets are selected by imposing a cut on E_T which sets the scale to distinguish the hard and soft processes. As can be seen from Fig. 6.2, the produced jets are phenomenologically not very dissimilar to those defined by the cone-type algorithm. However the longitudinally invariant k_T-cluster algorithm is less influenced by the soft particles than the cone-type algorithm resulting in smaller hadronisation and detector corrections for the "active parton" initiated jets used for the analyses. Qualitatively, the invariant k_T-cluster algorithm concentrates on the core of the jets and only merges neighbouring particles if they are close enough, whereas the cone algorithm, in order to maximize the jet energy, pulls in as much neighbouring energy as possible.

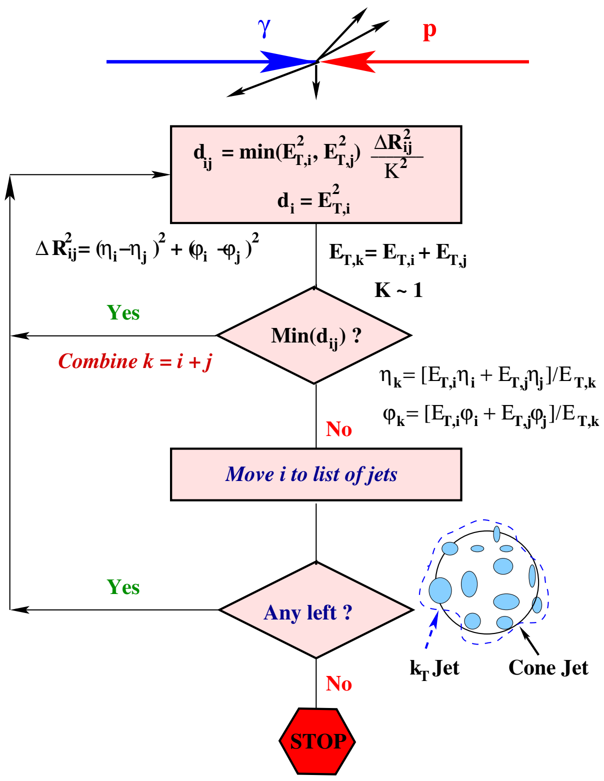

Figure 6.2: *Schematic representation of the longitudinal invariant k_T-algorithm and its comparison with the cone approach.*

6.2 Jet Reconstruction

In this thesis, the reconstruction of jets as "clusters" of hadronic energy deposited in the calorimeter cells was done in two ways. In the first way, the energy deposits in the calorimeter cells were directly used as an input to the jet algorithm. In the second

way, the tracks measured in the tracking detector were "matched" to these energy deposits in the calorimeter and defined as "objects". Based on the best available resolution and detector acceptance, these matched objects are then used as an input to the jet finding. For all presented analyses the KTCLUS algorithm [140] in the longitudinal invariant inclusive mode [142] is used for the jet finding. Although the hadrons are massive, the algorithm in a specific mode scales up their three-momenta in order to make the mass equal to zero. This procedure leads to a steep dependence of the cross section on the transverse energy of the jets.

As will be described in the next chapter, two analyses are presented in this thesis. In the analysis of dijet events associated with $D^{*\pm}$ mesons, the information using calorimeter cells alone is used, whereas for the charm fragmentation analysis, the matched objects called EFOs (Energy Flow Objects) are used. Both the jet reconstruction methods along with the correction procedures are discussed below. In the following subsection the MC simulated jets, reconstructed from the incoming generated particles without having passed through the detailed detector simulation (as discussed in section 4.2.5), are referred to as *hadron level* jets, whereas the jets reconstructed using the calorimeter cells or the EFOs are referred to as *detector level* jets.

6.2.1 Jet Reconstruction Using Calorimeter Cells

In the dijet angular distribution analysis, dijets are reconstructed from the energies measured in the calorimeter cells. Before the jet algorithm is applied, the calorimeter data needs to be corrected and optimised. Various optimal cuts and correction procedures, as outlined in section. 7.2 were applied. After these corrections, the jet algorithm is used to obtain the set of longitudinally invariant variables $\{E^{jet}_{T,cal}, \eta^{jet}_{cal}, \phi^{jet}_{cal}\}$ which contains all the information about the reconstructed jets.

In order to estimate the amount of energy loss due to the dead material in front of the calorimeter, to the calorimeter resolution and to the effects of the magnetic field on the trajectory of low energy charged particles, it is necessary to estimate to a high degree of precision the correlation between the reconstructed jet and the energy of the incoming particles. Once this correlation is established the energies can be corrected to take the detector effects into account. For this purpose, the Monte Carlo simulations of events from c-quark production in PYTHIA and HERWIG are used. The selection of the event sample and the association between hadron and detector level jets is given below.

- Jets are selected in the data and at detector level MC with $E^{jet}_{T,cal} > 3$ GeV, separately for two different data taking periods: 1996-1997 and 1998-2000. Jets at the hadron level are selected with a slightly higher transverse energy cut $E^{jet}_{T,had} > 4$ GeV. The difference in these cuts accounts for energy lost due to the inactive material located between the interaction point and the calorimeter.

- The calorimeter and the hadron jets in the MC are then matched for each event in the $\eta - \phi$ space. A pair of jets is considered to be matched when,

$$\Delta_{\eta\phi} = \sqrt{(\eta^{jet}_{cal} - \eta^{jet}_{had})^2 + (\phi^{jet}_{cal} - \phi^{jet}_{had})^2} \leq 1 \tag{6.14}$$

  and is the minimum. The procedure is repeated until no jet is left or the distance between the remaining pairs is larger than 1.

Fig. 6.3 `a)-d)` and `m)-p)` shows such correlation of the matched calorimeter with hadron level jets for ϕ^{jet} and η^{jet} respectively. The ϕ^{jet} resolution distributions Fig. 6.3 `e)-l)` shows that the difference in calorimeter to the hadron level matched jets purely reflects the detector resolution in the azimuthal direction and does not need any correction. On the other hand the same quantity as a function of η^{jet} in Fig. 6.3 `q)-t)` indicates some deviations from the nominal values. The variation in $\Delta\eta^{jet} = \eta^{jet}_{cell} - \eta^{jet}_{had}$, as a function of η^{jet}_{had}, in Fig. 6.3 `u)-x)` justifies the need for corrections in the bins of η^{jets}_{cal} corresponding to the different angular regions of the calorimeter. The distributions for $\Delta\phi^{jet}$ and $\Delta\eta^{jet}$ have been fitted to a Gaussian function and the resulting values for the means are $\sim 0.5\%$ and $\sim$ -0.55% whereas for the width the values are ~ 0.10 and ~ 0.074, respectively.

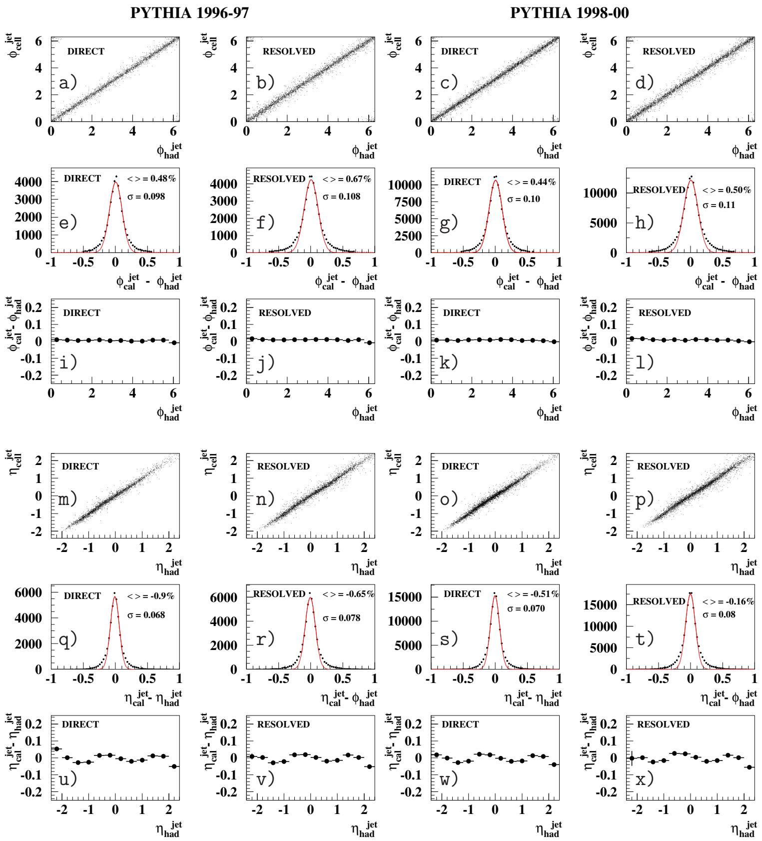

Figure 6.3: *Hadron to calorimetric correlation in ϕ^{jet} and its resolution* `a)-l)` *in radians. The corresponding quantities for η^{jet}* `m)-x)`*, shown separately for direct and resolved photon processes for two separate data taking periods: 1996-97 and 1998-2000.*

Fig. 6.4 `a)-d)` for E^{jet}_T distribution clearly shows a spread due to differences in calorimetric to the hadronic measured jets. The resolutions Fig. 6.4 `e)-h)`, fitted

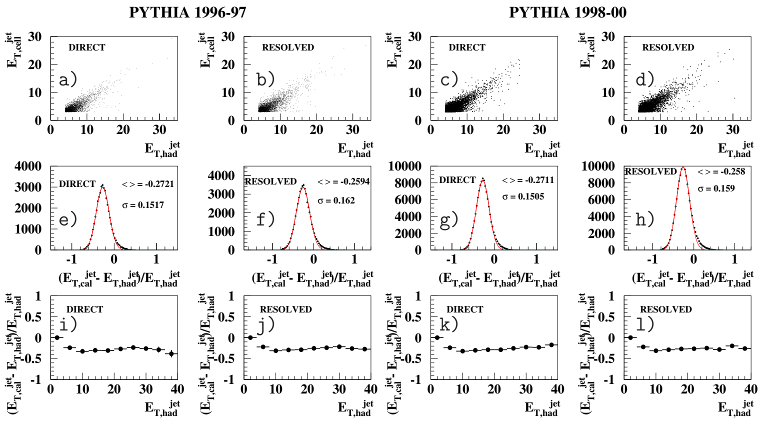

Figure 6.4: *Jet resolutions as a function of E_T^{jet} in GeV. Direct and resolved photon processes are shown separately, for the two separate data taking periods: 1996-97 and 1998-2000.*

to a Gaussian distribution gives a negative mean of about $\sim -27\%$ and a width of $\sim 16\%$. This large negative mean value indicates that the jets measured in the calorimeter have a smaller transverse energy than the hadron jets. The value of $E_{T,cal}^{jet}$ from Fig. 6.4 i)-l) is at most 30% lower than as expected from the hadronic E_T^{jet} distribution.

In Figs. 6.3 and 6.4, direct and resolved processes are shown separately for all jet parameters, and show good agreement with each other. This shows that the energy corrections are purely due to the detector related inefficiencies and do not have a physics origin. This fact can also be concluded from the same distributions when using HERWIG rather than PYTHIA. These results are consistent with the previous dijet analysis where the presence of charm was not required; for example, see [143].

6.2.1.1 Jet Energy Corrections

Considering the differences observed, a correction is needed as function of η_{cal}^{jet} and $E_{T,cal}^{jet}$ to the reconstructed jet topology. This correction was done in the laboratory frame as the detector effects in this frame can easily be localised, given that the η^{jet} dependence corresponds to the position, rather than any kinematics bias.

There are various ways one can do these jet energy corrections; the two main methods [144] and [145] used within ZEUS were analysed. It was found that the method [144], based on correlations with reconstructed variables, is good for high E_T^{jets} events, while it underestimates the correction needed for low E_T^{jets}. On the other hand [145], based on ratios of reconstructed variables, does a fairly good job for low E_T^{jets}, but can overcorrect the high E_T^{jets}, due to the restrictive form of the function used. The jet energy correction in this thesis was done in a slightly different way than the above mentioned methods and the procedure used is briefly described below:

- The sample of matched hadron and calorimetric simulated jets in the laboratory frame, is divided into 10 different pseudorapidity η^{jet}, bins: [-2.4,-1.2], [-1.2,-0.8], [-0.8,-0.4], [-0.4,0.0], [0.0,0.4], [0.4,0.8], [0.8,1.2], [1.2,1.6], [1.6,2.0] and [2.0,2.4]. These bin boundaries can only be made based on the "good" η^{jet} resolution shown previously in Fig. 6.3.

- The correction of the jet energy is then derived from the correlation between the calorimetric and the matched hadronic simulated jets. This correlation is parameterized with a linear function by fitting the distribution of the $E_{T,cal}^{jet}$ as a function of $E_{T,had}^{jet}$ separately for each η^{jet} bin as shown in Fig. 6.5. For a bin i in η_{cal}^{jet}, the fitted function has the form:

$$E_{T,cal,i}^{jet} = m(E_{T,i}^{jet}, \eta_i^{jet}) \cdot E_{T,had,i}^{jet} + c(E_{T,i}^{jet}, \eta_i^{jet}) \tag{6.15}$$

  where the slope m and the intercept c are a function of the jet transverse energy and the pseudorapidity for that bin.

- For a given calorimetric simulated jet the corrected energy is then obtained by inverting this function:

$$E_{T,corr}^{jet} = \frac{E_{T,cal}^{jet} - c}{m} \qquad (6.16)$$

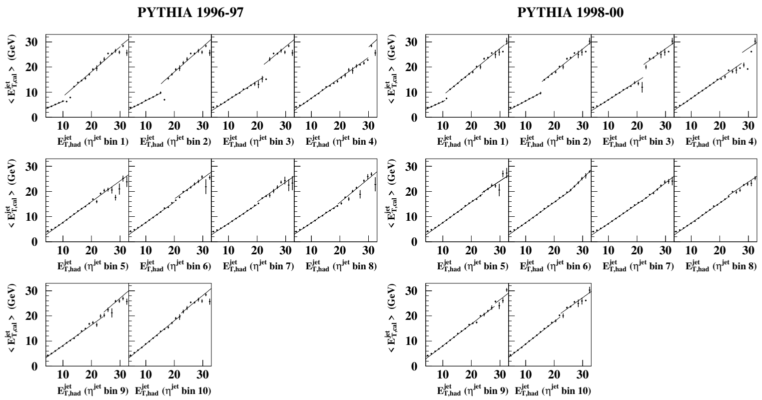

Figure 6.5: *Correlation of $E_{T,cal}^{jet}$ as a function of $E_{T,had}^{jet}$ in GeV, using matched samples of jets in PYTHIA for 1996-97 and 1998-2000 shown separately. The bin numbers correspond to the bin boundaries discussed in section 6.2.1.1, while the lines show the result of the fits. The breaks in the fitted lines correspond to transitions between BCAL and RCAL (or FCAL).*

As the parameters for each bin of η^{jet} also depend on the transverse energy of the jets, the parameterisations are performed by fitting functions of the above mentioned form in several regions of the transverse energy if a global parameterisation was not able to describe the hadron-calorimeter correlation for the whole E_T^{jet} range.

These parameters are then applied back to the simulated and the measured (data) calorimetric jet quantities exactly in the same way. The obtained corrected $E_{T,corr}^{jet}$, η_{corr}^{jet} and ϕ_{corr}^{jet} spectrum after an additional $E_T^{jet} > 5$ GeV cut can now be compared on an equal footing with the hadron level jet variable with $E_{T,had}^{jet} > 5$ GeV. Fig. 6.6 shows the effect of such correction procedure for the MC simulated jet variables both for PYTHIA and HERWIG combined for whole 1996-2000 data taking period.

The $\Delta\phi^{jet}$ distribution remained almost the same before and after correction, except for a slight improvement in the mean when fitted to a Gaussian distribution. $\Delta\eta^{jet}$ and $\Delta E_T^{jet}/E_{T,had}^{jet}$ give a significant improvement in their mean, while keeping the resolution roughly the same after as before correction.

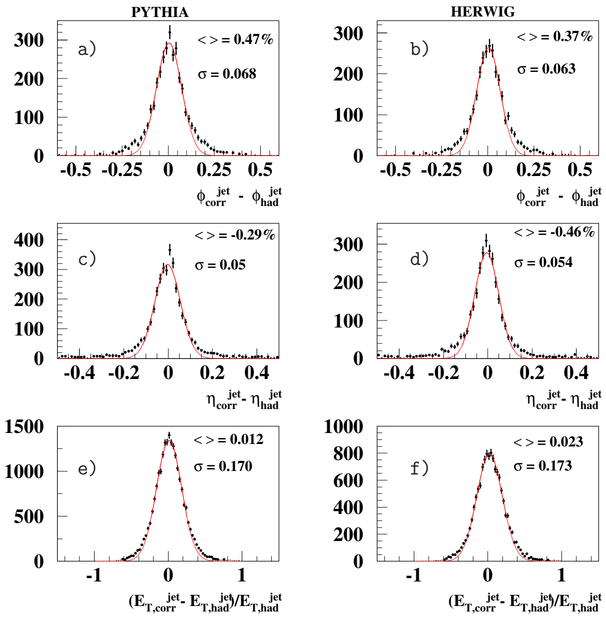

Figure 6.6: *Result on the jet resolutions, after applying the jet energy corrections, shown both for PYTHIA and HERWIG for combined 1996-2000 data taking period. The distributions are fitted to a Gaussian with the mean and the widths shown in the plots.*

6.2.1.2 Jet Energy Scale Uncertainties

The uncertainty in the calorimeter energy scale within the jet corrections is then estimated using the charged particle tracks associated with these jets and then balancing the jet in the central region (with the known uncertainty from the tracks) with the one in the forward region. In the central rapidity region where $|\eta^{jet}| < 1$, the multiplicity distribution and the p_T spectrum of charged particles associated with the calorimetric jets are first compared to the data and MC event samples using the reconstructed tracks. The tracks are required to be in the $|\eta^{track}| < 1.5$ and $p_T^{track} > 150$ MeV regions, where p_T^{track} is the transverse momentum of the track with respect to the beam axis and η^{track} is the track pseudorapidity. Tracks are then associated with a calorimetric jet when the extrapolated track trajectory reached the calorimeter within a cone of one unit radius in the $\eta-\phi$ plane concentric with the calorimetric jet axis. In this η^{jet} region, the momenta of the tracks in the calorimetric jets are used to determine the total transverse energy carried by the charged particles $E_{T,tracks}^{jet}$. The ratio $R_{tracks} \equiv E_{T,tracks}^{jet}/E_{T,corr}^{jet}$ was then calculated. The mean value of the distribution in R_{tracks} was determined in three bin;

$$(-1.0, -0.5), (-0.5, 0.5), (0.5 - 1.0)$$

as a function of η^{jet} for data ($< R_{tracks} >_{data}$) and MC events ($< R_{tracks} >_{MC}$). Differences between data and MC simulation were observed to be about 2% by examining the quantity (MC - DATA)/MC $\equiv 1 - (< R_{tracks} >_{data})/(< R_{tracks} >_{MC})$ as shown in Fig. 6.7.

In the forward region $1 < \eta^{jet} < 2$, where there is no acceptance of the tracks from the central tracking detector, the energy scale of the jets was studied using the transverse-energy imbalance in dijet events with one jet required to be in the central region (whose uncertainty is calculated from tracks mentioned above) and one in the forward region. The ratio, $R_{dijet} \equiv E_{T,corr}^{jet}(\text{forward jet})/E_{T,corr}^{jet}(\text{central jet})$, distributions in data and the MC samples are measured. Differences between data and MC simulation are found to be around 2%, as shown in Fig. 6.7 (dijet region). The widths of the distributions for R_{tracks} and R_{dijet} are reasonably well described

by the PYTHIA MC simulation. The use of HERWIG instead of PYTHIA gives similar results, though HERWIG shifts the scale uncertainty for R_{dijet} in the negative direction. Using the combined results from the differences of data to HERWIG and PYTHIA for all regions of η^{jet}, within the largest error given by the extremity of the error bars shown in Fig. 6.7, a scale uncertainty of 3% was then applied to the final measured cross sections.

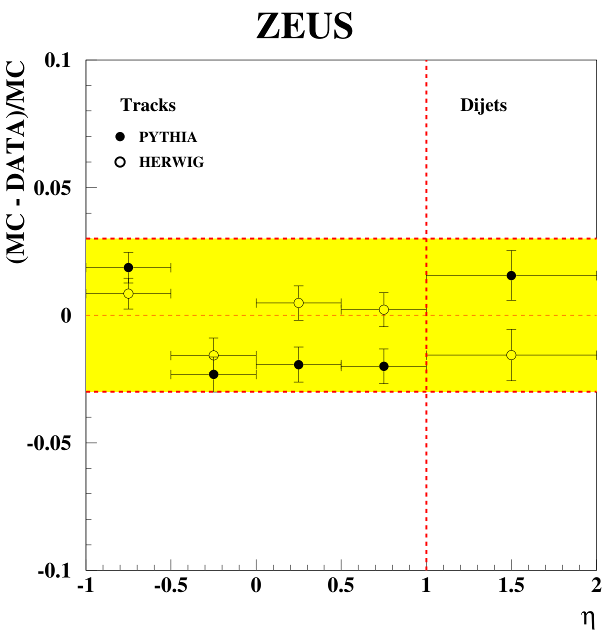

Figure 6.7: *The distribution for differences in data and MC using R_{tracks} and R_{dijet} is shown with a vertical dotted line separating the two regions (see text). The full and open dots correspond to the difference obtained using PYTHIA and HERWIG MC simulations, respectively. The shaded region displays the band of $\pm 3\%$ scale uncertainty.*

6.2.2 Jet Reconstruction Using EFOs

Hadronic energy consists of both charged and neutral particle components. Both of these are measured in the calorimeter, however a large fraction of the charged particles such as the decay products for hadrons like $D^{*\pm}$ relevant for the thesis, led to tracks (K, π, π_s) that are measured in the central tracking detector (CTD). The accuracy with which the energy of the charged particles can be measured, specially the low energy ones, is often better when using the tracking information. This is specially true in the situation where the charged particles traverse dead material after the tracking detector, for instance the solenoid coil between CTD and the calorimeter. Combining tracking and calorimeter information significantly improves the reconstruction of the hadronic final state jets. Following is the procedure used in order to combine energy deposited in calorimeter clusters with the tracks measured by the CTD.

First of all, using the angular information of the calorimeter, adjacent cells in each of the EMC, HAC1 and HAC2 sections are further clustered into cell islands as shown in Fig. 6.8 [146]. The resulting cell islands become 3-dimensional objects when they are clustered into cone islands based on the following:

- using iterative combinations of cells with their highest energy neighbours, local islands are defined in the EMC, HAC1 and HAC2 sections of the calorimeter.
- the obtained islands are then considered in (η, ϕ) space starting from the HAC2 islands and going inwards towards the center of the detector.

Secondly, only tracks originating from the interaction vertex are used[1]. These tracks are then required to have traversed at least 3 superlayers of the CTD and to have a transverse momentum between $0.12 < p_T^{tracks} < 30$ GeV. The basic strategy adopted to combine the tracks and the cone island is as follows:

[1] These are the tracks which can be unambiguously identified as particles produced in the primary interaction.

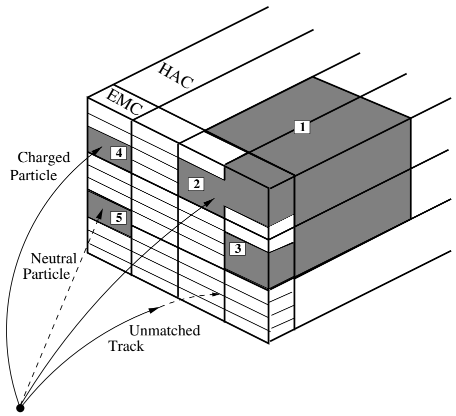

Figure 6.8: *The schematic picture shows four EMC cell island and one HAC cell island. EMC cell island 2 and 3 are joined with HAC cell island 1 to form a cone island. In the next step the cone islands are matched to the tracks.*

- for charged particles within the acceptance of the tracking detector and with low or intermediate transverse momentum in the above range, the tracking detector information should be used.
- for neutral particles, particles outside the tracking acceptance or particles with very high momenta, the energy measured by the calorimeter should be used.

Although this ensures quite reliable results, there are cases where neutral and charged particles overlap in the calorimeter. In those cases, the tracking and calorimeter information needs to be combined or "matched" based on a certain set of rules such that double counting is avoided. A track is considered to be matched to a cone island if the distance of the closest approach between the track and the island is less than 20 cm or less than the radius of the island. More than one track can be matched to one cone island and vice versa. The momenta of tracks that are not matched to an island or the energy of an island not matched to a track are retained. When tracks and islands are matched, the track momentum will be used, if:

1. $\sigma(p_{tracks})/p_{tracks} < \sigma(E_{cal})/E_{cal}$; the resolution of the track momentum is better than that of the island energy, where the track momentum resolution is given in Eq. 4.3 $\sigma(p_{tracks})/p_{tracks} = \sqrt{(0.0058p_T)^2 + (0.0065)^2 + (0.0014/p_T)^2}$ and the calorimeter resolution from section 4.2.2: $\sigma(E_{cal})/E_{cal} = 18\%/\sqrt{E} \oplus 2\%$ ($\sigma(E_{cal})/E_{cal} = 35\%/\sqrt{E} \oplus 2\%$) for electromagnetic (hadronic) islands.

2. $E_{cal}/p_{tracks} < 0.8 + \sigma(E_{cal}/p_{tracks})$; this ratio of the energies avoids throwing away the sizeable amounts of neutral energy that overlap with the energy deposited by a charged particle[2].

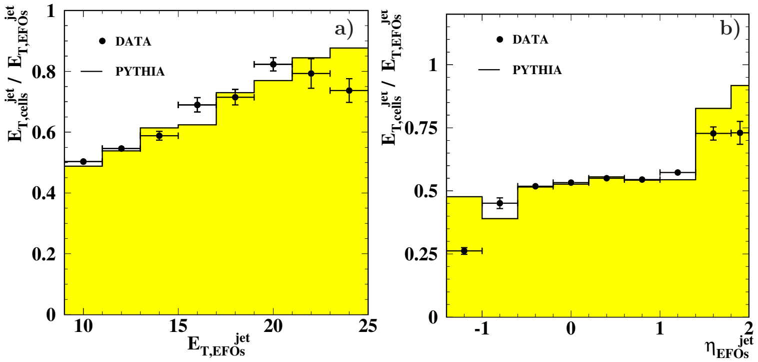

Figure 6.9: *The hadronic jet energy fraction determined from Calorimeter cells and EFOs as a function of a) $E_{T,EFOs}^{jet}$, b) η_{EFOs}^{jet}. The Monte Carlo gives a reasonable agreement to the data.*

When these requirements are not fulfilled, the island energy is used. The final output is a set of objects known as Energy Flow Objects (EFOs). These objects are then used as an input to the jet algorithm. The resulting jets obtained from

[2] $\sigma(E_{cal}/p_{tracks})/(E_{cal}/p_{tracks}) = \sqrt{(\sigma(E_{cal})/E)^2 + (\sigma(p_{tracks})/p_{tracks})^2}$.

the jet algorithm are then defined as the EFO jets. These jets, after an additional requirement of being associated to at least a $D^{*\pm}$ meson[3], naturally consist of a large fraction of energy essentially coming from the tracking information. Fig. 6.9 a),b) show such ratio distribution for $E_{\mathrm{T,cells}}/E_{\mathrm{T,EFOs}}$ of the EFO jets as a function of $E_{\mathrm{T,EFOs}}$ and η_{EFOs}. Reasonable agreement between data and Monte Carlo is observed without any jet energy corrections. More than 50% of the energy in jets comes from the tracking at low E_T, the tracking part decreases with increase in energy. Fig. 6.9 b) on the other hand shows that about 80% of the energy comes from tracking in the backward η^{jet} region, this fraction is stable (50%) in the central CTD acceptance region. For higher η^{jet} values, as there is no CTD acceptance, the major energy information comes from calorimeter cells. Thus no further jet energy corrections were done at the detector level. The loss of energy due to the calorimetric measured part of the jets is small and gets corrected using the acceptance correction procedure from the Monte Carlos presented in the specific analysis chapters.

[3] The $D^{*\pm}$ mesons are selected purely from the CTD tracks.

Chapter 7

Kinematics and Event Reconstruction

The primary goal of this thesis is to probe the structure of the photon in terms of its charm content, next to study the hard scattering dynamics and finally, to measure the charm fragmentation function. Any visible cross section at HERA can be written as the following convolution:

$$\sigma = \text{PDF} \otimes \text{Hard Scatter} \otimes \text{Fragmentation} \tag{7.1}$$

where the parton density function, PDF $\equiv$ PDF$_\gamma \otimes$ PDF$_p$. As previously mentioned it is impossible to measure these three components independently as they are related to each other via the convolution noted as $\otimes$. Thus measurements are performed on such observables which give a maximum sensitivity towards each or a combination of two of these components so that the true picture of charm dynamics can be revealed, or in other words, so that the uncertainty due to one or the other component can be constrained.

The first analysis defined as 'Analysis I: Dijet angular distributions in photoproduction of charm' is presented in Chapter 8. The studied observables are mainly sensitive to the PDF$_\gamma \otimes$ Hard Scatter. The former specifically deals with the multi-scale issues (charm, due to its heavy mass, can provide an additional scale, besides

the transverse energy of the jets), from which once the hard scattering is understood, the sensitivity towards charm originating from the photon can be probed. Chapter 9, referred to as 'Analysis II', on the other hand concentrates on the measurement of the charm fragmentation function, such that after a parameterisation within a given framework based on the measurement, the uncertainty due to fragmentation can completely be removed for all charm based analyses.

The analyses were performed using data collected with the ZEUS detector at HERA during 1996 – 2000. In this period, HERA collided electrons or positrons with energy $E_e = 27.5$ GeV and protons with energy $E_p = 820$ GeV (1996 – 1997) or $E_p = 920$ GeV (1998 – 2000), corresponding to integrated luminosities of 38.6 ± 0.6 and 81.9 ± 1.8 pb^{-1} and to centre-of-mass energies $\sqrt{s} = 300$ GeV and $\sqrt{s} = 318$ GeV, respectively. In this chapter, the complete description of the kinematics and event reconstruction for both analyses is presented, as well as the requirements for event selection in data and simulated events. The definition of the cross section is presented at the end of this chapter.

7.1 Kinematic Reconstruction

In order to perform the analyses on the observables that are sensitive to various aspects of QCD, the reconstruction of the kinematic variables must be properly defined. Some of these variables may not be directly measurable and must be constructed from quantities which are experimentally measurable.

The energy fraction y transferred to the photon and virtuality Q^2 are relevant variables for both of the analyses and are determined as follows, using the particle momenta as illustrated in Fig. 7.1.

$$y = \frac{q \cdot P}{k \cdot P} \simeq 1 - \frac{E'_e}{2E_e}(1 - \cos\theta_e) \tag{7.2}$$

$$Q^2 = -q^2 = -(k - k')^2 \simeq 2E_e E'_e(1 + \cos\theta_e) \tag{7.3}$$

where θ_e, is the polar angle of the scattered electron. In photoproduction events the photon virtuality, Q^2, is very small, the electron is scattered to a very low angle

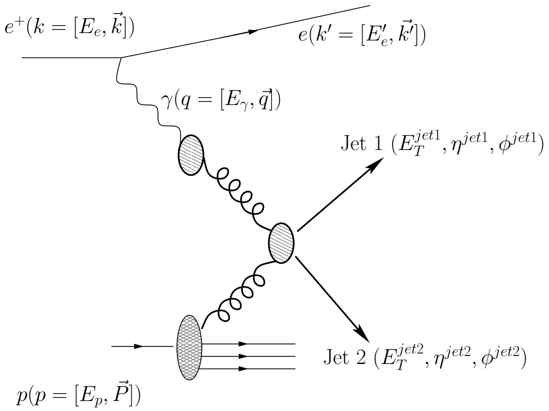

Figure 7.1: *Schematic diagram of a sub-process with particle four-momenta labeled on the plot.*

and will remain undetected in the detector. This property of rejecting the events with tagged scattered electrons or by requiring that it is lost in the beam pipe (anti-tagging) are used as a signature for photoproduction events. In the limit of low virtuality $Q^2 \to 0$ GeV^2, $q \to yk$, the photon and the scattered lepton are collinear

$$y = \frac{q \cdot P}{k \cdot P} \approx E_\gamma / E_e. \tag{7.4}$$

Given the condition of anti-tagging, the above equation for y and Q^2 cannot be used, thus they are reconstructed using the Jacquet-Blondel [147] method. This method relies entirely on the hadronic system in order to reconstruct the photon. The y_{JB} and Q^2 can then be written as:

$$y_{\mathrm{JB}} = \frac{\sum(E - P_z)}{2E_e} \tag{7.5}$$

$$Q^2_{\mathrm{JB}} = \frac{(\sum P_x)^2 + (\sum P_y)^2}{1 - y_{\mathrm{JB}}}. \tag{7.6}$$

where the sum is over all hadronic final state objects: calorimeter cells or EFOs (see section 6.2.2).

7.1.1 Kinematics for Analysis I

At leading order, the fractional momentum of the incoming partons from the photon and proton can be reconstructed from the two outgoing partons from the hard scatter, which within the collinear approximation ($E_\gamma \approx yE_e$) is:

$$x_\gamma^{\mathrm{LO}} = \frac{\sum_{partons} E_T e^{-\eta}}{2yE_e}, \tag{7.7}$$

$$x_p^{\mathrm{LO}} = \frac{\sum_{partons} E_T e^{\eta}}{2E_p}, \tag{7.8}$$

where E_T and η are the parton transverse energy and pseudorapidity. Thus, the photoproduction events in which the photon acts as a point like particle (direct photon processes) will have $x_\gamma^{\mathrm{LO}} = 1$, whereas for the resolved photon events will occur at low x_γ^{LO}. As jets are the experimental signatures of quarks and gluons, the analogous experimental variables x_γ^{obs} (x_p^{obs}) are defined [148] as the fraction of the photon (proton) energy contributing to the production of two highest E_T jets. It can be reconstructed at the parton, hadron and detector levels and is unambiguously defined to all orders in pQCD:

$$x_\gamma^{obs} = \frac{\Sigma_{\mathrm{jets}}\left(E_T^{\mathrm{jets}} e^{-\eta^{\mathrm{jet}}}\right)}{2yE_e}, \tag{7.9}$$

$$x_p^{obs} = \frac{\Sigma_{\mathrm{jets}}\left(E_T^{jet} e^{\eta^{\mathrm{jet}}}\right)}{2E_p}. \tag{7.10}$$

where yE_e is the initial photon energy and the sum is over the two jets with the highest E_T^{Jet}. Direct photon processes as defined at leading order have high x_γ^{obs}, since all the photon energy participates in the production of the hard jets, while resolved processes as defined at leading order have low values of x_γ^{obs}, since part of the photon energy goes into the photon remnant. Thus the selection of $x_\gamma^{obs} > 0.75$ and $x_\gamma^{obs} < 0.75$ yields samples enriched in direct and resolved photon processes, respectively.

Kinematic effect due to low E_T jets

In order to minimise the current uncertainties for both theory and experiment, the production of dijets originating from charm are considered, which are nearly back-to-back, have relatively high E_T and lie in the central rapidity region. The dijet centre-of-mass scattering angle, θ^*, and the invariant mass M_{jj}, of such jets are reconstructed using:

$$\cos\theta^* = \tanh\left(\frac{\eta^{\text{jet1}} - \eta^{\text{jet2}}}{2}\right) \tag{7.11}$$

$$M_{jj} = \sqrt{2E_T^{\text{Jet1}}E_T^{\text{Jet2}}[\cosh(\eta^{\text{Jet1}} - \eta^{\text{Jet2}}) - \cos(\phi^{\text{Jet1}} - \phi^{\text{Jet2}})]} \tag{7.12}$$

A dijet sample with $E_T > 5$ GeV and $|\eta^{jet}| < 2.4$ produced in association with a charmed meson is selected. The comparison between the invariant mass M_{jj} from Eq. 7.12, and the dijet invariant mass at leading order $M_{\text{jj}}^{\text{LO}}$ with $2 \to 2$ scattering is shown in Fig. 7.2 a). It can be seen that the $M_{\text{jj}}^{\text{LO}} = \sqrt{4E_eE_pyx_\gamma^{\text{LO}}x_p^{\text{LO}}}$, agrees quite well with M_{jj} after the addition of parton shower modeled in HERWIG, PYTHIA and CASCADE. In CASCADE the multi-gluon emission leads to higher jet multiplicities, the invariant mass is lower than, expected from $M_{\text{jj}}^{\text{LO}}$.

In the simple case in which two jets are back-to-back in the transverse plane and have equal transverse energies, the dijet invariant mass is given by $M_{\text{jj}} = 2E_T^{\text{jet}}/\sqrt{1-|\cos\theta^*|^2}$. Therefore, for a given M_{jj}, events with high values of $|\cos\theta^*|$ have a lower E_T^{jet}. Fig. 7.2 b) shows the $M_{jj} - |\cos\theta^*|$ plane with $E_T > 5$ GeV and $|\eta^{jet}| < 2.4$. The dense part in the plot corresponds to low E_T jets, which tend to produce a high scattering angle $|\cos\theta^*| \to 1$. Therefore in order to study the $|\cos\theta^*|$ distribution up to $|\cos\theta^*| = 0.83$ without bias from this E_T^{jet} cut, M_{jj} was required to be above 18 GeV.

Effects due to forward boosts and D^* pseudorapidity

At HERA, due to the asymmetric beam energies, the two-parton centre-of-mass is typically boosted in the forward direction. For resolved photon processes, this effect is larger because only a fraction of the photon's momentum participates in the hard scatter. To remove this bias, the average pseudorapidity $\bar{\eta}$ of the two jets:

$$\bar{\eta} = \frac{\eta^{\text{jet1}} + \eta^{\text{jet2}}}{2} \tag{7.13}$$

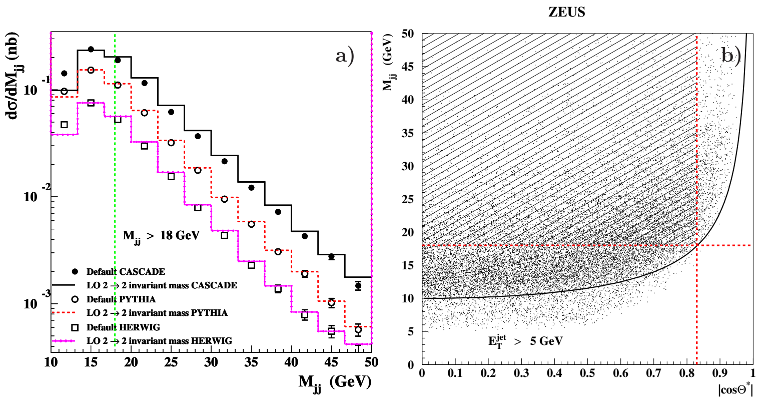

Figure 7.2: *a) Differential cross section as a function of M_{jj} compared with $2 \to 2$ LO dijet invariant mass for HERWIG, PYTHIA and CASCADE predictions. b) The scattering angle and invariant mass $M_{jj} - |\cos\theta^*|$ plane for events with two high E_T jets. The horizontal and vertical lines in b) shows the cuts with $M_{jj} = 18$ GeV and $|\cos\theta^*| = 0.83$, while the curve represents their functional relationship $M_{\text{jj}} = 2E_T^{\text{jet}}/\sqrt{1-|\cos\theta^*|^2}$.*

was approximated to be the measure of the boost of the dijet scattering system in the HERA frame, given by:

$$\eta_{boost} = \frac{1}{2}\ln\left(\frac{E_px_p}{E_\gamma x_\gamma}\right) \tag{7.14}$$

where x_p and x_γ are the momentum fractions of the incoming partons in the proton and photon respectively, and E_p is the incoming proton energy. Fig.7.3 a) shows the comparison between $\bar{\eta}$ and the longitudinal boost η_{boost} for HERWIG, PYTHIA and CASCADE. It can be seen that, irrespective of the different model assumptions, the three MCs show that the variable $\bar{\eta}$ can be used as a measure of the longitudinal boost.

In an inclusive dijet analysis, the variable $\bar{\eta}$ can be chosen to be less than 1.2, in order to study dijets with $E_T > 5$ GeV, $|\eta^{\text{jet}}| < 2.4$, $M_{jj} > 18$ GeV and scattering angles $|\cos\theta^*| < 0.83$. This cut on $\bar{\eta}$ is based on the relation obtained using Eq. 7.11

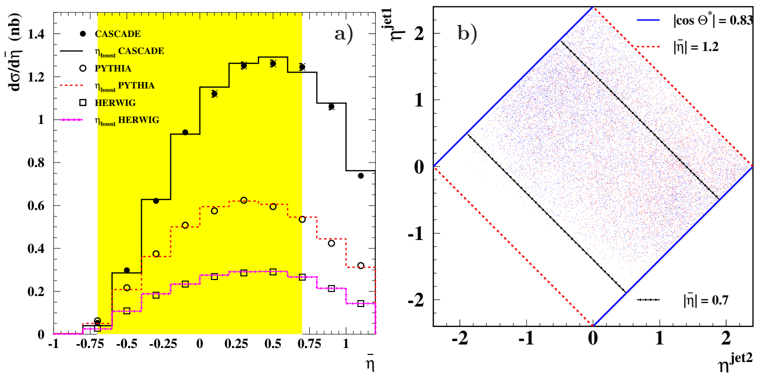

Figure 7.3: *a) Differential cross section as a function of $\bar{\eta}$ compared with the cross section as a function of longitudinal boost η_{boost}, for HERWIG, PYTHIA and CASCADE. b) Correlation between the two pseudorapidities of the jets with $|\cos\theta^*| \leq 0.83$ (solid line) and $|\bar{\eta}| \leq 1.2$ (dotted line). The shaded area in a) and dashed-line in b) shows $|\bar{\eta}| < 0.7$. The dark and light points are from PYTHIA and HERWIG simulations, respectively.*

and Eq. 7.13, within the boundary conditions of the two jet pseudorapidities being less than 2.4. Fig. 7.3 b) shows the correlation between the two jet pseudorapidities, with $|\cos\theta^*| < 0.83$. The correlation is plotted with $|\bar{\eta}| < 1.2$. The population of events towards higher $\bar{\eta}$ clearly indicates the effect due to the boost.

In this analysis, the additional requirement of an associated D^* meson, restricted within CTD acceptance range of $|\eta(D^*)| < 1.5$, can be a potential bias in the jets η, which in turn can affect the $|\cos\theta^*|$ distribution. Fig. 7.4 shows the effect of the cut, due to backward $\eta(D^*) < 0$ and forward $\eta(D^*) > 0$ D^* mesons. The only possible unbiased region in the $|\cos\theta^*|$ distribution can then be obtained by constraining $|\bar{\eta}| < 0.1$. Thus in [120] in order to study the dijet angular distribution for the forward and backward going D^* meson, the average pseudorapidity was chosen to be $|\bar{\eta}| < 0.1$.

Although in theoretical simulations such a reduced cut on the longitudinal boost

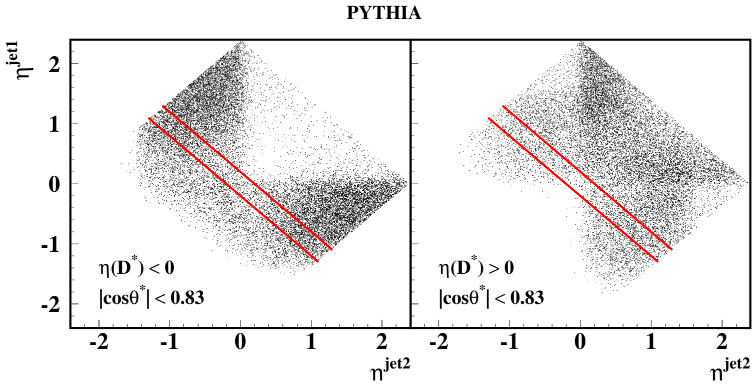

Figure 7.4: *Correlation between the two pseudorapidities of the jets with $|\cos\theta^*| \leq 0.83$ in backward $(\eta(D^*) < 0)$ and $\eta(D^*) > 0$ forward $(\eta(D^*) > 0)$ directions. The two lines show the unbiased region with $|\bar{\eta}| < 0.1$.*

$\bar{\eta}$ is possible, in data analysis due to limited statistics, some other measures need to be taken, to reduce this bias. One of the important aspects in this analysis is that these jets can be tagged or associated to a D^* meson in order to study the dynamics of the charm initiated jets. The two jets are then distinguished by associating the D^* meson to the closest jet in $\eta - \phi$ space (see the section 7.1.3 below). The associated jet is defined to be the jet with the smallest $R_i = \sqrt{(\eta^{\mathrm{jet},i} - \eta^{D^*})^2 + (\phi^{\mathrm{jet},i} - \phi^{D^*})^2}$ for $(i = 1, 2)$ and with $R < 1$, where ϕ^{jet} (ϕ^{D^*}) is the azimuthal angle of the jet (D^*) in the laboratory frame. Calling this "D^* jet" jet 1 in Eq. 7.11, the differential distribution as a function of $\cos\theta^*$ can be studied separately for the photon and proton directions.

The effect of the bias due to the restricted pseudorapidity range given by the D^* meson, was then estimated using a pure BGF physics channel $\gamma g \rightarrow c\bar{c}$ in the MC simulations. In this channel the two outgoing charm quarks hadronise to form D^* mesons, which will give rise to a symmetric dijet angular distribution due to a q-exchange as a function of $\cos\theta^*$ in the photon and proton directions. Any asymmetry in the distribution in the forward $(\cos\theta^* > 0)$ and backward $(\cos\theta^* < 0)$

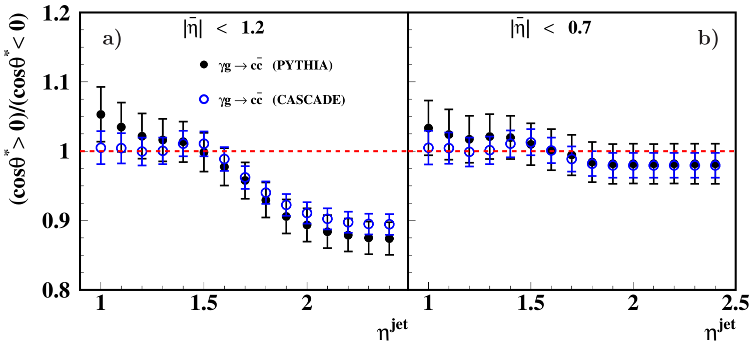

Figure 7.5: *Ratios of forward ($\cos\theta^* > 0$) to backward ($\cos\theta^* < 0$) scattering angle, as a function of jet pseudorapidity η are shown for a) $|\bar{\eta}| < 1.2$ and b) $|\bar{\eta}| < 0.7$.*

direction can be attributed to the bias due to the longitudinal boost $\bar{\eta}$. The ratio of forward ($\cos\theta^* > 0$) to backward ($\cos\theta^* < 0$) scattering angles, as a function of jet pseudorapidity η was studied for $|\bar{\eta}| < 1.2$ as shown in Fig. 7.5 a) for PYTHIA and CASCADE simulations. Because of the bias due to the cut on $\eta(D^*)$ and the boost, the events in the forward scattering region should be less numerous, than in the backward direction and hence the deviation from unity. It should be noted that this deviation starts after $\eta^{jet} > 1.5$. Thus $\bar{\eta}$ was varied in the input parameter space, yielding a value for $\bar{\eta}$, such that the forward to the backward distribution of the scattering angles can be symmetric. The ratio with $|\bar{\eta}| < 0.7$ in Fig. 7.5 a) show this symmetry. PYTHIA and CASCADE with BGF only agree with each other. The slight deviation between them and from unity can be attributed to tagging inefficiencies as well as effects from the parton shower.

Therefore, a cut on the average longitudinal boost, $\bar{\eta} = (\eta^{\text{jet1}} + \eta^{\text{jet2}})/2 < 0.7$ was applied. This selection limits η^{jet} to $|\eta^{\text{jet}}| < 1.9$ and removes the bias caused by the explicit cuts on η^{jet}. It also reduces the bias caused by the cut on $|\eta^{D^*}| < 1.5$ while retaining a sufficiently large number of events. The residual distortion due to the $|\eta^{D^*}|$ cut was then studied in detail. In Fig. 7.6 the dijet angular distribution

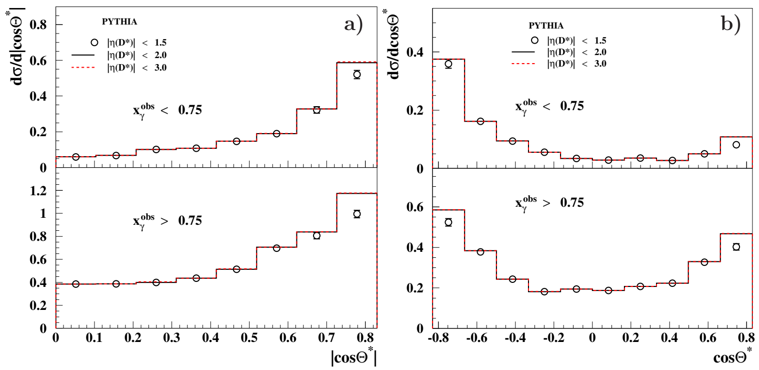

Figure 7.6: *Dijet angular distributions as a function of a) $|\cos\theta^*|$ and b) unfolded $\cos\theta^*$ obtained using PYTHIA simulations, for events enriched in resolved ($x_\gamma^{\text{obs}} < 0.75$) and direct ($x_\gamma^{\text{obs}} > 0.75$) enriched samples. The default cut on $|\eta(D^*)| < 1.5$ (open points) are compared to $\eta(D^*) < 2$ and 3 units. (histograms) after applying the cut on average pseudorapidity $|\bar{\eta}| < 0.7$.*

as a function of $|\cos\theta^*|$ and $\cos\theta^*$ with the default cut $\eta(D^*) < 1.5$ were compared with the distributions for $\eta(D^*) < 2.0$ and $\eta(D^*) < 3.0$ using PYTHIA. The residual distortion due to the $|\eta^{D^*}|$ cut is small and confined to the extreme bins of the $\cos\theta^*$ distribution.

In order to confirm that the different behaviour of the direct and resolved photon events as shown in Fig. 7.6 a) is not due to a bias from different shapes of the M_{jj} distribution (see section 8.2.3) for both samples [149], the MC $|\cos\theta^*|$ distribution for direct events (dashed histogram) is shown in Fig. 7.7 in addition to the direct events, reweighted using the ratio of resolved to direct values from the M_{jj} distribution (open dots). In this plot, the direct and resolved correspond to the true LO subprocesses from the MC, rather than by employing the x_γ^{obs} cut. Clearly, this reweighting does not change the shape of the distribution, which is significantly different than that for the resolved sample, even when both M_{jj} distributions are identical. A similar conclusion is obtained when the resolved distribution (full histogram) is compared with that after reweighting with the ratio of direct to resolved values from the M_{jj}

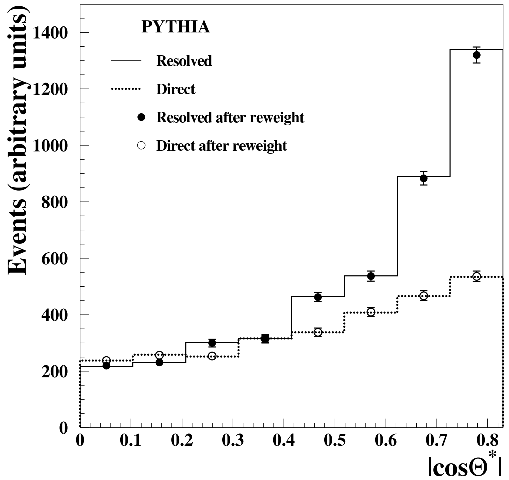

Figure 7.7: *Differential distributions $dN/d|\cos\theta^*|$ for MC with the true LO definition of direct/resolved. Direct(resolved) events are given by the dashed (full) histogram. Open (full) dots are the direct (resolved) events reweighted to reflect the M_{jj} distributions of resolved (direct) photon events. All distributions are normalised to the resolved photon events in the lowest 4 bins.*

distribution (full dots).

These cuts ensure that all features seen in the measured distributions can be attributed to the dynamics of the hard scattering processes.

7.1.2 Kinematics for Analysis II

For the study of charm fragmenting into a D^* meson, the fragmentation variable z is defined as the energy fraction of the meson containing the heavy quark, $z \equiv E_{D^*}/E_c$. In e^+e^- collisions, it is approximated by the fraction of the available centre-of-mass energy carried by the D^* meson. However, at hadron colliders like HERA, due to the large number of initial-state partons, the centre-of-mass cannot be uniquely

determined. It can only be assessed from the "active partons" in the incident hadron which participate in the hard scattering. Furthermore only a fraction of these "active partons" contributes to the production of charm quarks. On the other hand, charm quarks produced from these active partons form final-state jets of which the meson is a constituent. In such a case the meson should be uniquely associated with the jet.

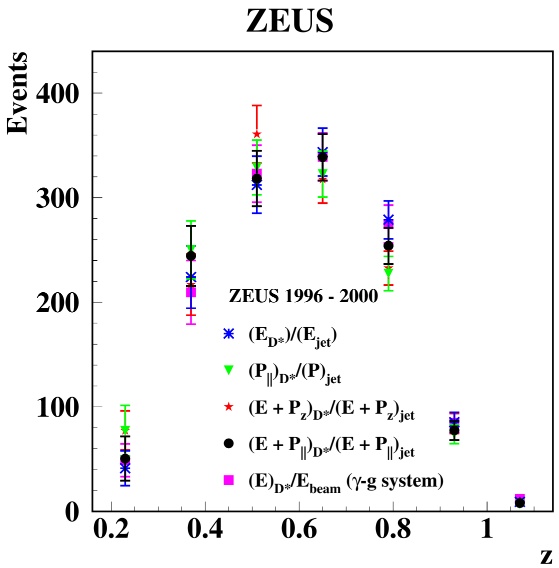

Figure 7.8: *Ratio of various energy or momentum fractions of the D^* meson with respect to the associated jet.*

All possible combinations of energy or momentum fractions of the meson relative to the corresponding jet were considered. Several studies are made here to measure this energy fraction. In Fig. 7.8 a summary of the relevant variables is shown. Although a similarity in shape is found, these variables are conceptually different. However fragmentation describes how the final state partons produce final state hadrons, which has nothing to do with the initial state. Thus, in studies involving jets, the z-axis should be along the jet direction. That is why the variables with z-axis in the laboratory frame such as $z = E_{D^*}/E_{jet}$, and $(E + p_z)_{D^*}/(E + p_z)_{jet}$ can be discarded. Although studies using $z = (P \;\|)/(P)_{jet}$, with $P_\|$ being the momentum component of the hadron along the axis of a jet with momentum $\vec{P}_{jet}$, were made, the results are still not conclusive [150]. Therefore the definition $z = (E + P_\|)_{D^*}/(E + P_\|)_{jet}$ was considered for this analysis, in accordance to the one from Bowler for heavy quarks [126].

In principle, the variable z can also be defined as the E_{D^*}/E_{beam} ratio, where the 'beam energy' is defined to be the centre-of-mass energy of the two incoming beams (γ and g) producing the D^* meson in that frame. This definition is much closer to the e^+e^- definition, but due to the forward boosted centre-of-mass energy at HERA, and the presence of remnants, the meson energy can have a bias in the γ-parton or parton-parton frame. The fragmentation variable, irrespective of the definitions should satisfy the following conditions:

- The energy fraction within the range $E_{D^*}/E_c < z < 1$ should be studied.
- In the case of jets approximated by the outgoing charm quarks called 'charm jets' (see Fig. 3.9), the D^* meson should be uniquely associated with the jet.

The second item will be discussed in detail in the next subsection. Because of the finite acceptance and resolution of the detector, a lower limit on the first item can not be avoided. In practice the lower cut on E_{D^*}, more specifically on p_T of the D^* meson, is intrinsically set during the D^* reconstruction process (see section. 7.2.4). The upper limit on the other hand depends on how the high E_T of the charm jets can be studied, with reasonable data statistics. In this analysis the D^* were selected with the lowest possible cut $p_T(D^*) > 2$ GeV, whereas the charm jets are required to have $E_T > 9$ GeV.

As the hadrons in a jet have small transverse momenta and the sum of their longitudinal momenta roughly gives the parton momentum, events with $z > 1$ are

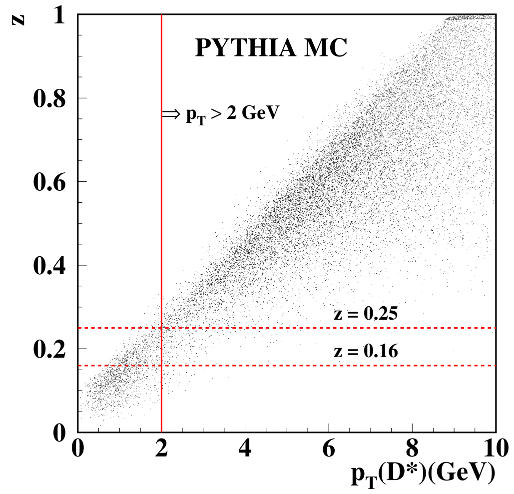

Figure 7.9: *Correlation between z and $p_T(D^*)$ of the associated D^* meson, simulated using PYTHIA.*

possible. The condition of $z < 1$, is only valid in the case of purely partonic c-jets, where the heavy quark c alone can be identified as a jet. Events with $z > 1$ can arise due to the limitations from the detector resolution. The fraction of events with $z > 1$ are found to be about 0.6% of the event sample for $z = (E+P_\|)_{D^*}/(E+P_\|)_{jet}$, with $p_T(D^*) > 2$ GeV and jet $E_T > 9$ GeV jets. These events are included in the systematic studies.

In order to study the possible bias due to the above cuts on the z distribution, the PYTHIA simulations were used a without transverse momentum cut on the D^* meson as shown in Fig. 7.9. A clear correlation between the fragmentation variable z and the $p_T(D^*)$ can be seen. A cut on $p_T(D^*) > 2$ GeV can introduce a mild bias up to $z \leq 0.25$. Although the kinematic region accessible by $z = (E+P_\|)_{D^*}/(E+P_\|)_{jet}$, can span the range $0.16 < z < 1$, this small bias between $0.16 < z < 0.25$, in the first bin was specifically checked, such that it does not produce any effect on the parameterisations to be extracted within a given theoretical framework. The lower limit of z is explained by the kinematics (Fig. 7.8). These cuts ensure that the events lie in a well understood acceptance region of the detector.

7.1.3 Tagging of Charm Initiated Jets

Jets can be associated or matched to a specific meson or parton (at parton level) using several methods. The most commonly employed method, used in almost all experiments, is based on the $\eta - \phi$ space. The second method, of associating particles to a jet developed in this thesis, was called k_T-association. The name is a derivative from the k_T-cluster jet algorithm used to select the jets. These two matching methods are discussed below.

Matching in the $\eta - \phi$ space:

This method of associating one or a group of particles to a jet is based on a fixed geometrical structure, which is positioned in an angular space around the jet axis. The particles within that conical space are considered to be part of the jet. The main assumption here is that the jet is considered to be a spray of particles, to which the particle to be matched belongs, if it lies within a certain angular range. This angular region is based on the distance in the (η, ϕ) plane between the particle and the jet, $\Delta R = \sqrt{(\Delta\eta)^2 + (\Delta\phi)^2}$, which is usually required to be taken less than a fixed value (e.g. 1.0). Here $\Delta\eta$ ($\Delta\phi$) is the difference between the particle and the jet pseudorapidities (azimuthal angles). For example, consider the matching of a D^* meson to a jet in an event consisting of a set of D^* mesons and jets. For each D^* meson, ΔR is calculated by looping over all jets. If the minimum of all the ΔR values in that loop, is less than a pre-defined constant, then the charmed meson is considered to be part of that jet. One of the advantages of this method is that there is no assumption made on the type of jet algorithm to be used. The question arises: what happens to the D^*, from which the jet is made of, when it is not in the $\eta - \phi$ cone ?

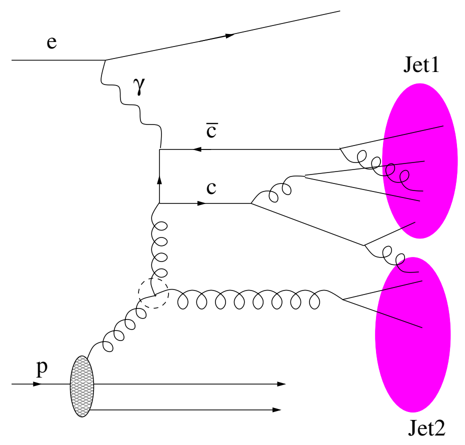

Figure 7.10: *Schematic diagram of a sub-process involving charm, leading to jets in the final state.*

k_T-association:

To address such issues, the k_T-association method was developed in this thesis. As most analyses use the k_T-cluster algorithm to define a jet either with partons or hadrons or with calorimeter cells, defining a cone on top of the k_T-algorithm in order to associate a D^* meson essentially leads to a difference in the definition in the final algorithm. Fig. 7.10 shows the formation of two jets out of partons from the hard scattering. Based on the complexity in configuration of partons or hadrons involved in jet formation, it is necessary to have unique association between the partons or hadrons to the jet.

In order to perform such an association, one needs to follow the pattern of jet formation in the algorithm. The following steps were used to associate the D^* meson to a jet in the cluster algorithm.

- A tag/reference to the D^* meson was initially set before it was sent as input to the k_T-cluster algorithm.

- This tag was traced until the final formation of the jets, including the user- and algorithm-defined E_T ordering.
- Based on this tag and the list of the particles, which the jet is made of, given by the cluster algorithm, the D^* was then associated to the jet.

The main advantage of this method is that in all cases, the tagged jet is formed out of the charmed meson. Hence, it can be used for the fragmentation studies. Fig. 7.11 shows the ΔR distribution obtained using the $\eta - \phi$ space and k_T-association methods. The number of events at low ΔR value for a k_T-associated jet to the D^* meson is higher than by simply using the cone method. In order to use this treatment, the hadronic final state (see section 9.1.3) has to be properly defined. In the fragmentation function analysis the D^* meson was considered to be the hadronic final state (not its decay products), which is compatible with the NLO QCD calculations for heavy quarks, which do use D^* as the final state particle.

7.2 Event Selection

The first step of the analysis consists in selecting the events which are under study out of an enormous amount of "background events" (containing other physics aspects and colliding beam properties). The initial sample consists of events taken with the detector when the trigger was fired based on a predefined selection of cuts or requirements, roughly directed towards a certain class of physics events. Depending on the kind of analysis, the final selection ofcourse requires different event properties.

In the case of the analyses described here, similar selection criteria for photoproduction events on the CTD tracks were required to select the charmed meson $D^{*\pm}$. Thus the global properties of the events described in next subsections are almost the same in all cases. After the event selection, the jet reconstruction is performed, followed by the identification of the charmed meson. The final selection and tagging of the charmed meson to a jet is different based on the physics properties under study and will be described towards the end of this section.

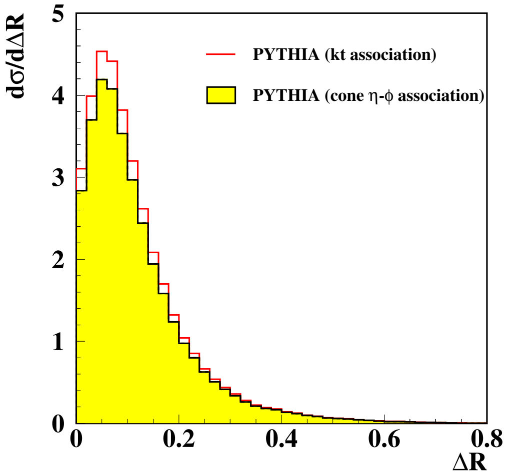

Figure 7.11: *Differential distribution as a function of ΔR for jets associated to a D^* meson using k_T-association and cone method.*

7.2.1 The Online Event Selection

As previously mentioned in section 4.2.4, the ZEUS data is selected using a complicated trigger system. It is then necessary to require the needed fired triggers not only satisfying the needed physics criteria but also remained unchanged throughout the 1996 - 2000 data taking period. In this way, it is possible to correct the trigger inefficiencies by applying the same trigger chain to the data and MC samples. In the presented analyses the following is two hardware (FLT and SLT) and a software (TLT) trigger chain used (see section 4.2.4 for the ZEUS trigger description).

First Level Trigger: `[FLT42 (1996-1997), FLT42.OR.FLT59 (1998-2000)]`

The FLT selection criteria are based on global and regional energy sums in the calorimeter[1] together with simple tracking requirement from the CTD FLT and vetoes from additional subcomponents. The FLT42 requires:

- large energy deposit in the calorimeter:
  $\mathrm{E}^{\mathrm{FLT}} > 14.968$ or $\mathrm{E}^{\mathrm{FLT}}_{\mathrm{EMC}} > 10.068$ or $\mathrm{E}^{\mathrm{FLT}}_{\mathrm{REMC}} > 2.032$ or $\mathrm{E}^{\mathrm{FLT}}_{\mathrm{BEMC}} > 3.404$
  where the energies are in GeV.

- timing information from the vetowall, SRTD and the C5 counter to veto events having a beam gas and non physics event timing.

- at least one track found by the CTD-FLT coming from the nominal interaction vertex region -50 cm $< z_{vtx} <$ 80 cm.

Although the FLT59 slot was present during the 1996-1997 data taking period, it suffered from a tighter CTD-FLT requirement `TRKclass=6`[2] rather than `TRKgood96` used in FLT42. This was cured during 1998-2000 and hence was used in for the aforesaid period.

Second Level Trigger: `[HPP01 (1996-1997), HFL01(1998-2000)]`

At the SLT, the following cuts are required to select the hard photoproduction events with high transverse energy (whence the name):

- a reconstructed vertex with -60 cm $< Z_{vertex} <$ 60 cm.

- $E - p_z > 8$ GeV, where E and p_z are the energy and the longitudinal momentum of the event measured in the calorimeter.

- $E_T^{cone} > 8$ GeV, where E_T^{cone} is the sum of transverse energy in all calorimeter cells outside a cone of 10° around the forward beam pipe.

[1] The total calorimetric energies in FLT are calculated by excluding the 3 inner rings around the FCAL and the inner ring around the RCAL beam pipe.
[2] These are the events with relatively high ratio of primary vertex tracks to total number of tracks.

- $E - p_z > 12$ GeV or p_z/E <0.95[3].

- Events are vetoed according to the timing information from different calorimeter sections.
  t_{down} - $t_{\mathrm{up}} > 10$ ns or t_{FCAL} - $t_{\mathrm{RCAL}} > 8$ ns or $|t_{\mathrm{RCAL}}| > 8$ ns or $|t_{\mathrm{FCAL}}| > 8$ ns
  where t_{down} and t_{up} are the timing of the lower and upper half of the BCAL described in section 4.2.2.

HPP01 (or HFL01) is a heavy flavour trigger designed for heavy quarks and was the only SLT trigger used for the $\mathrm{D}^{*\pm}$ meson at the TLT stage. It suffered the same problem from the tighter CTD-FLT requirement as mentioned for FLT59. It became fully operational since 1998-2000, hence was used.

Third level trigger: `[HFL10/DST27]`

At the TLT stage, more decision time is available during the data taking, and hence sophisticated algorithms can be used for a detailed discrimination of events. After the TLT decision, events go through a complete offline reconstruction and pass through additional offline filters. The two reconstructed-level filters relevant for the analyses are:

- DST27 - The $D^* \rightarrow K\pi\pi$ tracking trigger: This directly corresponds to the HFL10 slot of the TLT trigger and is based on events coming from the tracks produced by the inclusive charmed mesons in the tracking detector. It uses the full offline tracking VCTLT code with all online tracks originating from the primary vertex and VCTPAR to reconstruct the D^* mesons. The reconstruction method will be described in the following section. Tracks from all 9 CTD superlayers are used, which allows an improvement in the quality of the online tracks. These were however not as good as the offline tracks due to limitation of the processing time.

[3] Proton beam gas events get enormously boosted in the forward direction and are therefore characterized by $p_z \sim E$.

- DST77 - HPP dijet filter: This dijet filter corresponds to the online TLT bit HPP14. At the TLT, this filter uses a much relaxed cone-based EUCELL jet algorithm EUTLT, modified to run over cells in the calorimeter. After the jet finding, the events with at least two jets require $E_T^{jet} > 4$ GeV and $|\eta^{jet}| < 2.5$. Additional cuts are: $|Z_{vtx}| < 60$ cm, 5 GeV $< E - p_z <$ 75 GeV, $p_z/E < 1.0$ and $E_T(10^\circ\text{cone}) > 5$ GeV.

The DST77 trigger is obviously useful for dijet measurements, but the threshold for this trigger was raised to $E_T^{jet} > 4.5$ GeV in order to reduce the event rate during the years 1999-2000, hence is used only as a cross check for dijet with D* analysis. For all analyses presented, the DST slot 27 was used at the TLT/reconstruction stage. Trigger efficiencies and threshold effects on the measured observables are discussed in their respective analyses chapters.

7.2.2 The Offline Event Selection

The event sample obtained after the online trigger selections still contains contamination from non ep-physics and from non-photoproduction interactions, which must be rejected. This contamination not only consists of background from noise originating from the electronics and the radioactive decay from the Uranium Calorimeter (UCAL), but also from Neutral Current DIS events. Following are the procedures to reduce these contaminations. All requirements/cuts presented in this section correspond to identical selection criteria for both the analyses. In order to avoid repetition only plots from Analysis I are presented, excluding the cut on the observable which is plotted.

i) Calorimeter noise and 'sparks':

Noisy cells correspond to either the uranium noise contamination or the imbalance between the left and right photomultiplier tubes (PMT) of the calorimeter cell. The noise per calorimeter cell due to uranium radioactivity has approximately a Gaussian shape, centered around zero with a standard deviation of $\sim$ 18 MeV and

$\sim$ 27 MeV in the EMC and HAC sections respectively. A noise suppression cut of 60 MeV and 110 MeV for EMC and HAC cells respectively is therefore applied to each calorimeter cells at the offline level. A cut on the relative cell imbalance $I_{\text{imb}} = (E_l - E_r)/E_{\text{cell}} > 0.49 + 0.03/E_{\text{cell}}$ (where E_l, E_r are the signals measured by the two PMTs on the opposite sides of a cell) is also applied.

The pre-flagged cells, having significantly higher mean energy or 'firing' frequency compared to all other cells for each year are not included if their energy is less than three standard deviations above the noise level. To further reduce the noise level, a cut of 100 (150) MeV is applied to isolated EMC (HAC) cells. This imbalance and isolation cuts are predominantly used to suppress the contribution of cells due to 'sparks' in the PMTs and noise due to possible electronic malfunctions.

ii) Energy calibration in calorimeter cells:

The energy calibration (energy scale) for the data was then determined by comparing the p_T balance between the hadronic system and the scattered electrons in DIS to the corresponding simulated events with incorporated effects of the dead materials. From this comparison, it was concluded that the EMC energies were underestimated by $\sim$ 4%, whereas the HAC energies were overestimated by $\sim$ 5% in FCAL [151]. Similar procedures for BCAL and RCAL led to the following calibration corrections, thereafter applied **only to the data**.

	EMC(96-97)	HAC(96-97)	EMC(1998-2000)	HAC(1998-2000)
FCAL	+4.0%	-5.0%	+2.4%	-5.9%
BCAL	+4.3%	+8.0%	+5.3%	+9.6
RCAL	per cell +2.5% for all years			

Table 7.1: *Calibration corrections for each section of the Calorimeter corresponding to different data taking periods, with change in proton beam energy.*

iii) Proton beam gas/cosmic shower:

The simplest way to remove events coming from proton beam-gas interactions and/or from cosmic showers is the requirement of a primary vertex. For this reason the Z_{vertex} was required to be within $|Z_{\text{vertex}}| \leq 50$ cm from the interaction point, along with associated $\mathrm{N}_{\text{track}}^{\text{good}} \geq 2$. The variable $\mathrm{N}_{\text{track}}^{\text{good}}$ corresponds to the number of tracks fitted to the primary vertex traversing at least three superlayers and having the transverse momenta $p_T^{\text{track}} > 0.12$ GeV. Fig. 7.12 a) shows such vertex distribution after the cuts for dijet events associated at least with a charmed meson. PYTHIA and HERWIG simulations can well describe the distribution without having any proton beam gas/cosmic shower background within the analysis phase space.

iv) Non-γp background - Using scattered lepton:

Photoproduction events are defined through the requirement that the scattered lepton is not detected in the UCAL and is lost in the beam pipe. If the scattered lepton (lepton in this thesis corresponds to both electron and positron used during the different data taking periods) is detected then the event should be rejected (anti-tagging). The experimental signature of a lepton hitting the calorimeter is a deposit of energy in the electromagnetic calorimeter with little energy leaking into the hadronic section. The determination of the shower profile, i.e its width and depth, allows a distinction to be made between energy deposits originating from a lepton and those from other hadronic sources. Because the shower profile measurement depends in a complicated way on the position of incidence in the calorimeter, a specialised neural network (SINISTRA 95 [152]), which was trained on Monte Carlo events, was used to translate the profile measurement into a 'lepton probability' $\mathcal{P}_{elec}$ and lepton energy E'_{elec}. If the scattered lepton is detected with higher probability $\mathcal{P}_{elec}$, its energy E'_{elec} and scattering angle θ'_{elec} can be used to determine y_{elec}, using

$$y_{elec} = 1 - \frac{E'_{elec}}{2E_e}(1 - \cos\theta'{}_{elec}). \tag{7.15}$$

where E_e is the incident lepton energy. As can be seen from Eq. 7.15, for a small angle scattered lepton corresponding to a photoproduction event the y_{elec} has a

higher value, whereas the reverse is true for NC DIS events. Thus, the event is rejected if a lepton candidate is found with a higher probability $\mathcal{P}_{elec} > 0.9$, energy $E'_{elec} > 5$ GeV and lower $y_{elec} < 0.7$. Fig. 7.12 b) shows the effect of these cuts, restricting the photon virtuality towards lower values of Q^2.

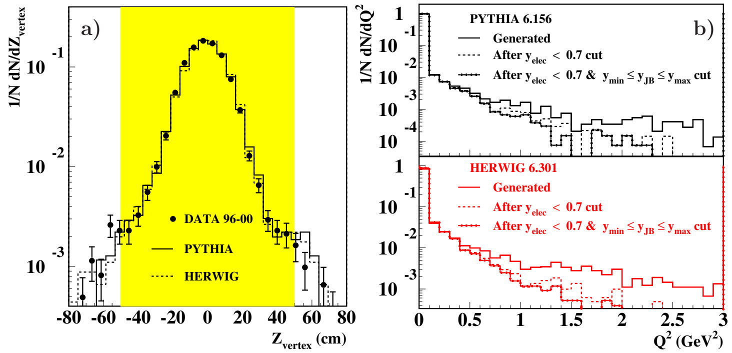

Figure 7.12: **a)** *Normalised distribution of Z_{vertex} compared to event simulations. The Z_{vertex} range is given by the shaded area.* **b)** *Effects of cuts to remove NC DIS candidates on the generated Q^2 distributions. y_{min} and y_{max} are the minimum and maximum limits obtained after imposing the cut $130 < W < 280$ GeV.*

v) Non-γp background - Using y_{JB}: The value of y_{JB} was calculated using the Jacquet-Blondel method described earlier in section 7.1. The hadronic final state consists of the energy sum over cells or EFOs (see section 6.2.2) separately for both data taking periods. The sums clearly deviate from the true values y_{true}, as shown in Fig. 7.13 a)-h) and Fig. 7.14 a)-h) obtained using PYTHIA and HERWIG simulations respectively. The true value is obtained using Eq. 7.2 at the hadron level. The systematic deviations of y_{JB} from y_{true}, are due to the energy losses as particles passing through the dead material in front of the calorimeter or are lost down the rear beam-pipe. The resulting mean for y_{JB} is shifted by about 10% for the reconstructed events using cells and 4% using EFOs. This dependence was corrected by parameterising the correlation with a linear function (shown in

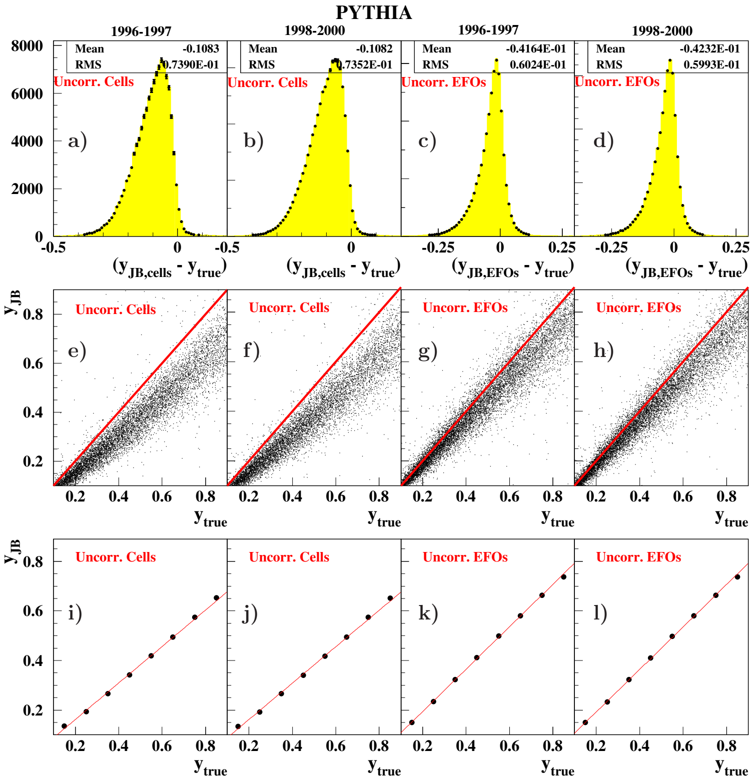

Figure 7.13: *Correction of the measurement of y. The difference between y_{JB} and y_{true} for cells a)-b) and EFOs c)-d), along with their correlation e)-h) from PYTHIA simulations. Also shown the parameterisation with a linear function by fitting the distribution of y_{JB} as a function of y_{true} i)-l). The shaded regions show the area under the distributions.*

Fig. 7.13 i)-l) and Fig. 7.14 i)-l) for PYTHIA and HERWIG respectively) by fitting the distribution of the y_{JB} as a function of y_{true}. The fitted function has the form:

$$y_{\mathrm{JB}} = m \cdot y_{true} + c \tag{7.16}$$

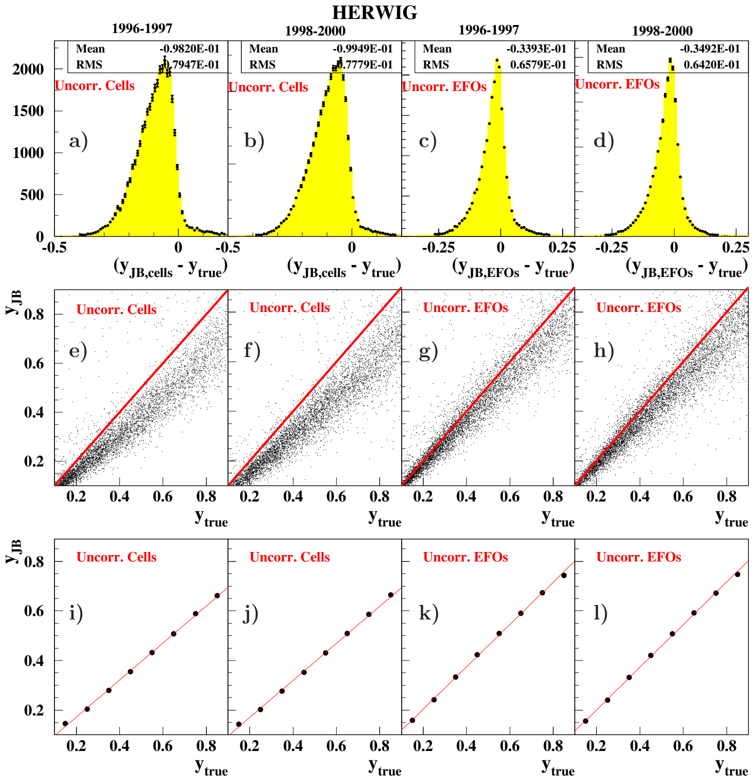

Figure 7.14: *Correction of the measurement of y. The difference between y_{JB} and y_{true} for cells a)-b) and EFOs c)-d), along with their correlation e)-h) from HERWIG simulations. Also shown the parameterisation with a linear function by fitting the distribution of y_{JB} as a function of y_{true} i)-l). The shaded regions shows the area under the distributions.*

where the slope, m, and the intercept, c, are determined from the fit. This fit was done for both PYTHIA and HERWIG simulations and was found to give identical

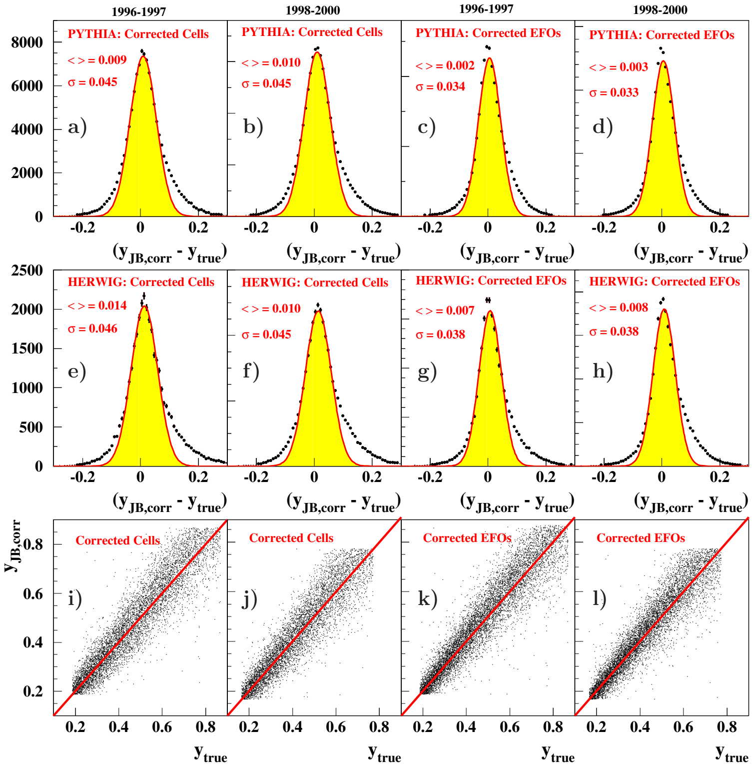

Figure 7.15: *Effect of the $y_{\rm JB}$ correction. The difference between the corrected $y_{\rm JB,corr}$ and y_{true} fitted to a Gaussian is shown for a)-b), e-f) cells and c)-d), g-h) EFOs for two different data taking periods. The correlation between the corrected and true quantities are also shown i)-l). The shaded regions shows the area under the fits.*

results. The correction was then applied by inverting the function in Eq. 7.16

$$y_{corr} = (y_{\rm JB} - c)/m. \tag{7.17}$$

The result of this correction is shown in Fig. 7.15. The mean of the distribution

after the correction is found to be well centered with an improvement in the resolution obtained by a Gaussian fit to the corrected distribution. The mean < > and standard deviation σ, are indicated on the respective plots. The two independent MC simulations after the correction provide similar results.

From here onwards the γp centre-of-mass energy W, obtained using the Jacquet-Blondel [147] estimator $W_{\rm JB} = \sqrt{4y_{\rm corr,JB}E_eE_p}$ will be used, after the above mentioned corrections for cells or EFOs. The cut on $130 < W < 280$ GeV imposes further cut on y_{corr} as illustrated in Fig. 7.15 i)-l). The lower W cut rejects events from a region where the acceptance is small because of the trigger requirements. The upper cut rejects possible background from DIS events, in which the scattered electron has not been identified. This cut and the no-scattered electron requirement given in section 7.2.2 iv) restricts the virtuality Q^2 to be below ≈ 1 GeV^2 as illustrated in Fig. 7.12 b) using PYTHIA and HERWIG simulations. The corresponding median Q^2 in this photoproduction sample, estimated from MC calculation is $\approx 3.28 \cdot 10^{-4}$ GeV^2.

vi) Non γp background - Missing transverse momentum:

The missing transverse momentum, $\not{P}_T$, arises due to the lepton conversion into an undetected neutrino of the same type in the DIS events, with the $W^\pm$ bosons, taking part in the hard interaction. These charged current (CC) DIS events have characteristic similar to the γp in terms of non detected scattered leptons. To remove CC-DIS events, a cut [153] was applied on missing transverse momentum, which was scaled with the inverse root of the deposited energy to account for the calorimeter resolution. Small fraction of events are rejected when $\not{P}_T/\sqrt{E_T} < 1.5\sqrt{\rm GeV}$, where E_T is the total transverse energy measured in the calorimeter cells. These quantities are computed as follows:

$$\not{P}_T = \sqrt{\left[\sum_{cells} E_i \sin\theta_i \cos\phi_i\right]^2 + \left[\sum_{cells} E_i \sin\theta_i \sin\phi_i\right]^2} \tag{7.18}$$

$$\text{and} \quad E_T = \sum_{cells} E_i \sin\theta_i. \tag{7.19}$$

All the above mentioned cuts are applied to the detector level simulated events in the same way as for the data. The selection requirements which only need to be applied to the data but not to simulated events are the noise suppression cuts and the cell energy calibrations outlined in i) and ii) of this subsection.

7.2.3 Jet Selection

Jets were reconstructed with the k_T-cluster algorithm [140] in its longitudinally invariant inclusive mode [142]. The events for Analysis I, using calorimeter cells were required to have at least two jets with pseudorapidity $|\eta^{\rm jet}| < 2.4$ and transverse energy $E_T^{\rm jet} > 5$ GeV. The measured jet energies were corrected as outlined in section. 6.2.1. The comparison between data and MC simulations, of the corrected[4] E_T and η^{jet} distributions with at least one charmed meson D^* is later discussed in Fig. 7.18. For Analysis II, jets with $E_T > 9$ GeV and $|\eta^{jet}| < 2.4$ were selected using the k_T cluster algorithm on EFOs (see section 6.2.2).

7.2.4 Charm Reconstruction

The D^* mesons were reconstructed using the mass-difference technique applied to the decay chain[5] $D^{*\pm} \to D^0\pi_S^{\pm} \to K^{\mp}\pi^{\pm}\pi_S^{\pm}$, where the π_S is the low momentum (slow) pion. As the decay length $\beta\gamma c\tau$, with $c\tau \sim 120\mu m$ of the D^0 meson is smaller than the vertex resolution from the CTD, all tracks used in the D^* reconstruction are required to be associated with the primary vertex. Tracks in the CTD with opposite charges and transverse momenta $p_T > 0.5$ GeV were combined in pairs to form D^0 candidates. Each of the two tracks is alternatively assumed to be a kaon or a pion, i.e. no particle identification being employed. Then an additional slow track with opposite charge to that of the kaon is assumed to be the slow pion from the D^* decay and is combined with the two tracks of the D^0 meson to form

[4] The comparison between uncorrected DATA and MC distribution can be found at [154].
[5] Throughout this document, D^0 refers to both D^0 and $\bar{D}^0$.

a D^* candidate. Events with a mass difference $\Delta M = M(K\pi\pi_S) - M(K\pi)$ in the range $0.1435 < \Delta M < 0.1475$ GeV around the nominal value [75] and the range $1.81 < M(K\pi) < 1.92$ GeV ($1.83 < M(K\pi) < 1.90$ GeV) around the D^0 mass in Analysis I (Analysis II) are called D^* candidates. In order to reduce the combinatorial background and to study only the relative cross section in Analysis II a narrower mass window for the D^0 meson was selected.

The reconstructed D^* mesons were required to have pseudorapidity in the range $|\eta^{D^*}| < 1.5$, $p_T^{D^*} > 3$ GeV in Analysis I and $p_T^{D^*} > 2$ GeV in Analysis II respectively. The following is the summary of the cuts applied on the (K, π, π_S) system for Analysis I:

- $p_T(D^*) > 3$ GeV and pseudorapidity in the range $|\eta(D^*)| < 1.5$.
- $0.1435 < \Delta M < 0.1475$ GeV and D^0 mass between $1.81 < M(K\pi) < 1.92$ GeV.
- $p_T(K,\pi) > 0.5$ GeV and $p_T(\pi_S) > 0.15$ GeV.
- to suppress combinatorial background, a cut $p_T^{D^*}/E_T^{\theta>10^\circ} > 0.15$ was applied [82], where $E_T^{\theta>10^\circ}$ is the transverse energy measured in the CAL outside a cone of $\theta = 10^\circ$ in the forward direction.

and for Analysis II:

- $p_T(D^*) > 2$ GeV and $|\eta(D^*)| < 1.5$.
- $0.1435 < \Delta M < 0.1475$ GeV and D^0 mass between $1.83 < M(K\pi) < 1.90$ GeV
- $p_T(K,\pi) > 0.5$ GeV and $p_T(\pi_S) > 0.12$ GeV.
- the cut on $p_T^{D^*}/E_T^{\theta>10^\circ} > 0.1$ was imposed, where $E_T^{\theta>10^\circ}$ is the transverse energy measured using the EFOs outside a cone of 10° in the forward direction.

The tracks used in the D^* meson reconstruction are required to be contained within the CTD i.e. only tracks that reach at least the third superlayer (SL3) of the

CTD were considered. This implicitly restricts the minimum transverse momentum $p_T^{track} \geq 0.12$ GeV and pseudorapidity $|\eta^{tracks}| \leq 1.75$. As the event selection for Analysis I requires two high transverse energy jets, a higher cut on the transverse momentum of D^* meson was applied to reduce the combinatorial background. The lower cut on $p_t(D^*)$ for Analysis II, was chosen because of the physics reasons explained in section 7.1.2. To keep the background at a reasonable level, a tighter cut $p_T(K,\pi) > 0.5$ GeV than the track $p_T^{track} > 0.12$ GeV was applied in both analyses. As the slow pion π_S shown in Fig. 7.16 is highly correlated with the $p_T(D^*)$ of the D^* meson, a difference in cut on $p_T(\pi_S)$ for the two analyses was considered. For Analysis I, $p_T(\pi_S) > 0.15$ GeV is sufficient at the edge of the correlation and hence was applied. For Analysis II, due to the low $p_T(D^*)$ requirement, the range of values for the transverse momentum of the π_S should avoid the lower corner region. On the other hand, π_S is a low momentum particle, and since the cuts cannot be lowered below the CTD threshold values, the $p_T(\pi_S) > 0.12$ GeV cut was acceptable. The cut on pseudorapidity ensures anyway that all tracks are within the range of good reconstruction in the CTD.

The D^* meson sample obtained using the method mentioned above is not a pure sample. A significant amount of combinatorial background can still be present, which needs to be statistically estimated and subtracted. Two different methods called 'wrong-charge' (WC) and 'control-region' (CR) were used to estimate the backgrounds. In the wrong-charge method, the charged track combinations which cannot form the genuine D^* mesons are selected in the signal region[6], whereas the sign of the slow pion was kept same as of the parent D^* meson. For example, the charge combination (K^-, π^-,π_S^+) for D^{*+} and (K^+, π^+,π_S^-) for the D^{*-} are considered as the wrong charges in the (K,π,π) system. In addition to the wrong charge combinations, the background contributions can be estimated by using the control region. In that case, the events in the range $0.15 < \Delta M < 0.165$ GeV lie outside, but remain close to the signal region. The combinatorial phase space is approxi-

[6] The signal region corresponds to the ΔM and $M(D^0)$ mass window, e.g for Analysis I this corresponds to $0.1435 < \Delta M < 0.1475$ GeV and $1.81 < M(D^0) < 1.92$ GeV.

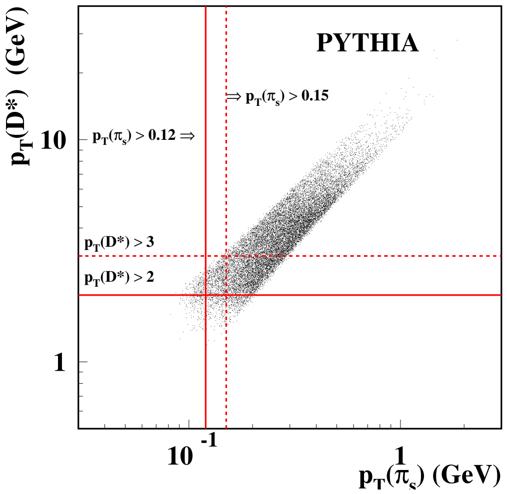

Figure 7.16: *Correlations between the D^* and π_S transverse momenta from the PYTHIA simulations.*

mately equal for both right and wrong charge combinations. Thus the control region consists of a much larger sample of combination for background estimation, which allows the statistical uncertainty in the measurement to be significantly reduced. In the presented analyses, the control region between $0.15 < \Delta M < 0.165$ GeV was therefore used (see Fig 7.17 a)). The exact normalisation of the wrong charge background in the signal region, was estimated using the ratio of the right to wrong charge combination in that region.

The mass difference ΔM and the invariant mass $M(K\pi)$ distributions for Analysis I, after all corrections and selection cuts including those from jet and D^* selection as described above are shown in Fig. 7.17. Clear signals can be seen. The excess of events with respect to the wrong charge distribution below the D^0 region originates mostly from D^0 decays involving neutral pions [155]. As the combinatorial background also passes the applied cuts, the overall Gaussian distribution for the signals

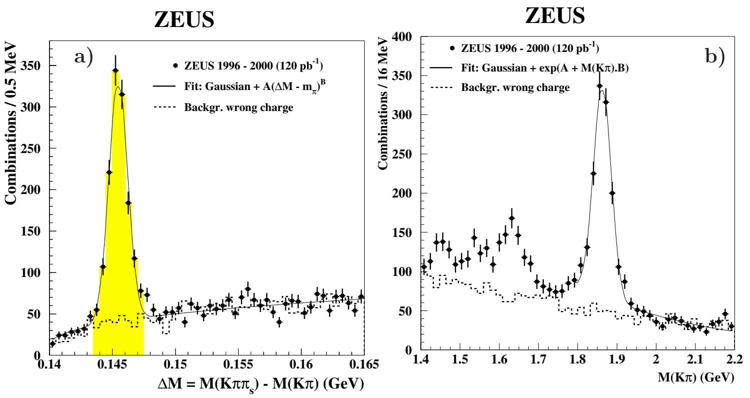

Figure 7.17: *Distribution in a) ΔM and b) $M(D^0)$ showing the right-charge combinations (points) and wrong charge combination (hashed histogram). The shaded area in a) shows the signal region $0.1435 < \Delta M < 0.1475$. The control region is taken to be $0.15 < \Delta M < 0.165$. The solid lines are fits to a Gaussian function plus $A(\Delta M - m_\pi)^B$ in a) and $\exp(A + M(K\pi) \cdot B)$ in b).*

are superimposed on a background of the form:

$$dN/d\Delta M = A(\Delta M - m_\pi)^B$$

for the mass difference ΔM distribution and of the form:

$$dN/dM(K,\pi) = \exp(A + M(K,\pi) \cdot B)$$

for the $M(K,\pi)$ invariant mass distribution. The parameters A and B (where m_π is the pion mass) are determined from the fits. The number of D^* mesons reconstructed in the signal region from the fit is found to be 1084 ± 58, with the following values for the masses:

$$M(D^*) - M(D^0) = 145.6 \pm 0.03 \text{ MeV} \quad \text{and} \quad M(D^0) = 1863.0 \pm 1.04 \text{ MeV},$$

which are found to be very good agreement with the PDG values of $M(D^*) - M(D^0) = 145.436 \pm 0.016$ MeV and $M(D^0) = 1864.5 \pm 0.5$ MeV respectively [75].

For this statistical method, if N_{sr}^{rc} (N_{sr}^{wc}) and N_{cr}^{rc} (N_{cr}^{wc}) are the right (wrong) charge in the signal and control region for each bin of a given observable respectively, the number of reconstructed D^* mesons N_{rec} in that bin, is given by

$$N_{rec} = N_{sr}^{rc} - N_{sr}^{wc} \cdot (N_{cr}^{rc}/N_{cr}^{wc})$$

with the error on N_{rec} estimated as:

$$\sqrt{N_{sr}^{rc} + (N_{sr}^{wc}.N_{cr}^{rc}/(N_{cr}^{wc})^2) \cdot (N_{cr}^{rc} + N_{sr}^{wc} + N_{sr}^{wc}.N_{cr}^{rc}/N_{cr}^{wc})}$$

The total number of reconstructed D^* mesons for the above mentioned sample is given by 1092 ± 43, which is similar to one obtained using the fit, but with a smaller error. In order to verify the method, the data was compared to MC, for both D^* and dijet observables, with the background subtraction done using bin-by-bin subtraction. This comparison is shown in Fig. 7.18. The MC samples from PYTHIA and HERWIG are in reasonable agreement with the data.

The D^* ($p_T(D^*)$, $\eta(D^*)$) and kinematic variable W are well reproduced by the MC simulations, although the underlying physics dynamics associated with the resolved photon processes shows a similar behaviour. The b quarks decaying to charm quarks subsequently forming a D^* meson, can also get reconstructed within the sample. These beauty component are also shown to provide about 10% contribution to this sample. The E_T and η^{jet} distribution of the corrected transverse energy of the jets show a rapid fall off with increasing E_T with a turnover at low values arising due to a cut on its invariant mass $M_{jj} > 18$ GeV (see section 7.1.1). The distribution in pseudorapidity of the jets is peaked in the central region, as a consequence of the cut on the pseudorapidity of the D^*. The confinement of η^{jet} within 1.9 units of pseudorapidity is mainly due to the cut on average pseudorapidity $\bar{\eta}$, which is a consequence of the D^* pseudorapidity cut $|\eta(D^*)| < 1.5$. The vertical lines in the distributions show the confinement region for the jet pseudorapidity.

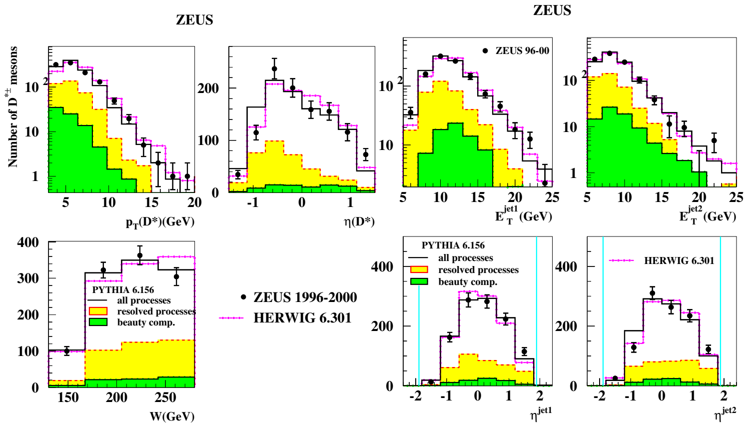

a) b)

Figure 7.18: *Differential data distribution (black dots) compared to results of PYTHIA (solid line) and HERWIG (dotted-dashed line) MC simulation. The distribution for D^* in a) and jet observables in b) are considered. The background is subtracted by performing a bin-by-bin wrong-charge background subtraction method.*

7.3 Definition of Cross Sections

Events with at least one charmed meson $D^{*\pm}$, together with high E_T jets in the processes $ep \to D^{*\pm} + jets + X$ were considered. Using these events, the cross section for the two analyses were measured in the photoproduction regime.

7.3.1 Analysis I

In this analysis, the dijet cross section associated with at least one D^* meson was measured in a region of phase space, where the theoretical uncertainties are expected to be relatively small, and the effect of the photon structure is visible. The differential cross sections sensitive to the hard scattering and the photon structure are

defined as:

$$\frac{d\sigma}{dx_\gamma^{\rm obs}}; \qquad 0 < x_\gamma^{\rm obs} < 1 \tag{7.20}$$
$$\frac{d\sigma}{dx_p^{\rm obs}}; \qquad 0 < x_p^{\rm obs} < 0.044 \tag{7.21}$$
$$\frac{d\sigma}{dM_{jj}}; \qquad 18 < M_{jj} < 50 \tag{7.22}$$
$$\frac{d\sigma}{d\bar\eta}; \qquad -0.7 < \bar\eta < 0.7 \tag{7.23}$$
$$\frac{d\sigma(x_\gamma^{\rm obs} < 0.75)}{dx_p^{\rm obs}}; \qquad 0 < x_p^{\rm obs} < 0.044 \tag{7.24}$$
$$\frac{d\sigma(x_\gamma^{\rm obs} > 0.75)}{dx_p^{\rm obs}}; \qquad 0 < x_p^{\rm obs} < 0.044 \tag{7.25}$$
$$\frac{d\sigma(x_\gamma^{\rm obs} < 0.75)}{d|\cos\theta^*|}; \qquad 0 < |\cos\theta^*| < 0.83 \tag{7.26}$$
$$\frac{d\sigma(x_\gamma^{\rm obs} > 0.75)}{d|\cos\theta^*|}; \qquad 0 < |\cos\theta^*| < 0.83 \tag{7.27}$$
$$\frac{d\sigma(x_\gamma^{\rm obs} < 0.75)}{d\cos\theta^*}; \qquad -0.83 < \cos\theta^* < 0.83 \tag{7.28}$$
$$\frac{d\sigma(x_\gamma^{\rm obs} > 0.75)}{d\cos\theta^*}; \qquad -0.83 < \cos\theta^* < 0.83 \tag{7.29}$$

This was done in the kinematic region defined by the following:

$$\begin{aligned} 130 < W < 280 \text{ GeV}, Q^2 < 1 \text{ GeV}^2; \\ E_T^{jet1,jet2} > 5 \text{ GeV}, |\eta^{jet1,jet2}| < 2.4; \\ M_{jj} > 18 \text{ GeV}, |\bar\eta| < 0.7, |\cos\theta^*| < 0.83; \\ p_T(D^*) > 3 \text{ GeV}; |\eta(D^*)| < 1.5. \end{aligned} \tag{7.30}$$

7.3.2 Analysis II

The Analysis II of charm fragmentation function was studied in the kinematic regime $Q^2 < 1$ GeV^2 and $130 < W < 280$ GeV. The D^* meson was required to be in the pseudorapidity region $|\eta(D^*)| < 1.5$ with transverse momentum $p_T(D^*) > 2$ GeV.

At least one jet was required in the event with transverse energy $E_T^{jet} > 9$ GeV in the pseudorapidity region $|\eta^{jet}| < 2.4$. The D^* meson was included in the jet-finding procedure and was thereby uniquely associated with one jet only. The differential cross section as a function of the fragmentation variable $z = (E+p_{\|})^{D^*}/(E+p_{\|})^{jet} \equiv (E+p_{\|})^{D^*}/(2E)^{jet}$ can be defined as $d\sigma/dz$ for $0.16 < z < 1$, where $p_{\|}$ is the longitudinal momentum of the D^* meson relative to the axis of the associated jet of energy E^{jet}.

Chapter 8

Analysis I : Dijet Angular Distributions in Photoproduction of Charm

In this chapter, the experimental results obtained for the first of the two analyses are presented. Before the results are given, several studies using the Monte Carlo samples used to correct the detector effects are described. The measurement of the corrected observables are compared with predictions from leading-order parton-shower Monte Carlo models and with the next-to-leading-order QCD calculations.

8.1 Description of the Measurements

The aim of this analysis is to study the dynamics of the hard scattering and to probe the structure of the photon, especially its charm content. Photoproduction events were selected with the three-level trigger [93, 104] as described in section 7.2.1. The inclusive photoproduction sample was defined by requiring a reconstructed vertex and no scattered electron (or positron) found in the calorimeter

(CAL), thus restricting the photon virtuality Q^2 to be below 1 GeV^2, with median $Q^2 \approx 3 \cdot 10^{-4}$ GeV^2. The photon-proton centre-of-mass energy W was restricted to the range $130 < W < 280$ GeV. The latter was measured using the Jacquet-Blondel [147] estimator $W_{\rm JB} = \sqrt{4y_{\rm JB}E_eE_p}$, where $y_{\rm JB} = \Sigma_i(E_i - p_{Z,i})/2E_e$, the sum runs over all CAL cells and $p_{Z,i}$ is the Z component of the momentum vector assigned to each cell of energy E_i. Jets were reconstructed with the k_T-cluster algorithm [140] in its longitudinally invariant inclusive mode [142]. The events were required to have at least two jets[1] with pseudorapidity $|\eta^{\rm jet}| < 2.4$ and transverse energy $E_T^{\rm jet} > 5$ GeV. The measured jet energies as well as $W_{\rm JB}$ were corrected for energy losses in the inactive material in front of the CAL using the MC simulation described earlier in section 6.2.1.1.

After the initial event selection mentioned above, the D^* mesons were reconstructed using the mass-difference technique applied to the decay chain $D^{*\pm} \to D^0\pi_S^\pm \to K^\mp\pi^\pm\pi_S^\pm$. Following is a summary of the cuts that were applied to the final event topology (see section 7.2.3 and 7.2.4).

- Photoproduction events with the photon-proton centre-of-mass energy W between $130 < W < 280$ GeV.
- Dijets with $E_T^{\rm jet} > 5$ GeV and $|\eta^{\rm jet}| < 2.4$.
- At least one reconstructed D^* meson with $p_T^{D^*} > 3$ GeV, $|\eta^{D^*}| < 1.5$ within the mass window $0.1435 < \Delta M < 0.1475$ GeV obtained using the (K, π, π_S) system with:

$$\begin{aligned} p_T(K,\pi) &> 0.5 \text{ GeV}, \\ p_T(\pi_S) &> 0.15 \text{ GeV}, \\ 1.81 < M(K\pi) &< 1.92 \text{ GeV} \end{aligned}$$

[1] The fraction of events with more than two jets are found to be 11% in the data, 5.5% in PYTHIA, 9% in HERWIG and 18% in CASCADE.

- To suppress combinatorial background, a cut $p_T^{D^*}/E_T^{\theta>10^\circ} > 0.15$ was applied [82], where $E_T^{\theta>10^\circ}$ is the transverse energy measured in the CAL outside a cone of $\theta = 10^\circ$ in the forward direction.
- $M_{jj} > 18$ GeV is applied in order to study the $|\cos\theta^*| < 0.83$ without any bias from the $E_T^{\rm jet}$ cut.
- The cut on $|\bar{\eta}| < 0.7$, removes the bias due to cut on $\eta^{\rm jet}$ and further reduces the effects due to $|\eta^{D^*}| < 1.5$.

The total number of dijet events with at least one associated D^* meson after all specified cuts, is found to be 1092 ± 43 over a background of 328 events from wrong charge combinations, normalised to the right charge in the control region $0.15 < \Delta M < 0.165$ GeV. Fig. 7.17 shows the ΔM distribution after the final event selection. The signal has similar characteristics as that in the previous ZEUS publication [82] except that the signal to background ratio has improved by a factor of three due to the tighter cuts on M_{jj} and $\bar{\eta}$.

8.1.1 Efficiency of Trigger Chain

The efficiency of the trigger chain needs to be checked before one can compare the data and the Monte Carlo predictions. It is needed in order to ensure that the final events are not affected by any trigger threshold boundaries. This was done by choosing an independent "looser" trigger which subsequently was fed into the rest of the trigger chain instead of the one under study. In the following studies are done for FLT and TLT slots; the SLT slot used was checked in a previous dijet analysis [82]. The SLT slot remained unchanged during the whole course of the data taking period and hence was not considered here.

Efficiency of the FLT42 Trigger

The FLT42 slot was studied by choosing an independent slot FLT59 which was subsequently fed into the SLT and TLT as described. The FLT59 was chosen such that, after the requirement of the observed scattered lepton in the LUMI detector with some low energy calorimeter threshold, it could be directly comparable to FLT42. The efficiency of this slot can then be given by

$$\varepsilon = \frac{\text{number of events passing } \texttt{FLT42 AND FLT 59}}{\text{number of events passing } \texttt{FLT59}}$$

Table 8.1 shows the overall efficiencies for the data compared to the Monte Carlo simulations. It was found that, although the data events represent a higher fraction than the PYTHIA and HERWIG expectations, the ratios are consistent within the given statistical uncertainties (see also Fig. 8.1).

In order to further understand this slot, a detailed study on the efficiency was performed as a function of the kinematic variables. Fig. 8.1 shows the ratio of the efficiencies for data and Monte Carlo simulations as a function of D^* and jet variables. As can be seen for all the plotted variables, the efficiencies measured in data and the two Monte Carlo simulations PYTHIA and HERWIG agree quite well within the given statistical error represented by the shaded and hatched bands respectively.

Efficiency of DST27

The DST slot 27 was extensively studied by considering an independent sample of events which have passed the inclusive dijet trigger DST77. As the two triggers are largely independent, the majority of events passing the DST77 with two high E_T jets will in fact not be due to charm events, thus can provide a largely unbiased sample. Table 8.1 gives the overall measured efficiency in comparison to the expectations from PYTHIA and HERWIG. The overall efficiency for the DST slot 27 was found to be 93%, for $E_T^{jet} > 5$ GeV. The Monte Carlo models describe the efficiency well. The DST slot 27 based on track requirements can have a bias due to the reconstructed D^* candidates contained within the CTD acceptance. The correlation between the jet and track directions will then effectively give rise to an implicit cut on the pseudorapidity on one of the jets. However this effect is taken care of via the cut on $\bar{\eta}$ and is hence acceptable.

It should be mentioned that the k_T-algorithm used for the jet finding has an

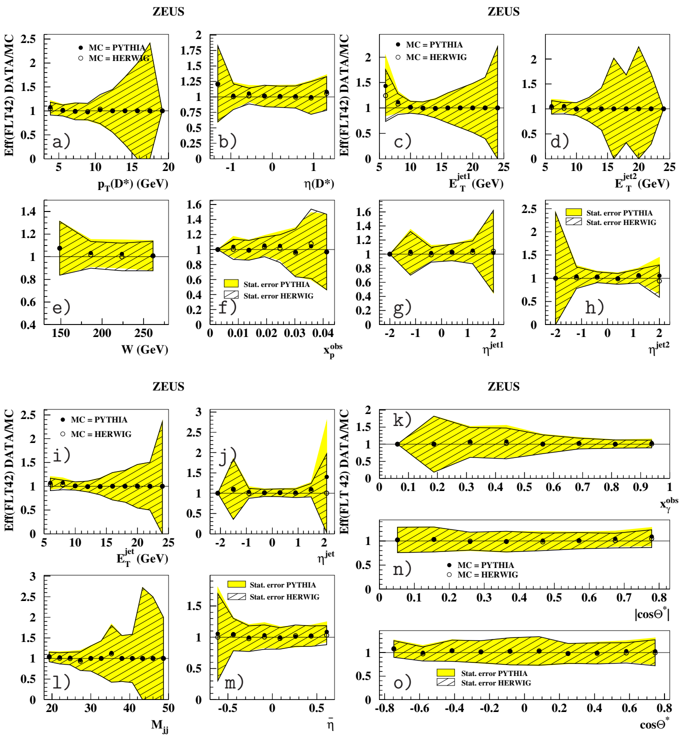

Figure 8.1: *The efficiency of the FLT slot 42 as a function of jet and D^* variables compared to PYTHIA and HERWIG simulations. The shaded region shows the statistical error on the ratio of data over PYTHIA, whereas the hatched region is the same for HERWIG.*

effective cone radius which is smaller than cone-algorithm used at TLT for DST77. This means that the E_T's of the jets using the DST bit 77 are on average higher than those found offline with the k_T-algorithm. Hence, due to this pre-requisite demand on the jets at the TLT level the tracks leading to D^* candidates can get pre-associated with one or the other jet. Therefore, DST77 although quite effective

Trigger Slot (Event frac.)	data	PYTHIA	HERWIG
(FLT42.AND.FLT59)/FLT59	96.18 ± 6.48%	93.72 ± 3.03%	95.35 ± 3.32%
(DST27.AND.DST77)/DST77	93.47 ± 5.57%	93.38 ± 2.62%	94.15 ± 2.92%

Table 8.1: *Overall efficiency of the trigger slots FLT42 and DST 27 for data, compared to the PYTHIA and HERWIG simulations.*

for the dijet studies was only considered for the efficiency checks. Fig. 8.2 shows the efficiency of DST27 as a function of D^* and jet observables. The Monte Carlo simulations agree well compared with the data, within the given statistical uncertainties.

8.1.2 Comparison between the Data and Monte Carlo Predictions

After the efficiency checks, kinematic cuts and various corrections (as described in the previous chapter), the next step is the comparison between the data and detector-level Monte Carlo predictions. The background was determined from the ΔM distribution (see section 7.2.4) for the wrong charge combinations, where the tracks forming the D^0 candidates had the same charge and the π_S had the opposite charge. The number of events in each bin of the measured variables was determined by performing a bin-by-bin wrong-charge background subtraction as outlined in section. 7.2.4. The comparison is then done after the background subtraction for all global variables, including the D^* and jet variables. The quantities compared can be seen in Figs. 8.3 and 8.4, where a number of jet variables are plotted for data and Monte Carlo simulations. The MC samples are normalised to the number of events in the data distribution and hence only a shape comparison is made. The light and dark shaded region corresponds to LO-resolved and beauty contributions in PYTHIA respectively. The fraction of charm dijet events that originates from beauty production is predicted to be ≈ 10% by PYTHIA and ≈ 6% by HERWIG.

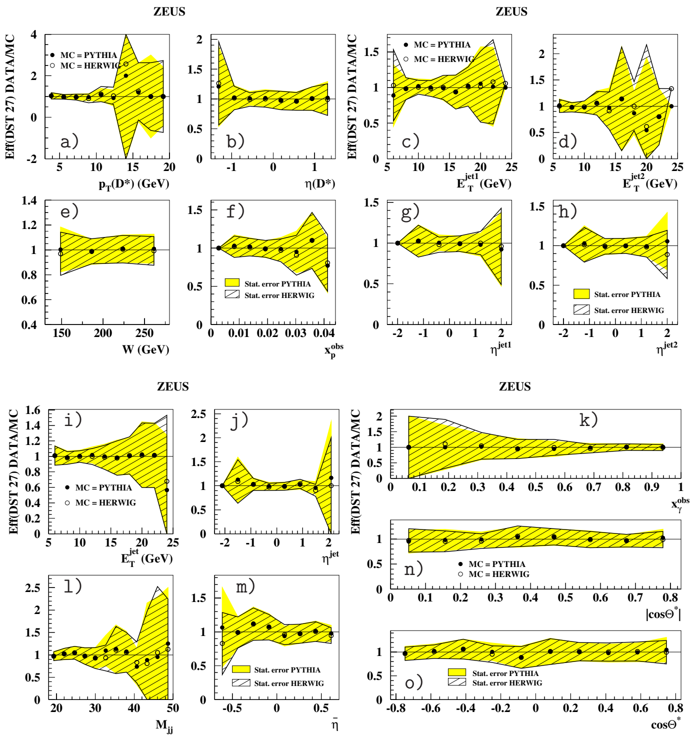

Figure 8.2: *The efficiency ratio of data over MC of the DST bit 27 as a function of jet and D^* variables compared to PYTHIA and HERWIG simulations. The shaded region shows the statistical error on the ratio of data over PYTHIA, whereas the hatched region is the same for HERWIG.*

The shape of the beauty component is similar to that of the overall distribution. All quantities are in reasonable agreement between data and Monte Carlo simulations. Fig. 8.5 shows the differential distribution as a function of $|\cos\theta^*|$ separately for the resolved-enriched ($x_\gamma^{obs} < 0.75$) and direct-enriched ($x_\gamma^{obs} > 0.75$) samples compared to PYTHIA expectations. The data points are given separately for direct-enriched

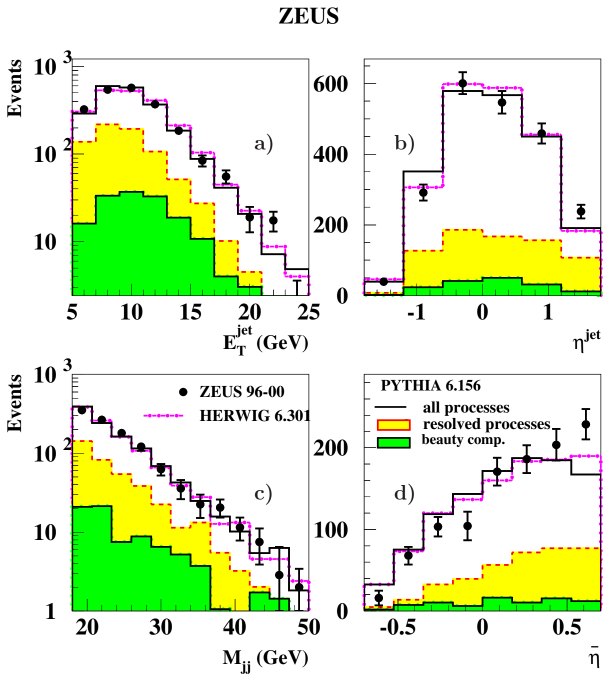

Figure 8.3: *Differential data distributions (black dots) compared to results of the PYTHIA (solid line) and HERWIG (dotted-dashed line) MC simulation. a) E_T^{jet}, b) η^{jet}, c) M_{jj} and d) $\bar{\eta}$. The light and dark shaded regions correspond to LO-resolved and beauty contribution in PYTHIA respectively. The MC samples are normalised to the number of events in the data distributions.*

(open dots) and for resolved-enriched (black dots) events. The direct-enriched sample is normalised to the resolved-enriched sample in the lowest 4 bins. The dashed (full) histogram is the PYTHIA distribution for the direct (resolved) enriched MC events, normalised to the data points.

The two jets are then distinguished into a charm-initiated jet (D^* jet), and the other jet in $\eta-\phi$ space ($\Delta R_i \equiv \sqrt{(\phi_{jet_i} - \phi_{D^*})^2 + (\eta_{jet_i} - \eta_{D^*})^2}$); with D^* jet having

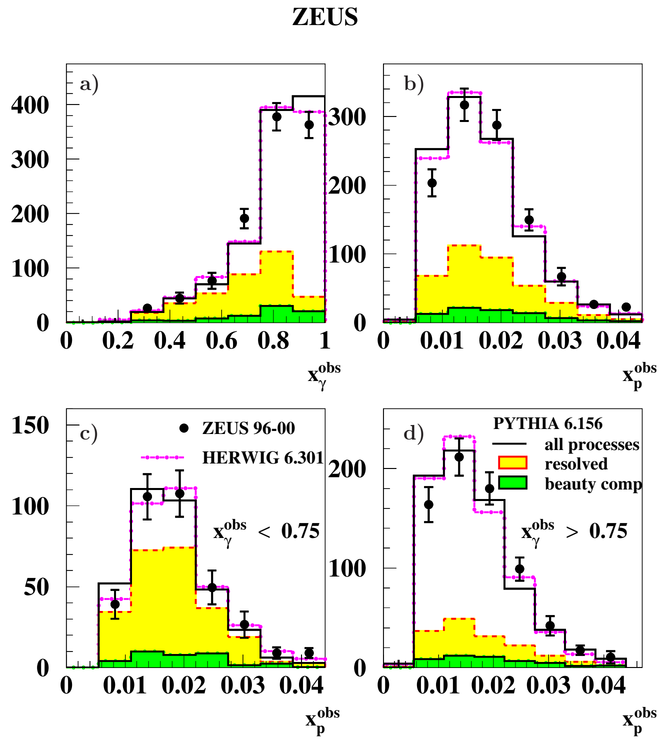

Figure 8.4: *Differential data distributions (black dots) compared to results of the PYTHIA (solid line) and HERWIG (dotted-dashed line) MC simulation. (a) x_γ^{obs}, (b) x_p^{obs}, (c) x_p^{obs} with $x_\gamma^{obs} < 0.75$ and (d) x_p^{obs} with $x_\gamma^{obs} > 0.75$. The light and dark shaded regions correspond to LO-resolved and beauty contribution in PYTHIA respectively. The MC samples are normalised to the number of events in the data distributions.*

the smallest $\Delta R_{i(1=1,2)} < 1.0$. Thus the sign of the unfolded $\cos\theta^*$ distribution is given by the direction of the D^* meson i.e. positive for the proton direction and negative for the photon direction. Fig. 8.6 shows the differential distribution as a function of $\cos\theta^*$ for the resolved- and direct-enriched samples. The direct-enriched

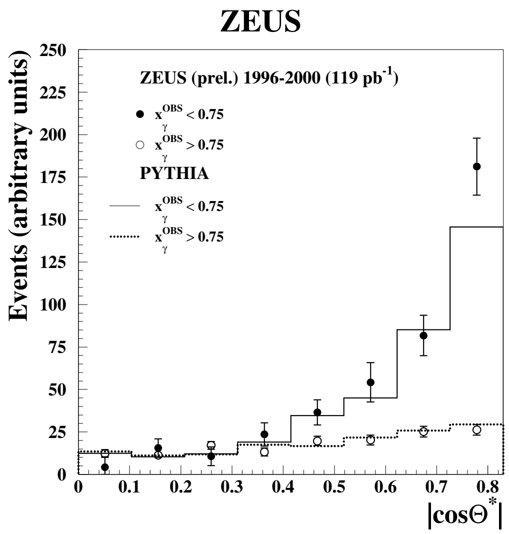

Figure 8.5: *Differential data distributions after wrong charge background subtraction (dots) and of the PYTHIA MC simulations (lines). Results are given separately for the direct-enriched (open dots/dashed lines) and for resolved-enriched (black dots/full histogram) events. All the distributions are normalised to the resolved data distribution in the lowest 4 bins.*

sample is normalised to central 8 bins of the resolved-enriched data sample. The full (dashed) histograms in PYTHIA (HERWIG) are normalised to the data points for the respective direct/resolved enriched contributions. Events that did not satisfy the requirement $R < 1$ for at least one of the two jets (8.7% for $x_\gamma^{\rm obs} < 0.75$ and 1.1% for $x_\gamma^{\rm obs} > 0.75$) were not included in these $\cos\theta^*$ distributions. Clearly a good agreement between data and PYTHIA MC simulations is found except for the last bin (see plots in section 8.2.5), hence PYTHIA is used for the detector to hadron correction. HERWIG, on the other hand, gives an adequate description of the data, although the rise in the differential distribution at low $x_\gamma^{\rm obs}$ is stronger in data, hence it is used only to study the systematic uncertainty on the detector to hadron correction.

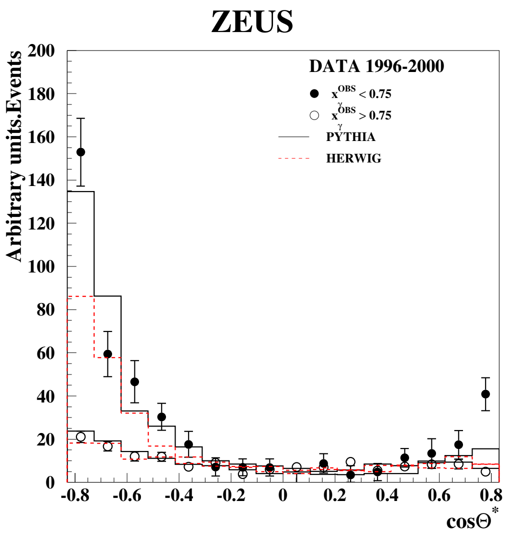

Figure 8.6: *Differential data distributions after wrong charge background subtraction (dots) and of the PYTHIA (full) and HERWIG (dashed lines) MC simulations. Results are given separately for the direct-enriched (open dots) and for resolved-enriched (black dots) events. All the distributions are normalised to the resolved data distribution in the middle 8 bins.*

8.1.3 Studies Using Monte Carlo Samples

As the Monte Carlo simulated events give a reasonable description of the data at the detector level, one can then expect that the underlying physics dynamics at the hadron level (which were passed through the detector simulation to obtain the detector level events) will have the similar feature as those observed in the data. Hence it is appropriate to correct ('unfold') the data for various detector effects, such as geometrical acceptances, detector resolution and efficiency, particle decays, interactions with inactive material and the effects related to the trigger and event selections. Before these corrections are implemented, a proper binning of the data is considered.

Binning the data

For a given observable, it is necessary to choose appropriate bin widths such that the effect of event migrations in and out of the bins can be reduced. The bins in this analysis are initially chosen to be at least twice the resolution, σ, of the relevant variable estimated using the MC simulation. The resolution for all variables under study is shown in Fig. 8.7 both for PYTHIA and HERWIG simulations. The mean $<>$ and the corresponding standard deviation σ for each of the variables is shown on the respective plots. The remarkable agreement between these values for PYTHIA and HERWIG, shows that the detector resolutions are well modelled.

Certain bins are combined either based on the limitation of the data statistics in and around the bin boundaries or due to known large migrations of events from parton to hadron transitions.

Correction from Detector to Hadron Level

Once the bin widths are appropriately defined, then the observables were corrected ('unfolded') for various detector related effects, in order to compare them with the theoretical predictions or with results from other experiments. A bin-by-bin unfolding procedure was performed using PYTHIA in order to avoid long-range migrations. The efficiency ε, purity p and the multiplicative correction factor C, for each bin i, of a given observable $\mathcal{O}^{det}$ at detector level (e,g $x_\gamma^{\rm obs}$, $x_p^{\rm obs}$, $|\cos\theta^*|$, etc.) and $\mathcal{O}^{had}$ at the hadron level are defined by:

$$\varepsilon(i) = \frac{\mathcal{O}^{had}(i) \cap \mathcal{O}^{det}(i)}{\mathcal{O}^{had}(i)}, \tag{8.1}$$

$$p(i) = \frac{\mathcal{O}^{had}(i) \cap \mathcal{O}^{det}(i)}{\mathcal{O}^{det}(i)}, \tag{8.2}$$

$$C(i) = \frac{p(i)}{\varepsilon(i)} = \frac{\mathcal{O}^{had}(i)}{\mathcal{O}^{det}(i)}, \tag{8.3}$$

where $\mathcal{O}^{had}(i) \cap \mathcal{O}^{det}(i)$ is the number of events that pass the hadronic criteria and are then reconstructed such that they pass the data selection cuts in the given bin i. The statistical errors associated with the efficiency $\Delta\varepsilon(i)$ and purity $\Delta p(i)$ are

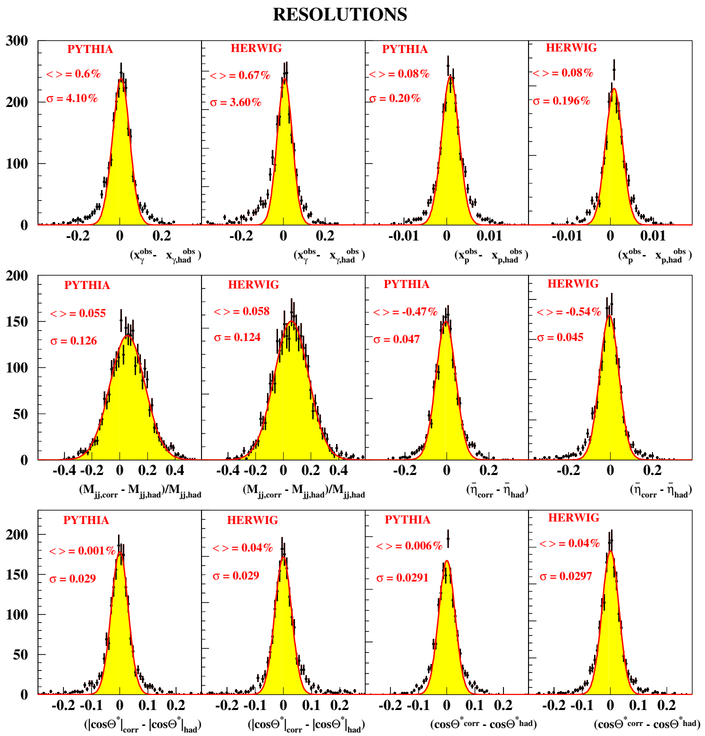

Figure 8.7: *Difference between variables simulated at detector and hadron level for PYTHIA and HERWIG simulations. The distributions are fitted to a Gaussian function at full width half maxima. The corresponding mean $<>$ and the standard deviations σ, are indicated on respective plots.*

given by the binomial expression:

$$\Delta\varepsilon(i) = \sqrt{\frac{[1-\varepsilon(i)]\cdot\varepsilon(i)}{\mathcal{O}^{had}}} \tag{8.4}$$

$$\Delta p(i) = \sqrt{\frac{[1-p(i)]\cdot p(i)}{\mathcal{O}^{det}}}. \tag{8.5}$$

The error $\Delta C(i)$ on the correction factor, taking into account the correlations between $\mathcal{O}^{had}(i)$ and $\mathcal{O}^{det}(i)$, can be written as:

$$\Delta C(i) = \sqrt{\frac{\mathcal{O}^{had}(i)}{\mathcal{O}^{det}(i)^3}[\mathcal{O}^{had}(i) + \mathcal{O}^{det}(i) - 2\mathcal{O}^{had}(i) \cap \mathcal{O}^{det}(i)]} \tag{8.6}$$

The efficiency $\varepsilon(i)$ can be regarded as the fraction of the hadron level events in a given bin which are also reconstructed in that bin, whereas the purity as the fraction of events reconstructed in a given bin which are also generated in that bin.

Fig. 8.8 and Fig. 8.9 show the efficiency, purity and correction factor as a function of observables that are of interest to this analysis. Although the efficiency is reasonably flat, the purity rises with the increasing dominance of direct photon events. These direct photon dijet events with the D^* requirements are harder than the resolved photon ones, where one of the jets is expected to be initiated via a gluon. This leads to more calorimetric reconstructed jets for high $x_\gamma^{\rm obs}$ above a certain threshold that are also above the same hadronic threshold. Thus, for the resolved dominated samples $x_\gamma^{\rm obs} < 0.75$, Fig. 8.8 `d)` and Fig. 8.9 `c)` and `e)`, the purity is found to be slightly lower. It should be noted that there is a slight decrease in efficiency for Fig. 8.9 `b)`, `c)`, `d)` and `e)` at the extreme bins. This can be accounted for by the "edge effects" due to the hard cuts introduced on the $\cos\theta^*$ distribution. The correction factor calculated for each bin, on the other hand shows a reasonably flat distribution for all variables under interest.

To obtain differential cross sections, each observable was multiplied by the corresponding correction factor proportional to the ratio of generated to reconstructed events from the PYTHIA MC simulation. Although to a good approximation these correction factors should be independent of the event generators used, a residual influence can remain. Therefore, even if PYTHIA was used to compute the correction factor in the unfolding process, HERWIG computed corrections was later on used into the estimation of the total systematic error on the final measurements. The differential cross section $\sigma(i)$, for a given observable $x(i)$ with the number of events passing the selection cuts after background subtraction $N(i)$ in a given bin i, can be given by:

$$\frac{d\sigma(i)}{dx(i)} = \frac{N(i) \cdot C(i)}{\int dt\mathcal{L} \cdot [\text{Bin width}] \cdot \text{BR}} \tag{8.7}$$

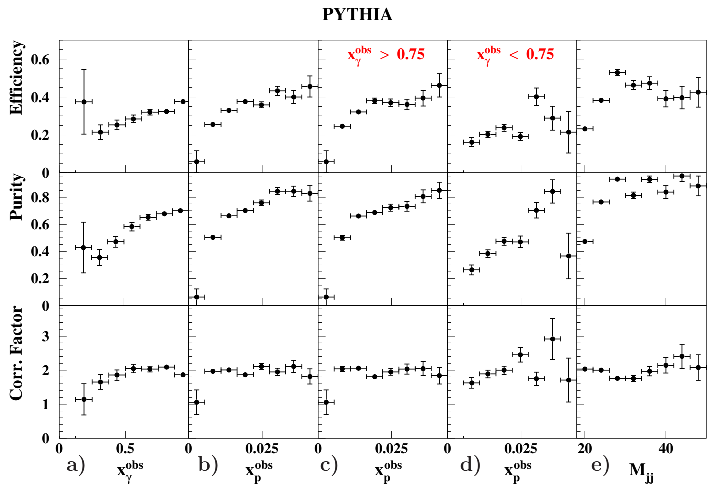

Figure 8.8: *Efficiency, purity and correction factors shown for the unfolding procedure as a function of a) $x_\gamma^{\rm obs}$, b) $x_p^{\rm obs}$, c) $x_p^{\rm obs}$ with $x_\gamma^{\rm obs} > 0.75$, d) $x_p^{\rm obs}$ with $x_\gamma^{\rm obs} < 0.75$ and e) M_{jj}.*

where $\int dt\mathcal{L}$ is the integrated luminosity for a given data taking period and BR is the branching ratio of the process $D^{*\pm} \to D^0\pi_S^\pm \to K^\mp\pi^\pm\pi_S^\pm$. The measured cross sections are the luminosity-weighted average of the cross sections at the centre-of-mass energies $\sqrt{s} = 300$ GeV and $\sqrt{s} = 318$ GeV.

8.1.4 Study of the Systematic Uncertainties

In order to estimate the sensitivity of the measured cross section to potential sources of systematic error, several checks have been performed. Most of these uncertainties come from the incomplete knowledge of detector effects, definitions used and methods used to analyse the data. The following are four major classes of uncertainty that were considered and are assumed to be approximately independent:

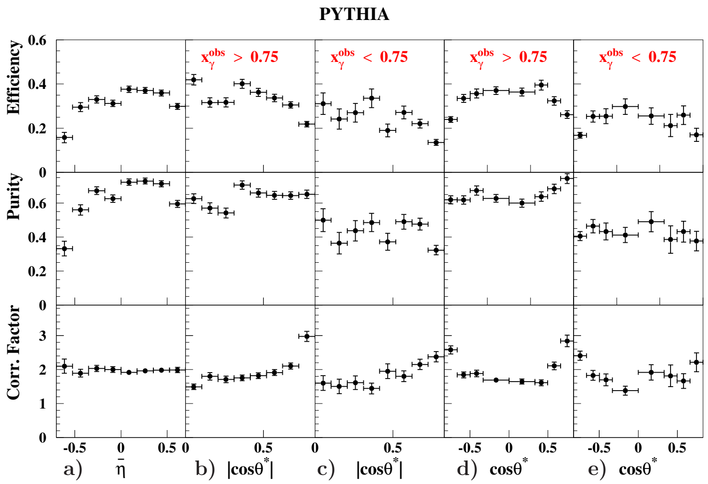

Figure 8.9: *Efficiency, purity and correction factors shown for the unfolding procedure as a function of a) $\bar{\eta}$, b) $|\cos\theta^*|$ with $x_\gamma^{\rm obs} > 0.75$ c) $|\cos\theta^*|$ with $x_\gamma^{\rm obs} < 0.75$ d) $\cos\theta^*$ with $x_\gamma^{\rm obs} > 0.75$ and e) $\cos\theta^*$ with $x_\gamma^{\rm obs} < 0.75$.*

Uncertainty arising from kinematic cuts: These have been investigated by varying the cuts given in section 8.1 on the reconstructed variables in the data and PYTHIA simulations.

- the cuts on the γp centre-of-mass energy were varied by approximately $\pm 1\sigma$ of its resolution i.e $138 < W < 264$ GeV and $122 < W < 296$ GeV.
- the cuts on E_T of the jet were lowered to $E_T > 4$ GeV, and raised to $E_T > 6$ GeV.
- the cut on the dijet invariant mass of the dijet, M_{jj}, was varied by $\pm 20\%$, which is the difference between the hadron to the detector level PYTHIA estimation.
- the cuts on average pseudorapidity $\bar{\eta}$ were lowered to $-0.65 < \bar{\eta} < 0.75$ and raised to $-0.75 < \bar{\eta} < 0.65$.

- similar variation on the jet pseudorapidity η^{jet}, between $-2.3 < \eta^{jet} < 2.5$ and between $-2.5 < \eta^{jet} < 2.3$.

Uncertainties associated with the Monte Carlo dependence:

- the HERWIG Monte Carlo was used for the unfolding procedure.
- the resolved photon fraction was increased from 35% up to 55% of the PYTHIA estimation.

Uncertainty due to the calorimeter energy scale:

The calorimetric measured quantities like transverse jet energy E_T and γp center-of-mass energy W were varied (only in the Monte Carlo samples) by $\pm 3\%$ according to the estimated uncertainty on the calorimeter energy scale as outlined in section 6.2.1.2.

Uncertainties arising from D^* cuts and background subtraction:

- the cut on $p_T(\pi_S)$ was lowered to $p_T(\pi_S) > 0.125$ GeV and raised to $p_T(\pi_S) > 0.175$ GeV.
- the cut on $p_T(K,\pi)$ was lowered to $p_T(K,\pi) > 0.475$ GeV and raised to $p_T(K,\pi) > 0.525$ GeV.
- $p_T^{D^*}/E_T^{\theta>10^\circ}$ cut was varied $\pm 1\sigma$ of its resolution.
- a softer cut on D^0 and wider ΔM mass window with $1.80 < M(D^0) < 1.93$ GeV and $0.143 < \Delta M < 0.148$ GeV was used to check the effect on the increase in the background, which must be subtracted from the peak.
- the control region (CR) for the track combination was varied between $0.152 < CR < 0.165$ GeV and between $0.15 < CR < 0.163$ GeV. This check was used to see the stability of the normalisation used for the wrong charge background to be subtracted from the signal.

For each of the changes outlined above, the analysis was repeated and the observed difference in the cross section was then considered as the systematic uncertainty coming from the corresponding aspect of the variation. Figs. B.1-B.10 show the effect of the systematic uncertainties associated with each of the above mentioned variations for the observable under study. To obtain the total systematic uncertainty, all the systematic uncertainties are added in quadrature for each bin. The total experimental uncertainties which are the sum of the contribution from statistical and systematic uncertainties added in quadrature, are shown in corresponding cross section distributions as the outer error bars, whereas the inner error bars correspond to the statistical uncertainty.

It should be mentioned that the uncertainties due to the knowledge of the CAL energy scale ($\pm 3\%$) are highly correlated between bins and are therefore shown separately as two dashed-dotted lines. The variation of the jet energy scale is less than 11% for all analysis bins. The dominant sources of the systematic uncertainty on the cross sections are due to the variation of the M_{jj} cut based on its resolution, cuts on W and the difference between the correction factors evaluated using HERWIG rather than PYTHIA. Statistical uncertainties dominate over systematic uncertainties in most bins. The measured cross sections and their uncertainties are given im Tables A.1-A.7. An overall normalisation uncertainty of 1.6%, arising from the luminosity determination, is not included.

8.2 Cross section Measurements

After having studied the issues of the various systematic uncertainties, the results with combined systematic errors are shown for each observable in the following subsections. As mentioned previously, the following measurements are done in order to not only study the various aspects of hard scattering but also to probe the structure of the photon, especially its charm content. In the following, each aspect of the hard scattering will be addressed, based on the measurements and the comparison to specific theoretical models. Conclusions related to either data alone or to the

model-initiated issues will be drawn.

8.2.1 Measurement of $x_\gamma^{\rm obs}$

The variable $x_\gamma^{\rm obs}$ is related to the momentum fraction of the parton from the photon, which according to Eq. 7.9 is defined as the fraction of the photon's energy participating in the production of the two highest transverse energy jets. The differential cross section as a function of $x_\gamma^{\rm obs}$ is shown in Fig. 8.10. The inner error bars show the statistical uncertainty, while the outer ones show the statistical and systematical uncertainties added in quadrature. The jet energy scale uncertainty is given by the two dashed-dotted lines. The data has not only a significant cross section at high

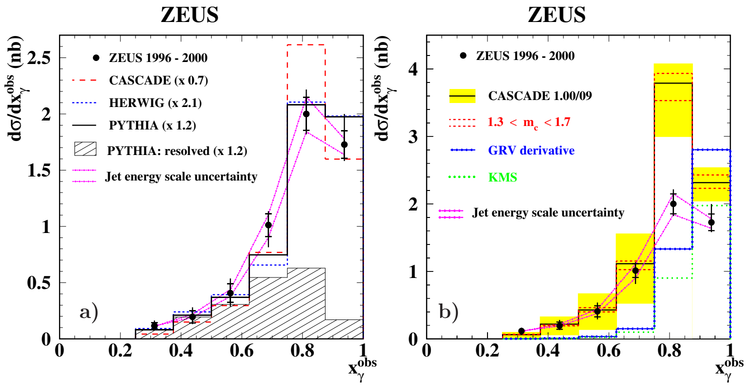

Figure 8.10: *Differential cross section $d\sigma/dx_\gamma^{\rm obs}$ for the data (dots) compared with a) various MC simulations (histograms); b) CASCADE predictions (full line), with various CASCADE related systematics (also see text) as indicated on the plot. The inner error bars show the statistical uncertainty, while the outer ones show the statistical and systematical uncertainties added in quadrature. The jet energy scale uncertainty is given by the two dashed-dotted lines.*

fraction of $x_\gamma^{\rm obs}$, but there is also a substantial tail at low $x_\gamma^{\rm obs}$ which, from Fig. 8.10 a), requires a LO-resolved component to describe the data. The sizeable contribution of the LO-resolved photon component is found to be $35.19 \pm 0.93\%$ in PYTHIA and $22.25 \pm 0.88\%$ in HERWIG. The contribution of events which are not due to 'charm excitation' in the photon[2] is found to be less than $\pm 1\%$ both in PYTHIA and HERWIG. Fitting the MC distribution to the data and allowing the resolved and direct contribution to vary independently result in a resolved contribution of $46.25 \pm 3.66\%$ for PYTHIA and $29.43 \pm 3.04\%$ for HERWIG.

The shape of the distribution is well reproduced by PYTHIA and HERWIG with an absolute normalisation factor of 1.2 and 2.1, respectively needed to describe the data. It should be noted that the LO-resolved photon contribution not only dominates at low $x_\gamma^{\rm obs}$ region, but extends up to the high $x_\gamma^{\rm obs}$. Based on these dominant regions for LO-resolved and LO-direct a cut on $x_\gamma^{\rm obs}$ with $x_\gamma^{\rm obs} < 0.75$ defined as resolved-enriched and $x_\gamma^{\rm obs} > 0.75$ as direct-enriched were considered. The $x_\gamma^{\rm obs}$ distribution of CASCADE, normalised to the data, with the normalisation factor shown in the parentheses within the figures, gives a larger contribution at high $x_\gamma^{\rm obs}$ and a smaller contribution at low $x_\gamma^{\rm obs}$.

Since there is a hope [156] that higher-order corrections to k_t-factorised calculations might be smaller than those to LO parton-shower calculations using DGLAP evolution, the absolute predictions from CASCADE for the differential cross section is shown in Fig. 8.10 b). As can be seen, CASCADE gives a very good description for the low $x_\gamma^{\rm obs}$ tail, but is too high for the 'collinearly'-defined direct photon region. Thus it can be concluded that the semi-hard or k_T-factorization approach in CASCADE with the CCFM unintegrated gluon density obtained by fitting to the HERA data [107], effectively simulates heavy quark excitation and indeed the hardest p_t emission frequently comes from a gluon in the initial state gluon cascade. The GRV derivative[3] and KMS [158] unintegrated gluon densities within CASCADE on the other hand give distribution similar to the 'collinearly'-defined direct photon region and hence cannot describe the data. The largest uncertainty on the CASCADE predicted differential cross section is found to be a maximum of $\pm 71\%$ (shown by

[2] These are the events where the parton from the photon is not a charmed parton.
[3] The GRV derivative is taken from a standard integrated gluon density [157].

shaded region in Fig. 8.10 b)), due to the variation on the maximum allowed angle η_{max}, for any gluon emission, twice and half of its nominal value in comparison to a maximum of $\pm 11\%$ obtained by changing the charm mass m_c between 1.3 GeV and 1.7 GeV.

It should be noted that there is a significant reduction in the resolved enriched photon events in comparison to [148], due to the hard cuts introduced on M_{jj} and $\bar{\eta}$.

8.2.2 Measurement of $x_p^{\rm obs}$

The differential cross section as a function of $x_p^{\rm obs}$ is shown in Fig. 8.11. $x_p^{\rm obs}$ (from Eq. 7.10) in its functional form is complementary to $x_\gamma^{\rm obs}$ and is defined as the fraction of the proton momentum contributing to the production of the two highest E_T jets. The data shown in Fig. 8.11 a) show a rise in distribution with decreasing $x_p^{\rm obs}$, with a slight fall in the first bin. The slight fall of for $x_p^{\rm obs} < 0.011$ is a result of the kinematic cuts, mainly on W. The $x_p^{\rm obs}$ range of the data is concentrated in the region $0.0055 < x_p^{\rm obs} < 0.044$, where the proton PDFs are well constrained/determined. PYTHIA and HERWIG give a good description of the shape. Although the hatched region indicating the LO-resolved PYTHIA contribution is dominant at the higher $x_p^{\rm obs}$ region, it is however similar in shape to the 'rest' of the contribution. Hence, $x_p^{\rm obs}$ cannot be used to separate the above mentioned subprocesses. CASCADE, as shown in Fig. 8.11 b) compared to the data, also gives a good description of the shape, but is too high for the low $x_p^{\rm obs}$ region while consistent within errors for the high $x_p^{\rm obs}$ in normalisation. The unintegrated gluon densities, GRV derivative and KMS within CASCADE are inadequate for describing the data both in shape and normalisation.

As the distinctive nature of the $x_p^{\rm obs}$ distribution allows to separate the gluon and the heavy/light quark from the proton, an attempt has been made to separate the $x_p^{\rm obs}$ distributions for both resolved enriched and direct enriched photon processes. Fig. 8.12 shows such distributions for samples with $x_\gamma^{\rm obs} < 0.75$ and $x_\gamma^{\rm obs} > 0.75$ as

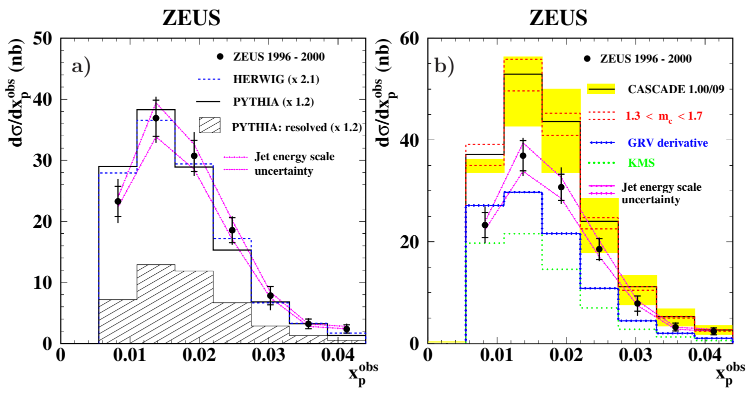

Figure 8.11: *Differential cross section $d\sigma/dx_p^{\rm obs}$ for the data (dots) compared with a) various MC simulations (histograms); b) CASCADE predictions (full line), with various CASCADE related systematics as indicated on the plot. The inner error bars show the statistical uncertainty, while the outer ones show the statistical and systematical uncertainties added in quadrature. The jet energy scale uncertainty is given by the two dashed-dotted lines.*

a function of $x_p^{\rm obs}$. The shapes of data distribution for these two samples shown in Fig. 8.12 a),b) are slightly different. PYTHIA and HERWIG can reproduce the shape reasonably well. The individual shapes for LO-direct and LO-resolved subprocesses in the residual part of the $x_\gamma^{\rm obs}$ separated regions, are shown as the light shaded region (LO direct) in $x_\gamma^{\rm obs} > 0.75$ Fig. 8.12 a) and dark shaded (LO-resolved) regions in $x_\gamma^{\rm obs} < 0.75$ Fig. 8.12 b) respectively.

The CASCADE results shown in Fig. 8.12 c) give a very good description for the low $x_\gamma^{\rm obs}$ region as a function of $x_p^{\rm obs}$. The largest uncertainty on the prediction is due to the variation of η_{max} is found to be a maximum of $\pm 83\%$, whereas the uncertainty due to the charm mass variations is $\pm 14\%$. This indicates that the higher order corrections in the k_T-factorisation approach can be large, especially at resolved-enriched low $x_\gamma^{\rm obs}$ region. The GRV derivative and KMS parton densities can neither describe the shape nor the normalisation of the distribution. For $x_\gamma^{\rm obs} > 0.75$ shown in Fig. 8.12 d) CASCADE overestimates the data by an average factor of

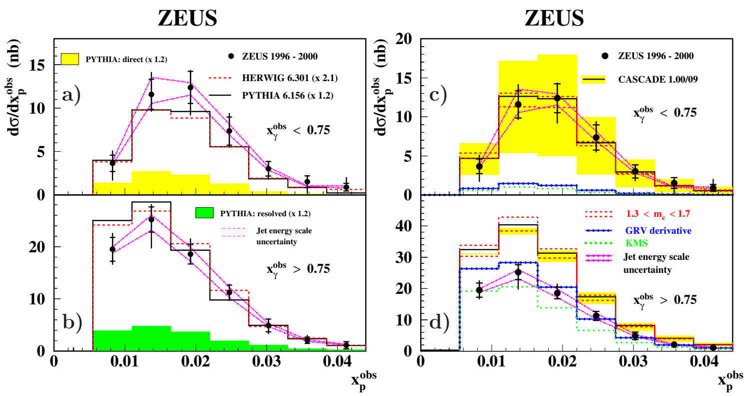

Figure 8.12: *Differential cross section $d\sigma/dx_p^{\rm obs}$ for the data (dots) compared with a-b) various MC simulations (histograms); c-d) CASCADE predictions (full line), with various CASCADE related systematics as indicated on the plot. Results are given separately in a,c) for samples enriched in resolved photon events and in b,d) for samples enriched in direct photon events. The inner error bars show the statistical uncertainty, while the outer ones show the statistical and systematical uncertainties added in quadrature. The jet energy scale uncertainty is given by the two dashed-dotted lines.*

≈ 1.6 in all regions of $x_p^{\rm obs}$, although it can describe the shape relatively well. The uncertainty due to η_{max} variation ($\pm 24\%$) and charm mass variation ($\pm 7\%$) are found to be smaller than at low $x_\gamma^{\rm obs}$ region. The GRV derivative and KMS parton densities can roughly describe this region of the data both in shape and normalisation.

8.2.3 Measurement of M_{jj}

In hadronic interactions, the distribution of the dijet mass M_{jj} provides a test of QCD. At high M_{jj} values, the theoretical uncertainties due to hadronisation, multi-partonic interactions and the limited knowledge of the photon and parton densities are expected to be reduced. Hence, the main influence on the distribution should directly come from the dynamics of the hard scattering. This should permit a pre-

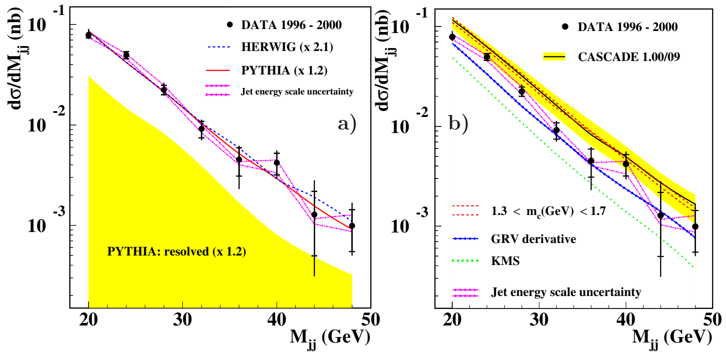

Figure 8.13: *Differential cross section $d\sigma/dM_{jj}$ for the data (dots) compared with a) various MC simulations (histograms); b) CASCADE predictions (full line), with various CASCADE related systematics as indicated on the plot. The inner error bars show the statistical uncertainty, while the outer ones show the statistical and systematical uncertainties added in quadrature. The jet energy scale uncertainty is given by the two dashed-dotted lines.*

cise test of the description of the dynamics of dijet photoproduction associated with at least one charmed D^* meson, to a smaller distance than ever previously studied with charm. The cross section $d\sigma/dM_{jj}$ measured in the M_{jj} range between 18 and 50 GeV is presented in Fig. 8.13. The data points are located at the mean of each M_{jj} bin. The measured $d\sigma/dM_{jj}$ distribution exhibits a steep fall-off over 2 orders of magnitude in the M_{jj} range considered.

PYTHIA and HERWIG can describe the shape of the measured $d\sigma/dM_{jj}$ well, as shown in Fig. 8.13 a) over the entire range of M_{jj}. The shape of the LO-resolved photon contribution, shown by the shaded region in Fig. 8.13 a), exhibits a much steeper fall than the data. As M_{jj} increases the jets become harder, which leads to the high $x_\gamma^{\rm obs}$ values along with a decrease in parton-parton interactions, at the end the entire contribution mainly arises from the photon-parton interactions, where the photon acts as a point like particle. Hence the high M_{jj} region is mainly dominated by the LO-direct photon processes. PYTHIA shows a more steeply falling

distribution than the HERWIG predictions.

CASCADE with off-shell matrix elements for the hard scattering overestimates the data distribution (see Fig. 8.13 b)) but gives a reasonable description of the shape. CASCADE with the GRV derivative and KMS unintegrated gluon densities can describe the shape relatively well, except at low M_{jj} values. The CASCADE predictions using KMS gluon density are below the data for all bins whereas the predictions with GRV are consistent at high M_{jj} and are lower than data at low M_{jj} region. The uncertainty due to η_{max} and charm mass variation of the CASCADE prediction are less than $\pm 36\%$ and $\pm 10\%$ respectively.

8.2.4 Measurement of $\bar{\eta}$

The cross section as a function of $\bar{\eta} = (\eta^{jet1} + \eta^{jet2})/2$ has maximal sensitivity to the parton distributions in both the photon and proton [159]. With the constraint that the direct photon processes are dominated via PGF, the photon and proton PDF dependence on the resolved photon processes can then be studied using this observable. Fig. 8.14 shows the differential cross section as a function of $\bar{\eta}$. The cross section rises from around 0.06 nb per unit of pseudorapidity at $\bar{\eta} = -0.6$ to around 0.8 nb per unit of pseudorapidity for $\bar{\eta} \approx 0.7$. The PYTHIA and HERWIG MC predictions can describe the shape of the data as shown in Fig. 8.14 a). The LO-resolved photon process increases with increase in the average pseudorapidity $\bar{\eta}$.

The comparison with CASCADE shown in Fig 8.14 b) on the other hand is found to be higher in almost all the measured regions, except at the extreme bins, where is agrees with the data within the given uncertainties. The unintegrated gluon densities GRV derivative and KMS within CASCADE are consistent for $\bar{\eta} < 0$ and are found to be below the data for $\bar{\eta} > 0$, where the 'collinearly'-defined resolved photon processes dominate. It should be noted that this is the same region from Fig. 8.10, where CASCADE agrees quite well with the data as a function of $x_\gamma^{\rm obs}$. The uncertainties related to CASCADE are quite large for $\bar{\eta} > 0$, corresponding to

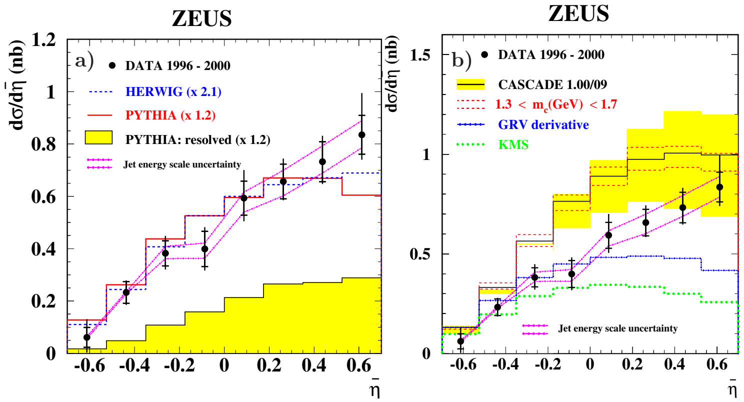

Figure 8.14: *Differential cross section $d\sigma/d\bar{\eta}$ for the data (dots) compared with a) various MC simulations (histograms); b) CASCADE predictions (full line), with various CASCADE related systematics as indicated on the plot. The inner error bars show the statistical uncertainty, while the outer ones show the statistical and systematical uncertainties added in quadrature. The jet energy scale uncertainty is given by the two dashed-dotted lines.*

the high sensitivity towards the photon PDF. The uncertainties due to variation of η_{max} to half and twice its value, are found to be less than $\pm 31\%$, whereas are less than $\pm 8\%$ for the variation in charm mass between 1.3 to 1.7 GeV. In general, data shows a rise in distribution towards higher average pseudorapidity.

8.2.5 Dijet Angular Distributions in $D^{*\pm}$ Photoproduction

Further studies were made to probe more directly the production mechanism. The angular distribution of outgoing partons in a hard partonic process was considered to study the parton dynamics of the underlying sub-processes. In leading order (LO) QCD these underlying sub-processes (Fig. 8.15) can be divided into either direct photon or resolved photon processes. In direct photon processes the photon participates in the hard scatter predominantly via the boson-gluon fusion process.

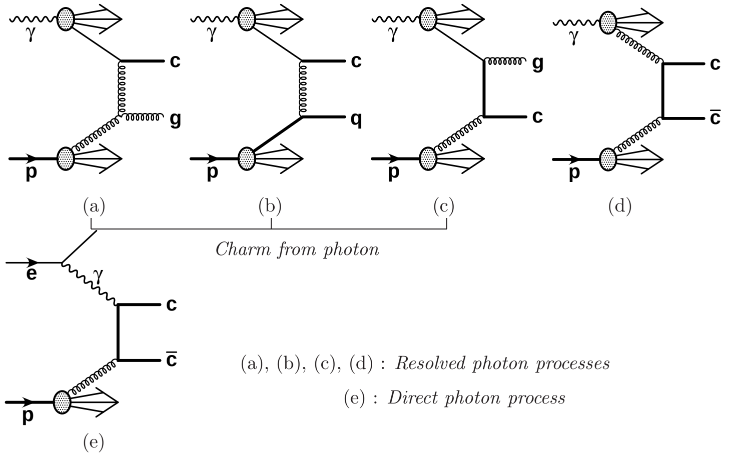

Figure 8.15: *Various LO sub-processes with charm, dominant in the HERA region of phase space.*

This process has a quark as the propagator in the hard interaction (Fig. 8.15 (e)). In resolved photon processes the photon acts as a source of incoming partons (quarks and gluons) and only a fraction of its momentum participates in the hard scatter. In this case both quark and gluon propagators are possible (Fig. 8.15 a)-d)).

In order to probe the charm dynamics in these sub-processes and in particular to study the charm content of the photon, the differential cross section $d\sigma/d|\cos\theta^*|$, (Fig. 8.16 a)-b)) as a function of $|\cos\theta^*|$ was measured, where θ^* is the angle between the jet-jet axis and the beam direction in the dijet rest frame. The distribution was measured for direct-enriched ($x_\gamma^{\mathrm{obs}} > 0.75$) and resolved-enriched ($x_\gamma^{\mathrm{obs}} < 0.75$) samples. The cross section for the sample enriched in resolved photons exhibits a more rapid rise towards high values of $|\cos\theta^*|$ than does the cross section for the sample enriched in direct photon. The measured differential cross section for both of these samples in comparison to the LO partonic matrix elements reflects the different spins of the dominant diagrams with quark and gluon propagators. Consequently the subprocess $gg \to c\bar{c}$ (8.15 d)) cannot be the dominant resolved photon process

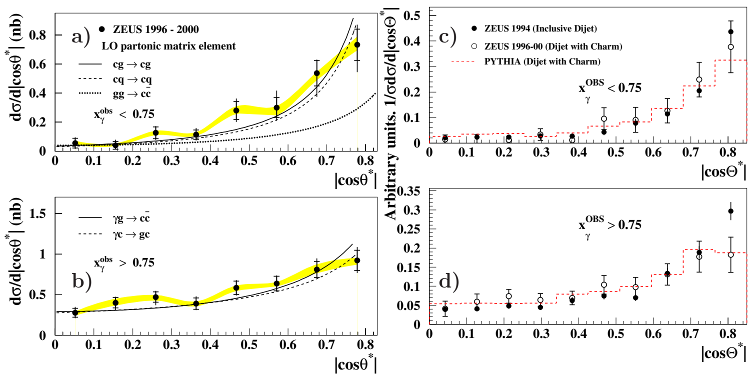

Figure 8.16: *Differential cross section $d\sigma/d|\cos\theta^*|$ for the data (dots) are compared to leading-order $2 \to 2$ matrix element with at least a charm in the final state in a)-b) and to the inclusive dijet data sample [64] c)-d), which did not require the presence of charm. Results are given separately in a),c) for samples enriched in resolved photon events and in b),d) for samples enriched in direct photon events. In a),b) the inner error bars show the statistical uncertainty, while the outer ones show the statistical and systematical uncertainties added in quadrature. The jet energy scale uncertainty is given by the shaded band. For c),d) the analysis was repeated in the phase space reported in [64], only statistical errors are shown.*

for charm dijet events. The partonic matrix element distributions are normalised at the first bin, in order to perform a shape comparison as shown in Fig. 8.16 a)-b).

In order to compare the cross section to the previously reported measurement on inclusive dijet angular distributions, which did not require the presence of charm, the analysis was repeated in the phase space given by [64]. The comparison between the two data samples for resolved and direct-enriched regions is shown in Fig. 8.16 c)-d). Only the statistical errors are shown for the charm dijet events. The two measured cross sections agree quite well in shape. Although PYTHIA agrees well with the charm data, there is a slight decrease in cross section in the extreme bin for $x_\gamma^{\rm obs} > 0.75$ in comparison to the inclusive dijet sample. This is due to the cut

on the pseudorapidity $\eta^{D*} < 1.5$ of D^*, which reduces the η^{jet} range.

Independent of any model assumption, according to the Rutherford scattering for a $q-$exchange diagram, the cross section $(d\sigma/d|\cos\theta^*| \approx (1-|\cos\theta^*|)^{-1})$ should show a mild rise, whereas for a $g-$exchange diagram a steep rise $(d\sigma/d|\cos\theta^*| \approx (1-|\cos\theta^*|)^{-2})$ is expected. To quantify this rise, the measured cross section for both direct and resolved enriched samples were fitted to a function $1/(1-|\cos\theta^*|)^{\kappa}$. The resultant values of κ are:

$$\kappa(x_\gamma^{\rm obs} < 0.75) = 1.74 \pm 0.18\ (\text{stat})\ ^{+0.09}_{-0.11}\ (\text{syst.});$$

$$\kappa(x_\gamma^{\rm obs} > 0.75) = 0.74 \pm 0.11\ (\text{stat})\ ^{+0.07}_{-0.03}\ (\text{syst.})$$

The statistical errors were evaluated by varying the χ^2 by 1 unit, and the systematic errors by refitting the distribution for each systematic change and then taking the difference to the central value, added in quadrature. Given the fact that the shapes are expected to be distorted due to the additional parton shower and hadronisation corrections, the results are consistent with the Rutherford scattering expectations, for a dominant gluon and quark exchange diagrams for the resolved-enriched and direct-enriched samples, respectively. This indicates that the dominant mechanism for direct photon-like events proceeds via $q-$exchange, while resolved photon-like events are dominated by $g-$exchange.

The shapes of the $|\cos\theta^*|$ distributions shown in Fig. 8.17 a)-b) are well reproduced by PYTHIA. The HERWIG predictions give an adequate description of the shape in the data, although the rise in the cross sections for low $x_\gamma^{\rm obs}$ is stronger in the data. The comparison to the CASCADE predictions in Fig. 8.17 c)-d), shows an excellent agreement with the data for low $x_\gamma^{\rm obs} < 0.75$ region, with a large uncertainties less than $\pm 61\%$ for the η_{max} variation and $\pm 17\%$ for the variation in charm mass. The GRV derivatives and KMS unintegrated gluon densities cannot describe the low $x_\gamma^{\rm obs}$ region neither in shape nor in normalisation. In the high $x_\gamma^{\rm obs} > 0.75$ region, the central CASCADE prediction is higher than the data, although it can reproduce the shape relatively well. The GRV derivative and KMS gluon densities are consistent with data both in shape and normalisation for this region, although

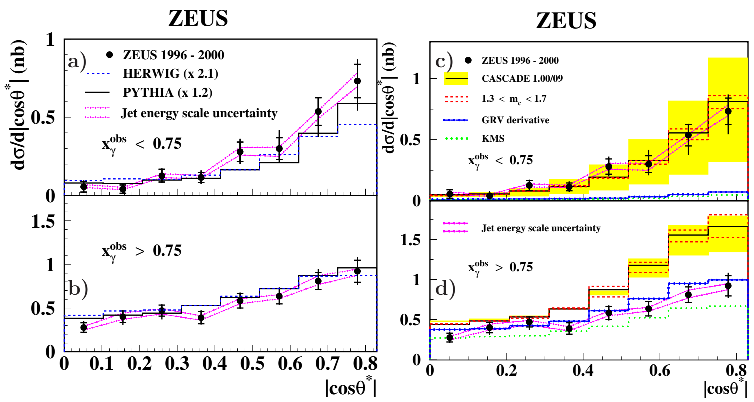

Figure 8.17: *Differential cross sections as a function of $|\cos\theta^*|$ (dots) compared with a)-b) PYTHIA and HERWIG MC simulations (histograms); c)-d) CASCADE predictions (full line), with various CASCADE related systematics as indicated on the plot. Results are given separately in a),c) for samples enriched in resolved photon events and in b),d) for samples enriched in direct photon events. The inner error bars show the statistical uncertainty, while the outer ones show the statistical and systematical uncertainties added in quadrature. The jet energy scale uncertainty is given by the two dashed-dotted lines. In a-b), each MC distribution is normalised to the data, as indicated in the parentheses.*

the KMS is slightly lower than the data. The uncertainties due to the charm mass and scale η_{max} are found to be less than $\pm 10\%$ and $\pm 19\%$ respectively, for the high $x_\gamma^{\rm obs}$ region.

In all previous analyses on dijet angular distributions, only the absolute value of $\cos\theta^*$ were determined. In the present study, the two jets were distinguished by associating the D^* meson to the closest jet in $\eta - \phi$ space. Calling the jet closest to the D^* meson a "D^* jet", the rise of $d\sigma/d\cos\theta^*$ was studied separately for each jet. The sign of the unfolded $\cos\theta^*$ is thus given by the direction of the D^* meson (positive for the proton direction). Fig. 8.18 a)-b) shows the differential cross sections as a function of $\cos\theta^*$ for the resolved- and direct-enriched samples. The PYTHIA estimation of the contribution of the direct process to the resolved-

enriched sample, $x_\gamma^{\rm obs} < 0.75$, and the resolved process to the direct-enriched sample, $x_\gamma^{\rm obs} > 0.75$, are also indicated.

Direct photon events originating from the dominant q-exchange process $\gamma g \to c\bar{c}$ (Fig.8.15 e)) should have a distribution symmetric in $\cos\theta^*$. The angular distribution of direct-enriched events ($x_\gamma^{\rm obs} > 0.75$) exhibits a slight asymmetry, which can be explained by the feedthrough from resolved photon processes near $\cos\theta^* = -1$, as predicted by PYTHIA (Fig. 8.18 b)).

The sample enriched in resolved photons (Fig. 8.18 a)) exhibits a mild rise in the proton hemisphere towards $\cos\theta^* = 1$, consistent with expectations from quark exchange. In contrast, they have a strong rise towards $\cos\theta^* = -1$, i.e. in the photon direction, consistent with a dominant contribution from gluon exchange. For the latter case, the charm quark emerges in the photon hemisphere (Fig. 8.15 a)-b)). Gluon-exchange diagrams with this topology can only come, at LO, from the processes $c^\gamma g^p \to cg$ and $c^\gamma q^p \to cq$, where the superscripts refer to an origin in either the photon or proton. The partonic cross sections for these $2 \to 2$ subprocesses are highly asymmetric in $\cos\theta^*$ and show a steep rise towards the photon direction (see Fig. 8.18), while the subprocess $gg \to c\bar{c}$ (Fig. 8.15 d)) is symmetric in $\cos\theta^*$. This observation suggests that the source of the LO gluon-exchange contribution as seen in Figs. 8.17 a) and c) is charm originating from the photon. This is consistent with the MC prediction [82] that most of the resolved photon contribution to charm dijet events at HERA is due to charm originating from the photon. The feedthrough from direct photon events in the low $x_\gamma^{\rm obs} < 0.75$ region is expected and found to be symmetric as shown by the PYTHIA predictions (shaded histogram) in Fig. 8.18 a). The shapes of all data distributions are well reproduced by PYTHIA and HERWIG, although the rise in the cross section as a function of $\cos\theta^*$ at low $x_\gamma^{\rm obs}$ is stronger in data, particularly in the photon direction in comparison to the HERWIG predictions.

To quantify the above mentioned behaviour, the measured cross sections for direct- and resolved-enriched samples were fitted separately in the photon and proton directions to a function $1/(1-(\cos\theta^*))^{|\kappa|}$. The resulting values for κ are:

$$\kappa(x_\gamma^{\rm obs} < 0.75)_{\rm Photon\ direction} = 6.69 \pm 0.86\ ({\rm stat})\ ^{+0.65}_{-0.85}\ ({\rm syst.});$$
$$\kappa(x_\gamma^{\rm obs} < 0.75)_{\rm Proton\ direction} = 0.97 \pm 0.27\ ({\rm stat})\ ^{+0.10}_{-0.19}\ ({\rm syst.});$$
$$\kappa(x_\gamma^{\rm obs} > 0.75)_{\rm Photon\ direction} = 2.71 \pm 0.46\ ({\rm stat})\ ^{+0.20}_{-0.31}\ ({\rm syst.});$$
$$\kappa(x_\gamma^{\rm obs} > 0.75)_{\rm Proton\ direction} = 0.39 \pm 0.15\ ({\rm stat})\ ^{+0.07}_{-0.07}\ ({\rm syst.})$$

The angular distribution in Fig 8.18 c) for low $x_\gamma^{\rm obs}$ region is well described by CASCADE predictions, within a large theoretical uncertainty less than $\pm 67\%$ on the scale η_{max} and $\pm 13\%$ on the choice of charm mass. CASCADE underestimates the data in the proton direction. The unintegrated gluon densities GRV derivative and KMS on the other hand clearly show a distribution symmetric in $\cos\theta^*$, which can only be accounted as the feedthrough from the 'collinearly'-defined direct photon events due to the $x_\gamma^{\rm obs}$ cuts. This confirms that these parton densities do not have any diagrams which can simulate the charm originating from the photon.

For $x_\gamma^{\rm obs} > 0.75$, the CASCADE prediction (Fig 8.18 d)) overestimates the data in all regions of $\cos\theta^*$, although the shape is described reasonably well. The GRV derivative can describe the shape and the normalisation within CASCADE in the photon direction but is above the data is the proton direction. KMS, on the other hand, can reproduce the data distribution for this region in the proton direction and is below the data for the photon hemisphere. The scale uncertainties are found to be less than $\pm 28\%$ and $\pm 12\%$ on the choice of η_{max} and charm mass, respectively. It should be noted that the theoretical uncertainties on CASCADE arise mainly in the photon direction for all presented $\cos\theta^*$ distributions.

8.3 Comparison with NLO QCD Calculations

The results presented in the previous section are now compared to the NLO QCD calculations. The Monte Carlo models considered earlier only contain the first order contribution in the perturbative expansion and include the effects of higher order

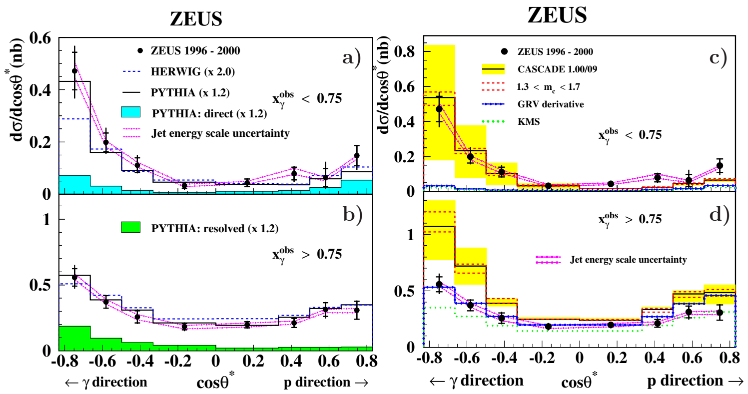

Figure 8.18: *Differential cross section $d\sigma/d\cos\theta^*$ (dots) compared with a)-b) PYTHIA and HERWIG MC simulations (histograms); c)-d) CASCADE predictions (full line), with various CASCADE related systematics as indicated on the plot. Results are given separately in a),c) for samples enriched in resolved photon events and in b),d) for samples enriched in direct photon events. The inner error bars show the statistical uncertainty, while the outer ones show the statistical and systematical uncertainties added in quadrature. The jet energy scale uncertainty is given by the two dashed-dotted lines. In a)-b), each MC distribution is normalised to data, as indicated in the parentheses. Also shown as shaded areas in a) and b) are the contribution of the direct photon process in PYTHIA to the resolved-enriched sample and the contribution of the resolved photon process to the direct-enriched sample, respectively.*

only in an approximate way. The NLO QCD calculations are computed to the second order in α_s and hence have more predictive power. Calculations for the photoproduction of charm events in the HERA kinematic region are available [71] in the fixed-order (FO) scheme.

In this collinear FO approach, only light quarks are active flavours in proton and photon. There is no explicit charm excitation component: the charm (and bottom) are only produced dynamically. Therefore, if there is really any charm originating from the photon, it should be reflected by the deficiencies in this scheme to describe the measured cross section[4]. The calculations were performed separately for the point-like and hadronic components. The differential distributions are obtained by integrating over the full photon beam energy spectrum, rather than at a fixed value of photon energy. The k_T-cluster algorithm and the selection cuts are then applied to the simulated partons in the final state in the same way it was applied to the data and the hadron-level simulated events. The jets obtained from the k_T-cluster algorithm are partonic jets, which are then corrected to hadron level using the hadronisation corrections described later in subsection 8.3.2. The PDF parameterisations used were CTEQ5-M1 [59] for the proton and AFG-HO [161] for the photon. The factorisation scales of the photon and proton PDFs, μ_F, and the renormalisation scale, μ_R, used for the calculation were set to $\mu_F = \mu_R = m_T \equiv \sqrt{m_c^2 + \langle p_T^2 \rangle}$, where $\langle p_T^2 \rangle$ was set to the average p_T^2 of the charm quark and anti-quark. The charm fragmentation into D^* was performed using the Peterson fragmentation function [127] with an ϵ parameter of 0.035 [162].

In all cases, the fraction of c quarks fragmenting into a D^* was assumed to be 0.235 [76] and a charm quark mass of $m_c = 1.5$ GeV was used.

8.3.1 Estimation of the Theoretical Uncertainties

To draw quantitative conclusions, the uncertainties related to the theoretical predictions must be evaluated. These uncertainties due to the truncation of the splitting function at a fixed order can indicate the missing amount of the higher order radiative corrections. In the present study, the following contribution to the theoretical uncertainties were considered:

- **Higher order dependence:** The higher order missing term dependence or the convergence of the perturbative expansion after being truncated at a fixed order,

[4] The NLO comparison with the inclusive dijet cross section reported earlier [160] gave a very good agreement between the data and the calculations.

was estimated by simultaneously varying the renormalisation scale μ_R and the factorisation scale μ_F between $m_T/2$ and $2m_T$.

- **Uncertainty on the charm mass:** The uncertainty on the charm mass m_c, was estimated by changing the mass between 1.3 and 1.7 GeV.

- **The PDF parameterisations for the photon:** The parton densities are obtained from fits to the experimental data. The uncertainty mainly arises from the data used to fit the PDFs and the assumption involved into the fits. Thus the estimation of this uncertainty can be done either by simply using two different parameterisations of the PDFs or by considering the actual uncertainties on the data used in the fits and propagating them to the results. Furthermore the uncertainty due to the assumptions in the fit procedure can then be estimated by using different PDFs in which modifications of these assumptions are available. At the time of this thesis, the former seemed reasonable due to unavailability of PDFs where the modification in the fits assumptions are possible. Thus the uncertainties on the photon PDF are estimated by using GRV-HO [84] instead of AFG-HO.

- **The PDF parameterisations for the proton:** Using the same arguments as above, the uncertainty due to the parameterisation for the proton PDFs are obtained using MRSG [163] instead of CTEQ5-M1.

- **Factorisation scale choice for the photon and proton:** The factorisation scale for the proton μ_{F_p}, is needed to remove the collinear singularities arising from the strong interactions. On the other hand the factorisation scale for the photon μ_{F_γ}, addresses the singularities arising from the electromagnetic vertex. In order to incorporate the higher order effects, one should include an explicit dependence of the structure functions up on the renormalisation scale. At fixed order this effect was estimated by keeping the renormalisation scale to be equal to m_T, while changing the scales μ_{F_p} and μ_{F_γ} to $m_T/2$ or $2m_T$.

- **Uncertainty due to hadronisation corrections:** As the correction from partons to hadrons cannot be calculated in QCD, the uncertainty was estimated by taking the half the difference between the predictions of the Lund and Cluster hadronisation models.

To incorporate the total uncertainties in the QCD prediction, the simultaneous variation of m_c between 1.3 and 1.7 GeV and $\mu_R = \mu_F = \mu_T$ between $m_T/2$ and $2m_T$ was considered. This simply means that the uncertainties arising from the mass variation and the scale choice are added linearly.

8.3.2 Parton to Hadron Corrections

The differential cross sections predicted by the FO NLO calculation are for jets at parton level associated with hadronic D^* mesons. These partonic jets are then corrected for the hadronisation effects using the Monte Carlo hadronisation models. The hadron level jets associated with at least one D^* meson were generated using the procedure that was previously described. For the partonic level distribution the k_T-cluster algorithm was used after the parton shower and before the hadronisation stage. Once the jet samples are obtained, the final state partons are allowed to undergo the hadronisation phase in order to obtain the D^* meson. Thus the ratio of the two jet distributions incorporates the hadronisation correction needed for the jets.

PYTHIA and HERWIG with Lund and Cluster hadronisation models, respectively were used to estimate the correction factor needed to transform the partonic into hadronic jets. For each bin, the partonic cross section obtained using FO NLO, was multiplied by the hadronisation correction factor, $C_{\text{had}} = \sigma^{\text{hadrons}}_{\text{MC}}/\sigma^{\text{partons}}_{\text{MC}}$, which is the ratio of the MC cross sections after and before the hadronisation process. The value of C_{had} was taken as the mean of the ratios obtained using HERWIG and PYTHIA. Half the spread between the two MCs was added in quadrature to the uncertainty in the NLO calculation. The deviation of C_{had} from unity is typically below 20% as shown in Fig. C.1 and Fig. C.2 in the Appendix (See also Tables A.1-A.7). The comparison between the differential cross sections obtained using PYTHIA and

HERWIG to the partonic ones from the same simulations as a function x_γ^{obs} shown in Fig. C.1 a), reflects large migration of events concentrated at high x_γ^{obs} region. To minimise the migration effects at $x_\gamma^{\text{obs}} > 0.75$ due to hadronisation, a wider bin than that of Fig. 8.10 was used. The deviation of C_{had} from unity is below 20%, except for the second-to-highest x_γ^{obs} bin.

The hadronisation corrections for x_p^{obs} in Fig. C.1 b),c),d) are typically below 24%, whereas the largest correction was found to be below 11% and 42% localised at the first bin for M_{jj} (Fig. C.2 a)) and $\bar{\eta}$ (Fig. C.2 b)) distributions respectively. The highest $|\cos\theta^*|$ (Fig. C.2 e) and lowest $\cos\theta^*$ (Fig. C.2 f)) bins of the sample enriched in direct photons, have corrections below 30% and for the sample enriched in resolved photons (Fig. C.2 c),d)) the corrections were 40 – 60%, in the two highest $\cos\theta^*$ bins.

8.3.3 Comparison with Theoretical Predictions

Fig. 8.19 shows a comparison for the differential cross section as a function of x_γ^{obs}. The LO Born part of the calculation, shown as the dashed lines in Fig. 8.19 a), cannot describe the x_γ^{obs} distribution and is found to be negligibly small for the hadronic part (low x_γ^{obs}). The correction to the Born part, NLO (without hadronisation correction), overestimates the data for the high x_γ^{obs} region and underestimates for the hadronic part (see section 3.1.1). The cross section can have a low x_γ^{obs} contribution at NLO due to three-parton final states in which one of the partons is treated as a photon remnant. The NLO correction to LO for the point-like part is found to be 31%, whereas the hadronic part is about 89%. The dominant uncertainty in the NLO predictions is due to the simultaneous variation of $m_c = 1.3$ GeV and $\mu_0 = m_T/2$ and found to be 92% in the 3^{rd} bin of Fig. 8.19 a). The rest of the uncertainties on the NLO prediction are found to be typically below 20%. Fig. 8.19 b) shows the NLO cross section before and after hadronisation correction. The low x_γ^{obs} tail of the NLO cross section is below the data, whereas for $x_\gamma^{\text{obs}} > 0.75$ the data are well described by the NLO predictions with hadronisation correction.

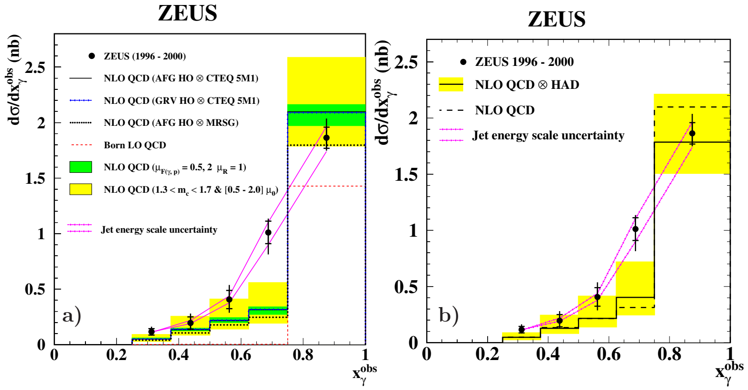

Figure 8.19: *Differential cross section $d\sigma/dx_\gamma^{\rm obs}$ for the data (dots) compared with: a) FO LO and NLO predictions with various theoretical uncertainties indicated on the plot. The uncertainties due to the choice of the photon PDF, GRV-HO instead of AFG-HO are quite small and is shown as the dot-dashed lines. The dark shaded band corresponds to the variation of the factorisation scale, μ_F, from $m_T/2$ to $2m_T$. b) NLO predictions after hadronisation correction (full lines) and at parton level (dashed lines). The inner error bars show the statistical uncertainty, while the outer ones show the statistical and systematic uncertainties added in quadrature. The jet-energy-scale uncertainty is given by the two dashed-dotted lines. Also shown in b) the uncertainty of the NLO prediction after hadronisation correction (shaded).*

The differential cross section as a function of $x_p^{\rm obs}$ is compared in Fig. 8.20 with LO and FO NLO calculations. The LO Born part is below the data for all bins. The NLO prediction is in reasonable agreement with the data within a maximum uncertainty of 47%, due to the variation of the charm mass and of the scale $\mu_0 = m_T/2$. The remaining uncertainties are typically below 10%, except for a maximum of 20% due to choice of MRSG as the proton PDF.

As expected from the $x_\gamma^{\rm obs}$ comparison, the NLO prediction for the resolved-enriched $x_\gamma^{\rm obs}$ distribution shown in Fig. 8.21 a),c) is below the data in almost all bins, but the shape is well reproduced. The LO prediction cannot match the data description. The maximum uncertainties associated with a variation of the charm

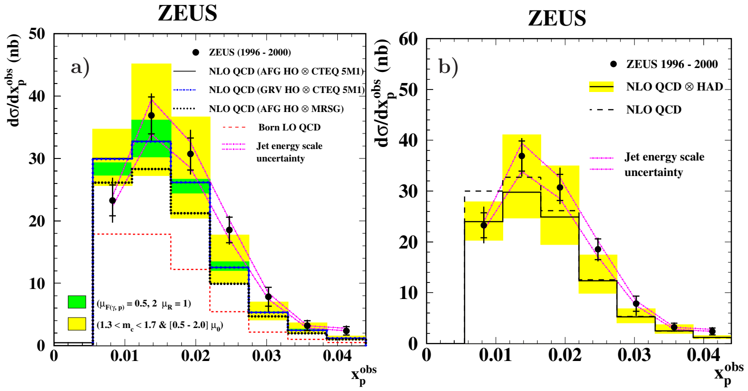

Figure 8.20: *Differential cross section $d\sigma/dx_p^{\rm obs}$ for the data (dots) compared with: a) FO LO and NLO predictions with various theoretical uncertainties indicated on the plot, b) NLO predictions after hadronisation correction (full lines) and at parton level (dashed lines). The inner error bars show the statistical uncertainty, while the outer ones show the statistical and systematic uncertainties added in quadrature. The jet-energy-scale uncertainty is given by the two dashed-dotted lines. Also shown in b) the uncertainty of the NLO prediction after hadronisation correction (shaded).*

mass and the scale $\mu_0 = m_T/2$, is less than 77% for the resolved enriched sample, whereas less than 45% for the direct enriched sample shown in Fig. 8.21 b),d). The data is well described by the NLO prediction for the $x_\gamma^{\rm obs} > 0.75$ as a function of $x_p^{\rm obs}$ both in shape and normalisation.

Fig. 8.22 shows the differential cross section as a function of M_{jj} compared to the LO and NLO predictions. Clearly the LO in Fig. 8.22 a) is below the data in all bins. The NLO agrees quite well for high M_{jj}, but is below the data in the low M_{jj} region. The NLO QCD calculation can in general describe the shape within the maximal uncertainty: less than 69% (next to last bin) on the variation of charm mass and the scale $\mu_0 = m_T/2$.

In Fig. 8.23 the differential cross section as a function of the average pseudorapidity is compared to the LO and NLO predictions. Again the LO part of the QCD

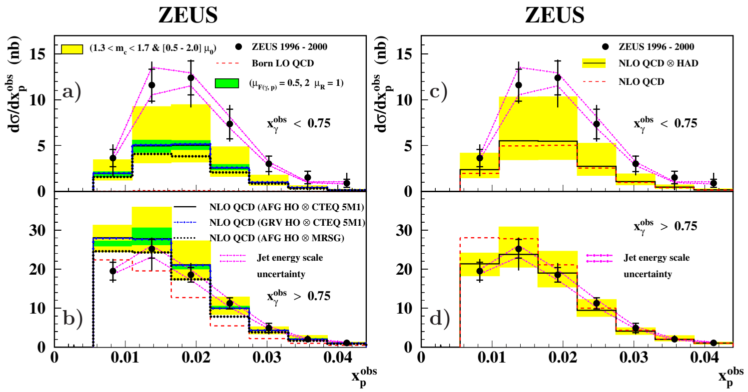

Figure 8.21: *Differential cross section $d\sigma/dx_p^{\rm obs}$ for the data (dots) compared with: a)-b) FO LO and NLO predictions with various theoretical uncertainties indicated on the plot, c)-d) NLO predictions after hadronisation correction (full lines) and at parton level (dashed lines). Results are shown separately in a),c) for samples enriched in resolved photon events and in b),d) for samples enriched in direct photon events.*

is well below the data distribution. The NLO in Fig. 8.23 a) is above the data in the first bin, and is below the data for $\bar{\eta} > 0$. The high $\bar{\eta}$ region, dominated by the resolved photon events, has large systematic uncertainties on the missing higher order terms of about 53% (next to last bin) due to the variation of the scale $\mu_0 = m_T/2$ and the charm mass. The other uncertainties due to PDF and μ_F variations are typically below 20%. The NLO distribution in Fig. 8.23 b), after the hadronisation correction, improves the data description for low $\bar{\eta}$, but is significantly below the data in the high average pseudorapidity region.

Fig. 8.24 compares the charm dijet angular distribution as a function of $|\cos\theta^*|$ to the LO and NLO calculations. For high $x_\gamma^{\rm obs} > 0.75$ (Fig 8.24 b) and d)), the NLO prediction gives a good description of the data. The description is greatly improved after the hadronisation correction. The LO prediction is slightly below the data but can describe the shape relatively well. The uncertainties associated with NLO are

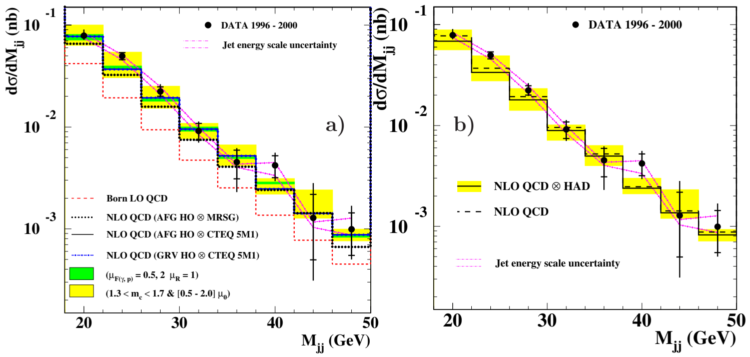

Figure 8.22: *Differential cross section $d\sigma/dM_{jj}$ for the data (dots) compared with: a) FO LO and NLO predictions with various theoretical uncertainties indicated on the plot, b) NLO predictions after hadronisation correction (full lines) and at parton level (dashed lines).*

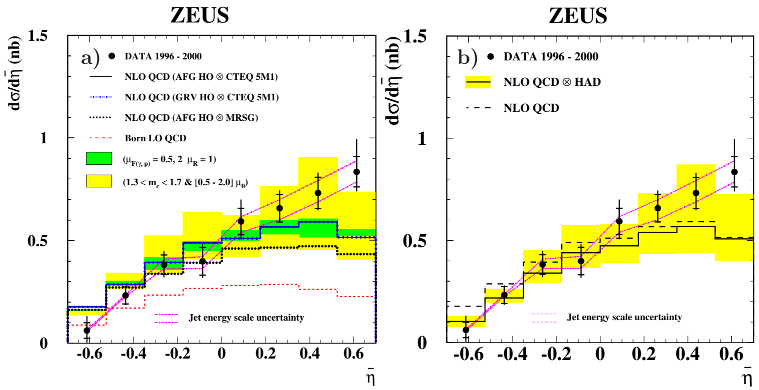

Figure 8.23: *Differential cross section $d\sigma/d\bar{\eta}$ for the data (dots) compared with: a) FO LO and NLO predictions with various theoretical uncertainties indicated on the plot, b) NLO predictions after hadronisation correction (full lines) and at parton level (dashed lines).*

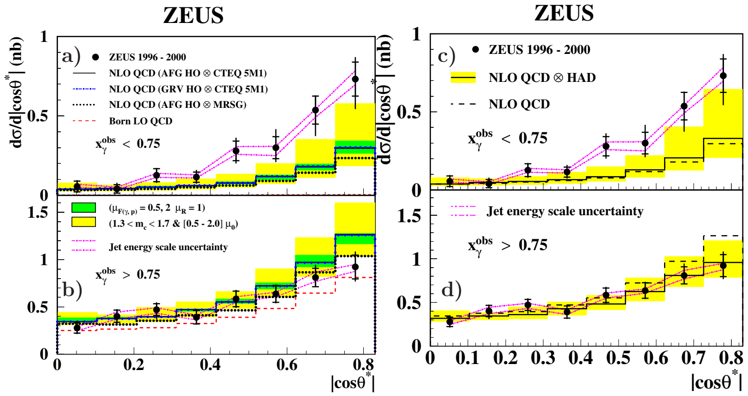

Figure 8.24: *Differential cross section $d\sigma/d|\cos\theta^*|$ for the data (dots) compared with: a)-b) FO LO and NLO predictions with various theoretical uncertainties indicated on the plot, c)-d) NLO predictions after hadronisation correction (full lines) and at parton level (dashed lines). Results are shown separately in a),c) for samples enriched in resolved photon events and in b),d) for samples enriched in direct photon events.*

small in comparison with the low $x_\gamma^{\rm obs}$ region shown in Fig. 8.24 a),c). The data is significantly higher than the NLO predictions in almost all bins for this low $x_\gamma^{\rm obs}$ region. This justifies the need for the higher order corrections to describe the data. The NLO can describe the shape of the low $x_\gamma^{\rm obs}$ region, thanks to the presence of the gluon as the propagator in the three-partonic system.

The differential cross section as a function of $\cos\theta^*$ is compared in Fig. 8.25 with the NLO FO calculations. The resolved- (Fig. 8.25 a),c)) and direct-enriched (Fig. 8.25 b),d)) regions are shown separately. The high $x_\gamma^{\rm obs}$ region is well described by the calculation particularly after the hadronisation correction both in the photon and proton directions. The NLO underestimates significantly the low $x_\gamma^{\rm obs}$ region both in proton and photon directions. The largest NLO uncertainties are found to be less than 134% in the proton direction and 93% in the photon direction mainly due to the scale variation $\mu_0 = m_T/2$.

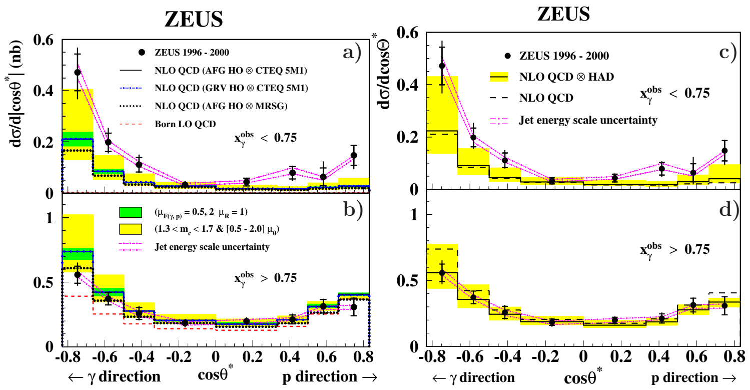

Figure 8.25: *Differential cross section $d\sigma/d\cos\theta^*$ for the data (dots) compared with: a)-b) FO LO and NLO predictions with various theoretical uncertainties indicated on the plot, c)-d) NLO predictions after hadronisation correction (full lines) and at parton level (dashed lines). Results are shown separately in a),c) for samples enriched in resolved photon events and in b),d) for samples enriched in direct photon events.*

The huge uncertainties in the proton and photon directions dominant at low $x_\gamma^{\rm obs}$ region arise from the collinear emission of gluons by the charm quark at large transverse momentum or from almost collinear branching of gluons or photons into the $c\bar{c}$ pairs. These terms are not expected to affect the total production rates [164], but they rather spoil the convergence of the perturbative expansions and cause large scale dependences on the NLO results. The proper procedure is to absorb the terms into the charm distribution functions of the incoming photon and proton and into the fragmentation of c quarks into charmed hadrons. Of course, to do this absorption one needs a charm contribution in the structure function in the first place. The NLO calculations used in this thesis have no explicit charm contribution in the structure functions and the quark is considered as massive. This strongly indicates the need of charm originating from the photon to describe the measured cross section.

An alternative way of making predictions at large $p_\perp$ is to treat the charm quarks as massless partons when compared with their transverse momentum. The mass singularities of the form $\log(p_\perp^2/m^2)$ can then be absorbed into structure and fragmentation functions in the same way as for the light quarks u, d and s. It is expected that the massless approach [73] could be better suited for the description of the differential cross section up to NLO in the region with $p_\perp \gg m$. At the time of this thesis such calculations for heavy quarks dijet events are not available.

8.4 Conclusions

The differential cross sections as a function of various observables for charm dijet photoproduction events (median $Q^2 \approx 3 \cdot 10^{-4}$ GeV^2) have been measured in the kinematic range $130 < W < 280$ GeV, $Q^2 < 1$ GeV^2, $p_T^{D^*} > 3$ GeV, $|\eta^{D^*}| < 1.5$, $E_T^{\rm jet} > 5$ GeV and $|\eta^{\rm jet}| < 2.4$. The cuts on the dijet invariant mass, $M_{\rm jj} > 18$ GeV, and on the average jet pseudorapidity, $|\bar{\eta}| < 0.7$, select an $M_{\rm jj}$ and $|\bar{\eta}|$ region where the biases from other kinematic cuts are minimised. The distributions have been measured separately for samples of events enriched in resolved ($x_\gamma^{\rm obs} < 0.75$) and direct ($x_\gamma^{\rm obs} > 0.75$) photon processes. The angular dependence for the two samples is significantly different, reflecting the different spins of the quark and gluon propagators. The cross section rises faster with increasing $|\cos\theta^*|$ for resolved photoproduction, where processes involving spin-1 gluon exchange dominate, than for direct photoproduction, where processes involving spin-1/2 quark exchange dominate.

The shapes of the measured differential cross sections are well reproduced by PYTHIA. Except for the angular distributions at low $x_\gamma^{\rm obs}$, HERWIG also gives an adequate description of these shapes. The predictions of CASCADE describe the data at low $x_\gamma^{\rm obs}$ in both shape and normalisation. For high $x_\gamma^{\rm obs}$, the predictions significantly overestimate the data, but still give a reasonable description of the shapes.

The comparison of measured differential cross sections as a function $\bar{\eta}$ with CAS-

CADE shows clear deficiencies in describing the region dominated by the collinearly defined resolved photon events. This indicates that not all the properties of the resolved photon events can be described using the k_T-factorization approach. The FO NLO calculation also cannot describe the high $\bar{\eta}$ region neither in shape nor in normalisation. The large uncertainties associated with CASCADE and FO NLO indicate strong deficiencies in the photon PDF.

The shapes of the measured angular distributions are approximately reproduced by the FO NLO predictions. The absolute cross sections predicted by the NLO FO calculation reproduce the data for the sample enriched in direct photons and high M_{jj} region, but are below the data for the sample enriched in resolved photons.

Associating the D^* meson with one of the jets allows the sign of $\cos\theta^*$ to be defined. In all cases, the $\cos\theta^*$ distributions show a mild rise towards $|\cos\theta^*| = 1$, as expected from quark exchange, except for the resolved-enriched sample, in which the cross section rises steeply in the photon direction ($\cos\theta^* = -1$), as expected from gluon exchange. This observation indicates that most of the resolved photon contribution in LO QCD charm production is due to charm originating from the photon, rather than to the competing resolved photon process $gg \to c\bar{c}$. This demonstrates that charm originating from the photon is the dominant component in the resolved photoproduction of dijet events with charm.

Chapter 9

Analysis II: Charm Fragmentation Function

The perturbative aspects of QCD studied in the last chapter mainly focus on the first two terms of the convolution (PDF $\otimes$ hard scatter $\otimes$ fragmentation). The measurements presented there are less sensitive to uncertainties in the fragmentation. However, the data comparison to the theoretical predictions in all hadronic colliders is done based on the assumption of the universality of charm fragmentation. This assumption, due to the lack of proper fragmentation measurements in hadronic collisions, entails the use of parameterisations of fragmentation functions obtained in e^+e^- annihilations for the calculation of charm production in ep or pp scattering. In order to test this assumption of universality in charm fragmentation and to provide exact parameterisations to the available functions, the charm fragmentation function was studied for the first time at HERA and is presented in detail in this chapter. In the following sections the complete description of the experimental results is given. The structure is similar to the analysis presented in the last chapter and hence some of those details will not be repeated.

9.1 Description of the Measurements

The aim of this analysis is to measure the non perturbative aspect of QCD, namely the charm fragmentation function in the transition from a charm quark to a D^* meson. The data collected during the 1996 to 2000 running periods corresponding to an integrated luminosity of 120 pb^{-1} was used for this analysis. The three-level trigger system outlined in section. 7.2.1 was used to select online events.

Kinematic variables and jets were reconstructed using a combination of track and calorimeter information referred as the Energy Flow Objects (EFOs) which are described in section. 6.2.2. Jets were reconstructed from these EFOs using the k_T-cluster algorithm in its longitudinally invariant inclusive mode, with at least one D^* meson (see below) associated to a jet which was required to have $E_T^{jet} > 9$ GeV and $|\eta^{jet}| < 2.4$. The measured γp centre-of-mass energy W_{JB} was corrected for energy losses in inactive material in front of the calorimeter as described earlier in section 7.2.2.

In these events, D^* mesons, decaying into $D^0\pi_S \rightarrow K\pi\pi_S$, were reconstructed using the mass-difference technique, following the method and with the cuts given in section 7.2.4. A summary of cuts which were applied to the final event sample is as follows:

- Photoproduction events with the photon-proton centre-of-mass energy $W_{\gamma p}$ between, $130 < W_{\gamma p} < 280$ GeV.
- Jets with $E_T^{jet} > 9$ GeV and pseudorapidity $|\eta^{jet}| < 2.4$.
- Reconstructed D^* meson with $p_T^{D^*} > 2$ GeV and $|\eta^{D^*}| < 1.5$ within the mass window $0.1435 < \Delta M < 0.1475$ GeV obtained using the (K, π, π_s) system with:

$$\begin{aligned} p_T(K,\pi) &> 0.5 \text{ GeV}, \\ p_T(\pi_S) &> 0.12 \text{ GeV}, \\ 1.83 < M(K\pi) &< 1.90 \text{ GeV}. \end{aligned}$$

- The combinatorial background was suppressed using $p_T^{D^*}/E_T^{\theta>10^\circ} > 0.1$, where $E_T^{\theta>10^\circ}$ is the transverse energy measured using EFOs outside a cone of $\theta = 10^\circ$ in the forward direction.
- The D^* meson was associated with a jet at the reconstructed level[1] by considering the closest jet in $\eta-\phi$ space, and requiring $\Delta R = \sqrt{(\eta^{jet} - \eta^{D^*})^2 + (\phi^{jet} - \phi^{D^*})^2} < 0.6$.

Fig. 9.1 shows a ΔR distribution after the background subtractions compared to PYTHIA simulations. The number of events above $\Delta R = 0.6$ is close to zero and hence justifies the validation of cut used. PYTHIA gives a good description of the data distribution.

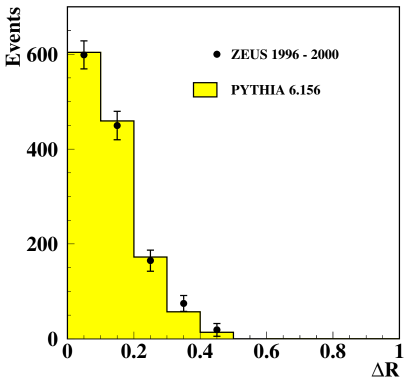

Figure 9.1: *ΔR distribution for the D^* associated with one of the outgoing jet. This distance in (η, ϕ) plane, is found to be less than 0.6, which is well reproduced by the PYTHIA simulations.*

After satisfying all the selection criteria outlined above, a clear ΔM and $M(D^0)$ mass peak above a relatively small background are observed, as shown in Fig. 9.2.

[1] The correction to this cone-based tagging between the jet and D^* meson was later done using k_T-association.

The overall shape is described by a Gaussian distribution for the signal imposed on a background of the form $A(\Delta M - m_\pi)^B$ for the ΔM distribution and of the form $e^{[A+B\cdot M(K\pi)]}$ for the $M(K\pi)$ invariant mass distribution, where A and B are determined from the fit and m_π is the pion mass. The number of D^* mesons reconstructed in the signal region from the fit is found to be 1308 ± 62, with the following values for the mass difference and D^0 mass:

$$M(D^*) - M(D^0) = 145.45 \pm 0.03 \text{ MeV} \quad \text{and} \quad M(D^0) = 1863.1 \pm 1.06 \text{ MeV},$$

respectively, in good agreement with the PDG values ([75] or see section 7.2.4).

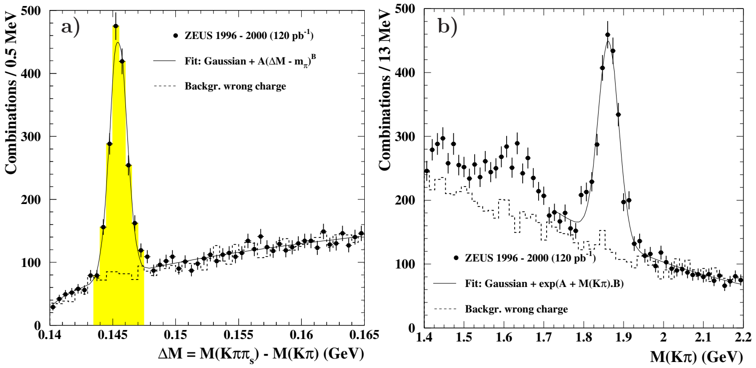

Figure 9.2: *Distribution in* **a)** *ΔM and* **b)** *$M(K,\pi)$, showing the right-charge combination (points) and wrong-charge combinations (dashed histogram). The shaded area shows the signal region $0.1435 < \Delta M < 0.1475$. The solid line is a fit to a Gaussian function plus $A(\Delta M - m_\pi)^B$ in* **a)** *and $\exp(A + B \cdot M(K\pi))$ in* **b)** *to describe the background, where A and B are constants. The excess of events with respect to the wrong charge distribution below the D^0 region originates mostly from D^0 decays involving neutral pions [155].*

After the background subtraction, estimated using wrong-charge pairs, a total of 1305 ± 53 D^* mesons were obtained, which is slightly lower than obtained using the fit, but also has a smaller error. The background subtraction was thus done using bin-by-bin subtraction for all subsequent distributions.

9.1.1 Comparison between the Data and Monte Carlo

In order to use the Monte Carlo samples to unfold the detector effects, the data should be reasonably described throughout a large region of its parameter space. This simply insures the proper modelling of the kinematic variables inside a given simulation, such that any systematic bias during the extraction of the cross section can be avoided. Before the comparisons between the data and the MC samples were made, the efficiency of the trigger slot was checked. The trigger slot FLT42, was studied using the similar procedure as outlined in the case of dijet angular distribution analysis (section 8.1.1). Table 9.1 represents the overall measured efficiency for the slot 42 in the analysis phase space, compared with the PYTHIA and HERWIG simulations. In general a very good agreement between the two is found, justifying the fact that the efficiencies are purely detector related effects and do not have any physics origin.

Trigger Slot (Event fraction)	data	PYTHIA	HERWIG
`(FLT42.AND.FLT59)/FLT59`	$91.9 \pm 6.2\%$	$91.7 \pm 2.9\%$	$91.2 \pm 2.8\%$

Table 9.1: *Overall efficiency of the trigger slot FLT42 compared with the PYTHIA and HERWIG expectations.*

Both PYTHIA and HERWIG simulations were then subjected to the selection procedure described in section 7.3.2. The two Monte Carlo simulations which were used to compare and to correct the data: PYTHIA has the option of various fragmentation schemes, the default of which is the Lund string model [121]; and the HERWIG MC, uses the Cluster model for the fragmentation [135]. These MCs are normalised to and compared with the data for both the D^* and the jet variables as shown in Fig. 9.3. There is very good agreement between data and the PYTHIA simulation. HERWIG gives a reasonable description of the data.

The next step is the comparison of the uncorrected distributions of the fragmentation sensitive variables. The Monte Carlo distributions are normalised to the

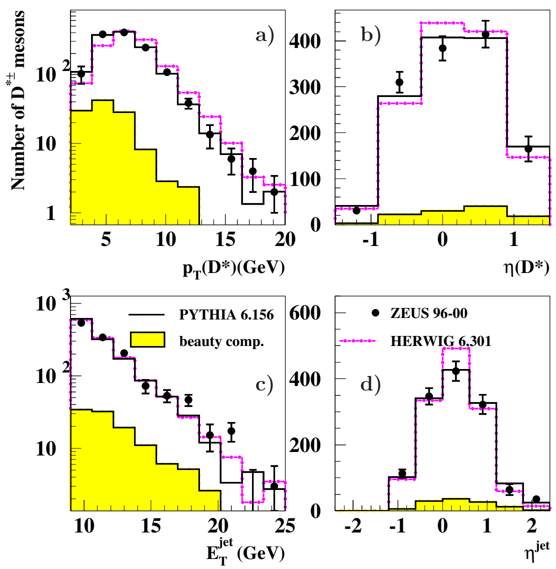

Figure 9.3: *Comparison between data and Monte Carlo simulation for a) $p_T(D^*)$, b) $\eta(D^*)$, c) E_T^{jet} and d) η^{jet}. The MC distributions are normalised to the data events. The component of beauty production as predicted by the PYTHIA simulation is shown as the shaded histogram.*

data. Fig. 9.4 shows the data comparison as a function of p_T^{rel} and z, where the p_T^{rel} is the transverse momentum of the D^* meson relative to the jet axis and z is defined to be $z = (E + p_{\parallel})^{D^*}/((E + p_{\parallel})^{\text{jet}})$. Also shown is the prediction of PYTHIA for the production of beauty quarks subsequently producing a D^* meson. The fraction of beauty component predicted by PYTHIA and HERWIG are $8.85 \pm 0.62\%$ and $4.75 \pm 0.46\%$ respectively. The z distribution is reasonably well described by the PYTHIA MC prediction with the default Lund string fragmentation, whereas the HERWIG prediction is significantly harder than the data. Hence, the cluster fragmentation implemented in HERWIG should be used with caution for the charm fragmentation to a D^* meson.

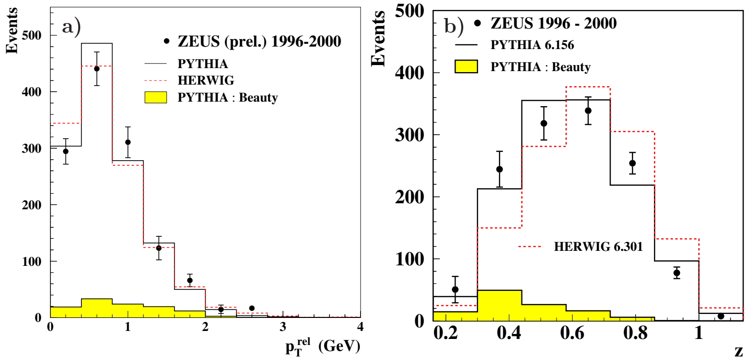

Figure 9.4: *Number of events verses a) p_T^{rel} and b) z for data and MC simulations. The data, shown as points, are compared with PYTHIA (solid histogram) and HERWIG simulations (dashed histogram). The component of beauty production as predicted by the PYTHIA simulations is shown by the shaded histogram.*

9.1.2 Studies Using Monte Carlo Samples

After the data and Monte Carlo comparisons, the z resolution was studied. In this case tracks from K, π and π_S were identified which originated from $D^* \rightarrow K\pi\pi_S$ in the detector level Monte Carlo. The D^* mesons were associated with the jet at the reconstructed level in the $\eta - \phi$ space. At the hadron level, D^* mesons were considered to be part of the hadronic final state (see below), and were uniquely associated to jets using the k_T-association method (see section 7.1.3). The difference between the hadron level and reconstructed z are histogrammed in a large number of bins. The resolution is obtained assuming a Gaussian distribution for this observable and the standard deviation is extracted from a fit to a Gaussian. Fig. 9.5 shows the resolution obtained using the PYTHIA and HERWIG simulations. The resolutions of z obtained using D^* as the hadronic final state and the reconstructed z with the three-track final state are in good agreement between the two MCs. The overall resolution is $\sim 6\%$ and the bin width was chosen to be at least twice the resolution

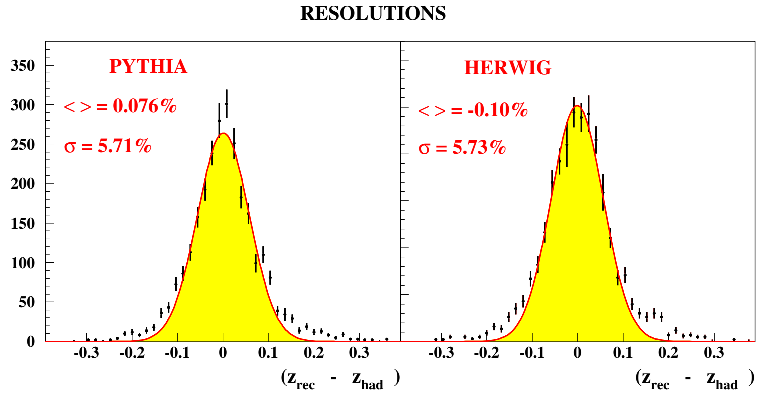

Figure 9.5: *Difference between the fragmentation variable z simulated at detector and hadron level by PYTHIA and HERWIG simulations. The distributions are fitted to a Gaussian function at full width half maximum. The corresponding means $< >$ and the standard deviations σ are indicated.*

in z.

After these preliminary studies, the PYTHIA Monte Carlo sample which gives the best description of the data was used to study the detector effects on the variables to be measured. The estimation of the cross section using a bin-by-bin unfolding method, relies on the correct simulation of the purity and acceptance in the kinematic region under study. Events migrating both into and out of the kinematic region have to be correctly modelled, as have migrations within the kinematic region itself.

A detailed study of the efficiency and purity was performed. As shown in Fig. 9.6, the purity of the sample is $60 - 80\%$, whereas the efficiency is reasonably flat of around 30%. Consequently, the form of the correction factor is dictated mostly by the purity. The correction factor shows a slight rise at low and high z values. This is due to the fact that events can only migrate into the bins at either end of the distribution due to the range of the kinematic cuts. As such the purity would be

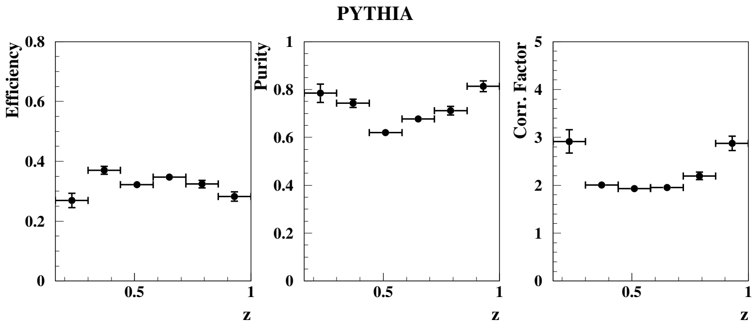

Figure 9.6: *Efficiency, purity and correction factors shown for the unfolding procedure as a function of z using PYTHIA simulations.*

expected to be higher in these regions, although this depends on the net flux of events which in turn depends on the form of the distribution itself.

9.1.3 Definition of the Hadronic Final State

As the main goal is the study of the fragmentation of c quarks into D^* mesons, the definition of the hadronic final state needs to be unambiguously specified. Based on the lifetime τ, all known particles can be divided into four groups: a) Stable ($e^{\pm}$, p, ν, γ), b) $\tau > 10^{-10}$ s ($\mu^{\pm}$, n, $\pi^{\pm}$, $K^{\pm}$), c) $10^{-11} < \tau < 10^{-10}$ s (K^0_S, Λ^0, Ω^-, Ξ^0) and d) $\tau < 10^{-12}$ s (π^0, D^0, D^+, Λ_c, B^+) etc. As an example, if a charmed meson D^{*+} is produced and decays as follows:

$$D^{*+} \rightarrow K^- + \pi^+ + \pi_s^+.$$

The decay products K^-, π^+ and π_s^+ get included in the reconstruction of the hadronic final state. Thus a jet can include any combination of the three. Unless all three particles are included in the same jet defined as a "charm jet", there is a high probability that either one or two of the other decay products get included into the "other" jet. This not only can cause misidentification of the jets, but also

the energy of the parent D^* can get shared between two or more jets. Moreover, all theoretical calculations consider D^* as the hadronic final state, not its decay products. Thus, in order not only to be consistent with the calculations but also to avoid the mistagging probabilities, the specific decay products in each event at the hadron level were removed and replaced by the parent D^* meson. Thereafter the stable particles including the parent D^* meson were used as input to the jet algorithm. This way the D^* meson gets uniquely associated with a given jet using the k_T-association method.

The correction due to $\Delta R < 0.6$ for the D^*-jet matching (at the reconstructed level) to the jet uniquely associated with a final state D^* meson (at the hadron level) is included in the evaluation of the correction factor. The data was then corrected for these and the detector effects using a bin-by-bin method with the PYTHIA simulation used as the central MC and the HERWIG simulation as a systematic check. The differential cross sections were obtained as a function of the fragmentation variable z using Eq. 8.7. The measured cross sections are the luminosity-weighted averages of the cross section at centre-of-mass energies $\sqrt{s} = 300$ GeV (1996 - 1997) and $\sqrt{s} = 318$ GeV (1998 - 2000). As the choice of the fragmentation variable is sensitive to the shape of the fragmentation function, the normalised cross section was measured. The normalised cross section has the advantage that the experimental and theoretical uncertainties are reduced, while allowing a precise test of the shape of various fragmentation functions in the calculations. The effect of b quarks was subtracted, such that the cross section in z is for processes where only a charm quark hadronises into a D^* meson. Due to the uncertain production rate of b quarks, the b fraction was varied by a factor two and the correction factors re-evaluated.

9.1.4 Study of the Systematic Uncertainties

The observable under study corresponds to a similar event topology (jets and D^*) as in the case of the dijet angular distribution analysis (chapter 8). The estimation of the systematic uncertainty was therefore performed in a similar way on both D^*

and jet related kinematic quantities. The sensitivity of the measured cross section to potential sources of systematic uncertainty was studied in detail, where each contribution was computed independently. The following sources of uncertainty have been considered.

- the jet transverse energy E_T threshold, was lowered to $E_T > 8$ GeV and raised to $E_T > 10$ GeV, based on approximately $\pm 1\sigma$ of its resolution.
- variation on the jet pseudorapidity η^{jet}, between $-2.3 < \eta^{jet} < 2.5$ and between $-2.5 < \eta^{jet} < 2.3$.
- the cut on the γp centre-of-mass energy was reduced and widened by approximately $\pm 1\sigma$ of its resolution i.e $124 < W < 267$ GeV and $136 < W < 293$ GeV.
- there is an uncertainty in the knowledge of the CAL energy scale between data and Monte Carlo which was estimated to be at most $\pm 3\%$ from section 6.2.1.2. To take this in account, only the calorimeter related informations on the EFOs was scaled by $\pm 3\%$ in Monte Carlo. The energy scale related variation is less than 11% for all analysis bins.
- the effect of the cuts on D^* quantities was estimated by increasing $p_T^{D^*} > 2.02$ GeV, and the pseudorapidity between $-1.503 < \eta^{D^*} < 1.497$ and $-1.503 < \eta^{D^*} < 1.497$.
- the control region (CR) for the track combination was varied between $0.152 < CR < 0.165$ GeV and between $0.15 < CR < 0.163$ GeV. Also the $p_T^{D^*}/E_T^{\theta>10^\circ}$ cut was raised to $p_T^{D^*}/E_T^{\theta>10^\circ} > 0.12$ and lowered to $p_T^{D^*}/E_T^{\theta>10^\circ} > 0.08$.
- the events for $z > 1$ were included.

The uncertainties due to the choice of HERWIG and subtraction of the b-component were the largest contributions to the total systematic uncertainty. Other major contributors arose from varying the requirement on the jet transverse energy, in accordance with the resolution and the knowledge of the absolute jet energy scale.

The effects of uncertainty in the simulation of the trigger were negligible. The effect of all the above systematic uncertainties is shown in Fig. B.11 and also given in table A.8.

To obtain the complete experimental uncertainty, the systematic and statistical uncertainties, including those related to the jet energy scale were added in quadrature.

9.1.5 Measurement of the Charm Fragmentation Function

Fig. 9.7 shows the measured relative cross section as a function of z compared to PYTHIA and CASCADE Monte Carlo predictions with different settings in the Lund string fragmentation model. The default setting for charm fragmentation function both in PYTHIA and CASCADE is the symmetric Lund fragmentation with Bowler's modification for the heavy quarks (See section 5.4.3.1).

The predicted value in the function of Eq. 5.7 is $r_Q \equiv 1$, but it is left as a free parameter so that a smooth transition to the original symmetric Lund form is possible ($r_Q \equiv 0$). The parameters a and b in Eq. 5.7 were set to their default values $a = 0.3$, $b = 0.58$ GeV^2. Three predictions for different values of r_Q are shown compared to data for both PYTHIA and CASCADE. The prediction with $r_Q = 1$ gives a reasonable description of the data. As r_Q decreases, the prediction deviates more and more from the data. The maximum scale uncertainty due to the variation on the maximum allowed angle for any gluon emission η_{max}, twice and half of its nominal value in the relative cross section prediction by CASCADE with the default $r_Q = 1$ was found to be $\sim 39\%$ in the first bin, all other bins have uncertainties less than 9%. It should be mentioned that, although both CASCADE and PYTHIA use the default Lund fragmentation, the observed difference in shape of the fragmentation function is attributed to the difference of initial state CCFM evolution in CASCADE and the DGLAP evolution in PYTHIA.

A parameterisation often used to describe the fragmentation of heavy quarks is

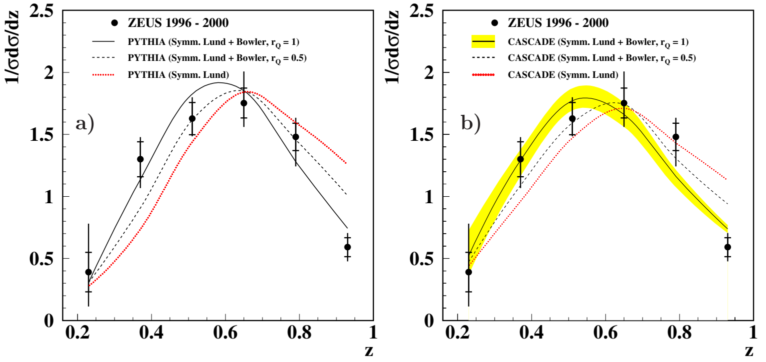

Figure 9.7: *Relative cross section $1/\sigma(d\sigma/dz)$, for the data (point) compared with a) PYTHIA and b) CASCADE Monte Carlo predictions for the Bowler's modified symmetric Lund fragmentation with $r_Q = 1$ (solid line), $r_Q = 0.5$ (dashed line) and the original symmetric Lund scheme $\equiv (r_Q = 0)$. The shaded area in b) represents the maximum scale uncertainty η_{max} in CASCADE as outline in section 5.2.2.*

the Peterson function as described in section 5.4.3.2. The form of the Peterson function in Eq. 5.10 has ϵ as a free parameter. The value of ϵ was varied for charm inside PYTHIA and CASCADE in the range 0.01 to 0.1, with the Lund string fragmentation model used for lighter flavours. For each value in the MC simulations, the full event record was generated and the kinematic requirements given in section 7.3.2 applied, allowing a direct comparison with the data. The MCs were fit to the data via a χ^2-minimisation procedure as shown in Fig 9.8 to determine the best value for ϵ.

The prediction shows a strong sensitivity toward the change in the Peterson fragmentation parameter ϵ. The result of varying ϵ is shown in Fig. 9.9. It can be seen that values as low as $\epsilon = 0.02$ are disfavoured, producing a much harder spectrum than the data, while values as high as $\epsilon = 0.1$ ($\epsilon = 0.12$) in PYTHIA (CASCADE) results in a too soft spectrum and are, therefore, also disfavoured. The results of the fit in PYTHIA and CASCADE are $\epsilon = 0.061 \pm 0.007$ (stat.)$^{+0.012}_{-0.010}$ (syst.) and

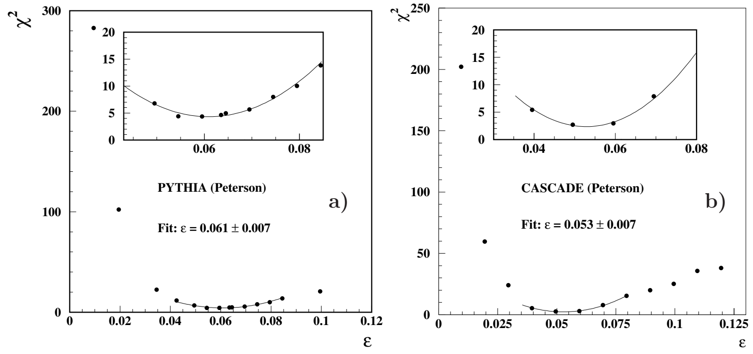

Figure 9.8: *χ^2-minimisation as a function of Peterson ϵ for a) PYTHIA and b) CASCADE respectively. The insets shows a blowup of the fitted region.*

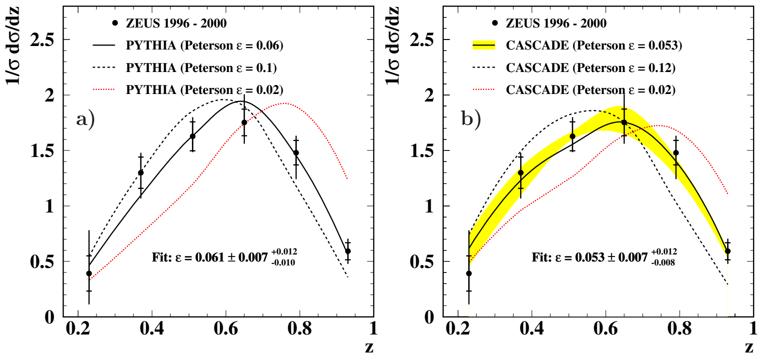

Figure 9.9: *Relative cross section $1/\sigma(d\sigma/dz)$, for the data (points) compared with a) PYTHIA and b) CASCADE predictions. The values for the parameter in a) $\epsilon = 0.1$, b) $\epsilon = 0.12$ (dashed line); a) $\epsilon = 0.06$, b) $\epsilon = 0.053$ (solid line) and $\epsilon = 0.02$ (dotted line), in the Peterson fragmentation function are also shown.*

$\epsilon = 0.053 \pm 0.007$ (stat.)$^{+0.012}_{-0.008}$ (syst.), respectively. The statistical uncertainties were obtained by varying the χ^2 by one unit and the systematic errors by re-evaluating the χ^2-minimisation for each systematic change following which the difference to the central values were added in quadrature.

These two values were then input into the respective MCs and the result is compared in Fig. 9.9. The data is well described. As mentioned earlier, the difference in the ϵ obtained using PYTHIA and CASCADE is due to the effect of initial state radiation obtained using CCFM evolution and DGLAP respectively. The scale uncertainties due to the η_{max} variation, on the relative cross section with the optimal ϵ in CASCADE are found to be maximum of 25% in the first bin, while the rest are below 10%. It should be mentioned that, due to known large scale uncertainties in the LO DGLAP corrections to PYTHIA, no scale uncertainties are shown in Fig. 9.9 a), and hence only the relative cross sections are compared. Also the main goal of this study being the non-perturbative fragmentation function, the difference in hard scattering dynamics and the PDF universality will not be further discussed.

9.2 Fragmentation in Theoretical Calculations

The phenomenological fragmentation models of Peterson *et al*. [127] and Kartvelishvili *et al*. [87] are considered in the framework of both leading-order and next-to-leading order QCD calculations. The calculation of the theoretical predictions is performed in a similar way as the hadron level of the Monte Carlo generated events in order to obtain the cross section separately for the point-like and hadronic component. The partonic jets obtained using the k_T-cluster algorithm are then associated with the D^* from a specific fragmentation model using k_T-association in the calculation. These partonic jets are then corrected to hadron level using the hadronisation corrections, described later in section 9.2.1. The differential cross sections are obtained by integrating over the full photon beam spectrum. The PDF, choice of the scale, and the uncertainties in the calculations are similar to the ones used for the angular distribution analysis (section 8.3.1). For each QCD calculation, the free parameters ϵ and α in the Peterson and Kartvelishvili function were varied, and the full cross section was generated with the kinematic requirements given in section 7.3.2. In all cases, the fraction of c quarks fragmenting into a D^* meson was

assumed to be 0.235 [76] and a charm quark mass of $m_c = 1.5$ was used.

9.2.1 Parton to Hadron Corrections

As mentioned in the last chapter, the differential cross sections predicted by the theoretical calculations are for partonic jets with a D^* meson. These partonic jets are corrected for the hadronisation effects using the PYTHIA and HERWIG simulations, which incorporate two different hadronisation models as described earlier in section 5.6.2. Large MC samples, about 200 times the data statistics, were generated for the hadronisation corrections. The hadron level jets with k_T-associated D^* mesons were obtained using the procedure that was described above. The parton level jets, were computed by using the jet algorithm on the partons after the parton shower. Care has been taken in order to ensure that the input to the jet algorithm is constituted of partons, just before the cluster or string formation in HERWIG or in PYTHIA. Thereafter, the final state partons were allowed to undergo hadronisation in order to obtain D^* mesons. Specific pointers to the parents of the D^* meson before hadronisation were implemented, such that a unique association of the partonic jet consisting of parents of the D^* meson to the final state charmed meson is made. Thus, the partonic jets associated with the D^* meson, containing the parents of the D^* meson and satisfying both the D^* and the jet kinematic cuts, were obtained. The ratio of the hadron level to the parton level distributions for the fragmentation variable z incorporates the hadronisation correction needed only for the jets.

For each bin, the cross section obtained using the theoretical calculations, was multiplied by the hadronisation correction factor $C_{\rm had} = \sigma_{\rm MC}^{\rm hadrons}/\sigma_{\rm MC}^{\rm partons}$, which is the ratio of the cross sections as a function of z, after and before the hadronisation process. The value of $C_{\rm had}$, as before, was taken as the mean of the ratios obtained using HERWIG and PYTHIA. Half the spread between the two MCs is considered as the errors on the theoretical calculation. The deviation of $C_{\rm had}$ from unity is typically below 19%, except the first and second bins where the correction is about 70% and 42% respectively. The values for $C_{\rm had}$ are given in Table A.8 along with the distribution (Fig. C.3) in the Appendix.

9.2.2 Parameterisations to the Theoretical Calculations

The parameterisations to leading-order (LO) QCD calculations were obtained by varying the Peterson fragmentation parameter ϵ in the range of 0.01 to 0.4. The obtained cross section was fitted to the data via χ^2-minimisation to determine the best value for ϵ. Fig. 9.10 shows the distribution for χ^2 as a function of Peterson ϵ before and after the hadronisation correction.

The distributions in Fig. 9.10 show a faster convergence of ϵ especially after the correction from partons to hadrons. The best fits were obtained within the leading-order framework. These values were used as an inputs to the leading-order calculations to obtain the relative cross sections as shown in Fig. 9.11, separately both before and after the hadronisation corrections. The extreme values with $\epsilon = 0.01$ and $\epsilon = 0.4$, shown for comparison, can be ruled out. The result of the fit before and after hadronisation corrections are $\epsilon = 0.183 \pm 0.019$ (stat.)$^{+0.024}_{-0.036}$ (syst.) and $\epsilon = 0.13 \pm 0.012$ (stat.)$^{+0.007}_{-0.042}$ (syst.) respectively. The best fitted value after the hadronisation correction is about 2.5 times higher then the one obtained by Nason and Oleari using the leading logarithmic approach [162]. The large negative systematic uncertainty on the fitted ϵ after the aforesaid corrections is due to uncertainty in the beauty contribution taken to be about twice the PYTHIA expectation.

The Kartvelishvili fragmentation function was used in a similar way, within the leading-order framework, with the free parameter α varied in the range of 0.2 to 4.0. Fig. 9.12 shows the χ^2 distribution, obtained using the χ^2-minimisation procedure as discussed above. The χ^2 convergence as a function of Kartvelishvili α is much better than the one obtained using the Peterson ϵ. The best fitted values of α within the leading-order framework, before and after the hadronisation corrections are found to be $\alpha = 1.71 \pm 0.13$ (stat.)$^{+0.25}_{-0.29}$ (syst.) and $\alpha = 2.06 \pm 0.12$ (stat.)$^{+0.21}_{-0.36}$ (syst.), respectively. Again, the dominant negative uncertainty on the best fitted α value is due to the uncertainty in the beauty component. These values were used as inputs

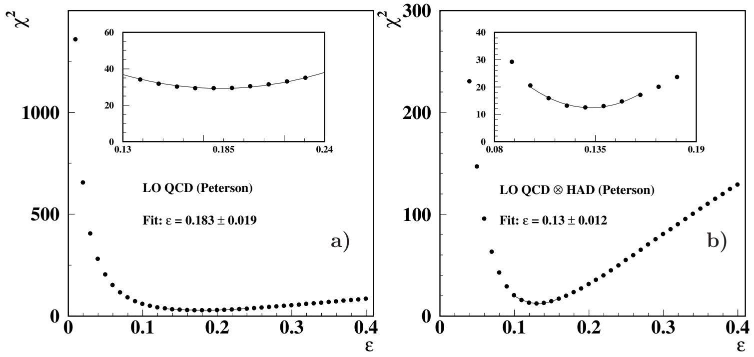

Figure 9.10: *χ^2-minimisation as a function of Peterson ϵ for leading-order QCD calculations a) before and and b) after the hadronisation corrections. The insets show a blowup of the fitted region.*

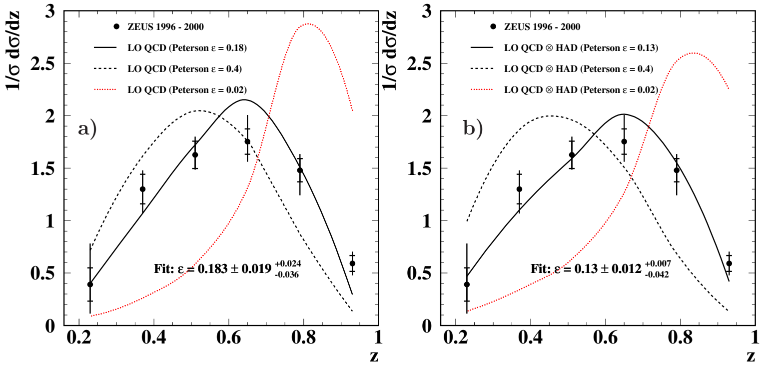

Figure 9.11: *Relative cross section $1/\sigma(d\sigma/dz)$, for the data (points) compared with leading-order QCD calculation with Peterson function, a) before and b) after the hadronisation corrections. The values for the parameter $\epsilon = 0.4$ (dashed line) and $\epsilon = 0.02$ (dotted line) are also shown. The best fit values, before and after hadronisation corrections are shown as solid lines.*

to the leading-order QCD calculation in order to obtain the relative differential cross section as shown in Fig. 9.13. The QCD calculations with the best fitted Kartvelishvili α are in much better agreement with the data than with the Peterson function. The uncertainties due to the renormalisation scale variation on the relative cross sections are found to be less than 1% except the first bin where it is about 5%.

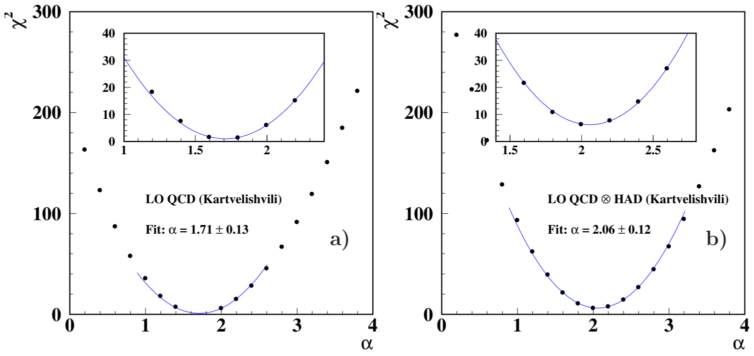

Figure 9.12: *χ^2-minimisation as a function of Kartvelishvili α for leading-order QCD calculation a) before and and b) after the hadronisation corrections. The insets shows a blowup of the fitted region.*

Similarly, in the next-to-leading order (NLO) framework, the values for Peterson ϵ and Kartvelishvili α were varied between 0.01 to 0.2 and 0.2 to 4.0, respectively. The minimum χ^2 was obtained by scanning through the input parameter space, yielding a set of parameters which give the best description of the measured relative cross section with the fragmentation model in question, both before and after the hadronisation corrections. Fig. 9.14 and Fig. 9.16 show the χ^2 distribution as a function of Peterson ϵ and Kartvelishvili α varied between the ranged mentioned above. In general, Kartvelishvili function shows a much better convergence than the Peterson parameterisation in the next-to-leading framework both before and after the hadronisation correction. The best fitted values of Peterson ϵ and Kartvelishvili α before

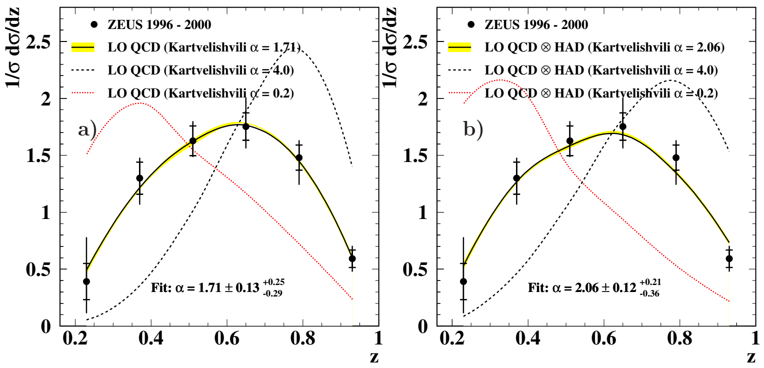

Figure 9.13: *Relative cross section $1/\sigma(d\sigma/dz)$, for the data (points) compared with leading-order QCD calculation with Kartvelishvili function, a) before and b) after the hadronisation corrections. The values for the parameter $\alpha = 4.0$ (dashed line) and $\alpha = 0.2$ (dotted line) are also shown. The best fit values, before and after hadronisation correction are shown as the solid lines.*

the hadronisation correction are found to be $\epsilon = 0.0986 \pm 0.011$ (stat.)$^{+0.014}_{-0.016}$ (syst.) and $\alpha = 2.43 \pm 0.17$ (stat.)$^{+0.33}_{-0.42}$ (syst.), respectively. The same parameters obtained after the hadronisation correction are $\epsilon = 0.074 \pm 0.008$ (stat.)$^{+0.008}_{-0.02}$ (syst.) and $\alpha = 2.89 \pm 0.16$ (stat.)$^{+0.27}_{-0.39}$ (syst.), respectively. As before, the dominant negative uncertainty on the fitted parameters is due to the uncertainty in the beauty component.

In Fig. 9.15 and Fig. 9.17, the measured relative cross sections are compared to the next-to-leading order calculations both before and after the hadronisation correction, with the best fitted ϵ and α for each fragmentation model. The fitted parameters within the given framework give a reasonable description of the data. The NLO uncertainties due to the charm mass and to the scale choice on the relative cross section are less than 20%.

The best fitted value of the Peterson ϵ obtained within the next-to-leading order calculation is much smaller than that obtained within the leading order framework

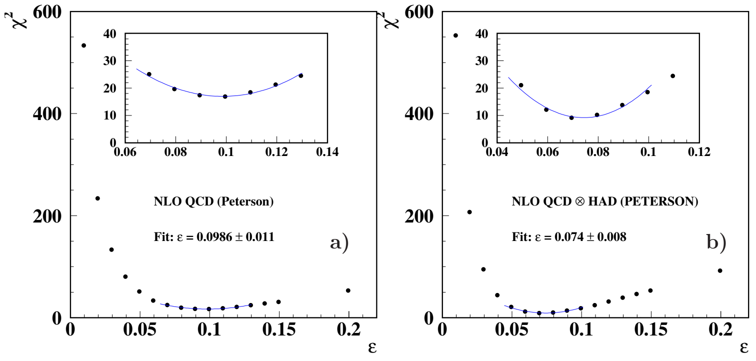

Figure 9.14: *χ^2-minimisation as a function of Peterson ϵ for next-to-leading order QCD calculation a) before and and b) after the hadronisation corrections. The insets shows the blowup of the fitted region.*

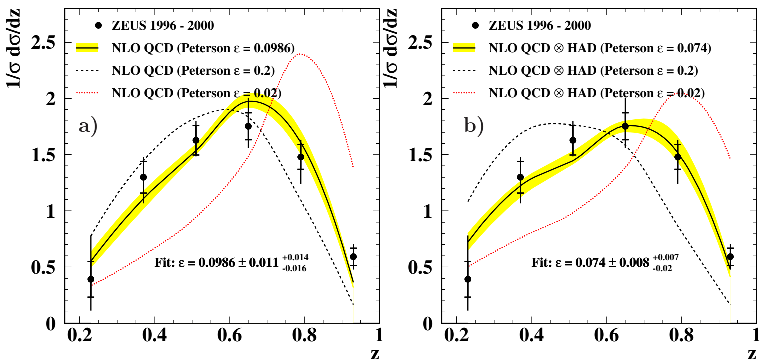

Figure 9.15: *Relative cross section $1/\sigma(d\sigma/dz)$, for the data (points) compared with next-to-leading order QCD calculation with Peterson function, a) before and b) after the hadronisation correction. The values for the parameter $\epsilon = 0.2$ (dashed line) and $\epsilon = 0.02$ (dotted line) are also shown. The best fit values, before and after hadronisation correction are shown as the solid lines.*

and hence confirms the expectation from [165]. The Peterson ϵ obtained after the hadronisation correction is about two times larger than the one used world wide [162]

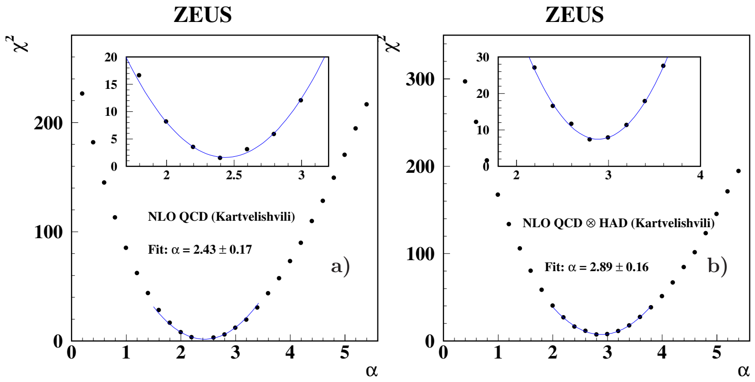

Figure 9.16: *χ^2-minimisation as a function of Kartvelishvili α for next-to-leading order QCD calculation a) before and and b) after the hadronisation correction. The insets shows the blowup of the fitted region.*

for charm fragmentation. In should be mentioned that the world wide used value, obtained using the fits in [162] was done by excluding the first three bins of the OPAL experimental data, along with a negative cross section in certain regions of the relative cross section.

Table 9.2 lists the results of comparison between various fragmentation models within leading and next-to-leading order frameworks. The Kartvelishvili function in the NLO framework before and after the hadronisation correction with $\alpha = 2.43$ and $\alpha = 2.89$ respectively gives the better description of the data in comparison to the Peterson function.

The parameters obtained after the hadronisation correction both in LO and NLO frameworks can directly be used as an input in the respective calculations in order to constrain the non-perturbative effects of the QCD calculation e.g. inclusive D^* production at HERA or TEVATRON. The values given before the hadronisation correction should only be used in the case of parton level jets, with D^* in the final state, e.g. charm contribution to unknown final state partonic jets at LHC.

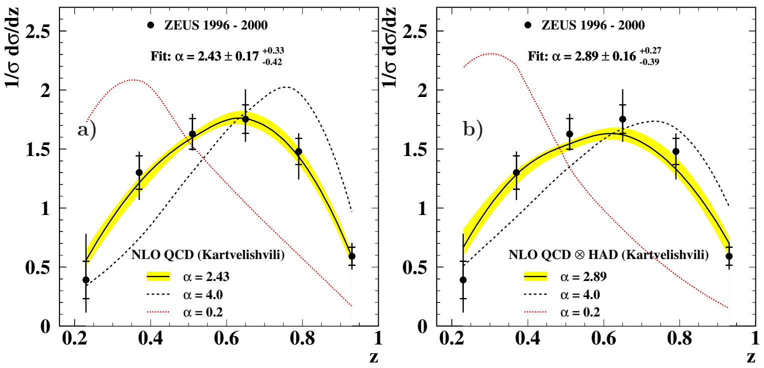

Figure 9.17: *Relative cross section $1/\sigma(d\sigma/dz)$, for the data (points) compared with next-to-leading order QCD calculation with Kartvelishvili function, a) before and b) after the hadronisation corrections. The values for the parameter $\alpha = 4.0$ (dashed line) and $\alpha = 0.2$ (dotted line) are also shown. The best fit values, before and after hadronisation correction are shown as the solid lines.*

9.3 Universality of Charm Fragmentation Function

In order to test the universality of the charm fragmentation function the data was compared to the measurements from e^+e^- annihilations. In e^+e^- collisions, the two produced charm quarks each carry half of the available centre-of-mass energy $\sqrt{s}$. The fragmentation variable of a D^* meson can therefore be trivially related to one of the two produced jets. In ep collisions, the definition of the fragmentation variable is not as simple, as described earlier in section 7.1.2. However, charm quarks produced in the hard scatter form final-state jets of which the meson is a constituent. Therefore, the fragmentation variable z defined to be $z = (E+p_{\parallel})^{D^*}/((E+p_{\parallel})^{\rm jet}) \equiv (E+p_{\parallel})^{D^*}/2E^{\rm jet}$, where the $p_{\parallel}$ is the longitudinal momentum of the D^* meson relative to the axis of the k_T-associated jet of energy $E^{\rm jet}$. The equivalence of $(E+p_{\parallel})^{\rm jet}$ and $2E^{\rm jet}$ arises because the jets were reconstructed as massless objects.

Model	Parameters			χ^2
Lund + PYTHIA	$a = 0.3$,	$b = 0.58$,	$r_Q = 1$	11.81
Lund + CASCADE	$a = 0.3$,	$b = 0.58$,	$r_Q = 1$	14.47
Peterson + PYTHIA	$\epsilon = 0.061$	± 0.007	${}^{+0.012}_{-0.010}$	5.05
Peterson + CASCADE	$\epsilon = 0.053$	± 0.007	${}^{+0.012}_{-0.008}$	3.09
Before Hadronisation correction				
Peterson + LO QCD	$\epsilon = 0.183$	± 0.019	${}^{+0.024}_{-0.036}$	29.40
Peterson + FO NLO	$\epsilon = 0.0986$	± 0.011	${}^{+0.014}_{-0.016}$	17.06
Kartvelishvili + LO QCD	$\alpha = 1.71$	± 0.13	${}^{+0.25}_{-0.29}$	1.00
Kartvelishvili + FO NLO	$\alpha = 2.43$	± 0.17	${}^{+0.33}_{-0.42}$	1.71
After Hadronisation correction				
Peterson + LO QCD	$\epsilon = 0.13$	± 0.012	${}^{+0.007}_{-0.042}$	12.55
Peterson + FO NLO	$\epsilon = 0.074$	± 0.008	${}^{+0.008}_{-0.020}$	8.89
Kartvelishvili + LO QCD	$\alpha = 2.06$	± 0.12	${}^{+0.21}_{-0.36}$	6.15
Kartvelishvili + FO NLO	$\alpha = 2.89$	± 0.16	${}^{+0.27}_{-0.39}$	8.52

Table 9.2: *Minimal χ^2 and corresponding parameters of the function for the comparison of the measured z distribution with different fragmentation models. The values within LO and NLO frameworks before and after the hadronisation corrections are also given. The errors quoted are the statistical and systematic errors. The χ^2 values are always for the 5 available degrees of freedom.*

In Fig. 9.18, the data is shown compared with measurements from the ARGUS [166] and OPAL [167] collaborations in e^+e^- collisions at two different centre-of-mass energies. Although using a different definition for z, the general features of the data presented in this analysis are the same as those at e^+e^- experiments. The data presented here have a similar accuracy to that of both the ARGUS and OPAL collaborations. The excess at low z from the OPAL collaboration arises from a sig-

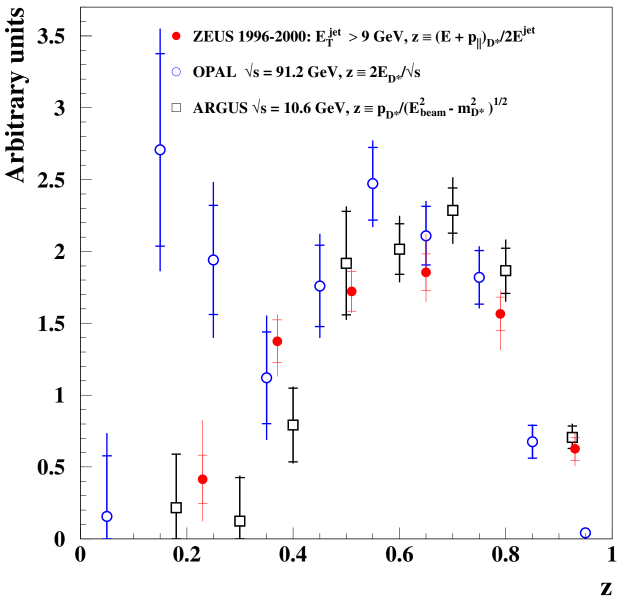

Figure 9.18: *Fragmentation function versus z for this analysis data (solid points) compared to measurements of the OPAL (open circle) and ARGUS (open squares) collaborations in e^+e^- collisions. For shape comparison the data sets were normalised to 1/(bin width) for $z > 0.3$, thus avoiding the first three bins from OPAL, which have a large gluon-splitting component.*

nificant gluon-splitting component. This is not seen in either ARGUS or in this data due to much lower energies. From a qualitative point of view, this comparison of the charm fragmentation function data to the e^+e^- data confirms the assumption of the universality of charm fragmentation. A more quantitative picture could emerge by simultaneously fitting the data within a given framework, such as the Kartvelishvili fragmentation within the FO NLO QCD calculations in both hadronic and leptonic colliders.

9.4 Conclusions

The fragmentation function for $D^{*\pm}$ mesons has been measured for the first time at HERA. The relative cross section as a function of the fragmentation variable z was obtained by requiring a jet with $E_T^{jet} > 9$ and $|\eta^{jet}| < 2.4$ to be associated with the D^* meson, with $p_\perp^{D^*} > 2$ GeV and $|\eta^{D^*}| < 1.5$ in the photoproduction regime $Q^2 < 1$ GeV^2, within the kinematic range $130 < W < 280$ GeV. The distributions show a strong sensitivity to the different fragmentation models in the leading order, leading order with parton shower, and next-to-leading order calculations.

The Lund string fragmentation model implemented within PYTHIA and CASCADE gives a reasonable description of the data. The parameterisation to the Peterson function as determined from the fit to the data within PYTHIA and CASCADE is given by $\epsilon = 0.061 \pm 0.007$ (stat.)$^{+0.012}_{-0.010}$ (syst.) and $\epsilon = 0.053 \pm 0.007$ (stat.)$^{+0.012}_{-0.008}$ (syst.), respectively.

Fits of the Peterson and Kartvelishvili fragmentation functions within leading-order and next-to-order QCD calculation by varying the free parameters ϵ and α respectively, have been done through χ^2-minimisation. The optimised values of ϵ for the Peterson function in the NLO framework, before and after the hadronisation correction, were found to be $\epsilon = 0.0986 \pm 0.011$ (stat.)$^{+0.014}_{-0.016}$ (syst.) and $\epsilon = 0.074 \pm 0.008$ (stat.)$^{+0.008}_{-0.020}$ (syst.), respectively. Similar optimisation to the Kartvelishvili function within NLO framework, results in $\alpha = 2.43 \pm 0.17$ (stat.)$^{+0.33}_{-0.42}$ (syst.) and $\alpha = 2.89 \pm 0.16$ (stat.)$^{+0.27}_{-0.39}$ (syst.), before and after the parton to hadron corrections, respectively. Comparing the measured z spectrum to different fragmentation functions in NLO, the Kartvelishvili function with the parameter given above is favoured. These values for the Kartvelishvili function in the leading and next-to-leading QCD calculations are obtained for the first time, whereas the values for the Peterson function are given for the first time in a hadronic collider.

The measured fragmentation functions agree with those obtained for charm production in e^+e^- annihilations, thus confirming the universality of charm fragmentation.

The results presented here have improved the current knowledge of the fragmentation of a charm quark hadronising into a D^* meson, an important non-perturbative ingredient in theoretical calculations of charm production cross sections. Using the obtained parameters within the same framework will therefore reduce a significant part of the uncertainty of the theoretical calculations and could explain differences observed recently in charm production between theory and experiments [92].

Chapter 10

Summary and Conclusions

In this document, the description and results of two different analyses sensitive to the parton dynamics and fragmentation are presented in charm photoproduction. The measurements of both of these aspects sensitive to perturbative and non-perturbative parts of QCD provide a clear picture and are essential to the understanding of the production mechanism of heavy quarks such as charm. These measurements have been performed for the first time at HERA.

10.1 Dijet Angular Distributions in Photoproduction of Charm

In the dijet angular distribution analysis, measurements related to hard scattering dynamics, more specifically to the charm content of the photon, have been made. The nature of the hard scattering was probed by studying the fraction of the photon momentum ($x_\gamma^{\rm obs}$) contributing to the production of two highest transverse energy jets. The fraction of events in the low $x_\gamma^{\rm obs}$ region then provided the evidence for the existence of large resolved photon processes ($\approx 40\%$). The nature of this resolved photon structure was then investigated by studying the dijet angular distribution as a function $|\cos\theta^*|$, where θ^* is the scattering angle of the jet with respect to the proton direction. The distribution is sensitive to the propagator in the hard scatter and thereby sensitive to the nature of the sub-process. The angular distribution as a function of $|\cos\theta^*|$, shows a steep rise for events enriched in resolved photon processes ($x_\gamma^{\rm obs} < 0.75$), in comparison to a mild rise for the events enriched with direct photon processes ($x_\gamma^{\rm obs} > 0.75$). The steep rise in the resolved enriched sample indicates the exchange of a gluon propagator in the hard-subprocess, while the mild rise is consistent with the expectation of the quark propagator. The nature of this rise is similar to classical scattering experiments and in particular done by Rutherford one hundred years ago.

In order to study the behaviour of this rise in the $|\cos\theta^*|$ distribution, in particular in the direction from which the parton arises by exchanging a gluon in the hard-subprocess, a D^* meson originating from a charm quark was tagged with one of the jets. The angular distribution was then studied as a function of $\cos\theta^*$, where the sign of the unfolded $\cos\theta^*$ is given by the direction of the D^* meson. The angular distribution enriched in the direct photon processes exhibits a symmetric distribution with a shallow rise to high values of $\cos\theta^*$. This is indicative of the exchange of a quark in the hard scattering with the charm produced via the boson-gluon fusion process. At low $x_\gamma^{\rm obs}$, where the sample is enriched in resolved photon processes, the data are highly asymmetric, exhibiting a rapid rise to negative $\cos\theta^*$. This demonstrates that the charm comes from the photon and exchanges a gluon in the hard process. The measurements are then compared to the best available theoretical calculations, NLO QCD including heavy quarks, which does not explicitly include the charm quark in the structure of the photon. The prediction of NLO, in which charm is only produced dynamically and is not an active flavour in the photon structure, lies clearly below the data. The description of the data could be improved by including a charm component in the photon structure function.

This measurement has therefore extended our knowledge of the constituents of light. Although it has been known for some time that the constituent of light, photons, themselves have constituents, it has now been revealed that the charm

quark is one of them. This can be of great value to future colliders using beams of photons.

10.2 Charm Fragmentation Function

A non-perturbative aspect of QCD, namely the charm fragmentation function was measured. The process of transforming coloured partons into colour singlet hadrons is typically characterized by a fragmentation function. The fragmentation variable z was defined as the fraction of jet energy carried by the D^* meson $z = (E + p_\|)^{D^*}/(E + p_\|)^{\rm jet}$, where the $p_\|$ is the longitudinal momentum of the D^* meson relative to the axis of the associated jet. The D^* meson was uniquely associated to a jet using the k_T-association method, such that it can be assumed to carry all characteristics of the final state charm quark. This assumption was verified using both Monte Carlo models and theoretical calculations. The fragmentation variable should then be comparable in definition to the energy fraction of charmed meson with respect to the beam energy used in e^+e^- annihilations.

In order to verify the assumption on universality of charm fragmentation and to provide an exact parameterisation especially suitable for the hadronic collisions, the relative cross section as a function of z was measured. The distribution shows a strong sensitivity towards changes in the parameter values used in specific fragmentation models like Peterson and Kartvelishvili, implemented within leading order and next-to-leading order calculations. Using a χ^2-minimisation method, the parameters which gave the best description of the data were extracted. Within the next-to-leading order framework, the best optimised value for the free parameters in the Peterson and Kartvelishvili functions, before and after the parton to hadron corrections to the jet, are given below:

$$\epsilon_{\rm NLO} = 0.0986 \pm 0.011\ ({\rm stat.})^{+0.014}_{-0.016}\ ({\rm syst.}) \tag{10.1}$$

$$\alpha_{\rm NLO} = 2.43 \pm 0.17\ ({\rm stat.})^{+0.33}_{-0.42}\ ({\rm syst.}) \tag{10.2}$$

$$\epsilon_{\rm NLO\otimes HAD} = 0.074 \pm 0.008\ ({\rm stat.})^{+0.008}_{-0.020}\ ({\rm syst.}) \tag{10.3}$$

$$\alpha_{\rm NLO\otimes HAD} = 2.89 \pm 0.16\ ({\rm stat.})^{+0.27}_{-0.39}\ ({\rm syst.}). \tag{10.4}$$

The extracted non-perturbative parameters should only be used together with a perturbative description of the same kind (leading, next-to-leading, etc) as the one it has been determined with. These parameters can then be implemented into a given QCD calculation to improve the precision of future calculations to be compared with charm production in ep and pp collisions. As every so often in experimental physics today's new results can become tomorrow's background. The above mentioned values can also be useful to estimate the charm contribution to the physics to be studied in future measurements at LHC.

Finally the assumption of the universality of charm fragmentation was verified by comparing the data to the measurements from e^+e^- collisions. Although there are independent ways of measuring the fragmentation function, the OPAL and ARGUS results having a different z definition are similar in shape, with precision of the HERA data competitive with the LEP data. This indicates that the formation of a D^* meson from a charm quark has the same characteristic, irrespective of collider, hence that the charm fragmentation is universal.

The results related to the measurement of the dijet angular distributions in photoproduction of charm, providing the evidence of charm originating from the photon, have been presented by the author in the Photon 2001 conference in Ascona, Switzerland Sept. 2001 [168] and in the DIS 2002 conference in Cracow, May 2002 [169]. Furthermore, the paper describing the results have recently been published in [170] and previously as a contributed paper to the International Conferences on High Energy Physics EPS HEP 01, Budapest, Hungary (July 2001) [154] and ICHEP 02, Amsterdam, The Netherlands (July 2002) [171]. Results related to the measurement of the charm fragmentation function have been published as a contributed paper to the same ICHEP 02, Amsterdam, The Netherlands (July 2002) [172], along with the recent review by the author during the Ringberg Workshop on "New Trends in HERA Physics" Ringberg, Germany (Sept. 2003) [173].

Appendix A

Tables of Cross Sections

$x_\gamma^{\rm obs}$ bin	$d\sigma/dx_\gamma^{\rm obs}$	$\Delta_{\rm stat}$	$\Delta_{\rm syst}$	$\Delta_{\rm ES}$ (nb)	$C_{\rm had}$
0.250, 0.375	0.115	±0.029	$^{+0.037}_{-0.017}$	$^{+0.004}_{-0.001}$	0.941 ± 0.040
0.375, 0.500	0.196	±0.055	$^{+0.064}_{-0.034}$	$^{+0.022}_{-0.005}$	0.950 ± 0.004
0.500, 0.625	0.407	±0.082	$^{+0.101}_{-0.086}$	$^{+0.032}_{-0.029}$	1.006 ± 0.008
0.625, 0.750	1.011	±0.102	$^{+0.073}_{-0.169}$	$^{+0.093}_{-0.112}$	1.285 ± 0.050
0.750, 0.875	2.000	±0.147	$^{+0.159}_{-0.105}$	$^{+0.150}_{-0.159}$	
0.875, 1.000	1.727	±0.122	$^{+0.243}_{-0.080}$	$^{+0.052}_{-0.089}$	
0.750, 1.000	1.864	±0.096	$^{+0.145}_{-0.066}$	$^{+0.101}_{-0.124}$	0.851 ± 0.041

Table A.1: *Measured cross sections as a function of $x_\gamma^{\rm obs}$. The statistical, systematic and jet energy scale (ES) uncertainties are shown separately. The multiplicative hadronisation correction applied to the NLO prediction is shown in the last column. The uncertainty shown for the hadronisation correction is half the spread between the values obtained using the HERWIG and PYTHIA models. These values were used in section 8.2 and 8.3.*

x_p^{obs} bin	$d\sigma/dx_p^{obs}$	Δ_{stat}	Δ_{syst}	Δ_{ES} (nb)	C_{had}
0.0055, 0.0110	23.28	± 2.47	$^{+2.70}_{-2.58}$	$^{+0.62}_{-0.95}$	0.799 ± 0.040
0.0110, 0.0165	36.90	± 2.96	$^{+1.95}_{-2.74}$	$^{+2.53}_{-3.05}$	0.910 ± 0.031
0.0165, 0.0220	30.72	± 2.57	$^{+2.91}_{-2.08}$	$^{+1.90}_{-2.20}$	0.953 ± 0.027
0.0220, 0.0275	18.55	± 2.05	$^{+0.97}_{-1.18}$	$^{+1.61}_{-1.49}$	0.985 ± 0.017
0.0275, 0.0330	7.84	± 1.50	$^{+0.33}_{-1.88}$	$^{+0.58}_{-0.37}$	0.984 ± 0.019
0.0330, 0.0385	3.21	± 0.77	$^{+0.56}_{-0.39}$	$^{+0.02}_{-0.41}$	1.020 ± 0.047
0.0385, 0.0440	2.37	± 0.69	$^{+0.55}_{-0.31}$	$^{+0.41}_{-0.02}$	1.022 ± 0.012

Table A.2: *Measured cross sections as a function of x_p^{obs}. For further details, see the caption to Table A.1.*

x_p^{obs} bin	$d\sigma/dx_p^{obs}$	Δ_{stat}	Δ_{syst}	Δ_{ES} (nb)	C_{had}
$x_\gamma^{obs} < 0.75$					
0.0055, 0.0110	3.65	± 0.94	$^{+1.15}_{-1.76}$	$^{+0.24}_{-0.19}$	1.21 ± 0.063
0.0110, 0.0165	11.59	± 1.73	$^{+1.91}_{-1.00}$	$^{+1.95}_{-1.05}$	1.11 ± 0.013
0.0165, 0.0220	12.39	± 1.85	$^{+0.77}_{-2.65}$	$^{+0.55}_{-0.87}$	1.09 ± 0.012
0.0220, 0.0275	7.36	± 1.62	$^{+1.31}_{-1.04}$	$^{+0.78}_{-0.46}$	1.08 ± 0.037
0.0275, 0.0330	3.02	± 0.85	$^{+0.32}_{-0.93}$	$^{+0.20}_{-0.18}$	1.07 ± 0.012
0.0330, 0.0385	1.52	± 0.68	$^{+0.25}_{-1.22}$	$^{+0.48}_{-0.55}$	1.13 ± 0.052
0.0385, 0.0440	0.89	± 0.45	$^{+1.06}_{-0.18}$	$^{+0.15}_{-0.08}$	1.11 ± 0.074
$x_\gamma^{obs} > 0.75$					
0.0055, 0.0110	19.49	± 2.28	$^{+2.16}_{-1.87}$	$^{+0.39}_{-0.75}$	0.76 ± 0.044
0.0110, 0.0165	25.20	± 2.40	$^{+1.65}_{-4.98}$	$^{+0.85}_{-2.04}$	0.86 ± 0.040
0.0165, 0.0220	18.55	± 1.87	$^{+2.37}_{-0.55}$	$^{+1.29}_{-1.34}$	0.90 ± 0.040
0.0220, 0.0275	11.23	± 1.44	$^{+0.71}_{-0.68}$	$^{+0.95}_{-0.97}$	0.95 ± 0.038
0.0275, 0.0330	4.91	± 1.21	$^{+0.52}_{-1.07}$	$^{+0.40}_{-0.20}$	0.95 ± 0.030
0.0330, 0.0385	2.06	± 0.59	$^{+0.81}_{-0.18}$	$^{+0.09}_{-0.22}$	0.98 ± 0.078
0.0385, 0.0440	1.12	± 0.67	$^{+0.34}_{-0.30}$	$^{+0.20}_{-0.04}$	0.998 ± 0.004

Table A.3: *Measured cross sections as a function of x_p^{obs} for $x_\gamma^{obs} < 0.75$ and $x_\gamma^{obs} > 0.75$. For further details, see the caption to Table A.1.*

M_{jj} bin	$d\sigma/dM_{jj}$	$\Delta_{\rm stat}$	$\Delta_{\rm syst}$	$\Delta_{\rm ES}$ (nb)	$C_{\rm had}$
18.0, 22.0	0.0787	± 0.0052	$^{+0.0109}_{-0.0047}$	$^{+0.0050}_{-0.0040}$	0.89 ± 0.027
22.0, 26.0	0.0487	± 0.0039	$^{+0.0013}_{-0.0029}$	$^{+0.0012}_{-0.0041}$	0.91 ± 0.030
26.0, 30.0	0.0224	± 0.0024	$^{+0.0032}_{-0.0014}$	$^{+0.0024}_{-0.0015}$	0.93 ± 0.037
30.0, 34.0	0.0091	± 0.0017	$^{+0.0013}_{-0.0013}$	$^{+0.0008}_{-0.0008}$	0.93 ± 0.038
34.0, 38.0	0.0045	± 0.0014	$^{+0.0009}_{-0.0017}$	$^{+0.0002}_{-0.0005}$	0.95 ± 0.021
38.0, 42.0	0.0042	± 0.0010	$^{+0.0009}_{-0.0007}$	$^{+0.0003}_{-0.0009}$	0.96 ± 0.044
42.0, 46.0	0.0013	± 0.0009	$^{+0.0012}_{-0.0004}$	$^{+0.0001}_{-0.0002}$	0.96 ± 0.063
46.0, 50.0	0.0010	± 0.0004	$^{+0.0005}_{-0.0002}$	$^{+0.0003}_{-0.0001}$	0.94 ± 0.032

Table A.4: *Measured cross sections as a function of M_{jj}. For further details, see the caption to Table A.1.*

$\bar{\eta}$ bin	$d\sigma/d\bar{\eta}$	$\Delta_{\rm stat}$	$\Delta_{\rm syst}$	$\Delta_{\rm ES}$ (nb)	$C_{\rm had}$
-0.700, -0.525	0.061	± 0.0378	$^{+0.0586}_{-0.0441}$	$^{+0.0030}_{-0.0046}$	0.58 ± 0.071
-0.525, -0.350	0.232	± 0.0417	$^{+0.0208}_{-0.0229}$	$^{+0.0027}_{-0.0051}$	0.76 ± 0.052
-0.350, -0.175	0.382	± 0.0479	$^{+0.0464}_{-0.0387}$	$^{+0.0266}_{-0.0200}$	0.86 ± 0.032
-0.175, 0.000	0.399	± 0.0672	$^{+0.0492}_{-0.0471}$	$^{+0.0224}_{-0.0358}$	0.90 ± 0.032
0.000, 0.175	0.593	± 0.0647	$^{+0.0855}_{-0.0598}$	$^{+0.0229}_{-0.0538}$	0.93 ± 0.023
0.175, 0.350	0.657	± 0.0665	$^{+0.0562}_{-0.0289}$	$^{+0.0422}_{-0.0550}$	0.95 ± 0.027
0.350, 0.525	0.732	± 0.0766	$^{+0.0622}_{-0.0373}$	$^{+0.0607}_{-0.0436}$	0.96 ± 0.026
0.525, 0.700	0.835	± 0.0742	$^{+0.1407}_{-0.0597}$	$^{+0.0541}_{-0.0498}$	0.99 ± 0.019

Table A.5: *Measured cross sections as a function of $\bar{\eta}$. For further details, ree the caption to Table A.1.*

$\lvert\cos\theta^*\rvert$ bin	$d\sigma/d\lvert\cos\theta^*\rvert$	$\Delta_{\rm stat}$	$\Delta_{\rm syst}$	$\Delta_{\rm ES}$ (nb)	$C_{\rm had}$
$x_\gamma^{\rm obs} < 0.75$					
0.00000, 0.10375	0.056	± 0.034	$^{+0.022}_{-0.022}$	$^{+0.014}_{-0.005}$	1.007 ± 0.014
0.10375, 0.20750	0.040	± 0.027	$^{+0.028}_{-0.010}$	$^{+0.011}_{-0.003}$	1.099 ± 0.003
0.20750, 0.31125	0.126	± 0.041	$^{+0.022}_{-0.026}$	$^{+0.011}_{-0.014}$	1.072 ± 0.026
0.31125, 0.41500	0.114	± 0.032	$^{+0.032}_{-0.025}$	$^{+0.015}_{-0.005}$	1.099 ± 0.048
0.41500, 0.51875	0.280	± 0.062	$^{+0.055}_{-0.051}$	$^{+0.027}_{-0.021}$	1.107 ± 0.041
0.51875, 0.62250	0.300	± 0.069	$^{+0.095}_{-0.059}$	$^{+0.009}_{-0.050}$	1.101 ± 0.029
0.62250, 0.72625	0.536	± 0.088	$^{+0.031}_{-0.138}$	$^{+0.005}_{-0.045}$	1.145 ± 0.014
0.72625, 0.83000	0.732	± 0.108	$^{+0.087}_{-0.155}$	$^{+0.053}_{-0.036}$	1.115 ± 0.018
$x_\gamma^{\rm obs} > 0.75$					
0.00000, 0.10375	0.277	± 0.055	$^{+0.049}_{-0.038}$	$^{+0.012}_{-0.030}$	0.923 ± 0.069
0.10375, 0.20750	0.401	± 0.065	$^{+0.037}_{-0.064}$	$^{+0.044}_{-0.030}$	0.919 ± 0.044
0.20750, 0.31125	0.471	± 0.063	$^{+0.045}_{-0.080}$	$^{+0.020}_{-0.039}$	0.910 ± 0.052
0.31125, 0.41500	0.390	± 0.070	$^{+0.055}_{-0.036}$	$^{+0.023}_{-0.028}$	0.906 ± 0.068
0.41500, 0.51875	0.584	± 0.082	$^{+0.048}_{-0.047}$	$^{+0.024}_{-0.034}$	0.876 ± 0.056
0.51875, 0.62250	0.636	± 0.089	$^{+0.044}_{-0.040}$	$^{+0.017}_{-0.030}$	0.863 ± 0.061
0.62250, 0.72625	0.810	± 0.098	$^{+0.094}_{-0.026}$	$^{+0.059}_{-0.041}$	0.832 ± 0.036
0.72625, 0.83000	0.922	± 0.126	$^{+0.105}_{-0.090}$	$^{+0.026}_{-0.046}$	0.756 ± 0.013

Table A.6: *Measured cross sections as a function of $\lvert\cos\theta^*\rvert$ for $x_\gamma^{\rm obs} < 0.75$ and $x_\gamma^{\rm obs} > 0.75$. For further details, see the caption to Table A.1.*

$\cos\theta^*$ bin	$d\sigma/d\cos\theta^*$	$\Delta_{\rm stat}$	$\Delta_{\rm syst}$	$\Delta_{\rm ES}$ (nb)	$C_{\rm had}$
$x_\gamma^{\rm obs} < 0.75$					
-0.830, -0.664	0.471	±0.072	$^{+0.065}_{-0.077}$	$^{+0.034}_{-0.023}$	1.063 ± 0.008
-0.664, -0.498	0.198	±0.036	$^{+0.043}_{-0.025}$	$^{+0.006}_{-0.018}$	1.065 ± 0.023
-0.498, -0.332	0.111	±0.028	$^{+0.028}_{-0.014}$	$^{+0.012}_{-0.007}$	1.084 ± 0.029
-0.332, 0.000	0.032	±0.011	$^{+0.009}_{-0.010}$	$^{+0.006}_{-0.003}$	1.056 ± 0.0004
0.000, 0.332	0.043	±0.015	$^{+0.009}_{-0.007}$	$^{+0.006}_{-0.004}$	1.105 ± 0.061
0.332, 0.498	0.079	±0.024	$^{+0.015}_{-0.021}$	$^{+0.020}_{-0.003}$	1.178 ± 0.140
0.498, 0.664	0.064	±0.035	$^{+0.050}_{-0.028}$	$^{+0.001}_{-0.013}$	1.374 ± 0.215
0.664, 0.830	0.148	±0.039	$^{+0.014}_{-0.038}$	$^{+0.001}_{-0.014}$	1.608 ± 0.248
$x_\gamma^{\rm obs} > 0.75$					
-0.830, -0.664	0.557	±0.066	$^{+0.069}_{-0.054}$	$^{+0.027}_{-0.017}$	0.758 ± 0.014
-0.664, -0.498	0.371	±0.048	$^{+0.024}_{-0.021}$	$^{+0.018}_{-0.016}$	0.842 ± 0.041
-0.498, -0.332	0.258	±0.046	$^{+0.034}_{-0.028}$	$^{+0.017}_{-0.023}$	0.880 ± 0.053
-0.332, 0.000	0.183	±0.024	$^{+0.022}_{-0.024}$	$^{+0.009}_{-0.017}$	0.914 ± 0.048
0.000, 0.332	0.198	±0.024	$^{+0.018}_{-0.018}$	$^{+0.013}_{-0.017}$	0.922 ± 0.062
0.332, 0.498	0.212	±0.035	$^{+0.029}_{-0.008}$	$^{+0.013}_{-0.008}$	0.892 ± 0.065
0.498, 0.664	0.313	±0.053	$^{+0.024}_{-0.043}$	$^{+0.001}_{-0.023}$	0.885 ± 0.076
0.664, 0.830	0.308	±0.068	$^{+0.031}_{-0.023}$	$^{+0.014}_{-0.019}$	0.831 ± 0.071

Table A.7: *Measured cross sections as a function of $\cos\theta^*$ for $x_\gamma^{\rm obs} < 0.75$ and $x_\gamma^{\rm obs} > 0.75$. For further details, see the caption to Table A.1.*

z bin	$1/\sigma(d\sigma/dz)$	$\Delta_{\rm stat}$	$\Delta_{\rm syst}$	$C_{\rm had}$
0.16, 0.30	0.391	±0.159	$^{+0.356}_{-0.228}$	1.701 ± 0.148
0.30, 0.44	1.300	±0.141	$^{+0.109}_{-0.186}$	1.421 ± 0.283
0.44, 0.58	1.627	±0.130	$^{+0.110}_{-0.061}$	1.178 ± 0.180
0.58, 0.72	1.753	±0.120	$^{+0.223}_{-0.151}$	1.054 ± 0.092
0.72, 0.86	1.480	±0.111	$^{+0.110}_{-0.208}$	0.966 ± 0.040
0.86, 1.00	0.592	±0.076	$^{+0.084}_{-0.085}$	1.195 ± 0.009

Table A.8: *Measured relative cross sections as a function of z. The statistical and systematic uncertainties are shown separately. The systematics uncertainties includes jet energy scale uncertainties. The multiplicative hadronisation correction applied to the NLO non-relative prediction is shown in the last column. The uncertainty shown for the hadronisation correction is half the spread between the values obtained using the HERWIG and PYTHIA models. These values were used in section 9.1.5, 9.2 and 9.3.*

Appendix B

Systematic Uncertainties

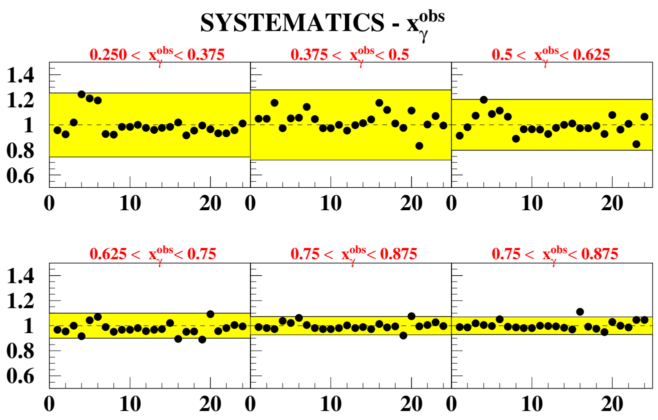

1) $E_T^{jet} > 4$ GeV	7) $-0.65 < \bar{\eta} < 0.75$	13) $p_t(\pi_S) > 0.125$ GeV	19) CAL scale +3%
2) $E_T^{jet} > 6$ GeV	8) $-0.75 < \bar{\eta} < 0.65$	14) $p_t(\pi_S) > 0.175$ GeV	20) CAL scale −3%
3) $138 < W < 264$ GeV	9) $-2.3 < \eta^{jet} < 2.5$	15) Resolved = 55%	21) $p_T/E_T^{\theta>10^\circ} > 0.1425$
4) $122 < W < 296$ GeV	10) $-2.5 < \eta^{jet} < 2.3$	16) HERWIG	22) $p_T/E_T^{\theta>10^\circ} > 0.1575$
5) M_{jj} − 20% reso.	11) $p_t(K,\pi) > 0.475$ GeV	17) $0.152 < CR < 0.165$ GeV	23) $1.80 < M(D^0) < 1.93$ GeV
6) M_{jj} + 20% reso.	12) $p_t(K,\pi) > 0.525$ GeV	18) $0.15 < CR < 0.163$ GeV	24) $0.143 < \Delta M < 0.148$ GeV

Figure B.1: *Systematic uncertainties on each bin of the cross section as a function of $x_\gamma^{\rm obs}$. The shaded band shows the statistical errors on the central ratio values. The systematics shown in Figs. B.1-10 were used in sections 8.2.*

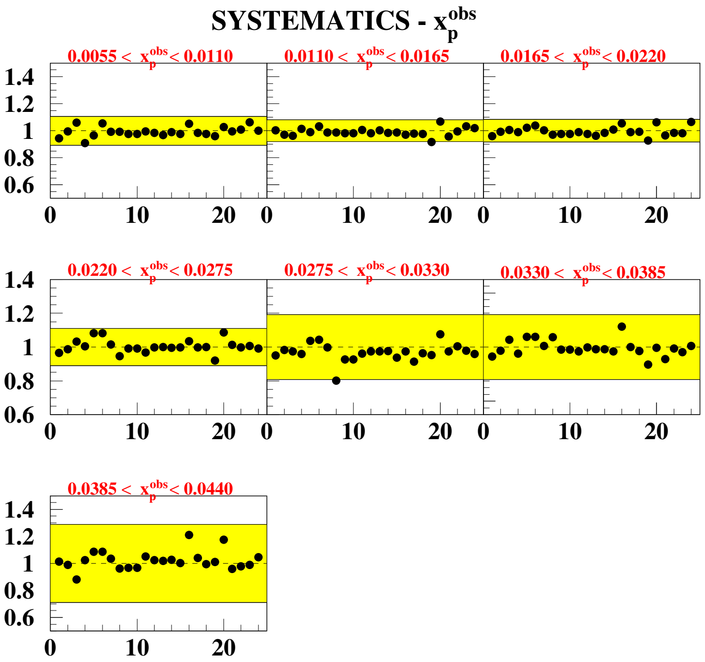

Figure B.2: *Systematic uncertainties on each bin of the cross section as a function of $x_p^{\rm obs}$. The shaded band shows the statistical errors on the central ratio values. For further details, see Fig. B.1.*

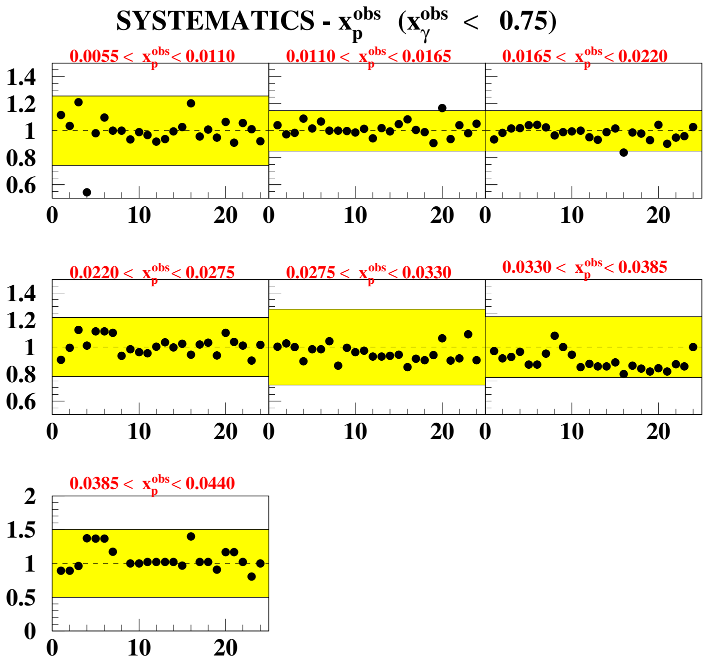

Figure B.3: *Systematic uncertainties on each bin of the cross section as a function of $x_p^{\rm obs}$ for $x_\gamma^{\rm obs} < 0.75$. The shaded band shows the statistical errors on the central ratio values. For further details, see Fig. B.1.*

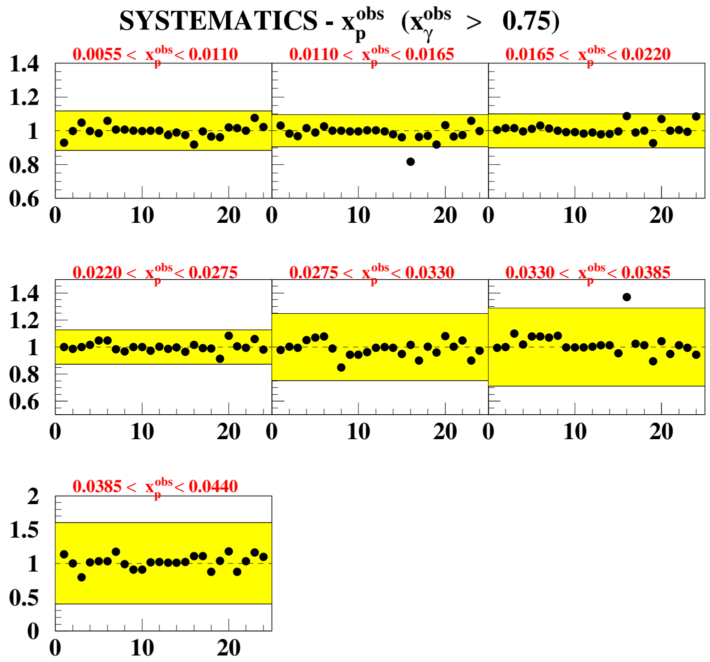

Figure B.4: *Systematic uncertainties on each bin of the cross section as a function of $x_p^{\rm obs}$ for $x_\gamma^{\rm obs} > 0.75$. The shaded band shows the statistical errors on the central ratio values. For further details, see Fig. B.1.*

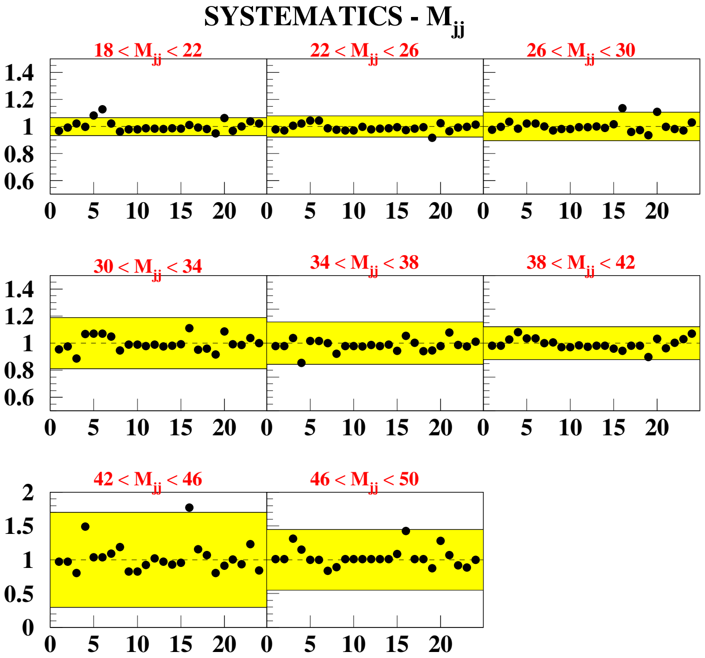

Figure B.5: *Systematic uncertainties on each bin of the cross section as a function of M_{jj}. The shaded band shows the statistical errors on the central ratio values. For further details, see Fig. B.1.*

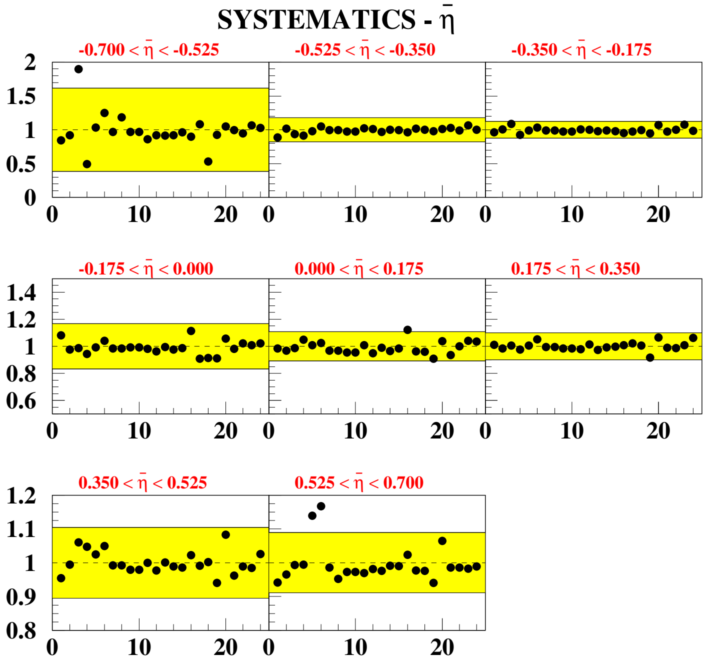

Figure B.6: *Systematic uncertainties on each bin of the cross section as a function of $\bar{\eta}$. The shaded band shows the statistical errors on the central ratio values. For further details, see Fig. B.1.*

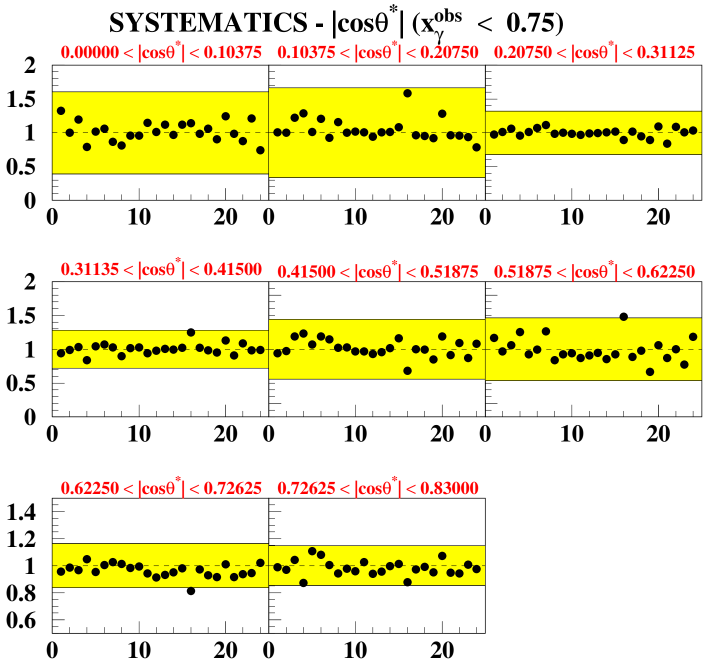

Figure B.7: *Systematic uncertainties on each bin of the cross section as a function of $|\cos\theta^*|$ for $x_\gamma^{\rm obs} < 0.75$. The shaded band shows the statistical errors on the central ratio values. For further details, see Fig. B.1.*

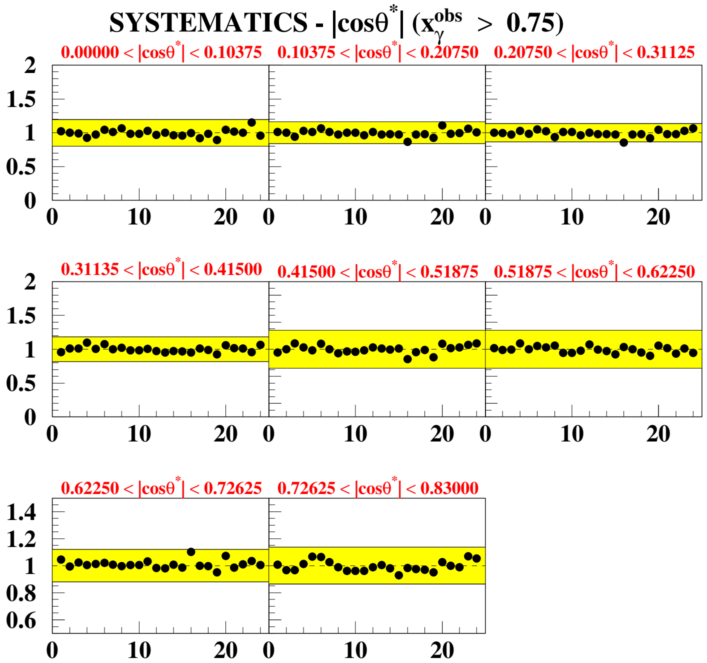

Figure B.8: *Systematic uncertainties on each bin of the cross section as a function of $|\cos\theta^*|$ for $x_\gamma^{\rm obs} > 0.75$. The shaded band shows the statistical errors on the central ratio values. For further details, see Fig. B.1.*

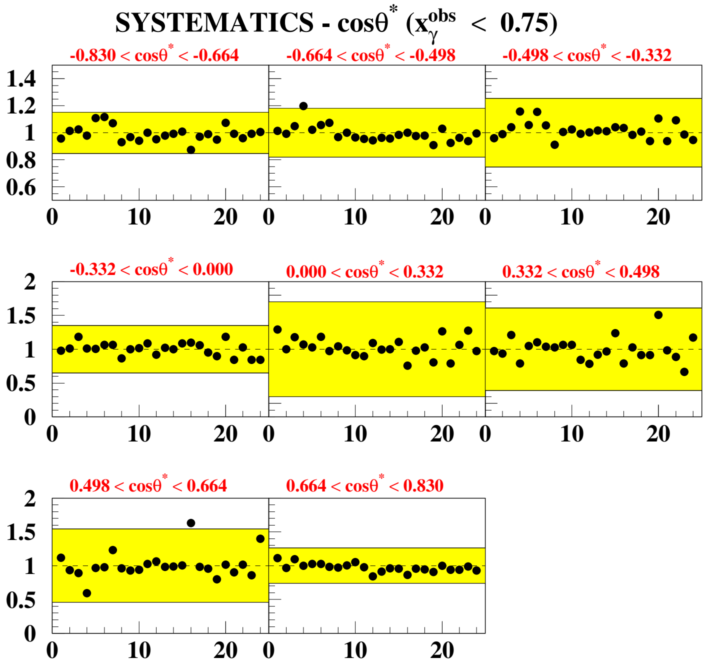

Figure B.9: *Systematic uncertainties on each bin of the cross section as a function of $\cos\theta^*$ for $x_\gamma^{\rm obs} < 0.75$. The shaded band shows the statistical errors on the central ratio values. For further details, see Fig. B.1.*

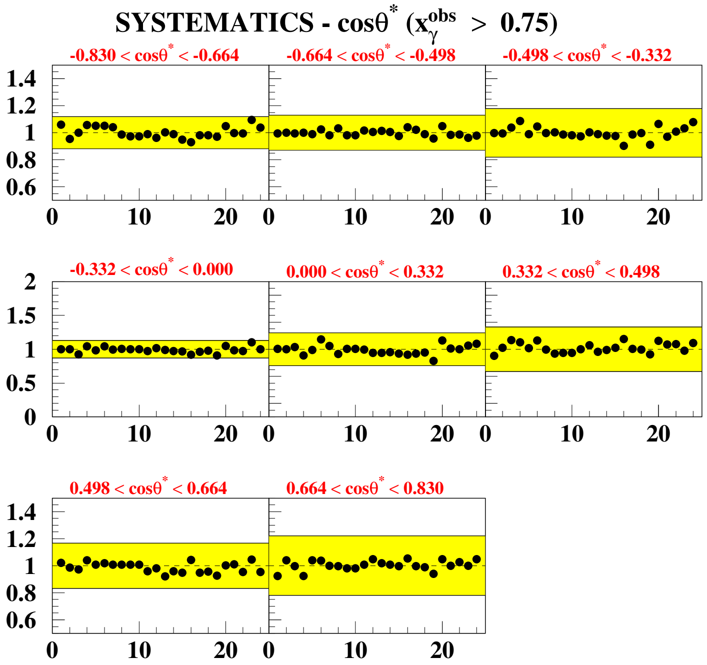

Figure B.10: *Systematic uncertainties on each bin of the cross section as a function of $\cos\theta^*$ for $x_\gamma^{\rm obs} > 0.75$. The shaded band shows the statistical errors on the central ratio values. For further details, see Fig. B.1.*

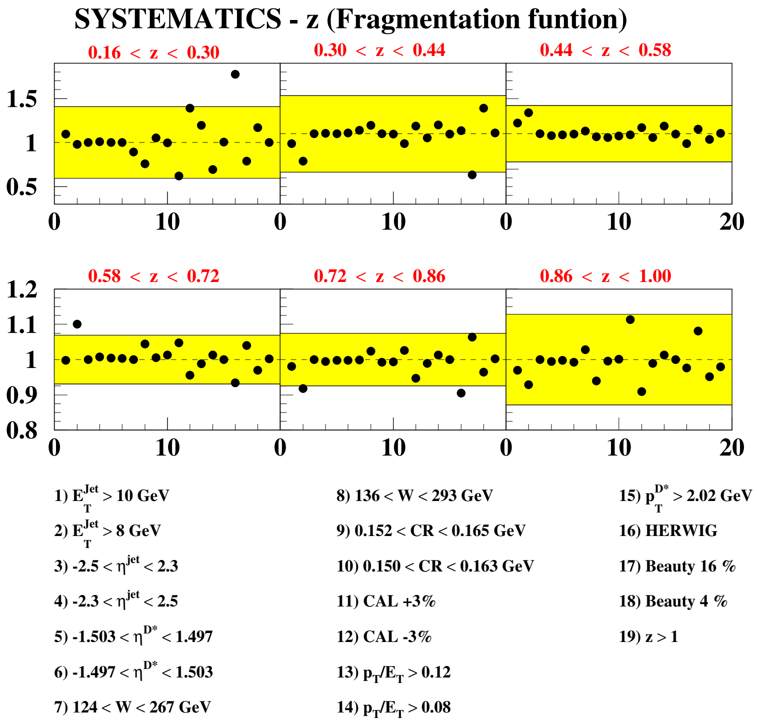

Figure B.11: *Systematic uncertainties on each bin of the relative cross section as a function of the z, used in section 9.1.5. The shaded band shows the statistical errors on the central ratio values.*

Appendix C

Hadronisation Corrections

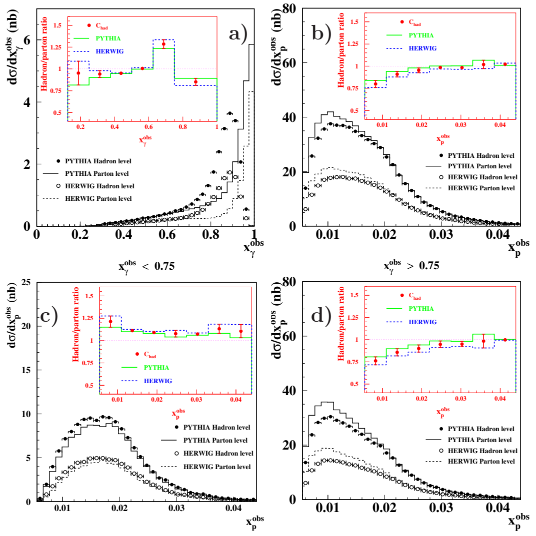

Figure C.1: *Differential cross section as a function of a) x_γ^{obs}, b) x_p^{obs}, with resolved- c) and direct-enriched d) events predicted by PYTHIA and HERWIG MC simulations, compared to the cross section obtained using the parton level jets. The insets are the hadronisation corrections obtained using PYTHIA and HERWIG respectively used in section 8.3.2. See also Fig. C.2.*

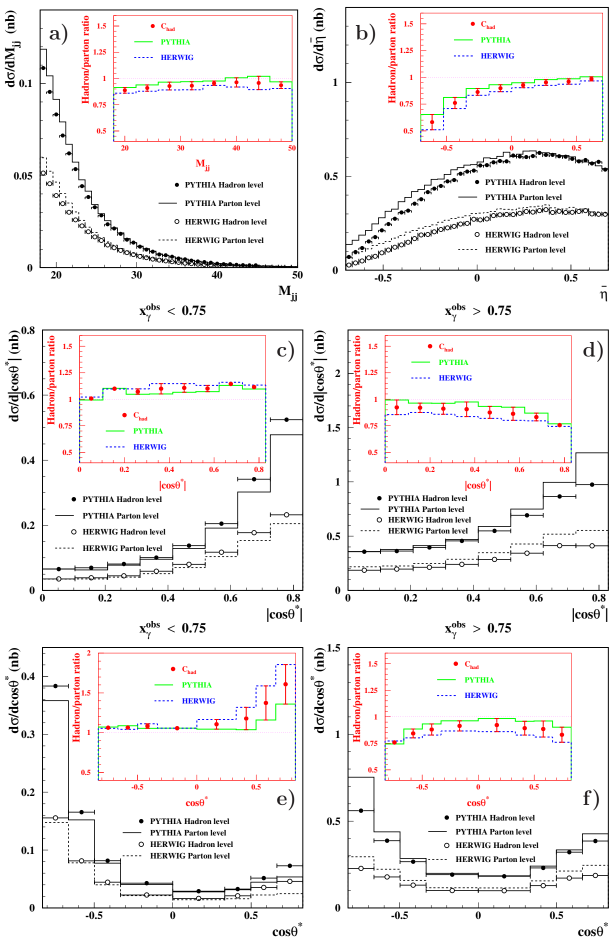

Figure C.2: *Differential cross section as a function of a) M_{jj}, b) $\bar{\eta}$, c) $|\cos\theta^*|$ with $x_\gamma^{\rm obs} < 0.75$ d) $|\cos\theta^*|$ with $x_\gamma^{\rm obs} > 0.75$ e) $\cos\theta^*$ with $x_\gamma^{\rm obs} < 0.75$ and f) $\cos\theta^*$ with $x_\gamma^{\rm obs} > 0.75$ predicted by PYTHIA (full dots) and HERWIG (open dots), compared to the cross section obtained using the parton level jets. The insets are the hadronisation corrections obtained using PYTHIA (solid line) and HERWIG (dashed line) respectively used in section 8.3.2. The full dots in the insets represents the mean of the ratios obtained using PYTHIA and HERWIG, whereas the errors on them are half the spread between the two MCs.*

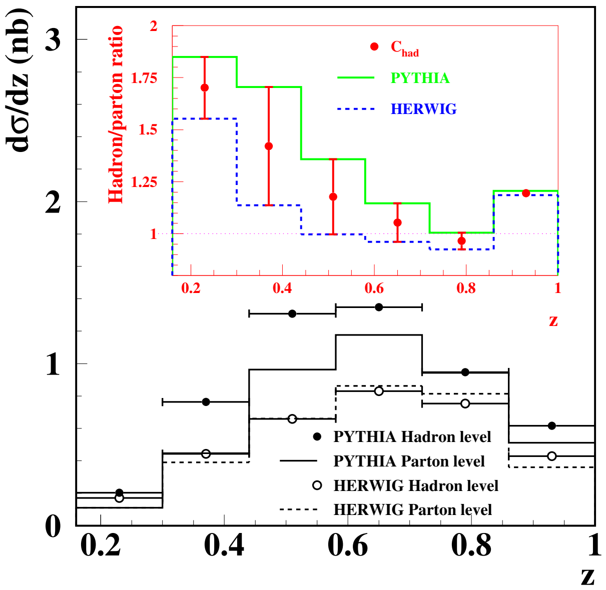

Figure C.3: *Differential cross section as a function of z, predicted by PYTHIA (full dots) and HERWIG (open dots), compared to the cross section obtained using the parton level jets. The insets are the hadronisation corrections obtained using PYTHIA (solid line) and HERWIG (dashed line) respectively used in section 9.2.1. The full dots on the insets represents the mean of the ratio obtained using PYTHIA and HERWIG, whereas the errors on them are half the spread between the two MCs.*

Glossary

AFG .... Aurenche, Fontannaz and Guillet, a photon density parameterisation, named after their authors.

ARGUS .... A complete particle detector, upgraded with a microvertex drift chamber for B-meson physics, at DESY DORIS-II.

BCAL .... Barrel Calorimeter.

BFKL .... Balitskii, Fadin, Kuraev, and Lipatov, the evolution equations, named after their authors.

BGF .... A leading order subprocess involving boson gluon fusion.

CAL .... Calorimeter.

CASCADE .... Full hadron level Monte Carlo generator for ep and pp scattering at small x according to the CCFM evolution equations.

CCFM .... Catani, Ciafaloni, Fiorani and Marchesini, the evolution equations, named after their authors.

CTD .... Central Tracking Detector.

CTEQ .... The Coordinated Theoretical-Experimental Project on QCD.

DESY .... Deutsches Elektronen-Synchrotron.

DGLAP .... Dokshitzer, Gribov, Lipatov, Altarelli and Parisi, the evolution equations, named after their authors.

DIS .... Deep Inelastic Scattering.

DST .... Data Summary Tape, the basic data output format.

EFO .... Energy Flow Objects, reconstructed detector objects using tracking and calorimeter information.

EMC .... The electromagnetic section of the calorimeter.

FCAL .... Forward Calorimeter.

FLT .... First Level Trigger.

FO .... Fixed Order.

FONLL .... Program to calculate heavy quark transverse momentum and rapidity distributions in hadron-hadron and photon-hadron collisions, matching Fixed Order next-to-leading order terms and Next-to-Leading-Log large-p_T resummation.

GRV .... Gluck, Reya and Vogt, a photon density parameterisation, named after their authors.

HAC .... Hadronic section of the calorimeter.

HERA .... Hadron Electron Ring Anlage

HERWIG .... An event generator for hadron emission reactions with interfering gluons.

IR .... A kind of divergence, Infra Red in the QCD calculations.

JB .... A method based on the hadronic system to reconstruct the photon parameter used at HERA named after their authors, Jacquet and Blondel.

KMS .... Unified approach towards DGLAP-BFKL evolution equation, named after their authors Kwiecinski, Martin and Stasto.

LEP .... Large Electron and Positron collider at CERN.

LO .... Leading Order, first term in a series expansion for the calculation of a cross section.

LUMI .... Luminosity detector.

MC .... Monte Carlo.

NLO .... Next-to-leading order QCD calculation.

OPAL .... OPAL, a detector at LEP.

PDF .... Parton Distribution Function.

PGF .... Photon Gluon Fusion.

PYTHIA .... A program for the generation of high-energy physics events, i.e. for the description of collisions at high energies between elementary particles.

QCD .... Quantum Chromodynamics

QPM .... Quark parton model.

RCAL .... Rear calorimeter.

SLT .... Second Level Trigger.

TLT .... Third Level Trigger.

UV .... A kind of divergence, Ultra Violet in the QCD calculations.

VFNS .... Variable Flavour Number Scheme.

VMD .... Vector meson dominance model.

WWA .... Weizsäcker-Williams approximation.

References

[1] J.J. Aubert et al., Phys. Rev. Lett. **33**, 1404 (1974);
J.E. Augustin et al., Phys. Rev. Lett. **33**, 1406 (1974).

[2] T. Appelquist and H.D. Politzer, Phys. Rev. Lett. **34**, 43 (1975);
A. De Rújula and S.L. Glashow, Phys. Rev. Lett. **34**, 46 (1975);
C.A. Dominguez and M. Greco, Nuovo Cim. Lett. **12**, 439 (1975).

[3] S.W. Herb et al., Phys. Rev. Lett. **39**, 252 (1977).

[4] CDF Coll., F. Abe et al., Phys. Rev. **D 50**, 2966 (1994);
CDF Coll., F. Abe et al., Phys. Rev. Lett. **74**, 2626 (1995);
D0 Coll., S. Abachi et al., Phys. Rev. Lett. **74**, 2632 (1995).

[5] T.H. Bauer et al., Rev. Mod. Phys. **50**, 261 (1978).

[6] L. Stodolsky, Phys. Rev. Lett. **18**, 135 (1967);
H. Joos, Phys. Lett. **B 18**, 103 (1967).

[7] E. Paul. Invited talk given at 21st Int. Symp. on Multiparticle Dynamics, Wuhan, China, Sep 23-27, 1991.

[8] E683 Coll., D. Adams et al., Phys. Rev. Lett. **72**, 2337 (1994).

[9] V.M. Budnev et al., Phys. Rep. **15**, 181 (1974).

[10] C.F. von Weizsäcker, Z. Phys. **88**, 612 (1934). In German;
E.J. Williams, Phys. Rev. **45**, 729 (1934).

[11] H1 Coll., S. Aid et al., Z. Phys. **C 69**, 27 (1995).

[12] ZEUS Coll., M. Derrick et al., Phys. Lett. **B 293**, 465 (1992);
ZEUS Coll., M. Derrick et al., Z. Phys. **C 63**, 391 (1994).

[13] D.O. Caldwell et al., Phys. Rev. Lett. **40**, 1222 (1978);
S.I. Alekhin et al.. CERN-HERA-87-01.

[14] A. Donnachie and P.V. Landshoff, Phys. Lett. **B 296**, 227 (1992).

[15] ZEUS Coll., S. Chekanov et al., Nucl. Phys. **B 627**, 3 (2002).

[16] P. Kessler, Acta Phys. Austriaca **41**, 141 (1975);
S. Frixione et al., Phys. Lett. **B 319**, 339 (1993).

[17] R.P. Feynman, Phys. Rev. Lett. **23**, 1415 (1969).

[18] J.D. Bjorken, Phys. Rev. **179**, 1547 (1969);
R.P. Feynman, *Photon-Hadron Interactions*. Benjamin, New York, 1972.

[19] F. Halzen and A.D. Martin, *Quarks and Leptons: An Introductory Course in Modern Particle Physics*. John Wiley & Sons, Inc, 1984.

[20] C.G. Callan and D.J. Gross, Phys. Rev. Lett. **22**, 156 (1969).

[21] E.D. Bloom et al., Phys. Rev. Lett. **23**, 930 (1969);
M. Breidenbach et al., Phys. Rev. Lett. **23**, 935 (1969);
G. Miller et al., Phys. Rev. **D 5**, 528 (1972).

[22] H. Deden et al., Nucl. Phys. **B 85**, 269 (1975).

[23] T. Eichten et al., Phys. Lett. **B 46**, 274 (1973).

[24] R. Brandelik et al., Phys. Lett. **B 86**, 243 (1979).

[25] H1 Coll., *Determination of the longitudinal proton structure function F_L at low Q^2 at HERA*, available on
`http://www-h1.desy.de/h1/www/publications/conf/conf_list.html`.

Abstract 083, *Int. Europhysics Conf. on High Energy Physics (EPS03)*, Aachen, Germany, July 17-23, 2003.

[26] ZEUS Coll., S. Chekanov et al., Eur. Phys. J. **C 21**, 443 (2001).

[27] S.G. Gorishnii, A.L. Kataev, and S.A. Larin, Phys. Lett. **B 259**, 144 (1991).

[28] V.E.Barnes, et al., Phys. Rev. Lett. **12**, 204 (1964).

[29] G. 't Hooft, and M.J.G. Veltman, Nucl. Phys. **B 44**, 189 (1972).

[30] Stefano Catani, Preprint hep-ph/9712442, 1997.

[31] B.R. Martin and G. Shaw, *Particle physics*. The Manchester physics series, Wiley, Chichester, UK, 1992.

[32] R.P. Feynman, *Photon-Hadron Interactions*. Benjamin, New York, 1972;
Y.L. Dokshitzer, D. Diakonov and S.I. Troian, Phys. Rep. **58**, 269 (1980).

[33] G. Parisi. Presented at Int. Meeting on Neutrino Physics, Flaine, France, Mar 6-12, 1976;
G. Altarelli and G. Parisi, Nucl. Phys. **B 126**, 298 (1977);
Guido Altarelli, Phys. Rep. **81**, 1 (1982).

[34] G. Altarelli and G. Parisi, Nucl. Phys. **B 126**, 298 (1977).

[35] W. Furmanski and R. Petronzio, Phys. Lett. **B 97**, 437 (1980).

[36] V.N. Gribov and L.N. Lipatov, Sov. J. Nucl. Phys. **15**, 438 (1972);
L.N. Lipatov, Sov. Phys. JETP **45**, 216 (1977);
Yu.L. Dokshitzer, Sov. Phys. JETP **46**, 641 (1977).

[37] Stefano Catani, Preprint hep-ph/0005233, 2000.

[38] A. De Rújula et al., Phys. Rev. **D 10**, 1649 (1974).

[39] H1 Coll., C. Adloff et al., Preprint hep-ex/0304003, 2003.

[40] Ya.Ya. Balitskiĭ and L.N. Lipatov, Sov. J. Nucl. Phys. **28**, 822 (1978);
E.A. Kuraev, L.N. Lipatov and V.S. Fadin, Sov. Phys. JETP **44**, 443 (1976);
E.A. Kuraev, L.N. Lipatov and V.S. Fadin, Sov. Phys. JETP **45**, 199 (1977).

[41] H1 Coll., I. Abt et al., Nucl. Phys. **B 407**, 515 (1993);
ZEUS Coll., M. Derrick et al., Phys. Lett. **B 316**, 412 (1993).

[42] M. Ciafaloni, Nucl. Phys. **B 296**, 49 (1988);
S. Catani, F. Fiorani and G. Marchesini, Phys. Lett. **B 234**, 339 (1990);
S. Catani, F. Fiorani and G. Marchesini, Nucl. Phys. **B 336**, 18 (1990);
G. Marchesini, Nucl. Phys. **B 445**, 49 (1995).

[43] G. Marchesini, Nucl. Phys. **B 445**, 49 (1995).

[44] S. Catani, M. Ciafaloni, and F. Hautmann, Phys. Lett. **B 242**, 97 (1990);
S. Catani, M. Ciafaloni, and F. Hautmann, Nucl. Phys. **B 366**, 135 (1991);
J.C. Collins, and R.K. Ellis, Nucl. Phys. **B 360**, 3 (1991);
G. Marchesini, and B.R. Webber, Nucl. Phys. **B 386**, 215 (1992);
S. Catani, and F. Hautmann, Phys. Lett. **B 315**, 157 (1993);
S. Catani, and F. Hautmann, Nucl. Phys. **B 427**, 475 (1994);
G. Camici, and M. Ciafaloni, Nucl. Phys. **B 467**, 25 (1996);
G. Camici, and M. Ciafaloni, Nucl. Phys. **B 496**, 305 (1997).

[45] S.J. Brodsky et al., Phys. Rev. **D 19**, 1418 (1979);
M. Chen and P.M. Zerwas, Phys. Rev. **D 12**, 187 (1975);
V.N. Gribov and L.N. Lipatov, Yad. Fiz. **15**, 781 (1972).

[46] TPC/Two γ Coll., M.P. Cain et al., Phys. Lett. **B 147**, 232 (1984).

[47] M. Drees and K. Grassie, Z. Phys. **C 28**, 451 (1985);
H. Abramowicz, K. Charchula and A. Levy, Phys. Lett. **B 269**, 458 (1991);
K. Hagiwara et al., Phys. Rev. **D 51**, 3197 (1995).

[48] M. Glück, E. Reya and A. Vogt, Phys. Rev. **D 45**, 3986 (1992).

[49] M. Glück, E. Reya and A. Vogt, Phys. Rev. **D 46**, 1973 (1992).

[50] M. Gluck, E. Reya and I. Schienbein, Phys. Rev. **D 60**, 054019 (1999).

[51] P. Aurenche, J.P. Guillet and M. Fontannaz, Z. Phys. **C 64**, 621 (1994).

[52] G.A. Schuler and T. Sjostrand, Phys. Lett. **B 300**, 169 (1993);
G.A. Schuler and T. Sjostrand, Nucl. Phys. **B 407**, 539 (1993);
G.A. Schuler and T. Sjöstrand, Z. Phys. **C 68**, 607 (1995).

[53] Ch. Berger and W. Wagner, Phys. Rep. **146**, 1 (1987).

[54] JADE Coll., W. Bartel et al., Z. Phys. **C 24** (1984);
PLUTO Coll., C. Berger et al., Phys. Lett. **B 142**, 111 (1984);
TASSO Coll., M. Althoff et al., Z. Phys. **C 31** (1986);
PLUTO Coll., C. Berger et al., Nucl. Phys. **B 281**, 365 (1987);
AMY Coll., T. Sasaki et al., Phys. Lett. **B 252**, 491 (1990).

[55] PLUTO Coll., C. Berger et al., Phys. Lett. **B 149**, 421 (1984);
PLUTO Coll., C. Berger et al., Z. Phys. **C 26**, 353 (1984);
TPC/2γ Coll., D. Bintinger et al., Phys. Rev. Lett. **54**, 763 (1985);
TPC/2γ Coll., H. Aihara et al., Phys. Rev. Lett. **58**, 97 (1987);
TPC/Two-Gamma Coll., H. Aihara et al., Z. Phys. **C 34** (1987).

[56] PLUTO Coll., C. Berger et al., Phys. Lett. **B 107**, 168 (1981).

[57] R. Nisius, Phys. Rept. **332**, 165 (2000).

[58] ZEUS Coll., S. Chekanov, et al., Phys. Rev. **D 67**, 012007 (2003).

[59] CTEQ Coll., H.L. Lai et al., Eur. Phys. J. **C 12**, 375 (2000).

[60] H1 Coll., T. Ahmed et al., Phys. Lett. **B 297**, 205 (1992);
ZEUS Coll., M. Derrick et al., Phys. Lett. **B 297**, 404 (1992).

[61] ZEUS Coll., M. Derrick et al., Phys. Lett. **B 322**, 287 (1994).

[62] ZEUS Coll., J. Breitweg et al., Eur. Phys. J. **C 1**, 109 (1998).

[63] T. Sjostrand and M.van Zijl, Phys. Rev. **D 36**, 2019 (1987);
G.A. Schuler and T. Sjostrand, Nucl. Phys. **B 407**, 539 (1993);
J.M. Butterworth et al., Z. Phys. **C 72**, 637 (1996).

[64] ZEUS Coll., M. Derrick et al., Phys. Lett. **B 384**, 401 (1995).

[65] UA1 Coll., G. Arnison et al., Phys. Lett. **B 136**, 294 (1984);
UA1 Coll., G. Arnison et al., Phys. Lett. **B 177**, 244 (1986);
CDF Coll., F. Abe et al., Phys. Rev. Lett. **62**, 3020 (1989).

[66] CDF Coll., F. Abe et al., Phys. Rev. Lett. **73**, 2296 (1994).

[67] H. Baer, J. Ohnemus and J.F. Owens, Phys. Rev. **D 40**, 2844 (1989).

[68] OPAL Collaboration, G. Abbiendi et al., Eur. Phys. J. **C 10**, 547 (1999);
OPAL Collaboration, G. Abbiendi et al., Preprint DESY-02-017 (hep-ex/0301013), 2003.

[69] S. Frixione et al., Nucl. Phys. **B 412**, 225 (1994).

[70] P. Nason, S. Dawson and R.K. Ellis, Nucl. Phys. **B 303**, 607 (1988).

[71] S. Frixione et al., Nucl. Phys. **B 412**, 225 (1994);
S. Frixione et al., Phys. Lett. **B 348**, 633 (1995);
S. Frixione et al., Nucl. Phys. **B 454**, 3 (1995).

[72] R.K. Ellis and Z. Kunszt, Nucl. Phys. **B 303**, 653 (1988);
M. Drees and R.M. Godbole, Phys. Rev. **D 39**, 169 (1989).

[73] M. Cacciari et al., Phys. Rev. **D 55**, 2736 (1997);
M. Cacciari and M. Greco, Phys. Rev. **D 55**, 7134 (1997);
J. Binnewies, B.A. Kniehl, and G. Kramer, Z. Phys. **C 76**, 677 (1997);
B.A. Kniehl, G. Kramer and M. Spira, Z. Phys. **C 76**, 689 (1997).

[74] M. Cacciari, S. Frixione and P. Nason, JHEP **03**, 006 (2001).

[75] K. Hagiwara, et al., Phys. Rev. **D 66**, 10001 (2002). Review of particle physics also available at http://pdg.lbl.gov.

[76] L. Gladilin, Preprint hep-ex/9912064, 1999.

[77] Particle Data Group, R.M. Barnett et al., Phys. Rev. **D 54**, 1 (1996).

[78] S. Nussinov, Phys. Rev. Lett. **35**, 1672 (1975);
G. J. Feldman et al., Phys. Rev. Lett. **38**, 1313 (1977).

[79] H1 Coll., *Measurement of Incusive D-meson Production in DIS at HERA*, available on
`http://www-h1.desy.de/h1/www/publications/conf/conf_list.html`.
Abstract 096, *Int. Europhysics Conf. on High Energy Physics (EPS03)*, Aachen, Germany, July 17-23, 2003.

[80] ZEUS Coll., *Measurement of D^* photoproduction at HERA*, available on
`http://www-zeus.desy.de/physics/phch/conf/amsterdam_paper.html`.
Abstract 786, *XXXIst Int. Conf. on High Energy Physics (ICHEP2002)*, Amsterdam, The Netherlands, July 24-31, 2002.

[81] H1 Coll., *Photoproduction of D^* Mesons at HERA*, available on
`http://www-h1.desy.de/h1/www/publications/conf/conf_list.html`.
Abstract 097, *Int. Europhysics Conf. on High Energy Physics (EPS03)*, Aachen, Germany, July 17-23, 2003.

[82] ZEUS Coll., J. Breitweg et al., Eur. Phys. J. **C 6**, 67 (1999).

[83] P. Nason, and C. Oleari, Nucl. Phys. **B 565**, 245 (2000).

[84] M. Glück, E. Reya and A. Vogt, Phys. Rev. **D 46**, 1973 (1992).

[85] J. Jalilian-Marian et al., Phys. Rev. **D 59**, 014014 (1999).

[86] J. Pumplin et al., Preprint hep-ph/0201195, 2002.

[87] V.G. Kartvelishvili, A.K. Likhoded, and V.A. Petrov, Phys. Lett. **B 78**, 615 (1978).

[88] S. Frixione et al., Adv. Ser. Direct. High Energy Phys. **15**, 609 (1998).

[89] M.I. Adamovich et al., WA92 Coll., Nucl. Phys. **B 495**, 3 (1997).

[90] E769 Coll., G.A. Alves et al., Phys. Rev. Lett. **77**, 2392 (1996).

[91] A. Heister et al., Eur. Phys. J. **C 28**, 437 (2003).

[92] CDF Coll., D. Acosta et al., Phys. Rev. Lett. **91**, 241804 (2003).

[93] ZEUS Coll., U. Holm (ed.), *The ZEUS Detector*. Status Report (unpublished), DESY (1993), available on `http://www-zeus.desy.de/bluebook/bluebook.html`.

[94] *A Proposal for a Large Electron-Proton Colliding Beam Facility at DESY.* (1981). Also in preprint DESY-HERA-81-10;
G. A. Voss, *Proceedings of the First European Accelerator Conference.* Rome, p. 7 (1988).

[95] G. Wolf, Preprint DESY-94-022, 1994;
H. Abramowicz and A. Caldwell, Rev. Mod. Phys. **71**, 1275 (1999).

[96] ZEUS Coll., Proposal DESY-PRC-97-01, DESY, 1997.

[97] N. Harnew et al., Nucl. Inst. Meth. **A 279**, 290 (1989);
B. Foster et al., Nucl. Phys. Proc. Suppl. **B 32**, 181 (1993);
B. Foster et al., Nucl. Inst. Meth. **A 338**, 254 (1994).

[98] G.F. Hartner et al., *VCTRAK(3.06/20): Offline Output Information* (unpublished). ZEUS-96-013, internal ZEUS-note, 1996.

[99] M. Derrick et al., Nucl. Inst. Meth. **A 309**, 77 (1991);
A. Andresen et al., Nucl. Inst. Meth. **A 309**, 101 (1991);
A. Caldwell et al., Nucl. Inst. Meth. **A 321**, 356 (1992);
A. Bernstein et al., Nucl. Inst. Meth. **A 336**, 23 (1993).

[100] M. Wing, ZEUS Coll., *Setting the jet energy scale for the ZEUS calorimeter.* 10^{th} International Conference on Calorimetry in High Energy Physics (CALOR 2002), Pasadena, California, 25-30 Mar 2002.

[101] J. Krüger, *The Uranium Scintillator Calorimeter for the ZEUS Detector at the Electron - Proton collider HERA: The Heart of ZEUS.* Habilitation Thesis, Universität Hamburg, Report DESY-F35-92-02, 1992.

[102] H. Bethe and W. Heitler, Proc. Roy. Soc. Lond. **A146**, 83 (1934).

[103] J. Andruszków et al., Preprint DESY-92-066, DESY, 1992;
J. Andruszków et al., Acta Phys. Pol. **B 32**, 2025 (2001).

[104] W. H. Smith, K. Tokushuku and L. W. Wiggers, *Proc. Computing in High-Energy Physics (CHEP), Annecy, France, Sept. 1992*, C. Verkerk and W. Wojcik (eds.), p. 222. CERN (1992). Also in preprint DESY 92-150B.

[105] L.A.T. Bauerdick et al., Report DESY-95-236, DESY, 1995.

[106] R. Brun et al., *GEANT3, Technical Report CERN-DD/EE/84-1.* CERN, 1987.

[107] H. Jung and G. P. Salam, Eur. Phys. J. **C 19**, 351 (2001);
H. Jung, Comp. Phys. Comm. **143**, 100 (2002);
H. Jung, J. Phys. **G 28**, 971 (2002).

[108] G. Marchesini et al., Comp. Phys. Comm. **67**, 465 (1992);
G. Corcella et al., **JHEP 0101**, 010 (2001);
G. Corcella et al., Preprint hep-ph/0107071, 2001.

[109] T. Sjöstrand et al., Comp. Phys. Comm. **135**, 238 (2001).

[110] J. C. Collins, D. E. Soper and G. Sterman, Nucl. Phys. **B 261**, 104 (1985);
J. C. Collins, D. E. Soper and G. Sterman, Nucl. Phys. **B 308**, 833 (1988).

[111] J.M. Butterworth et al., J. Phys. **G 22**, 883 (1996);
J.M. Butterworth et al., Z. Phys. **C 72**, 637 (1996).

[112] M.N. Mangano, P. Nason, and G. Ridolfi, Nucl. Phys. **B373**, 295 (1992).

[113] BEATRICE Coll., M. Adamovich et al., Phys. Lett. **B348**, 256 (1995);
BEATRICE Coll., Y. Aleksandrov et al., Phys. Lett. **B433**, 217 (1998).

[114] L.V. Gribov, E.M. Levin and M.G. Ryskin, Phys. Rep. **100**, 1 (1983);
E.M. Levin and M.G. Ryskin, Phys. Rep. **189**, 267 (1990);
E.M. Levin et al., Sov. J. Nucl. Phys. **53**, 657 (1991);
E.M. Levin et al., Sov. J. Nucl. Phys. **54**, 867 (1991).

[115] The Small x Coll., Bo. Andersson et al., Eur. Phys. J. **C 25**, 77 (2002).

[116] S.P. Baranov, H. Jung, L. Jonsson, S. Padhi, and N.P. Zotov, Acta Phys. Polon. **B 33**, 3257 (2002);
S.P. Baranov, H. Jung, L. Jonsson, S. Padhi, and N.P. Zotov, Preprint hep-ph/0301017, 2003.

[117] S.P. Baranov, H. Jung, and N.P. Zotov, *Proc. of the Workshop on Monte-Carlo Generators*, A. Doyle, G. Grindhammer, G. Ingelman and H. Jung (eds.), p. 484. DESY, Hamburg, Germany (1999). Also in preprint hep-ph/9910210.

[118] M.G. Ryskin et al., Phys. Atom. Nucl. **64**, 120 (2001).

[119] S.P. Baranov, and N.P. Zotov, Phys. Lett. **B491**, 111 (2000).

[120] S.P. Baranov, H. Jung, L. Jonsson, S. Padhi, and N.P. Zotov, Eur. Phys. J. **C24**, 425 (2002).

[121] B. Andersson et al., Phys. Rep. **97**, 31 (1983);
B. Andersson, G. Gustafson, and B. Soderberg, Z. Phys. **C 20**, 317 (1983).

[122] D. Amati, and G. Veneziano, Phys. Lett. **B 83**, 87 (1979);
A. Bassetto, M. Ciafaloni, and G. Marchesini, Phys. Lett. **B 83**, 207 (1979);
G. Marchesini, L. Trentadue, and G. Veneziano, Nucl. Phys. **B 181**, 335 (1981).

[123] A. Kupco, Preprint hep-ph/9906412, 1998.

[124] R.D. Field and R.P. Feynman, Phys. Rev. **D 15**, 2590 (1977);
R.D. Field and R.P. Feynman, Nucl. Phys. **B 136**, 1 (1978).

[125] X. Artru and G. Mennessier, Nucl. Phys. **B 70**, 93 (1974).

[126] M.G. Bowler, Z. Phys. **C 22**, 155 (1984).

[127] C. Peterson et al., Phys. Rev. **D 27**, 105 (1983).

[128] S.J. Brodsky, C. Peterson, and N. Sakai, Phys. Rev. **D 23**, 2745 (1981).

[129] OPAL Coll., R. Akers et al., Z. Phys. **C 67**, 27 (1995).

[130] S.D. Drell et al., Phys. Rev. **D 1**, 1617 (1970).

[131] Julius Kuti, and Victor F. Weisskopf, Phys. Rev. **D 4**, 3418 (1971).

[132] E. Norrbin, and T. Sjostrand, Preprint hep-ph/9905493, 1999.

[133] S. Padhi, *Beam Drag effects in charm-dijet Photoproduction.* Presented at ZEUS Heavy Flavour Group meeting, Jan 2002, available on `http://www-zeus.desy.de/~spadhi/beam_drag.pdf`.

[134] L.N. Lipatov, Sov. J. Nucl. Phys. **20**, 94 (1975).

[135] B. R. Webber, Nucl. Phys. **B 238**, 492 (1984).

[136] G. Hanson et al., Phys. Rev. Lett. **35**, 1609 (1975);
C. Berger et al., Phys. Lett. **B 78**, 176 (1978).

[137] G. Sterman, George and S. Weinberg, Phys. Rev. Lett. **39**, 1436 (1977).

[138] JADE Coll., W. Bartel et al., Z. Phys. **C 33**, 23 (1986);
JADE Coll., S. Bethke et al., Phys. Lett. **B 213**, 235 (1988).

[139] J.E. Huth et al., *Research Directions for the Decade. Proceedings of Summer Study on High Energy Physics, 1990*, E.L. Berger (ed.), p. 134. World Scientific (1992). Also in preprint FERMILAB-CONF-90-249-E.

[140] S.Catani et al., Nucl. Phys. **B406**, 187 (1993).

[141] B.R. Webber, *Proc. of the Workshop on Deep Inelastic Scattering and QCD.* DIS95, Paris (1995). Also in preprint hep-ph/9510283.

[142] S.D. Ellis and D.E. Soper, Phys. Rev. **D 48**, 3160 (1993).

[143] J. M. Butterworth, L. Feld, R. L. Saunders, *Measurement of Dijet Cross Sections in Photoproduction at HERA* (unpublished). ZEUS-97-057.

[144] J. Repond, *Jet Energy Corrections* (unpublished). ZEUS Note-96-104.

[145] J.M. Butterworth, E.A. Heaphy and M.R. Sutton, *How to Determine Correction Factors* (unpublished). ZEUS Note-98-032.

[146] G.M. Briskin, *Diffractive Dissociation in ep Deep Inelastic Scattering*. Ph.D. Thesis, Tel Aviv University, 1998. (Unpublished).

[147] F. Jacquet and A. Blondel, *Proceedings of the Study for an ep Facility for Europe*, U. Amaldi (ed.), p. 391. Hamburg, Germany (1979). Also in preprint DESY 79/48.

[148] ZEUS Coll., M. Derrick et al., Phys. Lett. **B 348**, 665 (1995).

[149] S. Frixione and G. Ridolfi, Nucl. Phys. **B 507**, 315 (1997).

[150] CDF Coll., F. Abe et al., Phys. Rev. Lett. **65**, 968 (1990).

[151] N. Tuning, *Proton Structure Functions at HERA*. Ph.D. Thesis, Amsterdam University, 2001.

[152] H. Abramowicz et al., Nucl. Inst. Meth. **A 365**, 508 (1995).

[153] ZEUS Coll., J. Breitweg et al., Eur. Phys. J. **C 11**, 35 (1999).

[154] ZEUS Coll., *Dijet Angular Distribution in D* Photoproduction at HERA*, available on `http://www-zeus.desy.de/physics/phch/ZEUS/eps01/index.html`. Abstract 499, *Int. Europhysics Conf. on High Energy Physics (EPS01)*, Budapest, Hungary, July 12-18, 2001.

[155] ZEUS Coll., J. Breitweg et al., Phys. Lett. **B 401**, 192 (1997).

[156] M.G. Ryskin et al., Phys. Atom. Nucl. **64**, 120 (2001).

[157] M. Glück, E. Reya and A. Vogt, Eur. Phys. J. **C 5**, 461 (1998).

[158] J. Kwiecinski, A.D. Martin and A.M. Stasto, Phys. Rev. **D 56**, 3991 (1997).

[159] J.R. Forshaw and R.G. Roberts, Phys. Lett. **B 319**, 539 (1993).

[160] ZEUS Coll., S. Chekanov, et al., Eur. Phys. J. **C 23**, 615 (2002).

[161] P. Aurenche, J.P. Guillet and M. Fontannaz, Z. Phys. **C 64**, 621 (1994).

[162] P. Nason and C. Oleari, Nucl. Phys. **B 565**, 245 (2000).

[163] A.D. Martin, R.G. Roberts and W.J. Stirling, Phys. Lett. **B 354**, 155 (1995).

[164] B.A. Kniehl, et al., Phys. Lett. **B 356**, 539 (1995).

[165] M. Cacciari and M. Greco, Phys. Rev. **D 55**, 7134 (1997).

[166] ARGUS Coll., H. Albrecht et al., Z. Phys. **C 52**, 353 (1991).

[167] OPAL Coll., R. Akers et al., Z. Phys. **C 67**, 27 (1995).

[168] Sanjay Padhi, *Proceedings of the International Conference on the Structure and Interactions of the Photon (Photon 2001), Ascona, Switzerland, 2-7 Sept. 2001.* World Scientific, Singapore (2001). Also in preprint hep-ex/0111023.

[169] Sanjay Padhi, Acta Phys. Polon. **B 33**, 3189 (2002).

[170] ZEUS Coll., S. Chekanov et al., Phys. Lett. **B 565**, 87 (2003).

[171] ZEUS Coll., *Dijet angular distributions in D^* photoproduction at HERA*, available on `http://www-zeus.desy.de/physics/phch/conf/amsterdam_paper.html`. Abstract 781, *XXXIst Int. Conf. on High Energy Physics (ICHEP2002)*, Amsterdam, The Netherlands, July 24-31, 2002.

[172] ZEUS Coll., *Measurement of charm fragmentation function in D^* photoproduction at HERA*, available on http://www-zeus.desy.de/physics/phch/conf/amsterdam_paper.html. Abstract 778, *XXXIst Int. Conf. on High Energy Physics (ICHEP2002)*, Amsterdam, The Netherlands, July 24-31, 2002.

[173] Sanjay Padhi, *Submitted to: Proceedings of the Workshop on New Trends in HERA Physics, Ringberg Germany, Sept. 28-Oct. 03*, G. Grindhammer, B.A. Kniehl, G. Kramer and W. Ochs (eds.). (2003), available on http://wwwth.mppmu.mpg.de/members/hera2003/talks.html.